UNIVERSITY OF SOUTHAMPTON

Faculty of Engineering and Physical Sciences
School of Engineering
Energy Technology Research Group

Designing for minimal impact: the development of an aqueous aluminium-ion battery

by

Nicole Leanne Melzack

MEng, CEng

ORCiD: 0000-0002-5578-4020

A thesis for the degree of
Doctor of Philosophy

June 2025

University of Southampton

Abstract

Faculty of Engineering and Physical Sciences
School of Engineering

Doctor of Philosophy

Designing for minimal impact: the development of an aqueous aluminium-ion battery

by Nicole Leanne Melzack

This thesis contains work related to the sustainable development of an aqueous aluminum ion battery. The battery consists of a titanium dioxide negative electrode and copper hexacynoferrate positive electrode, the electrolyte is 1 M aluminium chloride and 1 M potassium chloride. At the start of the PhD project the reported energy density was 15 Wh kg^{-1} and power density of 300 W kg^{-1}, with a cycle life of 1750 charge/discharge cycles.

Aluminium is a viable option for secondary battery technology, not only is the theoretical energy density high (8000 W kg^{-1}), but there are already well established mining, production, and recycling industries built around aluminium, making it a sustainable option too. Further, the use of an aqueous electrolyte, while limiting of the voltage range a cell can operate at - due to the electrochemical stability window of water - is an inherently safe option for an electrolyte, which also boasts an ease of manufacture.

The core concept throughout this thesis is that of minimising the environmental impacts of the battery as the design develops, and as such, a life-cycle assessment (LCA) is conducted on the current stage of the design, and compared to supercapacitors - this is due to the pseudo-capacitive, high power, nature of the battery. The design, in its current bench-based state, is found to be more environmentally friendly overall than commercial supercapacitors, and capacitors. A practical application of this battery in a dual energy storage system is studied for an EV car and bus, showing that, for a long lifetime of the EV, using dual energy storage systems has reduced environmental impacts. The LCA results were then compared to the market leader in energy storage (Li-ion) for environmental impacts.

Based on the comparison to Li-ion, development goals were set based on achieving the same or better lifetime CO_2 emissions, and it was found that by increasing the cycle life of the battery, and increasing the amount of utilised active material within

the battery, it would become environmentally competitive with Li-ion. Following this outcome, the focus for the experimental part of the PhD was split into active material increase and lifetime extension.

To increase the active material % within the battery, both increasing the actual amount of active material, and reducing the amount of support material were investigated. Coin-cell development of this battery to reduce support material found that a closed cell would not be appropriate - due to gas production, however 7000 stable cycles were achieved with an uncrimped cell. The loading of active material within the battery was investigated and found that a lower loading lead to increased discharge capacity (287.2 mAh g^{-1} for the positive and 205 mAh g^{-1} for the negative electrode). The performance of the TiO_2 electrodes were also investigated in terms of temperature. Given the porosity of the carbon felt, the impacts of compression on performance is being investigated in collaboration with Diamond Light Source, and initial findings are presented.

For increasing the lifetime of a battery it is prudent to understand the degradation mechanisms that occur over time as the battery loses capacity. Once this is known, design decisions and usage prescriptions can be made to mitigate or minimise these mechanisms and therefore increase the life of the battery. Based on this, a long duration experiment spanning eleven months was run at Diamond Light Source, which performed X-ray diffraction on six cycling coin cells each week. The resulting diffraction patterns, alongside X-ray computed tomography of the final coin cells have uncovered information about how the make up of the electrodes have changed over time.

Overall, this thesis shows that by working with the environmental impacts of a battery, we can produce development road-maps that both improve performance and respects the planet.

Contents

List of Figures

List of Tables

Declaration of Authorship

I declare that this thesis and the work presented in it is my own and has been generated by me as the result of my own original research.

I confirm that:

1. This work was done wholly or mainly while in candidature for a research degree at this University;
2. Where any part of this thesis has previously been submitted for a degree or any other qualification at this University or any other institution, this has been clearly stated;
3. Where I have consulted the published work of others, this is always clearly attributed;
4. Where I have quoted from the work of others, the source is always given. With the exception of such quotations, this thesis is entirely my own work;
5. I have acknowledged all main sources of help;
6. Where the thesis is based on work done by myself jointly with others, I have made clear exactly what was done by others and what I have contributed myself;
7. Parts of this work have been published as:

   N. Melzack, R. G. A. Wills, and A. J. Cruden, "Enhanced discharge capacity in carbon felt electrodes for aqueous aluminium-ion half-cells," *In draft*, 2024,

   J. Le Houx, N. Melzack, N. Aslani, A. James, H. Dehyle, A. Leonardi, M. Pimblott, O. King, R. Wills, and S. Ahmed, "Optimising the compression ratio of a carbon felt electrode through image-based modelling for an aqueous al-ion battery," *In draft*, 2024,

   N. Melzack, R. Wills, and A. Cruden, "An environmental perspective on developing dual energy storage for electric vehicles - a case study exploring al-ion vs. supercapacitors alongside li-ion," *Front. Energy Research*, vol. 11, 2024. DOI={https://doi.org/10.3389/fenrg.2023.1266670},

   N. Melzack and R. Wills, "A review of energy storage mechanisms in aqueous aluminium technology," *Front. Chemical Engineering*, vol. 4, 2022. https://doi.org/10.3389/fceng.2022.778265,

   N. Melzack, "Advancing battery design based on environmental impacts using an aqueous al-ion cell as a case study," *Sci Reports*, vol. 12, no. 1, 2022. https://doi.org/10.1038/s41598-022-13078-4,

D. Wu, X. Li, X. Liu, J. Yi, P. Acevedo-Peña, E. Reguera, K. Zhu, D. Bin, N. Melzack, R. G. A. Wills, J. Huang, X. Wang, X. Lin, D. Yu, and J. Ma, "2022 roadmap on aqueous batteries," *Journal of Physics: Energy*, vol. 4, no. 4, p. 041501, 2022. https://doi.org/10.1088/2515-7655/ac774d

N. Melzack, R. Wills, and A. Cruden, "Cleaner energy storage: Cradle-to-gate life cycle assessment of aluminum-ion batteries with an aqueous electrolyte," *Front. Energy Research*, vol. 9, no. 290, 2021. https://doi.org/10.3389/fenrg.2021.699919

Signed:..... Date:.....

Acknowledgements

PhDs are hard aren't they? I mean, I know people tell you it's going to be hard, and you read the stats about the pressure PhD students are under. But then, it's hard to know until you do one. But they are tough, right? So I guess that's why we have an acknowledgement section, because it's important to thank the people that helped, both directly and indirectly, with the hard thing of the PhD.

I want to start by thanking my supervisors, Prof Richard Wills, Prof Andy Cruden and Dr Martin Owen-Wilson. You knew how tough this was and you all helped me through it. Your insight, advice, and sense of humour was always appreciated. I am grateful for the trust you all gave me to explore ideas and the times you challenged me to look again at my work and see it in a new way. Thank you.

I want to thank others in the Energy Technology Group at Southampton, you all helped me through in different ways. Thank you for debates in the office Nick, thank you for showing me how to use the laser printer Ewan, thank you for sharing my excitement for felt James! Carlos and Dmitry - thank you for being there when I managed to break some lab equipment to help fix it or find a replacement. I literally would have no results without you!

Outside of Southampton I was lucky enough to be part of a brilliant and supportive cohort of Faraday Institution funded post graduate researchers. The support from Faraday itself was invaluable. But beyond that, the support from my peers all over the country was something I relied heavily on when things got stressful, we were all there for each other and each other's cheerleaders over the years. Thank you.

I suppose now I look to those who indirectly supported me. Who I want to thank for being there, for existing with me and putting up with me through the stress, the confusion, and the long monologues that I'm not sure you understood. Thank you. To my absolutely wonderful husband, Tom. You have been my rock over the last few years, I would not have gotten this far without you. Apart from Tom, I also share my home with a fluffy little scaredy-cat - Gizmo. Thank you Gizmo for adding so much whimsy to the last four years, for the hugs on the sofa while I was reading through papers, for the awkward appearances in my meetings, and of course, for just being the loveliest little study buddy anyone could ask for.

Suzette. My therapist. My goodness. Thank you for my sanity. Thank you for holding onto the hope for me when I couldn't see a way through. Thank you for looking after all of me, and making sure I did too.

And selfishly, and arrogantly, I want to thank myself. Because as much as I leaned on so many wonderful people and cats, I did this work, and I wrote this thesis, and I learnt so much for myself. I am so unbelievably proud of myself. I did it. How cool is that!

To Rachel, and the others we have lost in our academic community. You will not be forgotten. We will make this place better.

Definitions and Abbreviations

AC	Alternating current or activated carbon
Al	aluminium
Al/ion	Aluminium ion
$aq.$	aqueous
C	Capacitance, measured in Farads, F
$C/rate$	Charge rage required to fully charge in one hour
CB	Carbon Black
CF	Carbon Felt
CFC	chlorofluorocarbons
CO_2	Carbon dioxide
$COTS$	Commercial off the shelf
CPE	Constant Phase Element
CPT	Compact Power Tool
$cradle/to/gate$	part of the product lifecycle from raw material to when the product leaves the factory ga
$CTUe$	Comparative Toxic Units ecotoxicity
$CTUh$	Comparative Toxic Unit for human
$CuHCF$	Copper hexacyanaferrate, $KCuFe[CN]_6$
CV	Cyclic Voltammetry
DC	Direct Current
$DESS$	Dual energy storage system
DLS	Diamond Light Source - an X-ray synchrotron in Didcot, Oxfordshire, UK
E^0	Standard cell potential
$EDLC$	Electrochemical Double Layer Capacitor/Capacitance
EDX	Energy Dispersive X-Ray Analysis
EIS	Electrical Impedance Spectroscopy
EoL	End of Life
$eq.$	Equivalent
ESS	Energy storage system
ESW	Electrochemical Stability Window
$EUEF$	European Union Environmental Footprint
EV	Electric Vehicle

GCD	Galvanostatic Charge Discharge
GHG	Greenhouse Gas
H_2O	Water
I	Current, measured in Amperes, A
ICE	Internal Combustion Engine
$ISIS$	A muon and neutron spallation source in Didcot, Oxfordhire, UK
k	particle wave vector before atomic interaction
k'	particle wave vector after atomic interaction
kW	Kilowatt
kWh	Kilowatt-hour
LCA	Life Cycle Assessment
LCI	Life Cycle Inventory
LDE	Long Duration Experiment
Li/ion	Lithium ion
n	number of...
NMP	N-Methyl-2-pyrrolidone
$NMVOC$	non-methane volatile organic compounds
OCP	Open circuit potential
PAN	polyacrylonotrile
PAN	Polyacrylonitrile
$Pb/acid$	Lead acid
$PEEK$	Polyether ether ketone
PEF	Product Environmental Footprint
$PTFE$	Polytetrafluoroethylene
PVA	Polyvinyl alcohol
$PVDF$	Polyvinylidene fluoride
$PXRD$	Powdered X-ray diffraction
Q	Scattering Vector in Atomic Scattering, Charge potential in C in electrochemistry
RFB	Redox flow battery
RVC	Reticulated Vitrious Carbon
Sb	Antimony
SC	Supercapacitor
SCE	Saturated Calomel Electrode
SCM	standard Capacity Measurement
SEM	Scanning electron microscope
SHE	Standard hydrogen electrode
SoC	State of charge
t	time in seconds, s, unless otherwise stated
TiO_2	Titanium dioxide
TRL	Technology Readiness Level
V	voltage, potential measured in Volts V

VFRB	Vanadium Flow Redox Battery
WISE	Water In Salt Electrolyte
XCT	X-ray Computed Tomography
XRD	X-ray diffraction

Chapter 1

Introduction

1.1 Energy storage motivation

In recent years sustainable development and movement away from fossil-fuels has become increasingly important. Many reports calling for the further transition to renewable energies have been published, citing the damage to habitats (through mining, oil spills, pollution), the environment (increasing greenhouse gas emissions) and the imminent resource shortage due to the non-renewable nature of fossil fuels. (33; 34; 35; 36; 37)

Supply of energy (electricity), however, is still mainly an on-demand service. Power-plants can produce more electricity to increase demand in real-time, such as 'TV pickup', where after a World Cup Final, for example, there is a surge of kettles boiling across the UK. Power-plants have been built to take advantage of this and will mostly produce electricity (through burning fossil fuels) when it is needed.(38)

To shift to renewables fully, therefore, presents issues with availability. Solar and wind power are produced intermittently, with output changing throughout the day and depending on the season. This new way of energy production demands a shift to large scale energy-storage – enabling energy to be produced at one time and supplied to the grid when demand increases. This is known as a smart-grid, and much work has already begun to integrate this with more traditional power supply systems. (39)

However, further work is needed, to ensure the sustainable development of both large-scale energy storage for grid applications, as well as the smaller scale solutions to allow movement towards electric vehicles (EVs) and away from internal combustion engines (ICEs), and towards the sustainable and reliable use of renewable energy. Given the UK Government's ban on the production of new fully ICE vehicles in the coming years, the drive for developing these batteries is accelerating. Further,

the UK battery strategy released in December 2023, emphasises the importance of the continued development of battery technologies. (7; 35; 40; 41)

There is also a growing field of research looking into second life applications for many energy storage systems - primarily from those of EVs. When the capacity of an EV battery reaches about 80% capacity, it is considered to have reached the end of its life within the vehicle. However, these batteries can, and are, being used for home batteries to store energy generated from solar panels, as well as used in some experimental grid storage. In both these applications, the lower capacity of the battery is not a show-stopper - as there is less emphasis on low mass and volume for these stationary settings. (42)

The batteries we produce however, need to be manufactured in a sustainable manner with a view to further reduce the impact on the environment. Therefore, an approach which environmentally appraises supply chains, manufacture and use of batteries is just as important as appraising the battery performance.

Many chemistries have been commercialised, Table 1.1 provides a non/extensive summary of current available batteries.

TABLE 1.1: Non exhaustive summary of current commercially available battery technology

Battery type	**Voltage (single cell)**	**Working Energy Density**	**Lifetime (cycles)**	**Cost**	**Comment**
Li-ion	3.6 V	100-500 Wh kg^{-1} (39; 7; 43; 44; 45)	2000-4500 (45)	£££	Good performance, but flammable, potentially explosive (44; 46)
Pb-acid	2 V	30- 50 Wh kg^{-1} (43)	2000 (43; 45)	£	Cheap to produce, common in almost all motor-vehicles, but lead is toxic (47)
Zn-Br (RFB)	1.8 V	60-80 Wh kg^{-1} (43)	2000 (43)	££	Bromine leaking is a possibility which can cause skin and lung irritation (43)
$NaNiCl_2$	2.58 V	125 Wh kg^{-1} (43)	1000-2500 (43)	£	Cheap to produce, but high operating temperatures required (43)
Vandadium redox flow battery, VRFB	1.4 V	20-75 Wh kg^{-1} (43)	12000 (43)	£££	Excellent lifetime performance, but expensive and vanadium is toxic (43)
Nickel metal hydride, NiMH	1.2 V	60-120 Wh kg^{-1} (48)	180-2000 (48; 49)	££	Low toxicity and can tolerate overcharge and over-discharge.

1.2 Aqueous electrolyte motivation

An aqueous electrolyte uses water as the solvent for a variety of ionic salts. These electrolytes are often safer than organic liquids, or non-aqueous electrolytes, due to

their low flammability and ease of handling (7; 50). Organic electrolytes such as those in Lithium-ion batteries, can emit volatile, flammable, toxic solvents when punctured, as well as be hazardous to work with for second-life or recycling applications (51; 52). The solvent in aqueous electrolytes, water, is low-cost, widely available and does not require complex manufacturing or storage (compared to other electrolytes). This already shows advantages in the economic and social (safety) aspects of battery development. However, while cheaper in absolute terms, when thinking in terms of cost per kW or kWh, it is not yet comparable to non-aqueous commercial batteries. Commercial non-aqueous Li-ion batteries are expected to cost $362/kWh, $1446/kW in 2025 (53), compared to an aqueous commercial Pb-acid battery, which is expected to cost $464/kWh, $1845/kW (53). (7; 45; 8; 54)

There are performance reasons for not using aqueous electrolytes. The main concern being the narrow electrochemical stability window (ESW) of water – about 1.23 V. Beyond this point, electrolysis of water takes place and the H_2O decomposes into its constituent parts (55). This would limit the energy density of cells constructed in this manner. However, there has already been research establishing that a diluted aqueous electrolyte can have an ESW of up to 2 V, and even higher with different salt concentrations, which shows promise for further developments (56). A comparison of ESWs for other electrolytes is shown in Table 1.2.

Lithium-salts in an organic liquid are used in Li-ion commercial batteries today, they have a high ESW and can therefore deliver higher voltages with fewer cells in series. Polymer and gel-type electrolytes are still in their development stage and offer the advantage of a high ESW, with lower flammability, but are currently not used commercially. From this table, the aqueous WISE (water in salt electrolyte) in which the salt is saturated, have the potential for higher ESWs, but are still in the development phase.

Regardless of this low ESW, there is still high demand for aqueous electrolyte development. The potential ionic conductivity of such electrolytes is two orders of magnitude higher than that of organic non-aqueous electrolytes – this could enable far higher power capability (55). Other limiting factors, not bespoke to aqueous electrolytes, also apply. Corrosion of electrodes is likely in protic electrolytes, as well as dendrite formation on electrodes. These both limit lifetime and discharge voltage obtained over time. (55; 7)

Furthermore, in terms of sustainability, the energy density obtained is not the most key factor. Long lasting, reliable, safe, cost-effective, and scalable designs are far more critical. Therefore the narrow ESW, while being widened as new research is published, is by no means a reason to disregard aqueous electrolytes.(57)

It is, though, near impossible to fully evaluate the aqueous electrolyte in isolation. It forms part of a complex system involving the electrodes. With regards to aluminium,

few materials have been identified as sufficient electrodes that can both operate within the ESW and accommodate the large charge density. Having said that, the number of suitable electrodes is being added to currently, as discussed further in Chapter 2.

TABLE 1.2: Typical ESW for certain electrolytes

Electrolyte	Type	ESW	Reference
Lithium salts	Organic liquid	4-6 V	(58)
$LiPF_6$	Organic Carbonate	> 5.5 V	(58)
Li PAN-gels	Polymer/aqueous	>4.5 V	(59; 60)
Crosslinked	Polymer	3.9 V	(59)
Ionic Salt	aqueous	1.23 V	(61)
WISE	aqueous	3-4 V	(56; 62)

1.3 Aluminium motivation

Many battery options are commercially available, however Li-ion has accelerated the development of portable devices, electronic vehicles, and grid storage in the last two decades (63). Currently, this technology is difficult to recycle, and relies on sparse and often politicised resources (64; 65; 66; 67). To further our sustainable development, therefore, looking towards new energy storage technologies, it is important to co-develop them to be easier to recycle, and have a lower environmental footprint.

Secondary aluminium-ion (Al-ion) batteries have not reached wide-scale commercial viability and are often grouped together with other multivalent metals/ion systems in the literature (such as Mg and Ca) (36; 7). However, aluminium is the most abundant metal in the earth's crust (8.1 % wt), and third most abundant element (68). There are already established mining, production, and recycling industries for aluminium (69; 70), hinting at an easy and sustainable development roadmap ahead for utilising Al-ion technology within a circular economy.

The most common ionic form of Al is the Al^{3+}. This trivalent Al^{3+} ion is therefore capable of three electron transfers per ion, unlike Lithium's monovalent Li^{+} - i.e. one Al-ion is equivalent to three Li-ions in terms of charge transfer. While this work is not in direct competition with Li-ion technology, is useful to understand where Al-ion sits with regards to the present industry leader. The ionic radius of Al is slightly smaller than Li, leading to a high charge density, meaning in theory more charge transfer can occur with no increase in physical restriction to electrodes. Additionally, Al has a volumetric density of 2.7 g cm^3 at 25°C which leads to a volumetric energy density of almost four times Lithium, 8.04 Ah cm^{-3} and 2.06 Ah cm^{-3} respectively. This combined with the high abundance, safety, and well-established recyclability makes the Al-ion a suitable charge carrier. (71)

Two concerns with the higher charge density arise for intercalation-type processes;

1. the high charge density means it is difficult for Al^{3+} to lose its coordinating ligands in the solvated state and
2. while intercalating, the Al^{3+} ions can distort the lattice structures of electrodes.

The former negates the advantage of the small ionic radius of Al^{3+}, while the latter can reduce the lifetime significantly as the lattice distortions build and accumulate with each cycle.

An aqueous Al-ion cell developed at The University of Southampton (1; 18), using titanium dioxide and copper hexacyanoferrate electrodes with an aluminium chloride and potassium chloride electrolyte, shows promise in development (see Figure 1.1). A full description of this cell is found in Chapter 4. Work on an aqueous Al-ion battery system will therefore present advantages in terms of sustainability and charge transfer, but requires focus on design development with environmental impacts in mind. The benefit of this aq. Al-ion (aqueous aluminium-ion) system is that it behaves similarly to a supercapacitor (72), and therefore diversifies the range of energy storage options available. In the future this will ensure that energy storage can be better matched with specific needs.

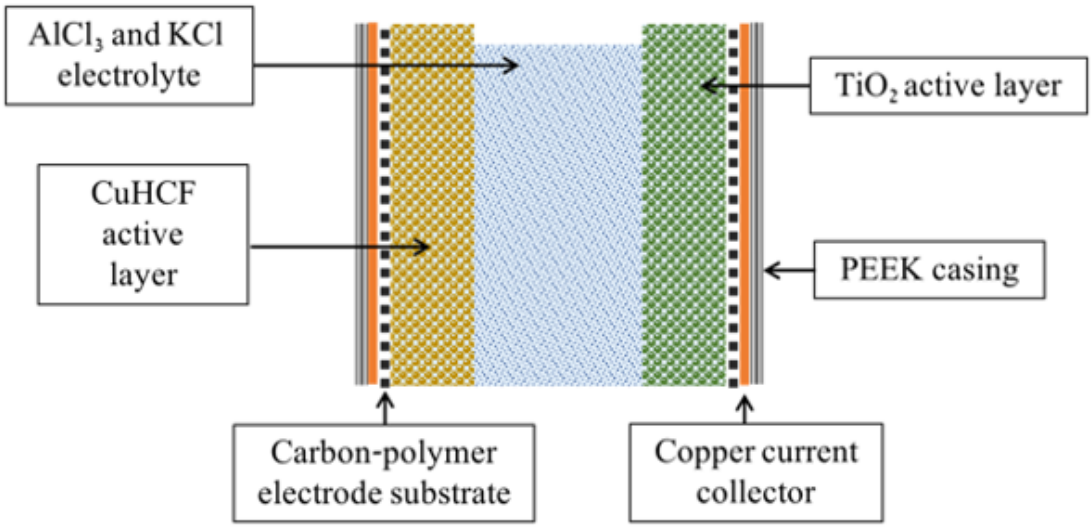

FIGURE 1.1: aqueous Al-ion cell developed at The University of Southampton (1)

1.4 Research focus

The aim of this PhD project therefore is to sustainably develop the design of this aq. Al-ion cell (with titanium dioxide, TiO_2, and copper hexacyanoferrate, CuHCF,

electrodes). This includes understanding the current environmental impacts and using them to guide the development decisions.

The research question is therefore; Can we use environmental impacts to drive the design of a sustainable battery?

This will be answered through:

1. Undertaking a literature review of the subject area - Chapter 2
   (a) Assessing current understanding of aqueous Al-ion energy storage
   (b) Reviewing the use of life cycle assessment (LCA) in general and within energy storage.
2. Life Cycle Assessment (LCA) analysis of the cell construction - Chapter 4
   (a) Undertaking a material inventory performing an initial LCA, comparing to other energy storage
   (b) Assessing the aq. Al-ion's environmental impacts in a case study example - dual energy storage systems
   (c) Assessing design changes using the LCA to ensure environmental impact is considered as well as performance
3. Investigating reducing the support material needed for the cell - Chapter 5
   (a) Verifying the electrodes work as presented in the literature
   (b) Assessing a suitable separator material for a the aq. aluminium-ion cell
   (c) Investigating a coin-cell in order to reduce the amount of support material used
4. Investigating alternative electrode substrate materials - Chapter 6
   (a) Investigating and characterising carbon felt as an electrode substrate for each electrode
   (b) Optimising the carbon felt electrode design through varying loading of active material, discharge capacity and temperature
   (c) beginning an investigation into how the compression of the carbon felt impacts the overall performance
5. Long term observations of the degradation of the aqueous Al-ion cell - Chapter 7
   (a) Creating a cell compatible for long duration measurements
   (b) Cycling the cells within the long duration facility at Diamond Light Source
   (c) Assess the X-ray diffraction measurements, and how they change over at least six months of cycling

(d) Using X-ray computed tomography to inspect the cell internally after cycling

1.4.1 Publications and notable achievement

Table 1.3 summarises the novelty associated with this thesis

TABLE 1.3: Novelty and contributions from this thesis

Chapter	Item	Novelty/Comment	Reference
2	D. Wu, X. Li, X. Liu, J. Yi, P. Acevedo-Peña, E. Reguera, K. Zhu, D. Bin, N. Melzack, R. G. A. Wills, J. Huang, X. Wang, X. Lin, D. Yu, and J. Ma, "2022 roadmap on aqueous batteries," *Journal of Physics: Energy*, vol. 4, no. 4, p. 041501, 2022. https://doi.org/10.1088/2515-7655/ac774d	Contribution to a Topical Review on aqueous batteries	(32)
2	N. Melzack and R. Wills, "A review of energy storage mechanisms in aqueous aluminium technology," *Front. Chemical Engineering*, vol. 4, 2022. https://doi.org/10.3389/fceng.2022.778265	Review on aqueous aluminium energy storage technology, focussing on the charge storage and charge transfer mechanisms within secondary aluminium-ion batteries	(31)
4	N. Melzack, R. Wills, and A. Cruden, "An environmental perspective on developing dual energy storage for electric vehicles - a case study exploring al-ion vs. supercapacitors alongside li-ion," *Front. Energy Research*, vol. 11, 2024. DOI={https://doi.org/10.3389/fenrg.2023.1266670}	Original research: First example of an environmental assessment of use-cases for dual energy storage systems in electric vehicles - introducing aq. Al-ion cell as a high power option	(21)

Continued on next page

Table 1.3 – *Continued from previous page*

Chapter	Item	Novelty/Comment	Reference
4	N. Melzack, "Advancing battery design based on environmental impacts using an aqueous al-ion cell as a case study," *Sci Reports*, vol. 12, no. 1, 2022. https://doi.org/10.1038/s41598-022-13078-4	Original research: Introducing an environmental framework for design development of energy storage systems using LCA	(22)
4	N. Melzack, R. Wills, and A. Cruden, "Cleaner energy storage: Cradle-to-gate life cycle assessment of aluminum-ion batteries with an aqueous electrolyte," *Front. Energy Research*, vol. 9, no. 290, 2021. https://doi.org/10.3389/fenrg.2021.699919	Original Research: First Life cycle assessment of an aqueous aluminium ion battery	(20)
6	J. Le Houx, N. Melzack, N. Aslani, A. James, H. Dehyle, A. Leonardi, M. Pimblott, O. King, R. Wills, and S. Ahmed, "Optimising the compression ratio of a carbon felt electrode through image-based modelling for an aqueous al-ion battery," *In draft*, 2024	Original research and collaboration with Diamond Ligh Source: Obtaining the relationship between electrode compression and battery performance	(25)

Continued on next page

Table 1.3 – *Continued from previous page*

Chapter	Item	Novelty/Comment	Reference
6	N. Melzack, R. G. A. Wills, A. J. Cruden, and M. Owen-Jones, "Enhanced discharge capacity in carbon felt electrodes for aqueous aluminium-ion half-cells," in *ECS 245th meeting*, 2024. https://doi.org/10.13140/RG.2.2.22413.76001 & N. Melzack, R. G. A. Wills, and A. J. Cruden, "Enhanced discharge capacity in carbon felt electrodes for aqueous aluminium-ion half-cells," *In draft*, 2024	Original research: Showing 3D carbon felt electrodes increase discharge capacity in aqueous Al-ion half cells	(73; 30)
7	Whole Chapter - Increasing Cycle Life	Original Research to be written up as publication: In situ long duration investigation of aqueous Al-ion using synchrotron X ray diffraction to understand degradation and changes in electrodes over time	N/A

1.5 Publications

I contributed to the following publications throughout my PhD. For paper 1 I developed the idea and top level methodology, made samples, assisted in image acquisition and analysis. In paper 2 I developed the idea, planned the experiments, ran the experiments, analysed the data and wrote the first draft of the paper. For 3, I developed the idea, built the model, ran the experiment and wrote up the first draft of the paper. In paper 4, I developed the idea, ran the experimental models did the analysis and wrote the paper. For 5, I contributed to the a section on aq. Al-ion batteries within a larger review paper of aqueous batteries. In paper 6, I performed the literature review and wrote the first draft of the paper. In paper 7, I developed the idea, built the model, ran the experiment and wrote up the first draft of the paper.

1. J. Le Houx, N. Melzack, N. Aslani, A. James, H. Dehyle, A. Leonardi, M. Pimblott, O. King, R. Wills, and S. Ahmed, "Optimising the compression

ratio of a carbon felt electrode through image-based modelling for an aqueous al-ion battery," *In draft*, 2024

2. N. Melzack, R. G. A. Wills, and A. J. Cruden, "Enhanced discharge capacity in carbon felt electrodes for aqueous aluminium-ion half-cells," *In draft*, 2024

3. N. Melzack, R. Wills, and A. Cruden, "An environmental perspective on developing dual energy storage for electric vehicles - a case study exploring al-ion vs. supercapacitors alongside li-ion," *Front. Energy Research*, vol. 11, 2024. DOI={https://doi.org/10.3389/fenrg.2023.1266670}

4. N. Melzack, "Advancing battery design based on environmental impacts using an aqueous al-ion cell as a case study," *Sci Reports*, vol. 12, no. 1, 2022. https://doi.org/10.1038/s41598-022-13078-4

5. D. Wu, X. Li, X. Liu, J. Yi, P. Acevedo-Peña, E. Reguera, K. Zhu, D. Bin, N. Melzack, R. G. A. Wills, J. Huang, X. Wang, X. Lin, D. Yu, and J. Ma, "2022 roadmap on aqueous batteries," *Journal of Physics: Energy*, vol. 4, no. 4, p. 041501, 2022. https://doi.org/10.1088/2515-7655/ac774d

6. N. Melzack and R. Wills, "A review of energy storage mechanisms in aqueous aluminium technology," *Front. Chemical Engineering*, vol. 4, 2022. https://doi.org/10.3389/fceng.2022.778265

7. N. Melzack, R. Wills, and A. Cruden, "Cleaner energy storage: Cradle-to-gate life cycle assessment of aluminum-ion batteries with an aqueous electrolyte," *Front. Energy Research*, vol. 9, no. 290, 2021. https://doi.org/10.3389/fenrg.2021.699919

Chapter 2

Literature review

The following literature review discusses

- Battery and electrochemistry overview
- the current understanding of aqueous aluminium-ion energy storage, which is adapted in part from (31) and (32)
- super capacitor technology, including the role of aqueous supercapacitors
- Life cycle assessments, and their application within battery technology, in part adapted from (20) and (21)

2.1 Battery storage

2.1.1 Faradaic charge storage

Batteries are electrochemical storage devices which rely primarily on the faradaic redox reaction as a means of charge storage and transfer. Secondary batteries, which facilitate reversible redox reactions, can be charged/discharged multiple times throughout their lifetime – these are rechargeable batteries. Primary batteries are non-reversible and thus can only be discharged a single time in their lifetime – i.e. non-rechargeable. There is also a pseudo- or mechanically rechargeable battery, such as the Al/air battery in which the electrode is easily replaced after discharge – effectively 'mechanically charging' the battery for use again (7). Batteries, in their simplest form, are made of three components: a positive electrode; a negative electrode; and an electrolyte. The electrolyte is ionically conductive, while the external circuit is electronically conductive. When both electrodes are connected via an external circuit – current flows, and the battery discharges its energy. There are both

ionic and electronic processes occurring during this discharge (74). Figure 2.1 illustrates a simple electrochemical cell and Figure 2.2 summarises the key differences between these battery types. The rest of this section focuses on secondary batteries.

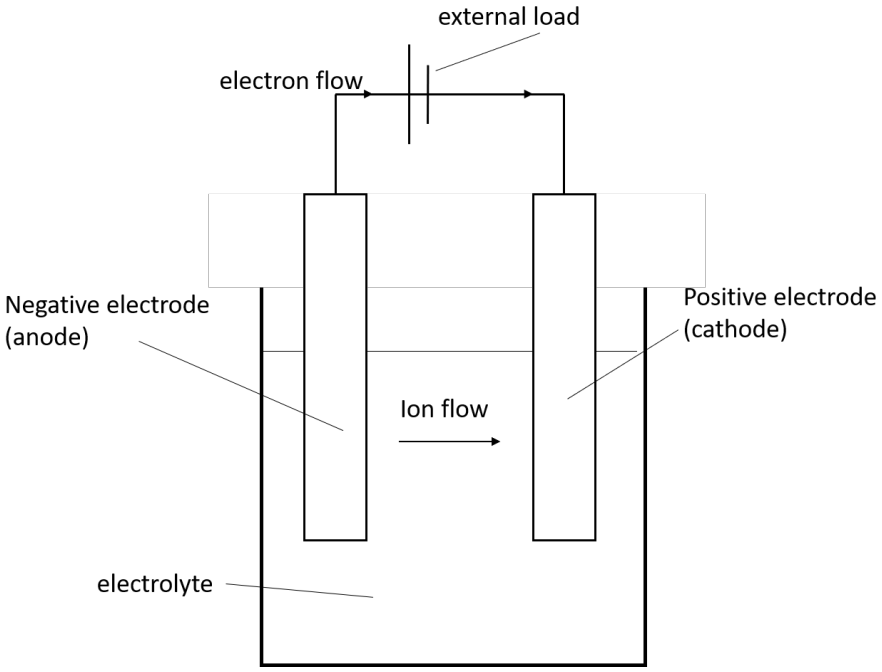

FIGURE 2.1: Diagram of simple electrochemical cell

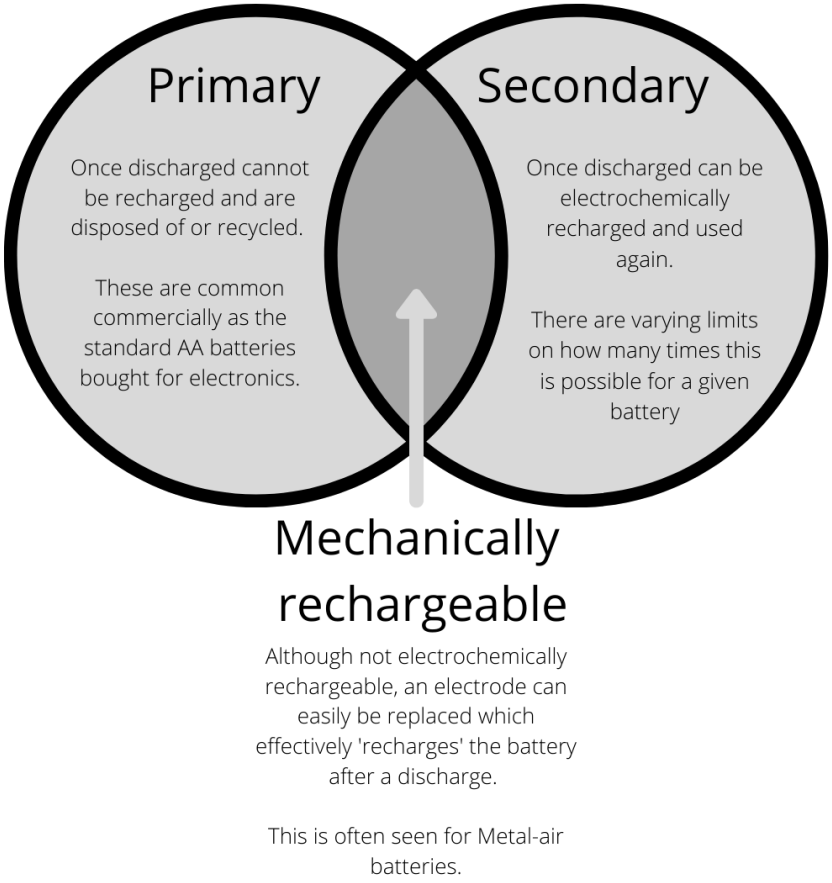

FIGURE 2.2: Top level summary of battery types based on recharge-ability

2.1.2 Rate of electrochemical reactions

There are two factors that determine the rate of a redox reaction at the electrodes - how quickly the ions can get to the electrode surface in order to react, and how quickly the electrons can transfer during these reaction. These are known as mass transport and charge transfer kinetics, respectively.(74)

Mass transport is controlled by diffusion, convection and migration. Diffusion is the movement of particles from high concentration to low concentration areas. The rate at which this movement occurs depends on the concentration of the overall particles, and the diffusion coefficient, D, which is highly dependent on temperature and the exact solution species. Convection refers to the movement of the solution, often done by stirring, which increases the flux of ions onto the electrode surface. Migration is the movement of ions within a solution based on their local electric field relative to other ions in the solution, this can be dependent on the charge of the ions, the concentration and the diffusion coefficient. (74)

Using the Randles-Sevcik equation (Eq. 2.1), the dominant kinetic process can be ascertained. Within Eq. 2.1, j_p is the peak current density, F the Faraday constant, R the universal gas constant, T is the absolute temperature, n is the number of electrons involved in the redox reaction, D_o is the diffusion coefficient, C_o is the molar concentration of the active redox species, A is the surface area of the electrode and v is the potential scan rate. (75)

$$j_p = 0.4463(\frac{F^3}{RT})^{\frac{1}{2}} n^{\frac{3}{2}} A D_o^{\frac{1}{2}} C_o^* v^{\frac{1}{2}} \tag{2.1}$$

In order to use this equation, a series of cyclic voltammeter must be obtained. Cyclic Voltammetry (CV) is an experimental technique in which a half cell (just one electrode with electrolyte) is subject to a varying potential with a constant sweep rate, while recording the current that this generates. The potential sweep is then reversed. The CV is performed within the ESW of the cell. This technique is used for many applications; by noting the potential at which the peak current is output, we can identify the faradaic reactions and their potential. If there is a pair of peaks - one on the forward sweep and one on the reverse, we can tell that there is a reversible reaction, in which oxidation and reduction are occuring. The size and shape of the CV curve can also tell us about whether the reaction is electrochemical or indeed capacitive (or, as can be the case, a bit of both).

Figure 5.6 is taken from Chapter 5, as an example of the output from a CV experiment. Here we can see two peaks and a clear reversible reaction with no other obvious side peaks or reactions indicated. By taking many CV sweeps using different voltage scan rates at a stable temperature, it is possible to then plot the scan rate against the current density. If the plots are symmetric around 0, then we can conclude that a reversible redox reaction is taking place, if the fit is linear, we can also conclude that there is a diffusion controlled limiting factor on the kinetics. Both of these are shown in Chapter 5 Figure 5.8.

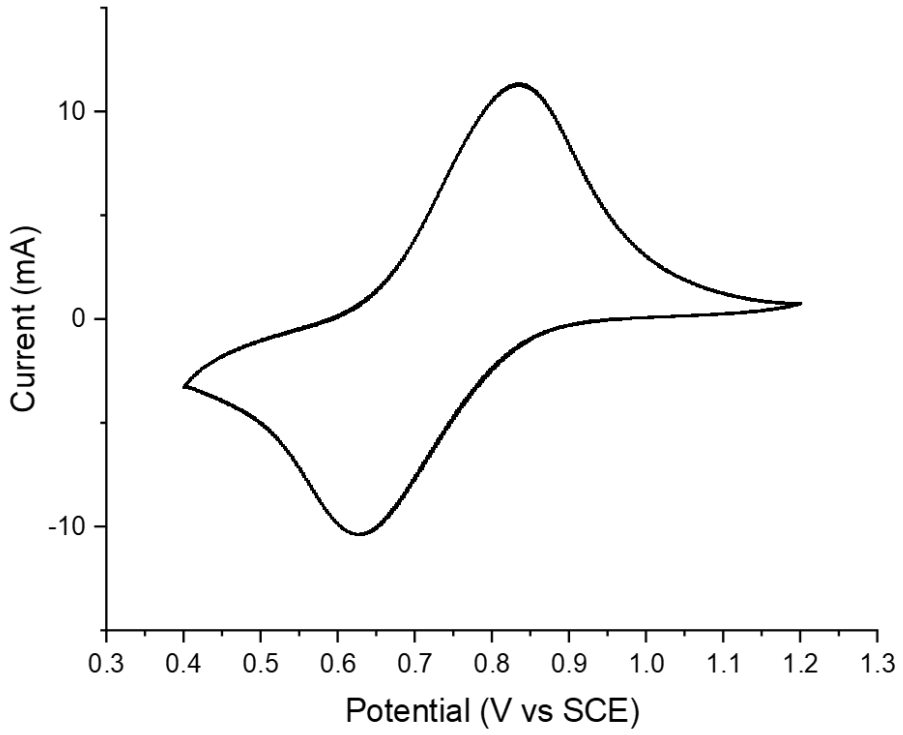

FIGURE 2.3: CV sweep of CuHCF electrode in 1 M $AlCl_3$ + 1 M KCl at 20 mV s^{-1}

Within the cyclic voltammetary technique there are limitations. For any calculation that requires the area of an electrode to be known, the precision used often becomes a factor. For nano-electrodes, this becomes more important, as any surface roughness or defects could add a large proportion of surface area to the electrode. In the case of pourous electrodes this again becomes a difficult value to precisely calculate as the 'surface' may extend entirely throughout the electrode. Further, when using CVs for porous electrodes, the rate of mass transport becomes increasingly important, as different parts of the electrode surface are at different depths from each other. If mass transport is slow here, we may have different parts of the electrode reacting at different times, which may dampen the current output, or spread out the peaks seen in the plot.

2.1.3 Electrochemical potential of a battery

The potential of a battery, E^o, is defined as the difference of potentials between the reduction and oxidation reactions.

$$E^o = E^o_{reduction} - E^o_{oxidation} \tag{2.2}$$

This can be related to the Gibb's free energy ΔG by

$$\Delta G = -nFE \tag{2.3}$$

$$\Delta G^o = -nFE^o \tag{2.4}$$

where n is the number of electrons involved in a balanced reaction and F is the Faraday constant (96,500 C mol^{mol}).

We can then relate the Gibbs free energy under standard and non-standard conditions:

$$\Delta G = \Delta G^o + RTlnQ \tag{2.5}$$

and substituting from eq. 2.3 gives a form of the Nernst equation,

$$-nFE = -nFE^o + RTlnQ \tag{2.6}$$

In this equation, R is the gas constant and T is the temperature in Kelvin. Q represents the reaction quotient - the ratio of reactants to products within the reaction. At equilibrium conditions Q becomes our constant K_{eq}, and, also at equlibruim there is no reaction and so $\Delta G = 0$. Using this we can find the a battery's potential through

$$0 = E^o - \frac{RT}{nF} lnK_{eq} \tag{2.7}$$

$$E^o \propto K_{eq} \tag{2.8}$$

Using these equations we can calculate the correct proportions of materials to balance a cell, ensuring that the active materials are fully utilised.

Further, we can see that within the Nernst equation, Temperature is a factor - and as such conditions for equilibrium will change as temperature changes. This relationship can be further represented through the Arrhenius equation (see eq. 2.9 which shows that the rate of reaction is exponentially tied to the temperature.

$$k = Ae^{\frac{-E_a}{RT}} \tag{2.9}$$

Where k is a rate constant and E_a is the activation energy. When looking at a diffusion controlled reaction, the k can become the diffusion coefficient.

2.1.4 Half cell potentials of the potential reactions

For a full battery system we need two electrodes, however, for a half cell, only a single electrode is used. Half cells are used to characterise individual electrode materials in order to eventually use them within a full battery system.

While a full cell redox reaction may look like this

$$A^{2+} + B \rightarrow A + B^{2+} \tag{2.10}$$

There are in fact two separate half cell equations occurring, an oxidation at the negative electrode

$$B \rightarrow B^{2+} + 2e^{-} \tag{2.11}$$

and reduction at the positive

$$A^{2+} + 2e^{-} \rightarrow A \tag{2.12}$$

It is from these half cell reactions that we come back to eq. 2.2. By understanding the half cell potentials, we find the equilibrium potential, which then tells us whether we have a spontaneous (positive E^o) or a non-spontaneous reaction (negative E^o).

By looking at half cell potentials, we can ensure we choose the right pair of electrodes to bring into our full battery system. We can also use understanding of half cell potentials to identify potential parasitic or side reactions which may occur.

Within the aq. Al-ion battery the following half cell potentials are important, V vs SCE.

- Al: $Al^{3+} + 3e^{-} \leftrightarrow Al = -1.42V$
- Ti: $2TiO_2 + 2H^{+} + 2e^{-} \leftrightarrow Ti_2O_3 + H_2O = -0.32V$
- Ti: $TiO^{2+} + 2H^{+} + 4e^{-} \leftrightarrow Ti + H_2O = -0.69V$
- Ti: $Ti^{+4} + e^{-} \leftrightarrow Ti^{3+} = -1.44V$
- Fe: $[Fe(CN)_6]^{3+} + e^{-} \leftrightarrow [Fe(CN)_6]^{4+} = 0.61V$
- Fe: $[Fe(CN)_6]^{4-} + 6H^{+} + 2e^{-} \leftrightarrow Fe + 6HCN = -0.92V$

(76)

2.1.4.1 Non-faradaic charge storage

With non-faradaic charge storage, charge separation (or capacitive storage) occurs. There are no chemical reactions here, but a build up of charge on the surface of electrodes which are facing eachother, but separated via a dielectric. This charge is maintained via applied voltage. Current can then be rapidly drawn from the capacitor when required, there is a fast discharge and capacitors are often high energy devices, discussed later in this chapter. (77)

There are also pseudo-capacitors of faradaic capacitors, which describe charge storage as a faradaic chemical reaction, but one that occurs only on the surface of the electrode, which again allows for fast discharge, and as such a high power can be drawn from these reactions.

2.2 The current understanding of aqueous aluminium-ion energy storage

The introduction (Chapter 1) introduced the idea that aqueous electrolytes are cheaper, safer, and more ionically conductive than other (i.e. organic) electrolytes. The concept of aluminium ions as the workhorse of a battery was also discussed, and the abundance, established production systems, as well as the high charge and volumetric energy storage were presented as benefits. It is, though, near impossible to fully evaluate the aqueous electrolyte, or the use of aluminium-ions, in isolation. They form part of a complex system. With regards to aluminium, few materials have been identified as sufficient suitable electrodes – that can both operate within the ESW of water and accommodate the large charge density. Having said that, the number of suitable electrodes is being added to currently, and this section will discuss some key developments in electrode material as well as the charge and degradation mechanisms found. Negative and positive electrodes will be discussed separately, taking into account (as much as the literature allows) the interactions between the electrolytes and electrodes in both half and full cells, to suggest charge storage and degradation mechanisms within the system. Figure 2.4 summarises the main materials being researched.

2.2.1 Negative electrodes

The negative electrode always has a more negative potential than the positive electrode when in a full cell. Sometimes this is referred to as the anode, but for secondary cells, since both reduction and oxidation takes place at the electrode depending on whether the cell is discharging or charging, it can be confusing to refer

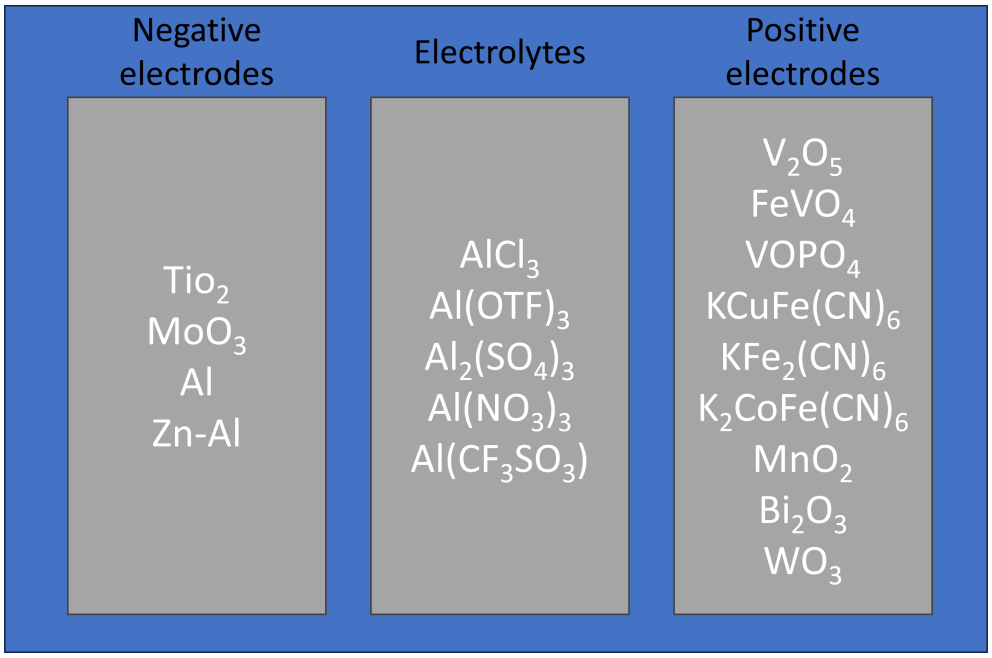

FIGURE 2.4: Summary of electrode and electrolyte materials researched in secondary aluminium-ion batteries

to it as the anode. Hence, negative electrode will be used throughout this section. Table A.1 in Appendix A summarises the materials that have, to date, been studied as a negative electrode for an aqueous aluminium-ion cell. It is important to understand the difference between electrodes tested as 'half cells' and full cells in terms of the capacities and fade values ascertained. For a half cell, only the electrode testing will have an influence on the capacity and fade characteristics reported. However, with a full cell, both the positive and negative electrodes will have an influence and the reported capacities are for the whole cell, not just the electrode highlighted in the table. For example, Holland et al studied TiO_2 in a full cell with a Copper Hexacyanoferrate (CuHCF) positive electrode and found cycle life of 1750 cycles and a Coulombic efficiency of ≈90% (1), however in a half cell with the same conditions, 5000 cycles were possible with ≈99% Coulombic efficiency (2). The majority of papers to date have focussed on TiO_2 as a negative active material with MoO_3 the next most cited material. Metallic aluminium, aluminium-alloys and T-Al (aluminium which has been pre-treated with chloroaluminate melts) have also been proposed. The materials are discussed by type in the following subsections.

There are two main types of negative electrode material - using Al metal itself, or a material that will accommodate the Al^{3+} ion. For Al metal a key issue is the overall reduction potential of Al - (1.66 V Vs SHE) which may lead to hydrogen evolution reactions and a decomposition of the electrolyte (78). Passivation layers can also form at the surface of the metal, creating a resistive layer. Further as is often noted with metal-only electrodes, dendrites are likely to grow (79). Electrodes which accommodate the aluiminium ions have different challenges. The ionic radius of Al^{3+}

is smaller than that of Li^{1+} (0.53 Å compared to 0.76 Å, which implies that any Li electrode materials would easily accommodate the Al ion. However due to the high charge density (364 C mm^{-3}) of Al^{3+} vs Li^{1+} (52 C mm^{-3}), the Al ion can have destructive effects on electrode materials. This increases local polarisation of the electrode, and increases the stresses and strains on the crystal structure itself - all of which degrade the electrode. Using hydrated ions as charge carriers can help to reduce this charge density, however the hydrated radius of Al^{3+} is large (4.75 Å) which leads to further issues in terms of physical accommodation in an electrode lattice. Due to these issues we see slow ion diffusion, a lower discharge capacity and poor charge retention (self discharge) and low cycling capabilities. The following subsections discuss the current state of negative electrode materials trying to overcome these challenges. (80)

2.2.1.1 Titanium dioxide

TiO_2 has been explored as an electrode in other cell designs, however, it was not reported as an option for Al-ion aqueous cells until 2012 at the earliest by Liu et al (3). Liu used TiO_2 nanotubes to construct the electrode, which the author had previously used for Li-ion aqueous cells (81), and a 1 M $AlCl_3$ electrolyte. This half-cell was shown to have a specific capacity of 75 mA h g^{-1}@ 4 mA cm^{-2}, 90% Columbic efficiency and voltage range of 1.1–0.4 V with a discharge plateau between 1.1 and ≈0.8 V (3). The method of electrochemical exchange is concluded to be intercalation of Al^{3+} into the TiO_2. This suggests the reaction including Ti-ions (Ti^{3+}/Ti^{4+}). The overall reaction equation would therefore be

$$TiO_2 + xAl^{3+} + 3xe^- \Leftrightarrow Al_xTiO_2 \tag{2.13}$$

where $0 < x < \frac{1}{3}$ due to the Ti^{3+}/Ti^{4+} charge limiting couple. There is also likely a non-reversible reaction to Ti^{2+}, as shown in Figure 2.5. An irreversible reaction would, over time, limit the amount of available TiO_2 for the Al-ion to interact with, thereby reducing the capacity of the electrode. The authors further find that an acidic electrolyte of pH 3 is vital for the effective insertion of Al^{3+}, as it is protective against the hydrogen reactions (82).

Following this in 2014, further development of the TiO_2 nanotube array was performed, looking at a variety of aqueous Al-ion electrolytes and concentrations (4). This study further investigated the role of Ti-ions in the Al^{3+} insertion into the electrode. More supporting evidence of the Ti^{3+}/Ti^{4+} role was found, with the author concluding that Ti^{4+} must reduce to $Ti^{3+}$where the Al^{3+} is present on the surface, to maintain charge balance. There was also speculation of the additional role of Cl^- on the process. Work on Mg-ion aqueous cells, which produce a divalent ion, Mg^{2+} has also concluded that the redox couple Ti^{3+}/Ti^{4+} is involved in the charge storage

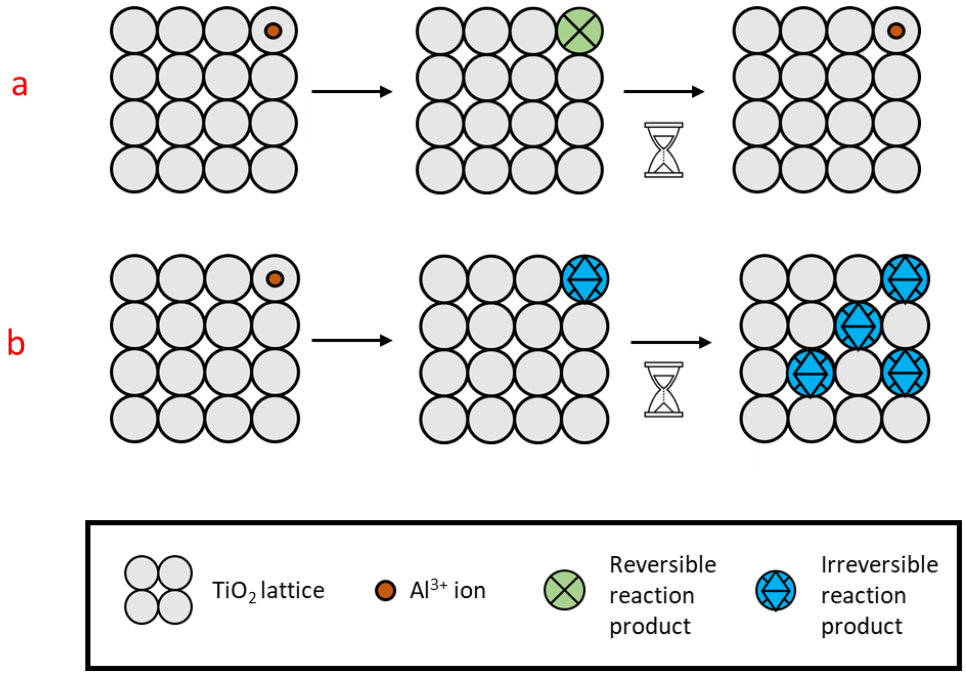

FIGURE 2.5: Schematic of proposed reactions in TiO_2 electrodes, showing a) reversible and b) irreversible

mechanism (83), where it was discussed that the role of oxygen vacancies within the TiO_2 electrode increase the insertion of the ions, which in turn increase the overall charge storage and capacity.

Holland et al (2; 84) further investigated the role of Ti in the charge storage; using anatase TiO_2 nano-powder for the basis of the electrode, in a 1M $AlCl_3$ electrolyte. Increasing the pH of the electrolyte with HCl (hydrochloric acid) increased the redox peaks seen on a cyclic voltammogram, CV (1; 18). Initial work suggested the Ti^{3+}/Ti^{4+} reduction only takes place at more negative potentials (≈-1.3 V v SCE), and that there is some capacitive charge storage at the interface between electrode and electrolyte. To further test the capacitive storage hypothesis, this experiment was repeated, using a vacuum impregnation method to construct the TiO_2 nano-powder electrode (2). By increasing the contact between the electrode and electrolyte (i.e. by using the vacuum impregnation method) Holland found a stable ≈100% Coulombic efficiency up to a specific current of 40 A g^{-1}. This, compared with the initial work of ≈100% Coulombic efficiency up to only 7.2 A g^{-1} (2), shows the direct impact of increasing contact between the TiO_2 and $AlCl_3$. This is convincing evidence for the pseudocapacitive nature at the interface, due to the high current density achieved.

The capacitive nature of the charge storage mechanism is further supported by the self-discharge seen in Al-ion aqueous cells with a TiO_2 electrode (85). High self-discharge is a trait often seen in capacitors, with batteries and cells often retaining their charge for far longer (19). Here we can find another clue to the pseudocapacitive

nature of the charge storage. This will be discussed in later sections on supercapacitors.

Up until this point, the crystal structure of the TiO_2 investigated has been anatase. However, another crystal lattice, rutile, was investigated in 2018 (86) as a potential electrode material. This computational analysis suggested that the rutile lattice has a far higher diffusion coefficient, D, than that of anatase, about 10^{-9} and 10^{-20} cm^2 s^1 respectively. In 2019, a rutile nano-powder was studied as an electrode, with 1 M $AlCl_3$ electrolyte (87). A solid phase diffusion of the Al-ions into the TiO_2 was seen. However, further work by (18) shows that at least with an $AlCl_3$ electrolyte, the rutile structure does not, in practise, work as an effective electrode.

Some interesting work on amorphous TiO_2 in mild acids and aqueous aluminium based electrolytes have also shed some light on a possible mechanism in which the protons (H) are inserted over the Al^{3+} - as they have a lower ionic radius. They propose a reaction equation of:

$$TiO_2 + xe^- + x[Al(H_2O)_6]^{3+} \Leftrightarrow TiOOH_x + x[Al(H_2O)_5(OH)]^{2+} \tag{2.14}$$

instead of the redox reaction with the Ti^{3+}/Ti^{4+} (88).

Further investigations into increasing the surface area available for the electrodes have been performed, looking at high surface nanospheres of TiO_2 which showed excellent performance and high discharge capacities around 108 mAh g^{-1}. (89) The high surface area provides a large interface between the electrolyte and electrode and therefore shortens the overall diffusion path to the active material. A further development of this study introduced carbon nanotubes into the electrode, further increasing the surface area available and providing more highly conductive paths within the electrode (90).

2.2.1.2 Aluminium and alloys

Using Al as the negative electrode is utilised in many ionic-liquid and non-aqueous based Al-ion systems. Within aqueous electrolytes however, a passivating oxide coating forms on the surface of such an electrode, making the aluminium electrochemically inert. In order to overcome this passivating layer, potentials higher than the ESW of water would be required, which would degrade the electrolyte itself.

Recently however, using Al anodes in aqueous systems have been explored, with Al anodes which have been treated with a synthetic SEI (solid electrolyte interface) on the surface of the electrode have shown to reduce dendrites and the formation of the passivation layer. Chloroaluminate melts have shown reduced amounts of the passivation layer, and demonstrated full cells using the treated Al (T-Al) anodes

(91; 92; 93). Polyethelene glycol and PVDF coatings have also been used with results of increased columbic effiency (with 1 M Al(OTF) 98% columbic effiency over 400 cycles were performed) (94; 95).

Combined with MnO_x cathodes, three key studies in recent years have shown the plating and stripping of aluminium as the mechanism for charge transfer. However, the capacity fade of these cells is high – about 42% after only 65 cycles (91; 93).

Alloys of Al are also being used, such as Zn-Al alloy (96). The Zn seemed to prevent a build-up of a passivating layer, while the Al-ions prevented Zn dendrites to form. It appeared both the plating and stripping of Al was seen on the surface, as well as an electrostatic/capacitive mechanism. Al-Cu and Al-Ce alloys are also being investigated, with very high discharge capacities (400 mah g^{-1} over 400 cycles and 360 mAh g^{-1} over 500 cycles respectively) highlighting alloys as a potential for future exploration with aq. Al-ion batteries (97; 98).

A recent study looking at Al foil with a nickel hexacyanoferrate positive electrode, ascribed the capacity fade (about 43% after 500 cycles) to the dissolution of nickel into the electrolyte (99). This then reacted with the Al electrode, creating an unstable electrode-electrolyte-interface, which could be seen clearly in X-ray Diffraction, XRD, and through studying the increase in Ni quantity within the electrode over time. This shows that correct electrode pairing is vitally important in creating a viable Al-ion cell.

2.2.1.3 Molybdenum oxides

Molybdenum oxides have also been investigated as a negative electrode for aqueous Al systems. In 2019, Lahan and Shyamal (6) investigated the role of electrolyte on the performance of MoO_3. They concluded that 1 M $AlCl_3$ in water was the superior electrolyte and found an impressive initial discharge capacity of 680 mA h g^{-1} @ 2.5 A g^{-1}. However, by the 20th cycle this had dropped considerably to 168 mA h g^{-1}. This then remained stable up to 350 cycles, with no sign of decaying further. This phenomenon was explained by initial 'trapping' of the intercalating Al^{3+} in the MoO_3 structure over the first cycles – an irreversible process occurring alongside the reversible one. Interestingly, in 1 M $Al(NO_3)_3$, the authors found an initial discharge of 21,296 mA h g^{-1} @ 2.5 A g^{-1}, which then decayed to 15 mA h g^{-1} by the 15th cycle.

Later work in 2019 and 2020 by Wang et al (60; 100) , found that 1 M $Al(NO_3)_3$ was a suitable electrolyte using MoO_3 nanobelts as the electrode material. The two studies show similar CV profiles for this set up, and also concur with the profiles reported in (101). Galvanostatic curves were collected for (60; 100), with (100) showing a more 'expected' profile and initial discharge of 308–232 mA h g^{-1} @ 1-8 A g^{-1}, two orders of magnitude less than (6). The profiles shown by (60) are for MoO_3 with a polypyrole (Ppy) coating, and show lower capacities still. There is no cycling data provided for

this half-cell set up to compare. However in (100) MoO_3 was then used to create solid state flexible cells with a gelatin-PAM electrolyte with 1 M $Al(NO_3)_3$, which performed 2800 cycles with only 13.8% capacity fade seen. The storage mechanisms were discussed in terms of the nanobelt structure and crystallographic plane of the MoO_3 (010) which was favourable for ion intercalation. XRD also showed that the d-spacing increased with Al^{3+} insertion but went back to pristine spacing on extraction – implying no permenant structural changes within the electrode, which could be a reason for the long cycle life.

2.2.2 Positive electrodes

The positive electrode, for secondary cells, is the electrode with higher potential when in a full cell. Table A.2 in Appendix A summarises the materials that have, to date, been studied as a positive electrode for an aqueous aluminium-ion cell. As with the previous section, a word of warning on comparing performance results from this table between half and full cells. For example, Holland et al studied CuHCF in a full cell with a TiO_2 negative electrode (and 1 M AlCl + 1 M KCl electrolyte) and found a cycle life of 1750 cycles (1), however in a CuHCF half-cell with the same conditions, 28,000 cycles were possible (102).

Key issues with the positive electrode are similar to those in the negative electrodes designed to accommodate Al^{3+}. These include slow diffusion, and breakdown of the electrode crystal lattice over time.

2.2.2.1 Vanadium containing electrodes

Vanadium oxides have been explored as cathodes (or positive electrodes) in a variety of metal-ion cells (27). Vanadium pentoxide xerogel (xero-V_2O_5) was first studied in aqueous Al-ion cells in 2016 (103), using an electrolyte of 1 M $AlCl_3$. It was shown that a discharge capacity of 120 mAh g^{-1} @ 60 mA g^{-1} could be achieved. With increasing current densities however, the performance suffered – 20 mA h g^{-1} @ 200 mA g^{-1}. This suggests that the reaction at the electrode is diffusion controlled. The authors suggest that both water and Al-ions are intercalating into the electrode simultaneously during discharge.

It is already known that within the interlayers of xero-V_2O_5, pronated water and charged ions (such as Al^{3+}) can be easily exchanged when in an aqueous media (104). Therefore, the ion exchange process may be happening alongside the intercalation. During charging, the ion-exchange may trap the Al-ions within the electrode structure and reduce the overall available capacity. This may be a reason for the high fade seen (38%) after only twelve cycles.(103)

Further work in 2019 (105), looked at $FeVO_4$ as a cathode material, again with an electrolyte of 1 M $AlCl_3$. However, in this study ammonium hydroxide was added to the electrolyte to increase the pH to 3.5. The increased pH showed a high specific capacity of 350 mAh g^{-1} @ 60 mA g^{-1} . Initial conclusions from this study were that the aluminium was reacting reversibly with the cathode, however the exact mechanisms were complex. The study concluded that there were reactions between the cathode and Al^{3+}, but also with the electrolyte itself. The rapid fading of this cell of 85% after 20 cycles is indicative of the parasitic reaction of the cathode with the electrolyte; loss of vanadium as V^{5+} to the electrolyte. These reactions also show a phase change of the cathode material, from a triclinic lattice to a more symmetrical system – there is some speculation about the reversibility of this change. Overall though, the need for an EEI (electrode-electrolyte Interface) layer is discussed to reduce the parasitic reaction and maintain the high specific capacities found.

More recently, bronze-type vanadium dioxide holey nanobelts (B-VO_2) have been studied as a positive electrode (106). The nanobelts act like layers and the holey nature increases the surface area of the electrode, allowing easier, shorter diffusion paths for the Al-ions. When investigated in a 5 M $Al(TOf)_3$ electrolyte, a high capacity of 234 mAh g^{-1} @ 150 mA g^{-1} was seen, and at higher current densities (1 A g^{-1}) achieved 1000 cycles with only 22.8% fade. Initially, the discharge capacity rose between cycles. This initial rise could be due to the electrolyte taking time to soak into all the pores of the electrode. The key reaction mechanism discussed was the parallel intercalation of both Al^{3+} and H^+ into the B-VO_2. This is due to the hydrated Al-ions within the aqueous electrolyte. This is a similar mechanism as suggested for the xero-V_2O_5 (103). Additionally, the reduction of V^{4+} to V^{3+} is seen alongside the intercalation. Similarly to (105), some vanadium (as V^{5+}) is also seen to dissolve into the 1 M AlCl electrolyte in the initial cycles between -0.8 and 1 V v Ag/AgCl.

Further evidence of Vanadium dissolution into the electrolyte was found by (107), with a V_2O_5 nanorod cathode. The same fast decaying capacity over cycles was observed and attributed again to the vanadium dissolving into the 2 M $Al(TOf)_3$ electrolyte. The capacity faded from 186 to 20 mAh g^{-1} @ 40 mA g^{-1} after fifty cycles. A barrier layer of Nafion was then placed on the surface of the electrode, to minimise the movement vanadium into the electrolyte. While the charge/discharge profiles were comparable to the unprotected electrode, the capacity fade was much improved. After 50 cycles the discharge capacity was still $\approx$ 120 mAh g^{-1} @ 40 mA g^{-1}.

In terms of the charge storage, analysis of SEM and EDX (Energy Dispersive X-Ray Analysis) data showed that the aluminium may not have been intercalating into the electrode during discharge but forming a soluble product on the surface of the V_2O_5. Due to the lower pH of this electrolyte ($\approx$2) it was reasonably assumed that H^+ were more likely intercalating into the V_2O_5 with fewer Al^{3+}. This compares well with

(105), which saw an increase in cell capacity at higher electrolyte pH, and other vanadium studies which see the proton intercalation occur alongside Al^{3+} (103; 106).

In 2020, a flexible hydrogel electrolyte was used with a $VOPO_4$ electrode to create a flexible battery (100). The long cycle life of this battery (2800 cycles @ 1 A g^{-1}) and low capacity fade (13.8%) shows promise for aqueous gel electrolytes combined with vanadium containing electrodes. The study did not mention any vanadium dissolution into the electrolyte; due to the long cycle life it seems reasonable that this was not present. The key charge transfer mechanism was identified as intercalation of Al^{3+} combined with the redox pairs V^{5+}/V^{4+} and V^{4+}/V^{3+} . Interestingly on intercalation, the d-spacing (distance between layers in a crystal lattice) between $VOPO_4$ layers decreased when accommodating the Al^{3+}. Usually the interlayers have been shown to increase as the Al^{3+} distorts the lattice to 'fit' in. However, in this case, the electrostatic charge of the Al^{3+} must be attracting the negative oxygen atoms in the lattice, these processes are illustrated in Figure 2.6. This process was confirmed as reversible, with the d spacing returning to pristine condition on de-intercalation.

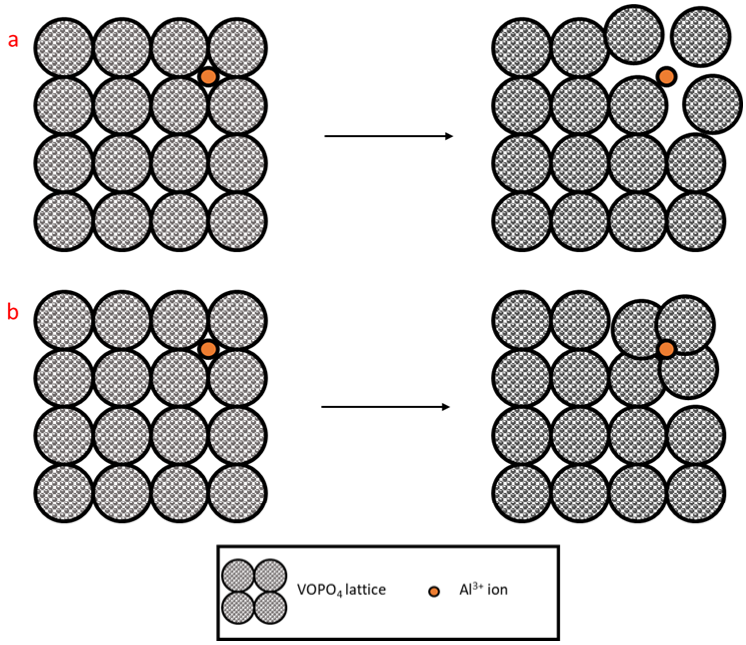

FIGURE 2.6: Schamitic of potential lattice effects for $VOPO_4$ interacting with Al^{3+}, with increased interlayers as Al-ion 'fits' in shown in a), and the charge of the Al-ion reducing the interlayer spacing shown in b)

2.2.2.2 Prussian blue analogues

Prussian Blue Analogues (PBAs) have the structure $A_xMFe(CN)_6$, where A is an alkali metal or alkaline earth metal, and M is a transition metal. PBAs have open lattice frameworks, characterised by large ionic channels and interstitial sites. These properties make them good candidates for electrode materials as they can

accommodate guest ions within the framework easily. PBAs have been investigated as electrodes for other multi-valent ions (108; 14; 109; 110). Copper hexacyanoferrate ($KCuFe(CN)_6$ but more commonly abbreviated to CuHCF) was investigated in an electrolyte of 1 M $AlCl_3$ + 1 M KCl (102; 1). With both K^+ and Al^{3+} present in the electrolyte, it was suggested that both ions were responsible for charge transfer within the electrode. CuHCF has been used in K-ion cells, citing the intercalation of K^+ (111; 11). However, more research is needed here to understand how both K^+ and Al^3+ are reacting within this cell system.

In 2019, Wang et al (60) investigated a flexible Al-ion cell with a CuHCF positive electrode and MoO_3 negative electrode (this work precedes (100) discussed already). Prior to building the cell, Al^{3+} was pre-inserted into the CuHCF electrode. During discharge, a reduction of Fe^{3+} to Fe^{2+} was observed, maintaining the charge balance of the electrode as the Al-ions were extracted. Unlike in previous discussions of CuHCF, there was no mention of loss of Fe to the electrolyte – however it seems cycle life in a half cell was not investigated, and only 100 cycles were investigated in the full cell.

Potassium cobalt hexacyanoferrate ($K_2CoFe(CN)_6$) nanocubes have also been studied as a positive electrode in 1 M $Al(NO_3)_3$ (112). Here the charge mechanism was identified as Al^{3+} intercalation into vacant potassium sites within the cubic lattice of the electrode. The corresponding reactions at the electrode to maintain balance are Fe^{3+}/Fe^{2+}, which is typical of all PBAs so far, but also the pair Co^{2+}/Co^{3+}. A two-step reaction is speculated on, with a 'dehydration step' involved prior to insertion into the lattice. The cycling performance is investigated, with 1600 cycles performed and a promising 25% capacity fade reported. It is suggested that side reactions involving the decomposition of water, or electrode corrosion may be in play here. Investigating the electrodes with SEM, the nanocubic framework had partially collapsed after 1600 cycles – suggesting that structural changes due to cycling are the cause of capacity decay. Of further interest – this electrode was examined with other electrolyte salts ($AlCl_3$ and $Al_2(SO_4)_2$) and the performance was superior with $Al(NO_3)_3$. This makes the clear argument that it is not just the choice of electrode, but appropriate electrolyte which can impact on the performance and overall electrochemical mechanisms involved.

Water-in-Salt Electrolytes (WISE) describe an electrolyte whereby the salt outnumbers the water (solvent) in both volume and weight (9). When this occurs, the water molecules do not fully solvate ions, and thus there are interionic pairs. This greatly increases the ionic conductivity and increases the ESW for the electrolyte (56). Using this approach, a WISE was created with 5 M $Al(OTF)_3$ to investigate $FeFe(CN)_6$ (chemical equation $K_{0.2}Fe[Fe(CN)_6]_{0.79}$) as an electrode material (113). The ESW was increased from 1.23 V to 2.65 V, which facilitated a high specific capacity of 116 mAh g^{-1} @ 150 mA g^{-1}, the highest seen for PBA electrodes currently. The reaction

mechanisms within this system are discussed extensively. On initial charges the capacity of the cell slowly increases – due to the removal of residual K-ions over the first few cycles (providing more vacancies for Al^{3+} on subsequent cycles). Additionally, within the first few cycles, irreversible structural changes of the electrode lattice are seen from XRD, which may reduce but also stabilise the overall capacity by 'trapping' some Al-ions.

The redox pair Fe^{3+} /Fe^{2+} was observed, as is expected for PBAs, alongside Al^{3+} intercalation. There is also speculation about the role of K^{+}, as well as protons within the charge/discharge process. However further studies are needed to understand these interactions. Further, the authors claim 'good cycling stability' (113), however, far superior PBA cycling stability have been observed in CuHCF discussed above (114; 102). Although not described as a WISE, a high concentration (5 M $Al(CF_3SO_3)_5$) was the electrolyte used with a potassium nickel hexacyanoferrate (KNHCF) electrode to make a cell with an Al foil negative electrode [88]. Again, the redox pair Fe^{3+} /Fe^{2+} was observed, alongside Ni^{3+} /Ni^{2+}, during reversable Al^{3+} intercalation. The KUHCF structure remained unchanged after 500 cycles, which suggests a stable positive electrode material for aqueous aluminium cells. Unfortunately, the capacity fade seems primarily due to the Al foil. It would be useful to see KNCHF studied as half cells, or with TiO_2 as the negative electrode, to fully see the limits of this material.

2.2.2.3 Manganese Oxides

In the last few years Manganese Oxides have been researched as electrodes, both when combined as an Mn-Al ion battery (91; 93), and with only Al-ions as the charge carrier. A multi-step process has been identified by a few studies, whereby Mn^{2+} initially dissolves into the electrolyte on the first discharge, forming an amorphous layer on the surface at the first charge. This layer is likely composed of Al, Mn, and O, and is likely soluble in water. It is this layer that then 'plates and strips' in subsequent cycles. By adding Mn salt initially into the electrolyte, this enhances the overall performance. These cells can therefore be described as Mn-Al ion cells.

When looking at the nanostructures, nanorods and nanowires have been investigated by Joseph et al (115; 116). A potassium-rich manganese oxide was investigated, which formed nano-wires, in 1 M $Al(NO_3)_3$. During charge, there was a switch between the K and Al, whereby K-ions would dissolve into the electrolyte and be replaced by Al^{3+} in the vacancies. Over time though, the K-ions did not re-insert and the concentration of K in the electrolyte increased as cycling continued (115). When researching the Magnesium doped MnO_2 nano-rods, a similar mechanism was suggested whereby the Mg^{2+} ions create large tunnels in the structure which allow for easy Al^{3+} intercalation (116). There is some speculation on whether this is a similar 'exchange'

as was seen in (115). In addition to intercalation, there is some capacitive charge storage observed at the surface of the electrode.

A mixture of surface mechanisms like the forming of a new layer, or capacitive storage is observed along with intercalation of Al^{3+} in the bulk of the electrode. If both surface and bulk processes can be taken advantage of, and optimised, this may be an exciting material pursue for high performance Al-ion aqueous batteries.

2.2.2.4 Other materials

The use of graphite is more common in non-aqueous Al-ion batteries, however two studies have recently used them as the positive electrode within an aqueous cell (117; 118). Multi-layer graphite (as discussed in (117)) showed an intercalation/de-intercalation of Al^{3+} between layers, however the expansion of the lattice during insertion led to cracking of the structure and hence a short cycle life. When looking at graphene with the addition of carbon nanoparticles, a capacitive storage mechanism is suggested, which may lead to longer cycle life (apparently 0% fade over 3500 cycles (118)), but potentially a higher self-discharge.

Bismuth oxide (Bi_2O_3) was investigated in 2020 by Nandi and Shayamal (119). Initial discharge capacities in a full cell with Al-ion negative electrode showed very high values (1130 mAh g^{-1} @ 1.5 A g^{-1}), and 99% columbic efficiency. However, this dropped significantly to 103 mA h g^{-1} within 20 cycles, and remained stable for the following 50, showing no additional signs of capacity fade. This behaviour suggests that more complex reactions are being set up in the initial cycles, which then stabilise past the first 20 cycles. Suggestions of both an alloying reaction between Bi and Al, as well as an interfacial storage between Bi and Al_2O_3 at the electrode/electrolyte interface. Although WO_3 electrodes show poor coulombic efficiency (80% (101)) over cycling in both 1 M $AlCl_3$ and 0.5 M $Al_2(SO_4)_3$, the capacity increases over cycling time, to around double the initial capacity seen. With no significant structural changes seen in the electrode after 100 cycles, and the main mechanism assumed to be intercalation/deintercalation of Al^{3+}, this could be an interesting material to study – if the Coulombic efficiency can be improved.

2.3 A note on half cells

Overall, the negative half cells reported in the literature can be summarised as TiO_2 based, or MoO_3 based. Figure 2.7 plots the reported the cycle life of these half cells against the specific capacity reported. While the current density is not shown in this plot, we can see a cluster of low specific capacity reported for TiO_2 based half cells.

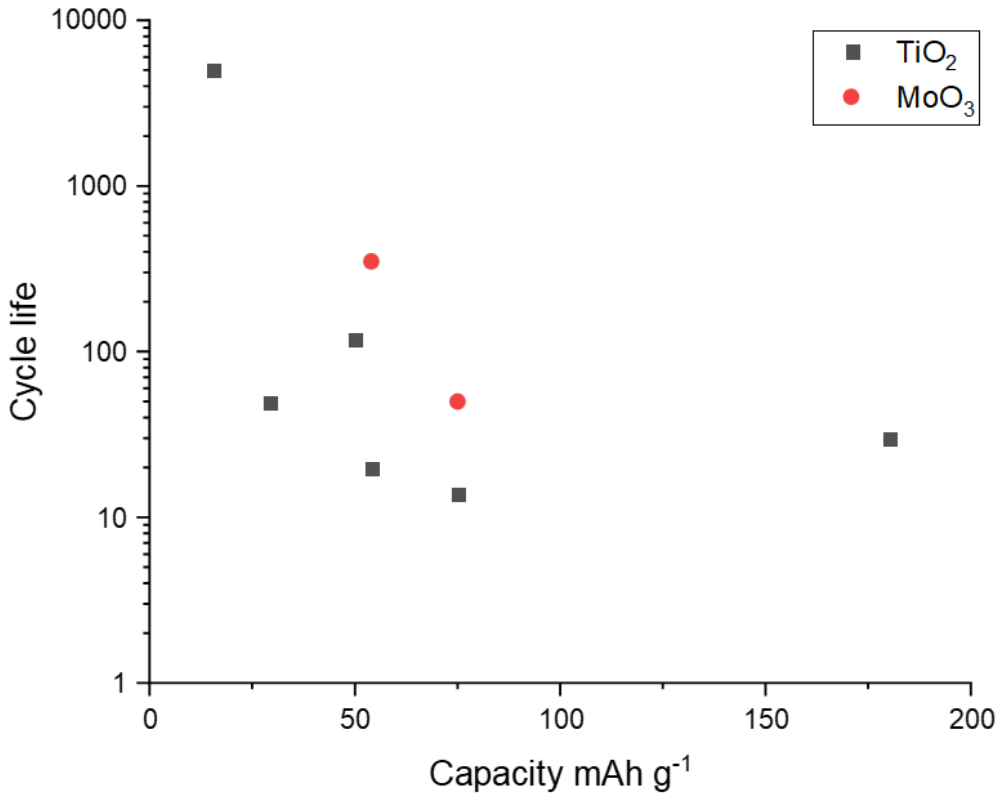

FIGURE 2.7: Cycle life plotted against specific capacity reported for TiO_2 and MoO_3 half cells (2; 3; 4; 5; 6)

There are only two MoO_3 based half cells reported with sufficient data to plot, however it appears a trend in higher specific capacity may be achievable with this electrode basis. All but one of the reported half cells have a cycle life below 350. TiO_2 anatase nanopowder, with 1 M $AlCl_3$ + 1 M KCl electrolyte shows excellent cycle life of 5000 cycles (2). Other TiO_2 based electrodes only use an aluminium salt in the electrolyte, and do not have an additional potassium salt – there may therefore be potential in exploring electrolyte additives to improve the cycle life.

There are many half-cells reported in the literature for the positive electrode. Figure 2.8 plots the cycle life against the specific capacity for half cells that have both these values reported in the literature. From the limited dataset provided. There is a suggestion that higher specific capacities (above 200 mAh g^{-1}) are achievable using vanadium based electrodes. Although the highest capacity example only reported a cycle life of 20 cycles. One data point for the graphite-based electrode of course does not provide a pattern, however the capacity reported (157 mAh g^{-1}) along with a promising cycle life of 3500 cycles would suggest further investigation into this electrode design (118). Interestingly, the highest cycle life reported is with the lowest

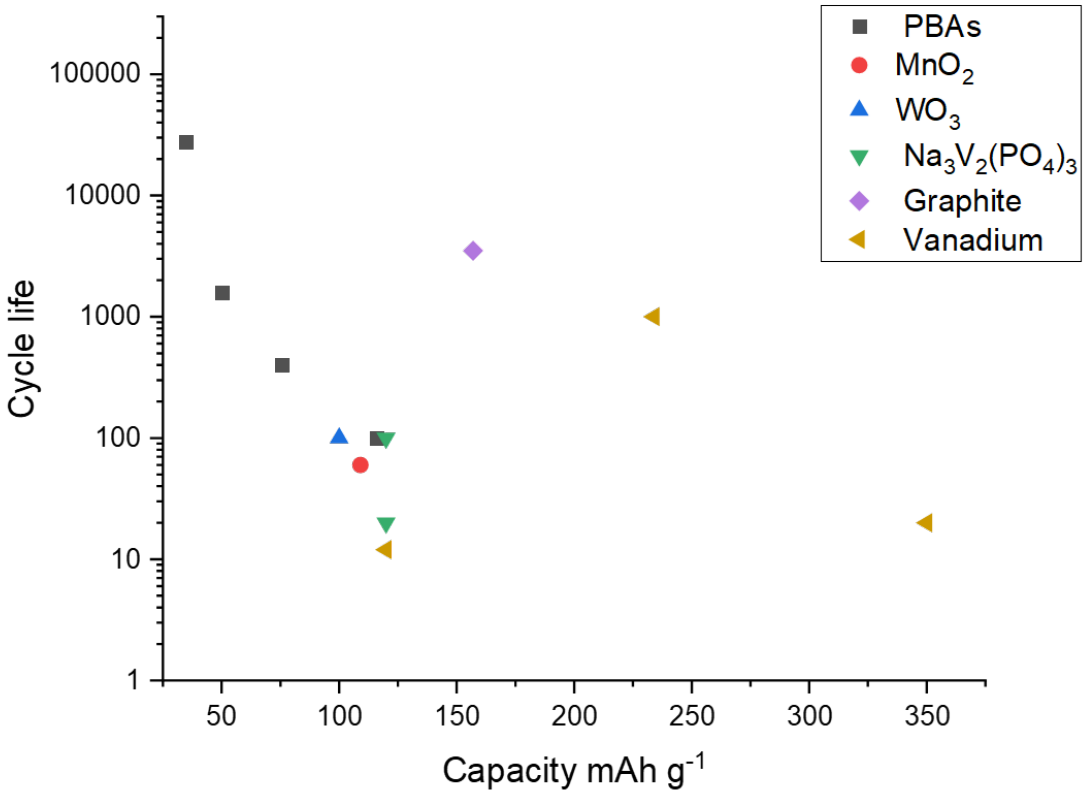

FIGURE 2.8: Cycle life plotted against specific capacity reported for positive half cells

specific capacity – although all the PBAs appear to have lower specific capacity, an anomalous 28000 cycles is reported for a CuHCF based electrode (102). As with the high cycle life TiO_2 from the negative electrode example, this electrode was tested in an electrolyte with both aluminium and potassium salts – suggesting that the potassium may help with cycle life extension – but perhaps not increase capacity. Figure 2.9 shows the potential ranges reported in literature for both positive and negative half cells.

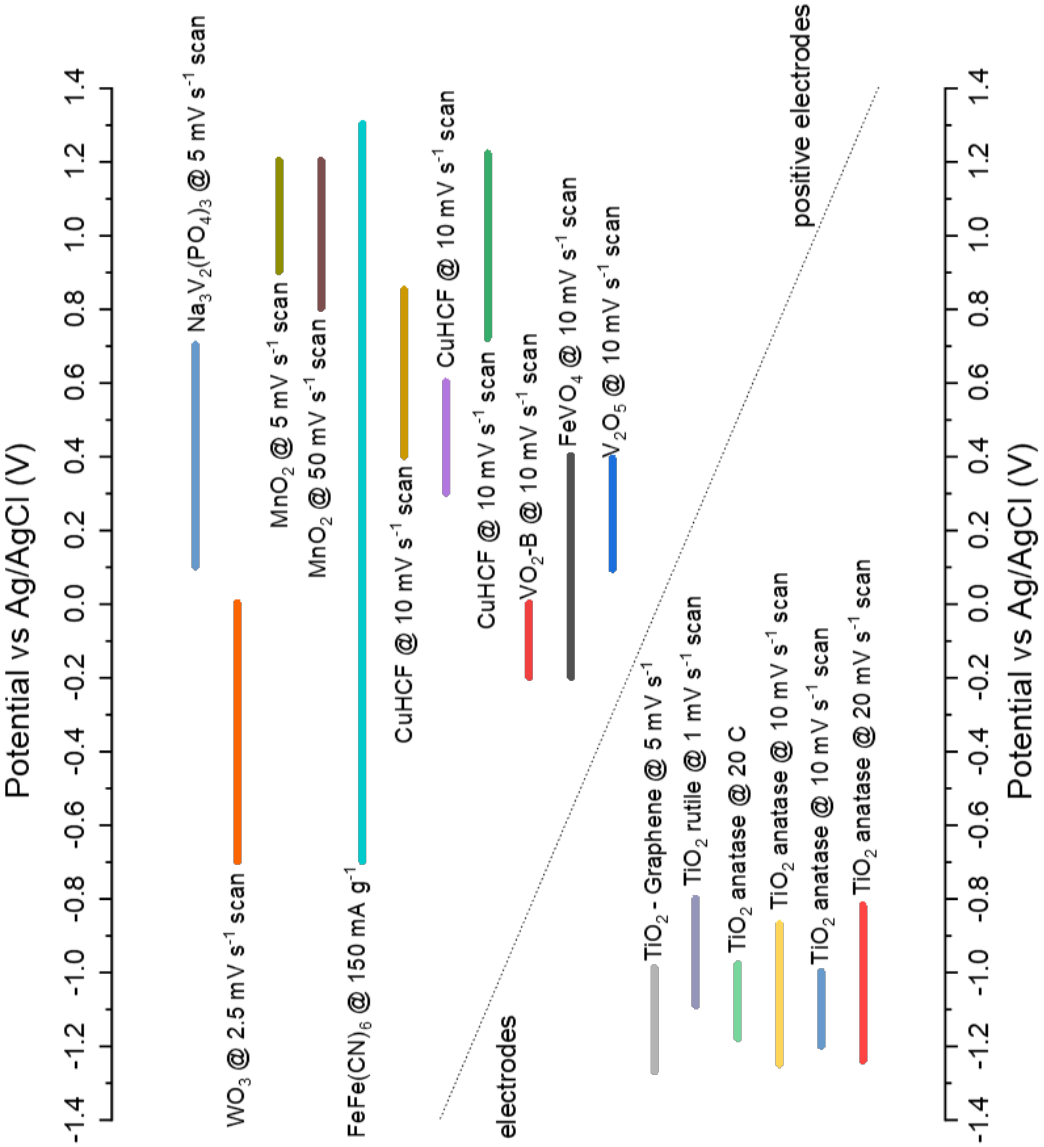

FIGURE 2.9: Reported potential ranges for electrodes in half cells

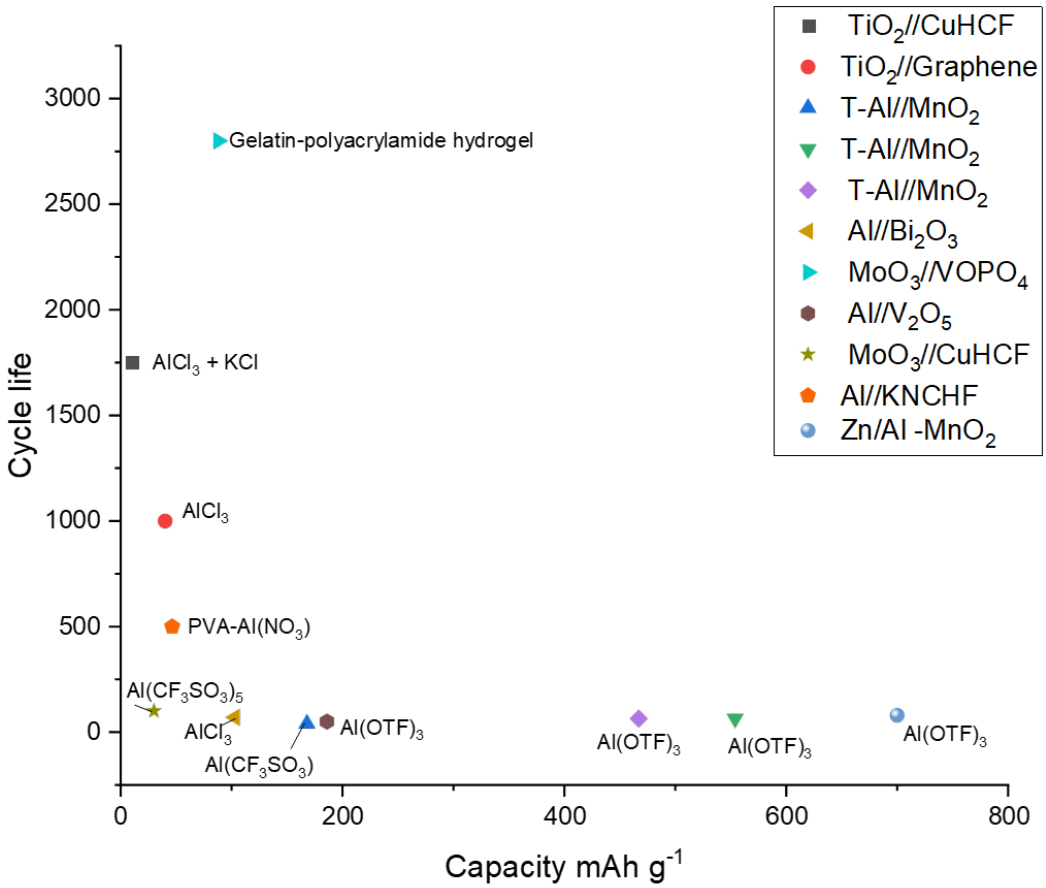

FIGURE 2.10: Cycle life plotted against specific capacity reported for full cells

As has been stressed throughout this review – understanding how electrodes behave as a full cell is important for the potential commercialisation of aqueous Al-ion technology. Figure 2.10 plots the cycle life against the specific capacity reported for full cells in the literature. The electrolyte used is overlaid. It could be suggested that full cells with an Al electrode, whether alloyed with Zn or pre-treated, have low cycle life regardless of the electrolyte. This can be seen with $AlCl_3$, $Al(CF_3SO_3)$, and $Al(OTF)_3$ all showing low cycle life when paired with an Al electrode in a full cell. This is most likely due to the passivating layer which forms on the Al in the cell, which in half cells may not have been such a limiting factor. Further, a case could be made that the $Al(OTF)_3$ also leads to lower cycle life cells, but since all examples reported have an Al based electrode, more research into this electrolyte may be useful. The $AlCl_3$ electrolyte appears to give good cycle life for TiO_2 containing electrodes – with the addition of KCl increasing cycle life further, although not to the same extent as with the half cells. Hydrogel electrolytes appear to increase cycle life substantially – with the PVA-$Al(NO)_3$ electrolyte combined with the Aluminium and PBA electrodes providing just over 500 cycles (60) – the highest reported for an Al containing electrode within a full cell. Clearly, the Gelatin- polyacrylamide hydrogel has the highest cycle life reported for a full cell, 2800, with 13.8% capacity fade (100). This

hydrogel result requires more research, as this increase in cycle life combined with the flexibility of the cell described would certainly show commercial potential.

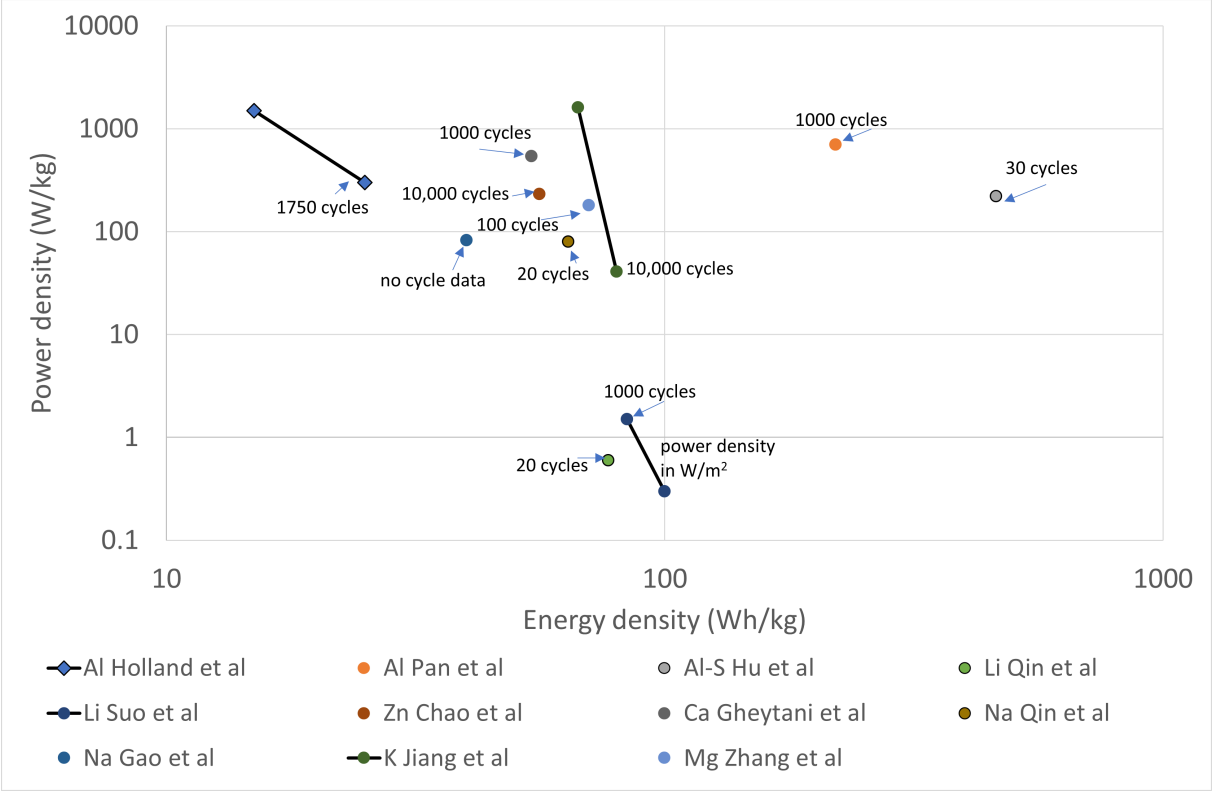

FIGURE 2.11: Ragone plot comparing various metal-ion lab-based aqueous electrolyte cells. Holland et al Al-ion cell in diamond (7; 8; 9; 10; 11; 12; 13; 14; 1; 15; 16; 17)

Figure 2.11 places the current aqueous Al-ion cell discussed in (1; 20) on a Ragone plot amongst other Metal-ion aqueous cells in similar developmental stages (i.e. lab based). The cell appears to have higher power density and lower energy density than the other cells reported here. These parameters may suit a capacitor more than an electrochemical battery cell.

2.4 Supercapacitors

Supercapacitors are another energy storage device, they boast high power densities (90 kW kg^{-1} (17)) compared to batteries, and high cycle lives ($\geq$1000 (**?**)). The energy density, however of many supercapacitors cannot compare with that of the current market leaders in the battery world ($\approx$ 2 Wh kg^{-1} for EDL supercapacitors (19)). Another disadvantage for supercapacitors is the self-discharge. This has not been discussed in previous sections of this chapter – as batteries tend to have very low self-discharge over time (months-years) (17; 77). Capacitors tend to self-discharge in a matter of days, where most supercapacitors self-discharge in a matter of weeks – making them ineffective energy storage over a medium- or long-term time frame.

Energy storage in capacitors is achieved due to charge separation, and in more typical supercapacitors, this is due to the electrochemical double layer capacitance (EDLC). Additionally, in what would be called a pseudocapacitor (or capattery or cabattery), a mix of EDLC and surface adsorption, or redox reactions can be seen (19). The primary charge storage of these devices however is charge separation. This can be seen on a CV plot, where there is no obvious peak in current (seen in electrochemical reactions at the standard electrode potential), but a flat current response to changing potential, as shown in Figure 2.12.

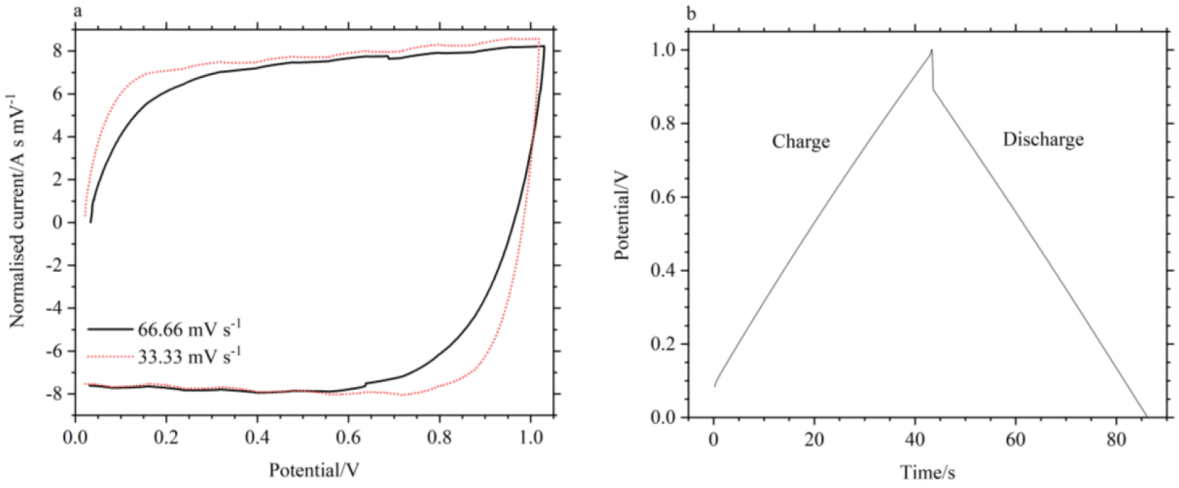

FIGURE 2.12: 2 a) CV scans of a 10 F, 2.7 V cylindrical supercapacitor at 33.33 and 66.66 mV s . b) Constant current cycle of the same supercapacitor at 167 mA. Figures from (18)

Supercapacitors in general have longer cycle life than batteries, as the electrochemistry doesn't occur within the electrode and therefore the structural changes seen in batteries are unlikely in supercapacitors. This can be seen with 10,000 cycles performed and around 10% fade in capacitance (120; 121).

2.4.1 Self-discharge mechanisms

The high self-discharge is proposed to be caused by three potential mechanisms; ohmic leakage of current, a faradaic reaction, and the redistribution of charges throughout the capacitor (122; 123). The ohmic leakage is due to any connections between the electrodes that can lead to a short circuit, usually due to the design or manufacture of the cell, as it is realistically impossible to completely isolate the electrodes. This can be measured and used to identify any faults in manufacture or show any improvements in the isolation of electrodes. This type of self-discharge is proportional to the ohmic resistance of the leakage (connection between electrodes) as well as the capacitance of the full capacitor. It should also be noted that this type of self-discharge can only be measured in full-cells and is not seen when looking at

half-cells. This mechanism, while easy to understand as a short-circuit, does not help isolate any electrochemical mechanisms involved in self-discharge, or improve understanding of electrode/electrolyte design. (122; 123; 124; 125; 126)

The faradaic reaction is the oxidation or reduction reactions at the surface of the electrodes which lead to self-discharge. For example, on a positive electrode, there will be a build-up of negative ions (anions) from the electrolyte on the surface, and this charge will be balanced in the double layer. However, the potential of the electrode may be higher still than the oxidation potential of the ions in the electrolyte (either in solution or on the surface of the electrode). This will lead to the oxidation of the surface, which releases the anions from the double layer and thus reduces the charge held at the electrode. A similar situation occurs on the negative electrode, with the cations being released from the double layer during a reduction reaction at the electrode surface. (123; 125; 126; 127)

The faradaic self-discharge can thus be limited by either activation – due to the reaction rate at the surface of the electrode, or diffusion – due to the transport of ions to the electrode. However, the diagnostic plots of activation controlled faradaic discharge appear similar to that of charge redistribution, the third mechanism of self-discharge. (122)

Charge redistribution works under the (usually correct) assumption that when charging a capacitor, different parts of the electrode will have different charges, thus there will be a charge gradient across the electrode material. The charge redistribution therefore is the movement of charges from high potentials to low potentials through the material to reduce the charge gradient. As the charge is only measured on the surface of the electrode, this will result a lower charge being measured and thus a self-discharge can be reported. However, there is no loss of charge from the electrode. During the redistribution though, parts of the initial energy (electrostatic potential) are lost due to heat – which reduces the overall energy of the system.(122; 123; 128)

The use of nanostructures for electrodes, with many pores and a high surface area increases the potential for charge-redistribution as there are more areas for the charges to diffuse into. There has been an increase in research of this mechanism, as the nano-materials, while increasing this form of self-discharge, also increase the energy density of the electrodes and so a design that can inhibit the self-discharge while maintaining the benefits is the drive behind much of this research. (122; 123; 126; 129)

An increase in temperature has been found to increase the rate of all self-discharge mechanisms. This follows from diffusion, resistance, and activation controlled faradaic reactions all increasing with temperature. While this note appears simple, or obvious, it is a key piece of information that can help design storage or usage procedures which reduce temperature in order minimize all self-discharge mechanisms. (130)

As with capacitors, batteries also see self-discharge, however this is usually on a much larger timescale and thus has not been investigated in as much detail (19). Aqueous Al-ion batteries however, have shown a fast self-discharge (85) and so there may be scope in assessing the mechanisms described above in relation to this specific battery.

2.4.2 Aqueous supercapacitors

The same electrolyte variation exists in supercapacitors as in batteries. The focus of this section therefore focuses on aqueous supercapacitors – due to their lower cost, higher safety and higher availability.

As shown in Figure 2.13, the Al-ion cell described in (1; 20) seems to match the parameters of the supercapacitors more than other metal-ion aqueous cells as shown in Figure 2.11 where it sits off to the top right of the Ragone plot. The capacitive behaviour of the Al-ion cell puts it in a unique position, where it could be utilized where other capacitors are now. This would include within electric vehicles to provide a high-power surge for acceleration, or to assist in regenerative braking [33]. Given the high cost of supercapacitors, a cheaper Al-ion alternative would be extremely beneficial.

2.4.3 Al-ions in aqueous supercapacitors

In recent years only a few aqueous Al-ion supercapacitors have been investigated. However for batteries, the TiO_2 (2) and the graphite (118), capacitive storage has been identified as one of the storage mechanisms (121; 131). Research by Krishnamoorthy and Jha (121), suggests using their electrode as a cathode for an Al-ion battery, before demonstrating its use in a supercapacitor with an ionic liquid. Therefore, it is useful to bear in mind the potential for Al-ion use as a hybrid capacitor – which could reduce the cost and complexity for these applications (85). Table A.3 in Appendix A summarises recent aqueous aluminium supercapacitors.

2.5 Life cycle assessment

2.5.1 Motivation for use of life cycle assessment

A life-cycle assessment (LCA) is a framework for measuring the environmental impact of a product. This can consider the whole product life cycle – considering raw material extraction, manufacturing and processing, distribution, usage as well as end of life (waste disposal or recycling) – or just a section of it (see Figure 2.14). The

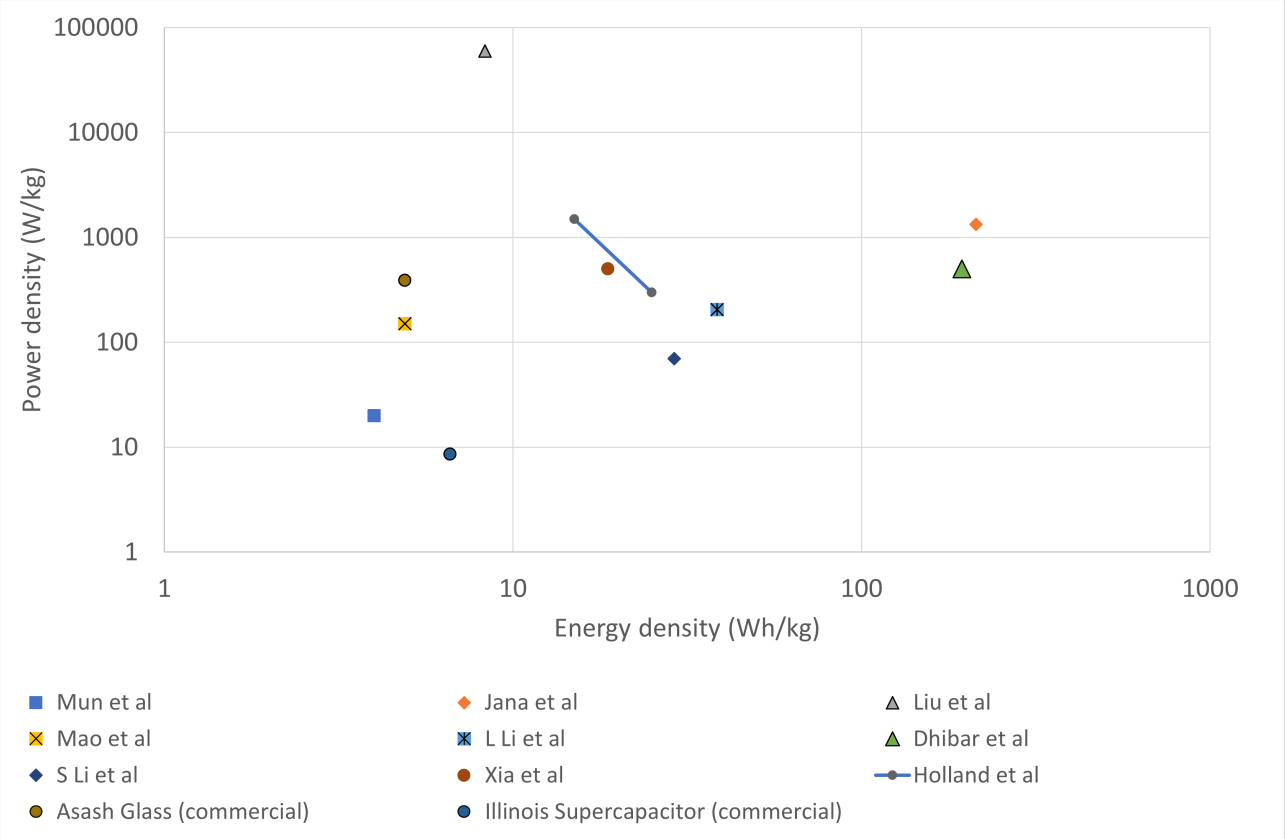

FIGURE 2.13: Ragone plot comparing lab-based aqueous electrolyte supercapacitors (circles) with commercially available supercapacitors (squares). Al-ion cell is also illustrated from Holland et al as a comparison (diamond). NB electrolyte composition of commercial supercapacitors was not available and have been provided for context between lab based and real-life parameters. Adapted from (19)

lifecycle analysis framework is defined by the international standard BS EN ISO4040 (132). (133; 134)

Performing an LCA on the Al-ion cell is a useful tool in understanding the sustainability of the cell itself, in terms of its constituent parts. Further, once the model has been set up, assessing design changes such as the use of carbon felt instead of a polycarbonate for the electrode substrate can be assessed in terms of its environmental impact alongside performance assessments. This will shape a sustainable development of the design.

2.5.2 Format of a life cycle assessment

There are four key stages to an LCA:

1. Goal and Scope are identified – the intended output is defined and the scope (what will and will not be assessed) is described to ensure there are no ambiguities in the study.(133)

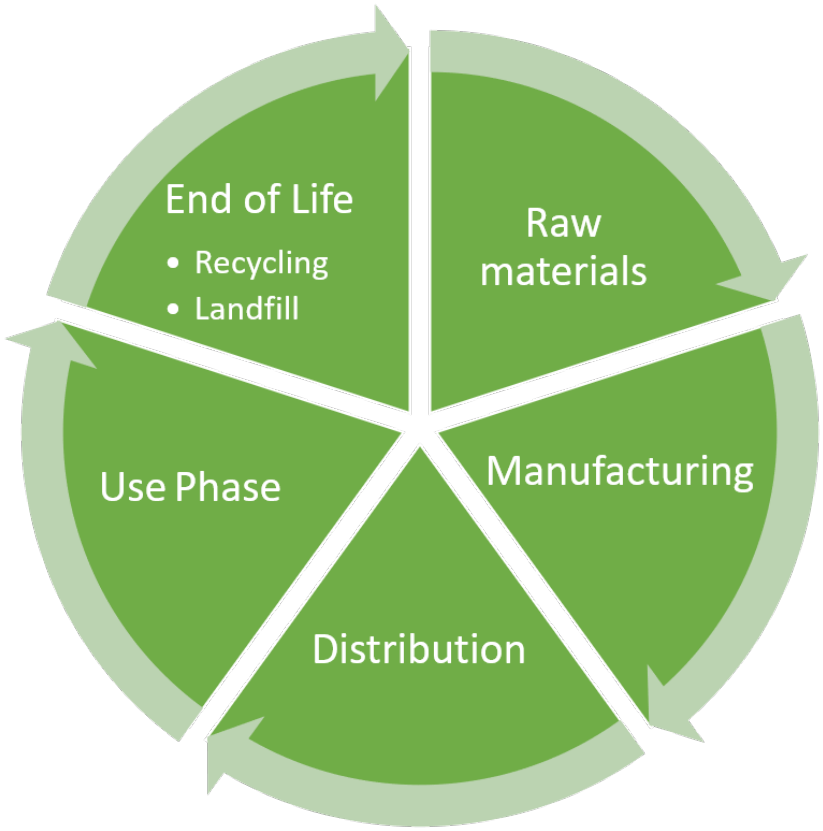

FIGURE 2.14: Product life-cycle

2. Life Cycle Inventory – this is the data collection phase of the LCA and is often the most labour intensive. All the environmental inputs and outputs are recorded, such as raw materials, emissions, different types of energy. This can be complex as it involves looking at supply chains, and different stakeholders in the product cycle. Often, industry standards and averages are used which may not be completely representative.(133)

3. Impact assessment – once all the different processes and flows are recorded, their overall impact can be assessed. This requires impact parameters (based on the initial goals) to be produced, usually in some 'equivalent' such as for emissions, CO_2 equivalent. All the impacts from each step are summed to produce the overall impact of the lifecycle (133).

4. Interpretation – this is where the key conclusions are drawn. The stages with the highest impact can be identified which can steer action to help reduce or minimise the effect. The LCA itself is also reflected upon here, limitations of the model are outlined so that the whole picture can be understood – this may lead to further data collection in areas where industry standards were used or where there wasn't much relevant data.(133)

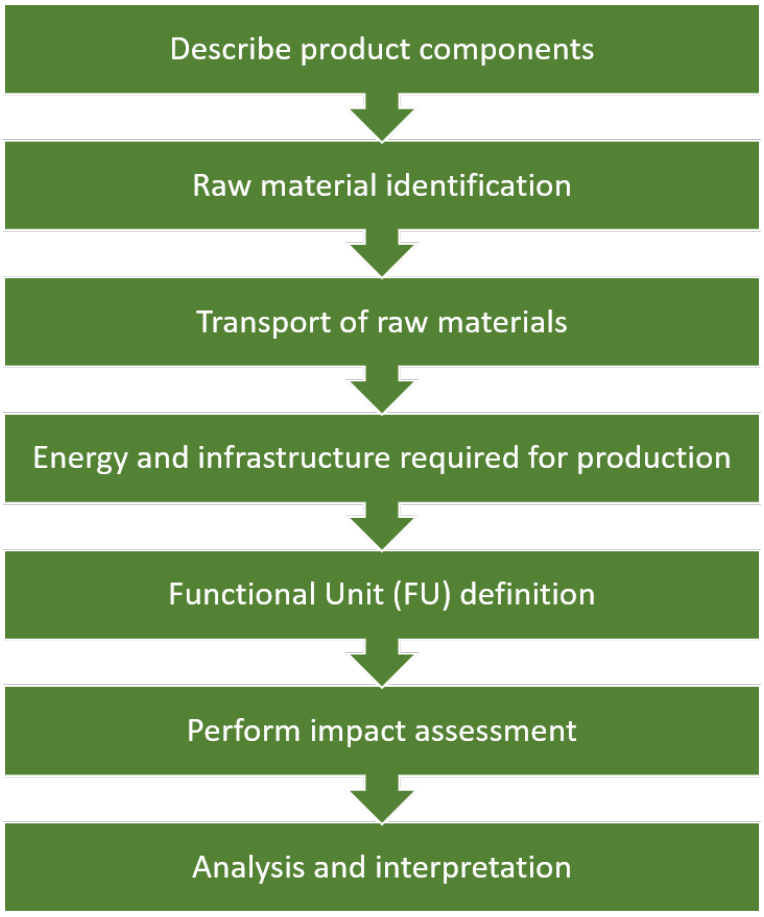

FIGURE 2.15: LCA flow followed

Within existing literature, Al-ion batteries have been studied, however there has not yet been a comprehensive LCA of an aqueous Al-ion battery. Maczka et al (135) and Salgado Delgado et al (136), both studied Al-ion batteries with ionic electrolytes. A key take-away from these studies is that the overall inputs into an Al-ion battery have fewer environmental impacts than Li-ion, and due to the lower energy density of Al-ion, more overall inputs are required to manufacture an equivalent energy output. The results therefore depend on how the data is interpreted and what questions are being answered through LCA. This is where the choice of a functional unit (FU), the quantified performance of a product system for use as a reference unit (132) is important. The FU can be in terms of mass, energy, or any other useful reference unit that enables the correct analysis to be performed.

2.5.3 Batteries and dual energy storage systems (DESS)

Many LCAs have found that while the initial resource use of an electric vehicle, EV, battery is higher than for internal combustion engines, ICEs, (137; 138), overall, the use of EVs reduces environmental impacts of cars and other vehicles. Various Li-ion based batteries have been used in EVs and assessed environmentally, with Lithium

iron phosphate (LFP) often being seen as overall better for the environment than the Nickel-Manganese-Cobalt (NMC) batteries (137; 139). The use of energy storage system (ESS) is a large portion of the overall environmental impact of a vehicle and it is essential to explore different options for electrifying our vehicles. A dual energy storage system (DESS), often called Hybrid energy storage system (HESS), in the context of an electric vehicle (EV) is an energy storage system composed of a high energy (HE) component and a high power (HP) component. The use of the term DESS is to avoid confusion between hybrid electric vehicles (HEV), which refer to a combination of electric and internal combustion power sources. There is also some use of DESS within an HEV, which may further the confusion of definitions (27). Within a DESS, the high energy component provides energy for cruising and other low power manoeuvres, and the high-power component provides additional (or all) power for accelerations along with being a sink for energy generated from braking – limiting the demand on the HE part and extending its lifetime (140). In this work, the life cycle assessment is topology agnostic, however, a schematic of a typical DESS is shown in 2.16.

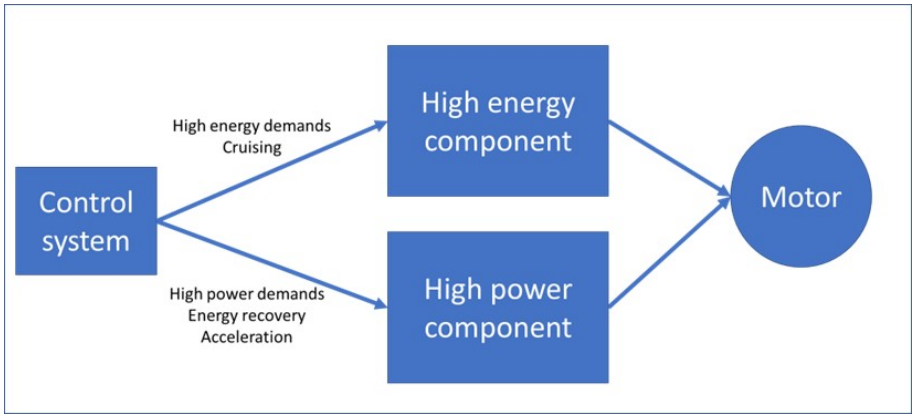

FIGURE 2.16: Schematic of a DESS

Usually, the HE component is an energy dense battery, such as lithium-ion, with the HP component being provided by supercapacitors (often called ultracapacitors). The use of DESS in EVs is not widely adopted with many discussions of use cases based on different driving styles and different vehicle applications, which are summarised in Table 2.1. There is a range of configurations for DESS, depending on the specific scenario and vehicle scale, from a city bus driving a normal route (141) , to a sports car being driven aggressively (142). While adoption of DESS is in its infancy, some parallels can be made with conventional hybrid (internal combustion engine – battery) systems (143). From Table 2.1 it is clear that the number (1 - 38406), the voltage (136 - 444 V), and capacity (0.9 – 115 kWh) of the Li-ion cells as well as the capacitance of the SCs varies widely depending on application. Factors which can impact the configurations are the criteria which are optimised such as minimising weight, cost and charge time. However, there may also be a desire to keep battery

replacements to a minimum or reduce the number of charge/discharge cycles or state of charge optimisation over the vehicle's lifetime. The focus is highlighted in Table 2.1. Ensuring the overall battery and DESS state of health is also a driving factor in system configuration (144; 145). Overall, only one study was found to use environmental impact as a key driver (146), instead of a reported output or 'bonus' to the other optimisations. For example, two papers optimising a DESS for the Tesla Model S, report differences in power requirements of $\tilde{1}20$ kW in the supercapacitors, and $\tilde{9}$ Wh difference in battery provided energy. The higher power and energy demanding result looked at optimising for cost reduction (147), whereas the other took a balanced look at cost, mass and volume reduction to provide a different result (142).

A further distinguishing factor is the ratio of HE:HP components, whether the HP component is being used purely for power-smoothing, or as the main contributor to all high-power needs (such as accelerations). For a power-smoothing application, the HP component makes up a smaller proportion of the DESS. Both options show improvements in terms of overall lifetime of the energy storage system and cost savings, however, there has not been an environmental assessment into which DESS version has the fewest environmental impacts over the lifetime of the vehicle used. This will be addressed as the focus of the assessment presented in this paper. There has been an initial LCA looking at a DESS with two types of Li-ion battery, a high power and high energy version, which saw environmental benefits compared to a single type of Li-ion battery (148), however noted that the emissions produced through manufacturing were higher than a HE only Li-ion battery pack (a 50% increase for CO_2 emissions and almost double for the impact on water acidification), and environmental benefits were only seen here if the lifetime of the car could be doubled. Many LCAs have been performed of different Li-ion battery configurations (149; 26; 24), as well as for capacitors and supercapacitors (SCs) (28; 150; 151), however these have not been evaluated within a DESS from an environmental perspective. The manufacturing process is a key source of emissions for Li-ions, if emissions can be reduced at production by using different HP components, while providing the same lifetime extension, then overall environmental impacts can be further reduced. Continued reliance on lithium batteries will put more pressure on the already politicised mining of associated minerals and may increase the costs beyond the lifetime extension benefits. Therefore, looking at non-lithium, lower cost and easier to produce options for the high-power component of a DESS is crucial to making them accessible.

Example vehicle	Supercapacitor configuration	Battery cell configuration	Li-ion cell chemistry	DC-DC converter power rating	Optimisation aim	Ref
1. City bus	12876 total 222s58p (3000 F2.7 V 4870 W ea.)	38406 total 37s1038p 318 kWh, 136.9 V total	$LiFePO_4$	62 kW	Cost reduction	(141)
2. Tesla Model S	150 150s1p (1500 F 1850 W ea.)	11840 74s160p 82 kWh 236.8V total	$LiFePO_4$	268kW	Mass, volume, cost reduction lifetime extension	(147)
3. Tesla Model S	90 90s1p (3400 F 2.7 V 4420 W ea.)(152)	7104 96s74p =92.4 kWh 345.6 V total (153)	$LiFePO_4$	342 kW	Cost reduction lifetime extension	(142)
4. VW e-golf	1 (0.17 kWh)	1 31080 Wh, 444 V	Not specified	200 kW	Cost reduction lifetime extension	(154)

Continued on next page

Table 2.1 – *Continued from previous page*

Example vehicle	Supercapacitor configuration	Battery cell configuration	Li-ion cell chemistry	DC-DC converter power rating	Optimisation aim	Ref
5. BMW i3	94s 350 Wh total	96s =36.8 kWh 307.2 V total	NMC	35 kW	Cost reduction and lifetime extension	(155)
6. 800 kg EV model	5s (36 F, 9.5 kg ea.)	1 33.2 kWh 239 V total	Not specified	Not specified	Increasing drive range and mass reduction	(156)
7. EV car model	72 350 F, 0.06 kg, 5.9 Wh/kg ea.	100s71p 75.0 Wh 320 V total	$LiFePO_4$	Not specified	Cost reduction and lifetime extension	(157)
8. Military-All Terrain Vehicle (M-ATV)	2114 151s14p (1430 F, 1.52 Wh 1848 W)(152)	116s1p 0.9 kWh 429.2 V total	NMC	120 kW	Fuel reduction	(158)

Continued on next page

Table 2.1 – *Continued from previous page*

Example vehicle	Supercapacitor configuration	Battery cell configuration	Li-ion cell chemistry	DC-DC converter power rating	Optimisation aim	Ref
9. Tesla Roadster	24 24s1p (58 F 16 V ea.)	1869 89s21p 24.3 kWh 320.4 V total (153)	$LiFePO_4$	7.24 kW	Mass, volume, cost reduction lifetime extension	(159)
10. City bus	50 25s2p 140 F 27 V 14.2 Wh	600 120s5p =115.2 kWh 384 V total	Not specified	Not specified	Reduced temperature dependence and cost reduction	(27)
11. Mid-size EV	72 (2000 F, 2.7 V ea., 5 Wh kg^{-1})	152 22.1 kWh 250.8 V total	Not specified	Not specified	Lifetime extension	(160)

TABLE 2.1: Summary of optimised SC/battery DESSs from literature and, where available, the configuration (no. in series X, no. in parallel, Y) will be stated as XsYp, as well as Li-ion cell chemistry.

2.6 Conclusion

Aluminium has the capability to be a major player in energy storage solutions. Its high volumetric energy density, 8.04 Ah cm^{-3} , abundance, pre-existing production industry and recyclability make it a sustainable option. Pairing this technology with aqueous electrolytes in batteries and supercapacitors, has the potential produce inherently safe and cheap energy storage. The versatility of these systems has been discussed in the Chapter.

Secondary Al-ion batteries have had an increase of attention in the last five years or so, with the exact charge storage mechanisms for some systems remaining complex and unknown for many electrodes. This is clearly a space with the potential for growth, with better elucidation of reaction mechanisms and refinement of electrode choice. Al-ions have a variety of charge transfer mechanisms; for the TiO_2 negative electrodes, increasing surface area clearly increases the capacity, and so short diffusion paths are critical here to enable the reactions - which may be a combination of surface and pseudocapacitive. Lattice expansion due to Al^{3+} insertion in vanadium containing positive electrodes shows that bulk reactions are also possible. There are many unknowns still, regarding the charge transfer within many electrode materials – with an engineering focus primarily on 'does it work' prior to the investigation into how. This is illustrated for CuHCF electrodes with as yet unexplained displaced Fe in the electrolyte. There are few studies into supercapacitors with Al-ion technology. However, many of the secondary batteries have pseudo-capacitive behaviour. It is expected that as the exact charge storage for some electrodes (such as TiO_2) is determined, the role of Al-ion technology may shift towards supercapacitor storage.

To fully comply with the goals of sustainable development and reduction in not just CO_2 but in all environmental impacts, the use of life cycle assessment in all stages of design is useful. They allow the design drivers to align with environmental concerns as well as performance. Further, the practical applications of aq. Al-ion can be understood environmentally, for example within a dual energy storage system. DESS's have been shown to increase overall lifetime and reduce overall cost of many electric vehicles compared to a single battery energy storage system (BESS). However, the DESS has not been assessed using an LCA, and this may be a rare opportunity to display where both economic and environmental goals align.

Chapter 3

Methodology

This chapter describes the experimental and manufacturing methodologies that are referred to within the thesis. They are organised by chapter, and are described for the chapter in which they first appear

3.1 Life cycle assessment (Chapter 4)

OpenLCA v1.10.3 (161) software was used to perform the LCA analysis within this thesis. Data for specific materials were sourced from the ecoinvent database v3.2 (162; 163) as well as the GaBi Thinkstep (164) datasets. The European Union Environmental Footprint (EUEF) Midpoint analysis was performed, following guidance laid out for LCAs of batteries set out in (23).

The OpenLCA Manual states (165):

> OpenLCA is open-source software for Life Cycle Assessment (LCA) and sustainability assessment. It has been developed by GreenDelta since 2006 (www.greendelta.com). As open-source software, it is freely available, without license costs (www.openlca.org). The source code can be viewed and changed by anyone. Furthermore, the open-source nature of the software makes it very suitable for use with sensitive data. The software, as well as any models created, can be shared freely if the database license allows it.

The software takes datasets of products (flows) and processes, some have been compiled elsewhere (such as the ecoinvent and GaBi) and the dataset compiled for the Al-ion cell was done using components of these.

3.1.1 Impact categories within the EUEF framework

Overall there are 19 impact categories, grouped as (a) water impacts, (b) carcinogenic properties, (c) climate impact, (d) land usage, (e) o-zone impact and (f) energy resource:

1. Acidification of water, reported as in increase in Mole of H+ eq., reduces the amount of carbonate available for sea life, and affects their environment. Most notably it can limit growth of corals and plankton which serve as vast ecosystems for many marine life . Ecotoxicity of freshwater measured in Comparative Toxic Units ecotoxicity (CTUe), attempts to understand the overall pollution to freshwater, from air, land run-off (such as pesticides) and direct chemical release into the water (166). Eutrophication refers to the increase of nutrients to water, such that algae and other organisms thrive on the surface, blocking sun and depriving oxygen to those living below the surface. Due to the processes by which eutrophication takes place in different bodies of water, it is measured in kg P eq. in freshwater, kg N eq. for marine water, and as an increase in Mole of N eq. for terrestrial water.

2. Cancer causing human health effects, measured in Comparative Toxic Unit for human (CTUh), provides the increased risk of morbidity from cancer for the entire human population, given the chemicals emitted during the production process. Similarly, non-cancer-causing human health effects are also measured in CTUh and summarise other potential hazards. Ionising radiation is assessed in a separate category, given as kBq U235 eq. released. The release of respiratory inorganics, in the form of particles less than 2.5 µm in diameter, can also cause lung disease and irritation, and are measured as kg PM2.5 eq.

3. Climate change impact is given as kg CO_2 eq. added to the atmosphere. This category is then subdivided into impacts from biogenic sources (such as burning wood or other bio-fuels), fossil sources (such as petrol or other crude oil products) and through land use change (such as from deforestation and the reduction of carbon sinks).

4. Land use is given in eco-points, Pt, which takes into account the use of the land, the area and the amount of time for which the land is in use – for example, grazing an animal may take a different amount of time than growing crops for the same area.

5. O-zone contribution is split into two categories, O-zone depletion, given in kg CFC eq. (kg chlorofluorocarbons eq.) which is in terms of the upper atmosphere. O-zone formation is also assessed, as at a local level this impacts human health, in kg non-methane volatile organic compounds eq. (kg NMVOC eq.).

6. Resource use is quantified as an energy in MJ. The use of minerals and metals (such as through mining) is measured in kg Sb eq. The use of water is assessed in m^3 water.

3.1.2 Al-ion LCA methodology

This LCA looked at the cradle-to-gate section of the product lifecycle, using the methodology set out in (23; 167). Cradle-to-gate includes the mining and production of raw materials through to manufacture, but does not include the use phase, or any second-life applications or end of life activities (such as recycling). Using this cradle-to-gate method provides a use-agnostic assessment of the battery production, showing only the environmental impacts of the manufacture, which is where the design of the battery itself can have the highest impact.

Using the information available from Holland (18; 1), the raw materials that formed each component were listed. The mass of each raw material used was then calculated based on the electrode masses given to construct the cell described. Using OpenLCA version 1.10.3 (161; 165) software, the processes and emissions involved in obtaining the raw materials were backed with either the ecoinvent 3.2 database (162), or the Gabi ThinkStep database (163) – as used in (23). Further, additional manufacturing, transport and packaging items were estimated based on (23). The distance from key production locations to the UK was calculated. Production of the overall cell was then scaled to provide the correct mass for 1 functional unit (FU), and the impact assessment was performed. (20)

The environmental impact across 19 categories were then assessed per FU using the European Union's Environmental Footprint (EUEF) methods (167). The process used in this chapter followed that shown in Figure 2.15, from detailing the cell components through to analysis of the full cell.

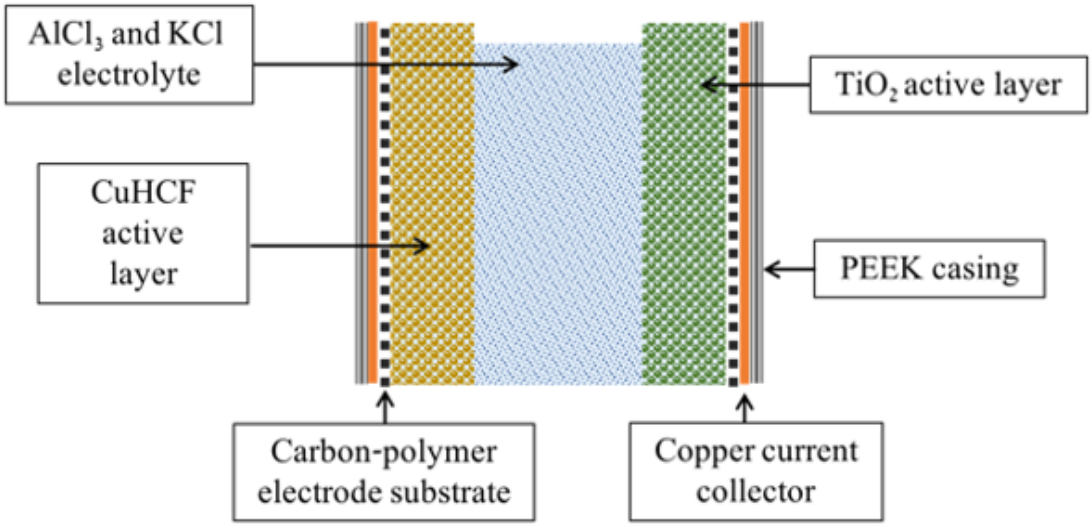

FIGURE 3.1: aqueous Al-ion cell developed at The University of Southampton (1)

3.1.2.1 Raw Material Identification

The cell components were first identified as (see Figure 1.1, reproduced above as Figure 3.1):

- the positive electrode, which comprised a carbon-fluoropolymer substrate (PV10 from Sigracell) onto which an active layer was coated. The active layer contained copper hexacyanoferrate, CuHCF, (active material), carbon black to improve electrical conduction and Nafion as an electrolyte/ion permeable binder.
- negative electrode, which comprised a carbon-fluoropolymer substrate (PV10 from Sigracell) onto which an active layer was coated. The active layer contained TiO_2 (active material), carbon black to improve electrical conduction and Nafion as an electrolyte/ion permeable binder.
- current collectors, which were copper foil, placed on the outer (non-electrolyte) face of the carbon-polymer substrate.
- electrolyte, which comprised an aqueous solution of KCl and $AlCl_3$.
- cell chamber, which comprised a PEEK (polyether ether ketone) gasket to separate the electrodes and provide a reservoir for the electrolyte.
- battery casing, which comprised PEEK.

The cell manufacturing process was taken from the literature (1) and shown in Figure 3.2. The active materials for the positive and negative electrode active layers were mixed into inks, which were then spray coated onto the carbon-polymer substrates

and cut to shape to form the electrodes. The components were assembled and clamped together with the PEEK casing. A cross-sectional diagram of the resulting cell is provided in Figure 1.1, which shows the PEEK cell casing on each outer face, inside which is the copper current collector and carbon-polymer substrate. The positive and negative active material layers are shown on the left and right carbon-polymer substrate respectively and between the two electrodes is the electrolyte reservoir. The PEEK gasket forming the cell chamber and holding the electrolyte reservoir is not shown. A full material inventory can be found in Appendix B. (20)

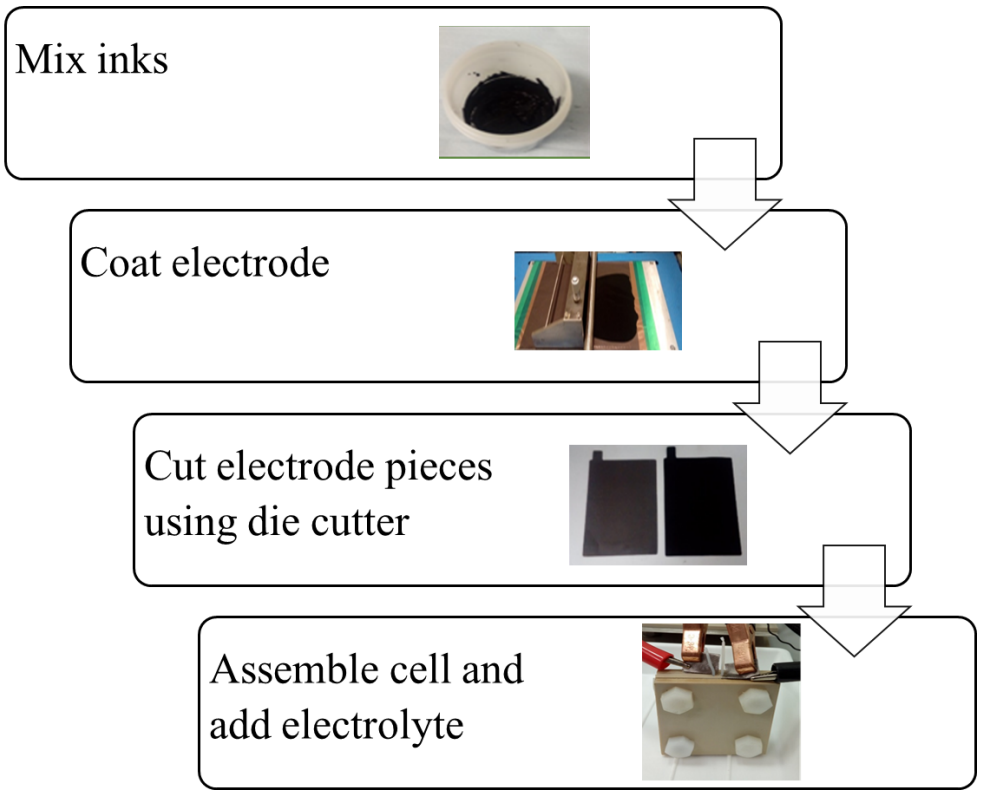

FIGURE 3.2: Electrode manufacturing methodology

3.1.2.2 Positive electrode manufacture

The steps used to make the positive electrode are:

1. CuHCF was made using the method described in Chapter 3. The processes involved in the production of both $Cu(NO_3)2$ and $K_3[Fe(CN)_6]$ are taken from the ecoinvent 3.2 database.
2. CuHCF, carbon black, and a Nafion binder were mixed in the ratio 8:1:1 by wt% to create a mix
3. Isopropanol was then added to form inks in the proportions of approximately 3:1 (isopropanol:active material).

4. The ink was mixed with a sheer blade mixer at 5000 rpm for 30 minutes, then sonicated for 20 minutes.

5. The ink was then spray painted on Sigracell PV10 carbon fluoropolymer electrode substrate from SGL.

The total weight of the electrode ink layer was 38 mg, and the Sigracell PV10 substrate weighs ≈10 g (168). Figure 3.3 shows the production flow from the positive electrode to its constituent parts. The positive electrode materials comprise the carbon-polymer substrate and CuHCF ink. The electrode substrate further comprises polycarbonate and polyvinyl fluoride, while the CuHCF ink comprises seven materials: isopropanol, copper nitrate, potassium ferrocyanide, alcohol ether sulphate chlorine dioxide, hydrogen fluoride and tetrafluoroethane. Details on specific masses, processes, and datasets used for these raw materials can be found in Appendix B. The packaging and transport has been taken into account for the items shown – a plastic packaging or glass bottle is assumed based on the item. The packaging processes are taken from the ecoinvent 3.2 database. (20)

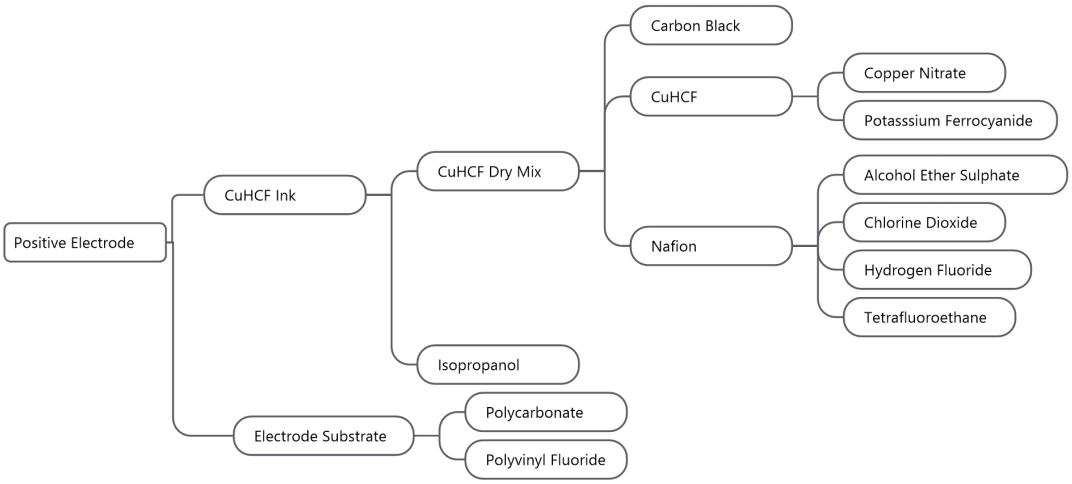

FIGURE 3.3: Production flow for the positive electrode redrawn from the ecoinvent 3.2 database output (20)

3.1.2.3 Negative electrode manufacture

The steps used in making the negative electrode are:

1. Anatase TiO_2 commercial nano-powder from Sigma Aldrich, carbon black, and a Nafion binder were mixed in the proportion 9:0.5:0.5 by wt% to create a mix. Standard TiO_2 was assumed as the base of the nano-powder, with the processes involved in the mining and production taken from the ecoinvent 3.2 database.
2. Isopropanol was then added to form inks in the proportions of approximately 3:1 (isoproponol:active material)
3. The ink was mixed with a sheer blade mixer at 5000 rpm for 30 minutes, then sonicated for 20 minutes.
4. The ink was then spray painted on Sigracell PV10 carbon fluoropolymer current collectors from SGL.

The total weight of the dry ink layer was 85 mg. As with the positive electrode, Figure 3.4 shows the production flow for the materials of the negative electrode. The negative electrode materials comprise the carbon-polymer substrate and TiO_2 ink. The electrode substrate further comprises polycarbonate and polyvinyl fluoride, while the TiO_2 ink comprises seven materials: isopropanol, TiO_2, alcohol ether sulphate chlorine dioxide, hydrogen fluoride and tetrafluoroethene. Details on specific masses, processes, and datasets used for these raw materials can be found in Appendix B. (20)

3.1.2.4 Electrolyte manufacture

The electrolyte used was 1 M $AlCl_3$ and 1 M KCl in de-ionised water. The processes involved in the production of these chemicals have been taken from the ecoinvent 3.2 database. A total of 6 g of electrolyte was used, given the spacing in the electrolyte cavity (1). Figure 3.5 shows the production flow for the electrolyte. (20)

3.1.2.5 Battery casing and other supporting components

The current collectors are copper sheets, given the 10 × 10 cm layout of the electrode (1), and typical values for copper current collectors (169) 1 g is used for each current collector. This value will be investigated further in future cell-builds. The processes involved in the production of copper sheets have been taken from the ecoinvent 3.2 database. The battery casing is assumed to be a thermosetting plastic (processes for production taken from the GaBi ThinkStep database), and that 2.5 g total was used for a cell of this size. The overall construction of an Al-ion cell will be similar to a Pb-acid,

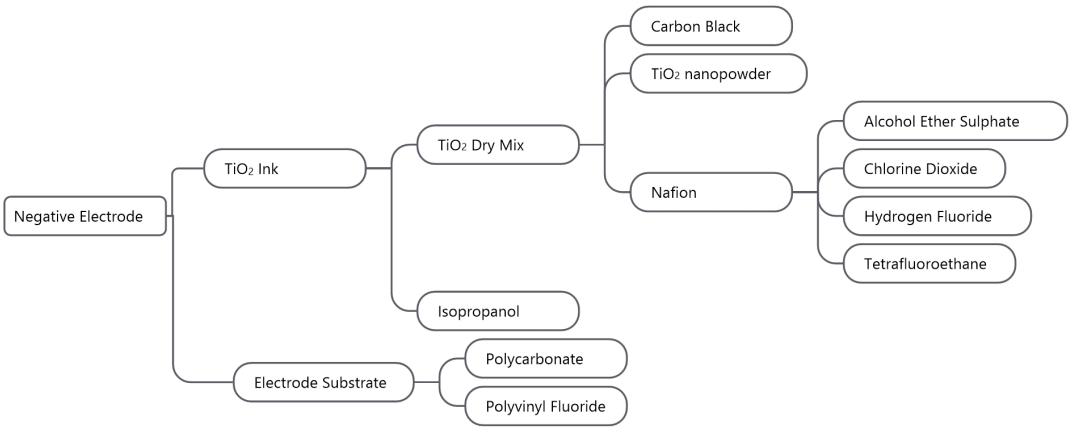

FIGURE 3.4: Production flow for the negative electrode redrawn from the ecoinvent 3.2 database output (20)

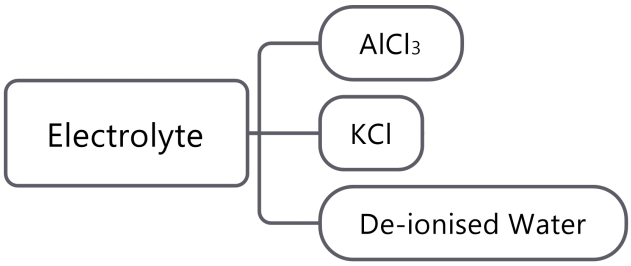

FIGURE 3.5: Production flow for the electrolyte redrawn from the ecoinvent 3.2 database output (20)

which have varying casing contributions around 10% (47; 170), with other Li-ion cases being between 8% an 24% of the total mass (23; 26; 171). The full cell therefore is made up of both electrodes, current collectors, the electrolyte and the battery casing. A

summary of the percentage by weight of each component is presented in Figure 3.6. The positive electrode, negative electrode and electrolyte each contribute slightly over one quarter of the overall mass (27%), with the casing and current collector combined making up the remaining 20%. (20)

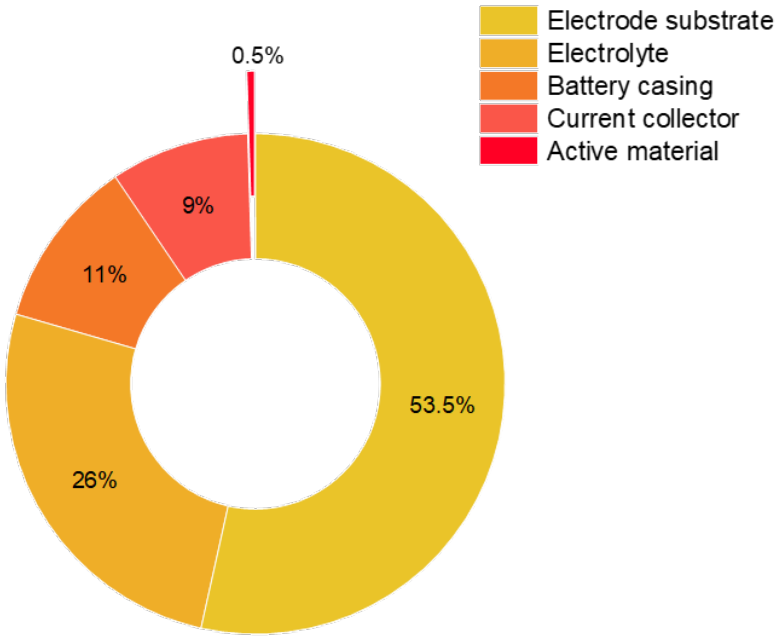

FIGURE 3.6: Cell component breakdown by % wt for baseline cell with active material highlighted (20)

3.1.2.6 Transportation of raw materials

Transportation of raw materials has been considered from the point of mining/processing/production to delivery to the UK. Countries of high production were based on the US Geological Survey (70). A summary of the main components for the aqueous Al-ion cell are presented in Table 1. Their geographical source area is identified along with the approximate distance for transporting the component to a manufacturing plant in the centre of Great Britain. Potash shown in the table, for the production of KCl and potassium ferricyanide, are not shown in Figures 3.3 or 3.5, as the datasets which comprise manufacture of these materials (from ecoinvent 3.2) already take this into account. However to understand the transport distances of such items, potash was considered. This is similar for aluminium, as $AlCl_3$ production from

the dataset already considers the aluminium component. The transport is not shown in Figures 3.3, 3.4 or 3.5. (20)

TABLE 3.1: Geographical location of production and associated delivery distance to the UK for key components of the aqueous Al-ion cell. (20)

Material	**Global Area (70)**	**Distance (km)**
Potash (for KCl and potassium ferricyanide)	Canada	6000 (23)
Copper (for current collector and copper nitrite)	Chile	11900 (23)
Titanium dioxide	China	8000 (23)
Aluminium (for $AlCl_3$ production)	China	8000 (23)
Carbon/hydrocarbons (for carbon black and plastics)	Europe Mainland	1000 (23)
Nafion (used in electrode ink)	Europe Mainland	1000 (23)
Isopropanol (used in electrode ink)	Within UK	500[a]

[a] values estimated from graph data

3.1.2.7 Functional unit identification

The functional unit is a reference unit which normalises the results in a useable way (172). For the use of this study, the functional unit of per kWh was chosen. The functional kWh is defined as the total amount of energy given over a lifetime (per kg) and is calculated using

$$\text{Functional energy density} = \text{energy density} \times \text{number of lifetime cycles} \tag{3.1}$$

When taking values from Holland et al. (1) on this cell's performance, we obtain

$$15 \text{ Wh kg}^{-1} \times 1750 \text{ cycles} = 26.25 \text{ kWh kg}^{-1}$$

Taking the inverse gives 0.038 kg per functional kWh. From values given in (1) for the electrode mass, the mass per kWh is determined as 0.026 kg for the negative electrode and 0.0118 kg for the positive electrode. Supporting material (such as electrolyte or battery casing) is scaled accordingly – with the cell mass assessed at ≈7 kg. Assessing a 7 kg cell therefore provide the impacts per 1 kWh. It is important to note that given the Al-ion cell's high power density (300 W kg^{-1}) it has applications similar to a supercapacitor (85), and so a second functional unit defined as functional power density will also be assessed when comparing the environmental impacts to supercapacitors in section 3.2, to give a more realistic understanding of the impacts. (20)

$$\text{Functional power density} = \text{power density} \times \text{number of lifetime cycles} \tag{3.2}$$

$$300 \text{ W kg}^{-1} \times 1750 \text{ cycles} = 525 \text{ kW kg}^{-1}$$

with values from (18). Taking the inverse gives 0.0019 kg kW^{-1}. Therefore, the results presented per kWh can be multiplied by a factor of 0.053 to provide the impacts per kW. (20)

3.1.3 DESS LCA methodology

The life cycle inventory for the Li-ion battery pack modelled in (173) has been adapted from the dataset made available in (26). The supercapacitor (SC) inventory is adapted from (28) – however, as the study presents an LCA for 5 F Maxwell supercapacitors, there is likely more packaging and other supporting materials assessed than would be present in a single 140 F supercapacitor for example. This would make the resulting overall mass slightly higher than reality, which makes this a conservative assessment. A single 5F supercapacitor is 2.1 g (174) and the data is scaled to 1 kg. The aqueous Al-ion cell inventory is taken from this chapter and (20) a single battery is about 25 g, and again this is scaled to 1 kg. (21)

A summary of the key components is provided below. Table 3.2 summarises the Li-ion battery pack, Table 3.3 summarises the SC, with full summaries found in (26; 28) and Table 3.4 summarises the Al-ion cell, with the full inventory found in B. Per kg, both the batteries (Li-ion and the SC) require a similar amount of energy (≈60 MJ), whereas the Al-ion battery only requires 37 MJ per kg. We can also see that the amount of electrolyte required per kg is similar for the Al-ion and supercapacitor

(about 0.25 kg) while the amount required for the Li-ion is about half – 0.12 kg. The amount of additional water was not provided in the inventory for supercapacitors, which introduces limitations of the comparison. However, given the overall mass of SCs assessed is below 2% of the total mass of assessed cases, see Table 3.5, the overall impact of this is - while not ideal - minimal. (21)

TABLE 3.2: Summary of Li-ion Battery Pack components from (26; 27), normalised to 1 kg (21)

Item	Value	Unit
Battery Management System (BMS)	0.03	kg
Cell container – aluminium	0.201	kg
Electrode substrate, anode – copper	0.083	kg
Electrode substrate, cathode – aluminium	0.036	kg
Electrolyte -lithium hexafluorophosphate	0.12	kg
Graphite anode paste - graphite, tetrafluoroethylene	0.08	kg
LFP cathode paste - lithium iron phosphate, carbon black	0.25	kg
Li-Ion battery pack housing - polyethylene terephthalate (PET)	0.17	kg
Separator - polyethylene, polypropylene	0.03	kg
transport, freight train	1.276	t*km
transport, freight, lorry 16-32 metric ton, EURO5	0.274	t*km
water, decarbonised, used during manufacture of 1kg	380	kg
Electricity, used during manufacture of 1kg	60.48	MJ
Total mass	**1**	**kg**

TABLE 3.3: Summary of Supercapacitor components normalised to 1 kg, from (28) (21)

Item	Value	Unit
Electrode active material -Activated carbon (48)	0.169	kg
Electrode substrate -Aluminium foil	0.134	kg
Case - aluminium	0.225	kg
Collectors - aluminium	0.046	kg
Electricity	63.077	MJ
Electrolyte - acetonitrile	0.252	kg
Paper Separator	0.043	kg
Rubber	0.088	kg
Lid - aluminium	0.043	kg
Total mass	**1**	**kg**

TABLE 3.4: Summary of aqueous Al-ion cell components normalised to 1 kg (21)

Item	Value	Unit
Battery Case	0.11	kg
Current Collector - copper	0.09	kg
Electrode substrate - polycarbonate	0.53	kg
positive electrode - copper hexacyanoferrate, carbon black, Nafion	0.005	kg
negative electrode - titanium dioxide, carbon black, Nafion	0.005	kg
Electrolyte - $AlCl_3$ and KCl	0.26	kg
Electricity	37	MJ
Water	8.83	kg
Hydrochloric Acid	0.40	kg
Total Mass	**1**	**kg**

3.1.3.1 City bus

A city bus will be assessed based on that described in (27). For this case the proposed DESS is 50 x 140 F supercapacitors in a 25s2p configuration, alongside 600 LFP cells in a 120s5p configuration, as described in (27). The equivalent battery only ESS and a DESS using Li-ion/Al-ion have been calculated as follows: Data interpreted from Figure 7 in (27) suggests that the SC array provides a maximum of 150 kW, with an assumed power density of 5.7 kW kg^{-1} taken from the BCAP150F, which was the closest comparable Maxwell supercapacitor (175). The total mass of the SC component in this example is therefore 26.3 kg. A similar approach was taken for the Al-ion high power component. Given the power density of 300 W kg^{-1} of the cells, and the 150 kW requirement, a mass of 500 kg active material is needed for the HP component for the Al-ion/Li-ion system. When taking into account the support materials and battery casing (20) a total of 833.3 kg of Al-ion cell mass was required, a much larger proportion of the overll mass than the SC. The BMS and casing mass is assumed to be identical across cases, as this is based on the battery system, with the additional casing required for the Al-ion included in the 833.3 kg. Additionally, as shown in Table 2, 3% of the total mass is for the BMS (battery management system) which has been added in an additional column. It is assumed that the BMS will remain constant for all cases. (21)

3.1.3.2 EV

Lu et al (157) describes the DESS optimisation for an electric vehicle of 1100 kg (mass without any ESS). The proposed DESS is 7,100 LFP cells in an 100s71p layout, with 72 SC cells – no configuration given. Again an additional mass equivalent to 3% the Li-ion mass is added to model the BMS (as listed in Table 2). The supercapacitors modelled within this paper were based on the Maxwell BCAP0350 (152) which states

TABLE 3.5: Summary of modelled DESS cases (21)

Case	HE (LFP) mass	HP type	HP mass	BMS/casing mass	Total mass
CityBus Li-ion Only	1200 kg	N/A	N/A	39.8 kg	1239.8 kg
CityBus SC/Li-ion	1200 kg	SC	26.3 kg	39.8 kg	1266.1 kg
CityBus Al-ion/Li-ion	1200 kg	Al-ion	833.3 kg	39.8 kg	2073.1 kg
EV Li-ion Only	568 kg	N/A	N/A	17.6 kg	585.04 kg
EV SC/Li-ion	568 kg	SC (described as ultracapacitors in the paper)	4.32 kg	17.6 kg	589.92kg
EV Al-ion/Li-ion	568 kg	Al-ion	1100 kg	17.6	1668 kg

4.6 kW kg^{-1}. Given the total mass of the SCs used is 4.32 kg, a total of 19.9 kW is delivered by the SCs. For the Al-ion/Li-ion case, given the Al-ion cell has a power density of 300 W kg^{-1}, a mass of 66.24 kg of active material is required for the Al-ion HP component, which equates to 1100 kg of total battery mass. Again, the mass of the overall vehicle with the Al-ion HP component is significant, and more than doubles the overall mass of the DESS. For now, however the primary assessment is the environmental impact of the system, while the next section of this chapter will explore means of reducing overall mass and therefore enabling the Al-ion battery to become a more viable solution. The battery only case described in the paper uses only the 71,000 LFP cells with no additional cells.(21)

A summary of the cases is shown in Table 3.5.

However, the lifetime of both the energy systems and the vehicles must be considered

in order to understand the full environmental impacts of the ESSs. When looking at the city bus, analysis showed that with the Li-ion only ESS, the battery pack would be replaced once within a ten-year vehicle lifetime, however, with the DESS modelled, this replacement was not necessary (30). Therefore, we can in theory double the battery mass required for this bus over a ten-year period, while keeping the DESS at the same size. For a Tesla Model S, work from (8) assessing battery degradation shows that the degradation of the Li-ion battery pack is halved when using an optimised DESS with supercapacitors, compared to Li-ion only, over one drive cycle. Again, this can be used to estimate the number of battery replacements required over the vehicle lifetime. (21)

3.1.3.3 Cycle life and replacement modelling

In each case presented, beginning of life (BOL) and end of life (EOL) are modelled. For each vehicle lifetime modelled, the corresponding number of Li-ion battery, supercapacitor, and Al-ion replacements required will be calculated based on an average cycle life of each component. At BOL there are no replacements required and it is assumed the vehicle has not been used. At EOL, the replacement rates for the Li-ion only and SC/Li-ion cases are taken from their respective studies. The city bus Li-ion only replacement values are taken from (27). Taking into account 124 miles and 34 drive cycles per day for the bus, during the ten year lifetime modelled, two replacements would be needed. The projected lifetime of 10 years for the supercapacitor noted in (175) means that no replacements are required during the lifetime. The addition of the supercapacitor further eliminates the need for Li-ion replacements. The Al-ion battery will perform the same as the supercapacitor, and thus eliminate the need for Li-ion replacements during the Al-ion/Li-ion case. Cycle life data from (1) indicates a lifetime of 1750 full cycles for the Al-ion cell, but based on (27), the supercapacitor (and thus Al-ion battery in this case) never completes a full cycle. It is therefore assumed that two replacements for a ten-year lifetime will provide a conservative estimate. For the electric car example, the lifetimes are stated in charge/discharge cycles, assuming a 240 km per charge. The stated lifetime of the Li-ion system is 5129 cycles, whereas the lifetime for the SC/Li-ion system is 6241 (157), offering a 20% lifetime extension. The EOL modelled is therefore the SC/Li-ion lifetime, therefore requiring one replacement of the Li-ion only system during this lifetime. The Al-ion/Li-ion system will be modelled as one Al-ion replacement over the lifetime. Table 3.6 summarises the replacement rates. (21)

TABLE 3.6: Summary of replacement rates (21)

Case	Beginning of life (BOL)		End of life (EOL)[a]	
	HP	HE	HP	HE
City bus Li-ion only[a]	N/A	0	N/A	3
City bus SC/Li-ion[a]	0	0	0	0
City bus Al-ion/Li-ion[a]	0	0	2	0
EV Li-ion only[b]	N/A	0	N/A	1
EV SC/Li-ion[b]	0	0	0	0
EV Al-ion/Li-ion[b]	0	0	1	0

[a] EOL defined as 516000 km over a 10 year lifetime (27)

[b] defined as 6241 charge/discharge cycles over the car's lifetime (157)

3.1.4 Normalisation

Normalisation of the data was done via the EUEF's methodology (23).

3.2 Initial cell measurements and manufacture (Chapter 5)

3.2.1 Electrode preparation

3.2.1.1 Copper hexacyanoferrate

Copper hexacyanoferrate, $KCuFe(CN)_6$, will be abbreviated to CuHCF in this thesis. The active material for the positive electrode is synthesised in the lab by mixing copper nitrate $(CuNO_3)_2$ and potassium ferracyanide $(K_3Fe[CN]_6)$ in a 3:2 ratio taken from (18) and described below.

This was done by mixing 0.15 M copper nitrite (Sigma Aldrich) in 50 ml deionised water (1.81 g) - blue liquid - and 0.15 M potassium ferricyanide (Alfa Aesar) in 50 ml deionised water (1.65 g) - yellow liquid - and combining the two slowly with a burrette (see Figure 3.7 at a rate of 0.45 ml $s^{-}1$ while stirring at 500 rpm, then allowing them to mix for a further 2 hours at 500 rpm. After this, the resulting brown mixture was decanted into tubes and placed in a centrifuge at 4000 rpm for 3 minutes at a time.

Between each washing in the centrifuge, water was removed and the tubes topped up with fresh de-ionised water. After five washes, the remaining thick brown paste was spread onto a petri dish and dried overnight at 80°C in an oven, after which the dried CuHCF was ground in a pestle and mortar - ready to use in the electrode ink.

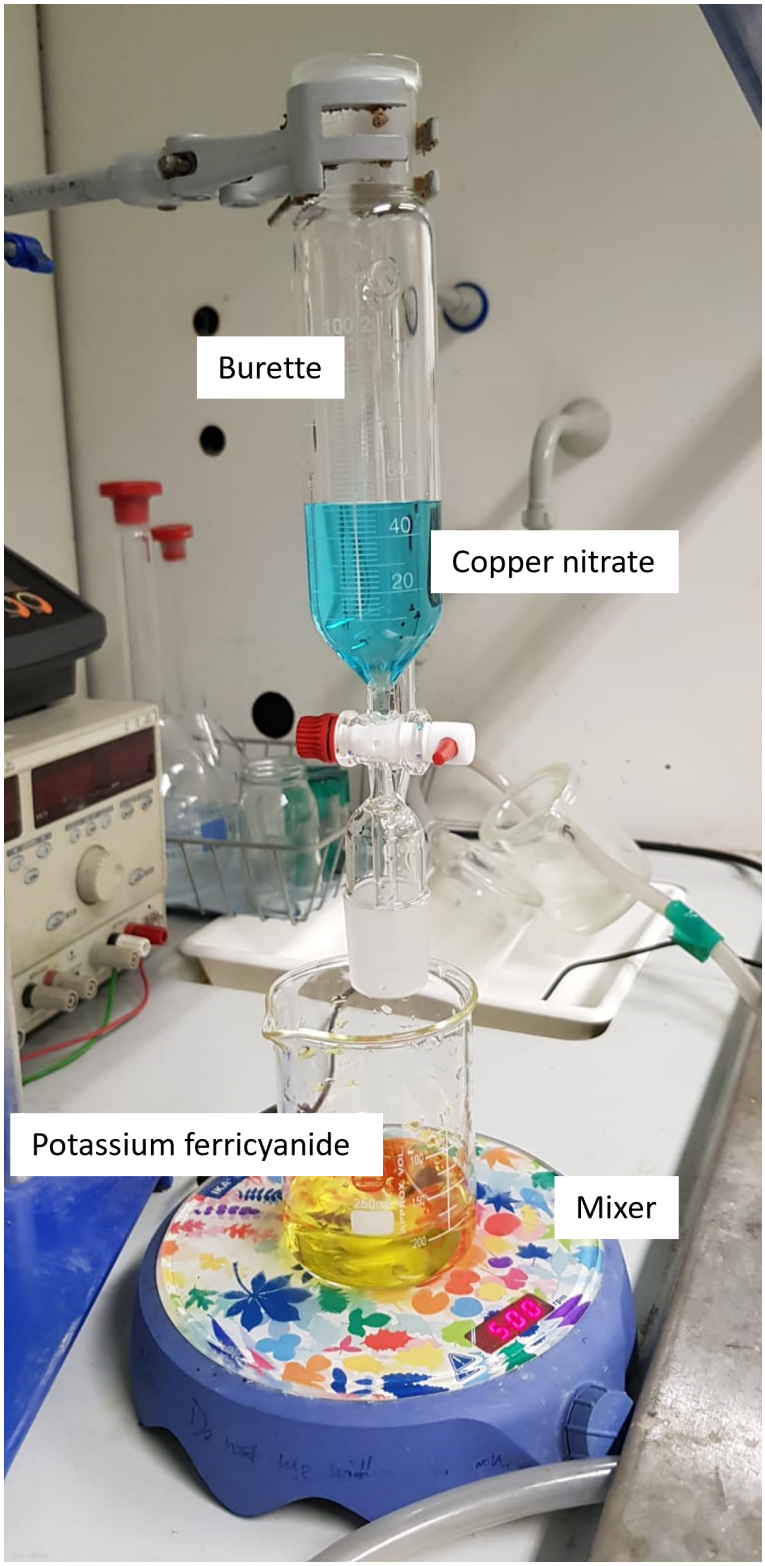

FIGURE 3.7: Mixing $(CuNO_3)_2$ and $K_3Fe[CN]_6$

FIGURE 3.8: Final ground CuHCF powder

3.2.2 Mixing electrode ink

Inks were mixed using a Silverson shear blade mixer, using a $\frac{5}{8}$" tubular mixing head. The ingredients below were mixed, along with isopropanol (ratio 1:3 ink:isopropanol) for thirty minutes at 5000 rpm. They were then placed in an ultrasonic bath for twenty minutes.

The negative electrode used TiO_2 anatase powder (particle size <25 nm, Fisher), Nafion (Alfa Aesar) and carbon black (Alfa Aesar) in a 9:0.5:0.5 ratio by %wt, batches were made with the values 1.5 g:0.833 g:0.833 g, with 5 g isopropanol.

The positive electrode used CuHCF, Nafion and carbon black in a 8:1:1 ratio by %wt, batches were made with values 1.5 g:0.188 g:0.188 g, with 5.625 g isopropanol.

3.2.3 Electrode coating

Electrode inks were used with two main electrode substrates, namely Sigracell PV10 carbon fluoropolymer, and a 2.5GDA carbon felt from SG Carbon.

3.2.3.1 Spray coating

For spray coating the Sigracell PV10 carbon fluoropolymer electrode substrates, the ink was placed in an airbrush from airbrushland.com and sprayed evenly over the electrode substrate, each layer was allowed to dry in ambient conditions overnight. The substrate was weighed before and after spray coating to ascertain the mass of active material. For coin-cell spray coating, a mask was used to control the diameter of the electrode ink - Figure 3.9 shows the mask with electrode substrate attached, Figure 3.10 shows this after spraying, with Figure 3.11 showing the final coin-cell electrodes.

FIGURE 3.9: Spraying mask with electrodes set up pre spraying

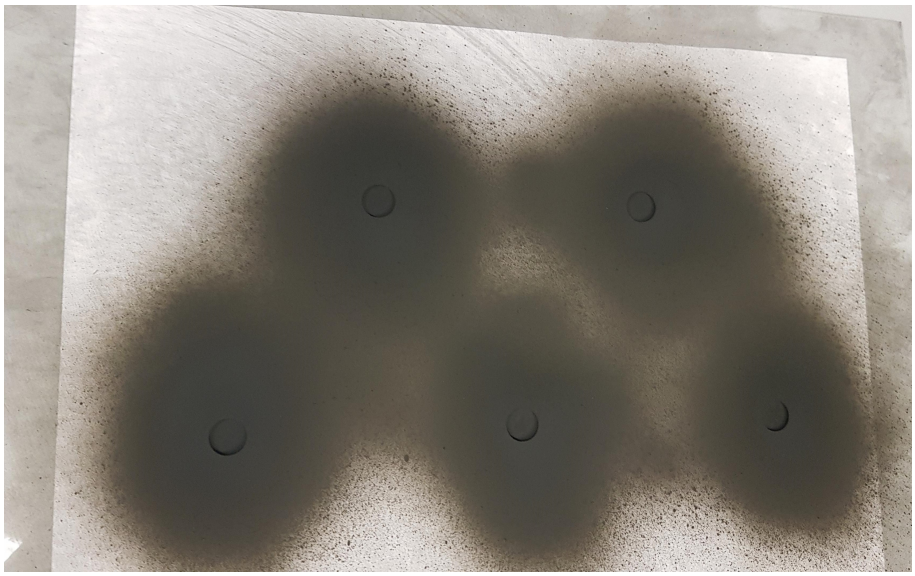

FIGURE 3.10: Sprayed mask - coated electrodes prior to removal from mask

FIGURE 3.11: Final electrodes after removal from mask - left CuHCF electrodes, and right,TiO_2

3.2.4 Three electrode cell

The set up for the three electrode cell is shown in Figure 3.12, with a Pt counter electrode and a Saturated Calomel reference electrode (SCE) - the working electrode is clamped to the cell, and a diagram of the cross section (within the white box) is shown in Figure 3.13. The clamps are not shown in the diagram. The electrolyte used was 1 M $AlCl_3$ + 1 M KCl.

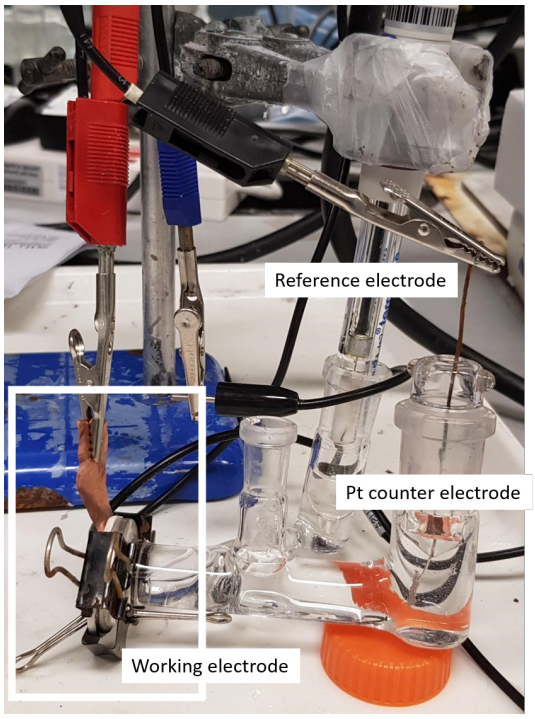

FIGURE 3.12: Image of set up for cyclic voltammetry

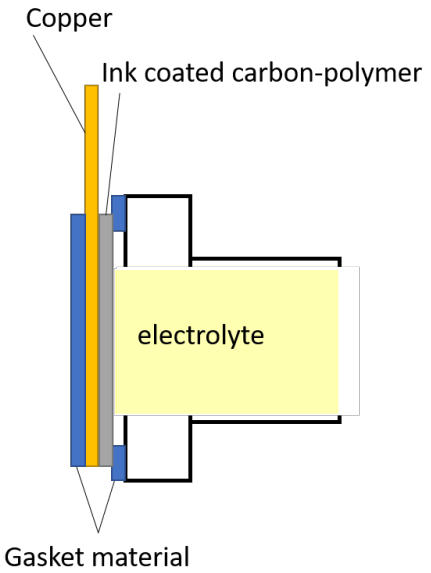

FIGURE 3.13: Diagram of working electrode set up

3.2.5 Electrochemical measurements

Cyclic voltammetry, CV, is an experimental technique used to understand the relationship between the current, I, and potential, V, of an electrochemical cell. Potential is controlled and is increased linearly with time at a constant sweep rate, within the ESW of the cell, after which the process is reversed, and the potential is

swept back to the starting value. An IviumStat multichannel electrochemical analyser alongside IviumSoft software was used to perform CV experiments, and discharge capacity measurements in the three electrode cells.(176)

3.2.6 Final cell manufacture methodology

3.2.6.1 Coin-cell manufacture

A coin-cell is a closed cell, and is less likely to lose electrolyte over time, it would also be easier to transport and use as spills and leaks are unlikely. With the closed cell, there is a potential for hydrogen bubbles to remain inside and limit the performance, or cause bloating and opening of the coin-cell. To control for potential hydrogen formation within a closed cell, the voltage range may therefore be limited, again limiting the performance of the cell. Overall, the potential for gassing and bloating can be tested and controlled for, with the environmental and general usability benefits making the coin-cell a clear development step. This section therefore discusses the development of a closed coin-cell.

Construction of the final coin-cells was performed as follows. After the electrodes were sprayed with ink as described above, the positive electrode was soaked in 1 M sodium thiosulphate for 30 minutes to ensure a fully reduced state (102), it was then washed in de-ionised water and allowed to dry in ambient conditions. Stainless steel 2032 coin-cell cases were used for the coin-cells, which were cleaned with isoproponal before being used. Small amounts of Leit-C carbon-cement were applied to the inside of the cases with a fine paintbrush - a synthetic sable size zero brush - using a mix of water and isopropanol to wash between applications. The electrodes were then pressed into the cases with slight pressure to ensure full contact. The cell cases were then left 30 minutes to allow the carbon-cement to dry fully. Two layers of separator paper which had been cut to size and soaked in electrolyte (1 M $AlCl_3$ + 1 M KCl) for 15 minutes were then placed into the negative case - corresponding to 0.22 ml of electrolyte, an additional 0.05 ml of electrolyte was added to the cell. The coin-cell was then closed and excess electrolyte wiped off the edge, before crimping in a coin-cell crimper. Figure 3.14 shows the set up before cell assembly, Figure 3.15 shows the construction stage pre-crimping and Figure 3.16 an image of a fully crimped, completed coin-cell.

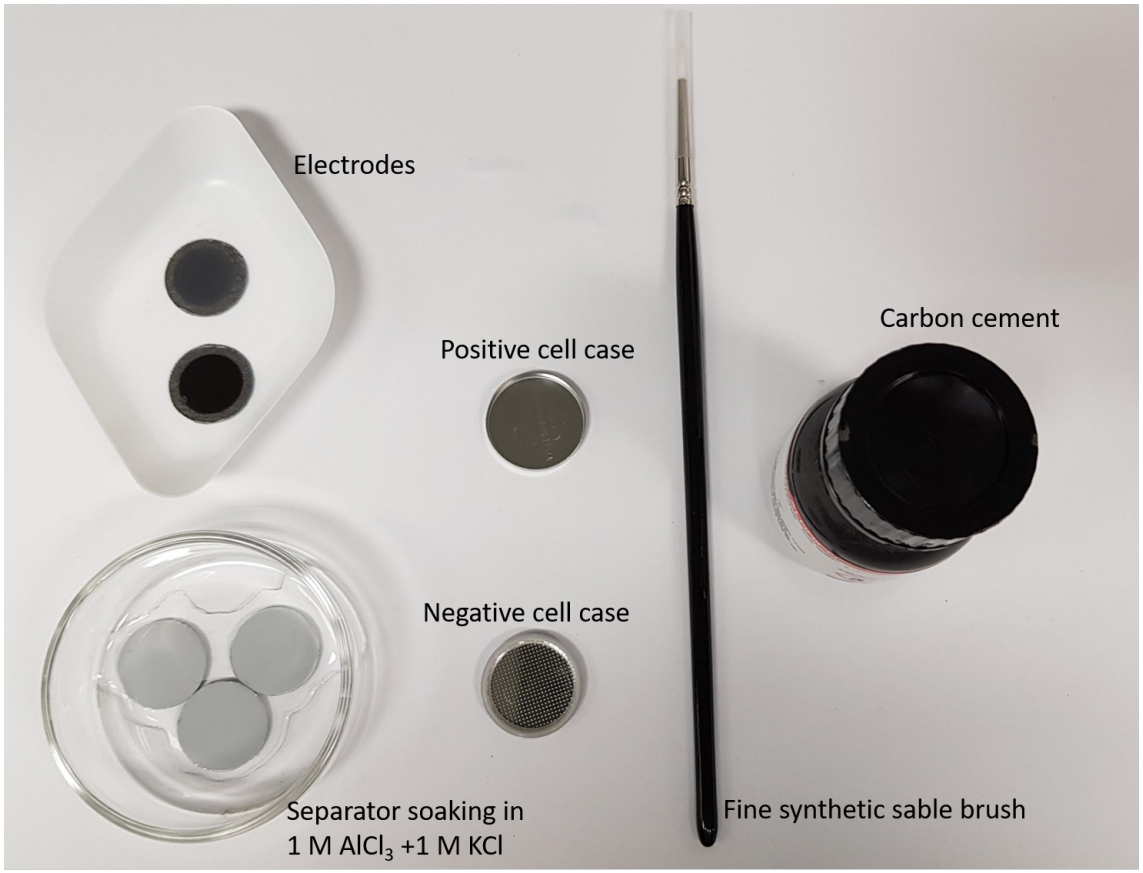

FIGURE 3.14: Electrodes, soaked separators, cell case, carbon cement and a paintbrush

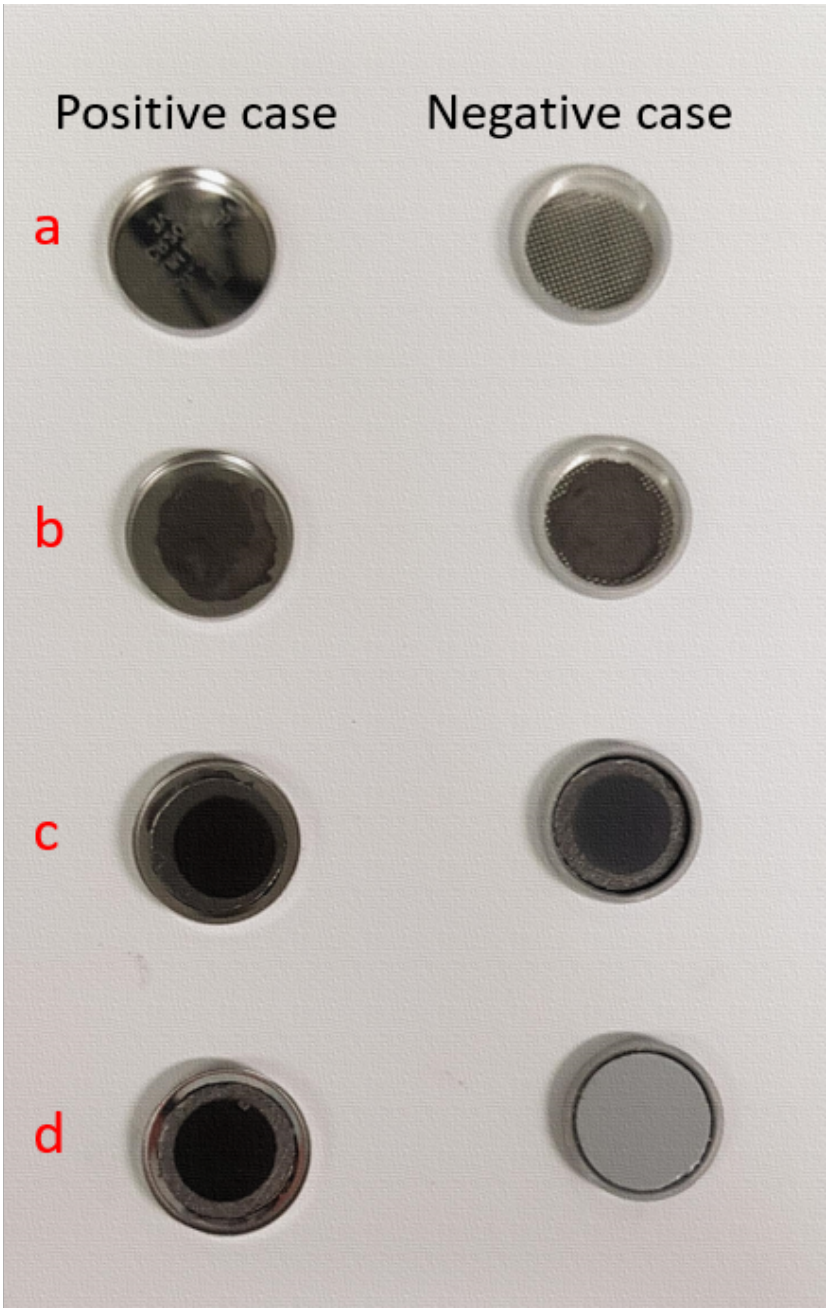

FIGURE 3.15: Stages from cell construction showing a) cleaned cases, b) carbon cement application, c) electrode placement and d) separator and electrolyte addition

FIGURE 3.16: Final crimped cell

3.2.7 Powdered X-ray diffraction

The physics behind X-ray diffraction (XRD) is explained in detail in Section 3.4. For the PXRD performed for Chapter 6 was done using a Bruker D2 phaser, with a Cu tube wavelength of 1.5418 Å.

3.3 Carbon Felt preparation and measurements (Chapter 6)

3.3.1 Carbon felt electrode preparation

Carbon felts from SGL Carbon were cut to size and soaked in a mix of isopropanol and de-ionised water (1:1) to ensure that any contamination was washed off. The samples were then left to dry in ambient conditions overnight. Electrode inks were then prepared as described above, and the carbon felts were coated using a dip coating method.

For dip coating the carbon felt electrode substrates, the ink was placed in a petri dish and the substrate was lowered in, the substrate was then compressed slightly, and released, to allow it to absorb ink. The substrate was then removed from the dish and allowed to dry in ambient conditions overnight. This process was not repeated more

than once. The substrate was weighed before and after dip coating to ascertain the mass of active material.

For creating different proportions of active material within the carbon felt electrodes, additional isopropanol was added to the ink to dilute it prior to dip coating.

3.3.2 Scanning electron microscope

The scanning electron microscope used was the Joel JSM7200 model. A SEM works by using accelerated electrons focused on the sample in a vacuum. The electron interactions with the sample produce secondary electrons to be released, which are detected and used to produce an image of the sample.

3.3.3 Carbon felt three cell electrode

The three electrode cell was set up in an identical manner to that described above, with the addition of the carbon felt clamped with uncoated carbon-polymer(PV10). A diagram of the set up is shown in Figure 3.17 - the clamps are not shown in this diagram. To ensure that the electrode was fully wetted by the electrolyte prior to measurements, it was vacuum impregnated with electrolyte, by filling a flask with electrolyte and placing the electrode in, and then pulling a vacuum on this set up until there were no more visible bubbles in the solution . At this point it can be assumed that the air has been removed from the electrode and filled with electrolyte.

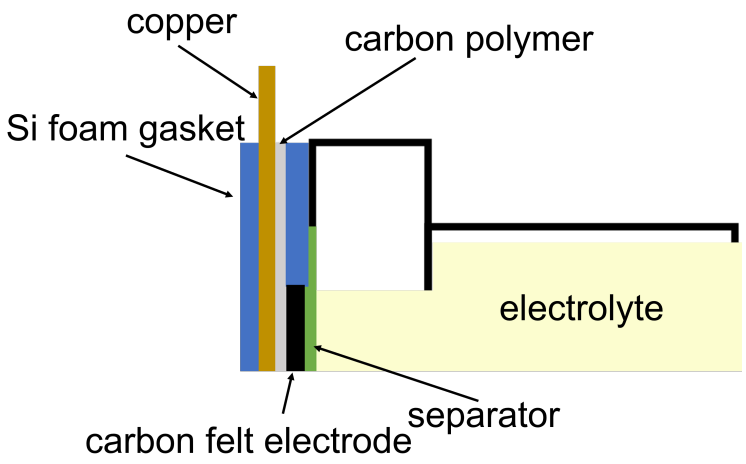

FIGURE 3.17: Diagram of 3-electrode cell with carbon felt substrate

3.3.4 Temperature control

When performing temperature or humidity controlled characterisation, the Aralab FitoClima 30EC45 Climatic Chamber was used. This chamber uses ClimaPlus software to control the temperature and humidity.

To ensure the temperature was accurate, a thermometer was used to verify the set point of the chamber's own system. The thermometer was also used to find the time lag between the chamber temperature being reached, and that temperature being reached in the electrolyte. The value varied from 15-60 minutes, depending on the set point (5°C saw the largest time lag of 60 minutes). Therefore a wait period of 60 minutes after the chamber set point was reached was used before starting any measurements.

3.3.5 Powdered X-ray diffraction preparation for carbon felts

When preparing the used (or cycled) electrodes for PXRD, they were first soaked in deionised water for 15 minutes to clean them then left to dry overnight in ambient conditions. Following this the dried electrode was ground up using a pestle and mortar to create a powder which contained the carbon felt alongside the materials within the electrode.

3.4 Increasing cycle life (Chapter 7)

3.4.1 coin-cell manufacture for Diamond Light Source

Coin-cells were manufactured for Diamond Light Source using the methods already described in this chapter. The coin-cell cases used had 50 micron laser-thinned centres to allow for the X-rays to pass through.

3.4.2 Imaging Techniques

3.4.2.1 Atomic Scattering Techniques

Atomic scattering techniques can be used to probe a material in a non-destructive way. Particles interact with a material, and these reactions can then be measured and analysed. During this thesis X-ray scattering experiments have been performed.

Scattering can be divided into two types – elastic and inelastic. In elastic scattering, the energy of the probing particle, in this case the X-ray, is unchanged during its

interaction with a sample. The probing particle wave vector before, **k**, and after, **k'**, the interaction are equal. The value **Q** is derived as the scattering vector and is zero for elastic scattering. (177)

Due to conservation of momentum, **Q**, **k** and **k'** are related through;

$$\frac{h}{2\pi}\mathbf{Q} = \frac{h}{2\pi}(\mathbf{k} - \mathbf{k'}) \tag{3.3}$$

and so it follows that

$$\mathbf{Q} = (\mathbf{k} - \mathbf{k'}) \tag{3.4}$$

where h is Plank's constant. Figure 3.18 shows the elastic scattering vectors.

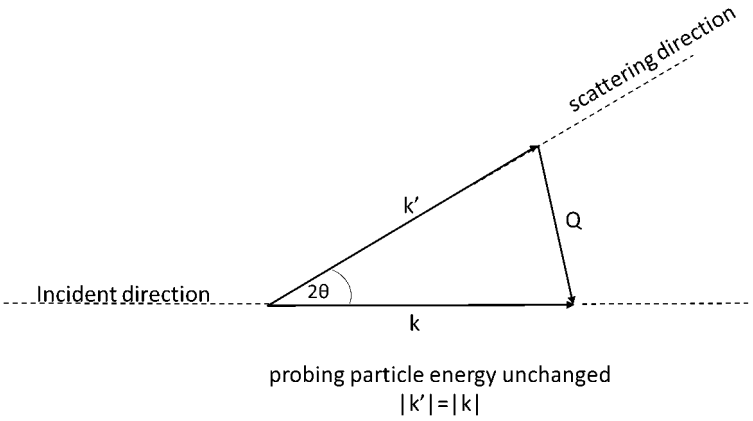

FIGURE 3.18: Elastic scattering vectors

However, for inelastic scattering, the particle's energy changes due to its interaction with the sample, and therefore $\mathbf{Q} \neq 0$, as demonstrated in Figure 3.19.(177)

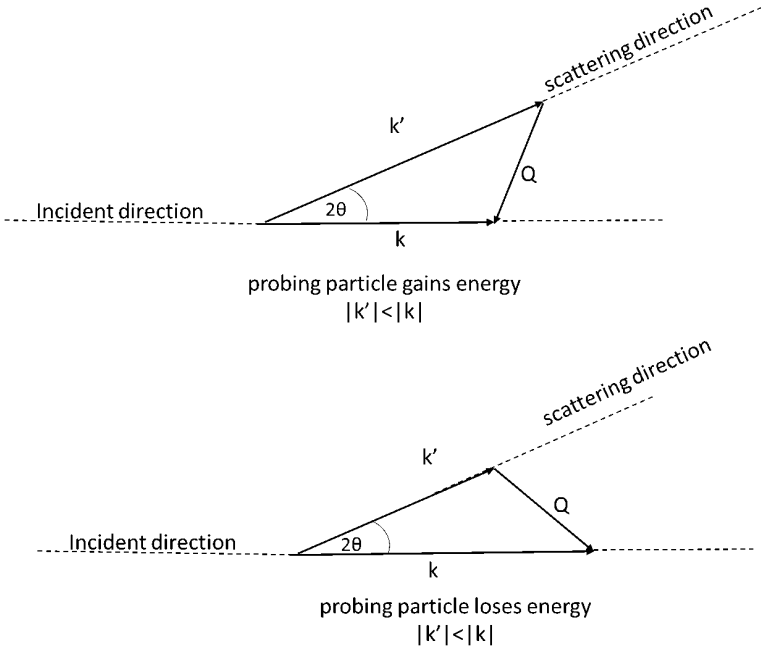

FIGURE 3.19: Inelastic scattering vectors

Both types of scattering can be measured using time-of-flight detectors.

The time taken by the probing particle to travel from the source to the detector is measured. This is called 'time of flight'. Figure 3.20 shows the flight-path from the target to the detector.

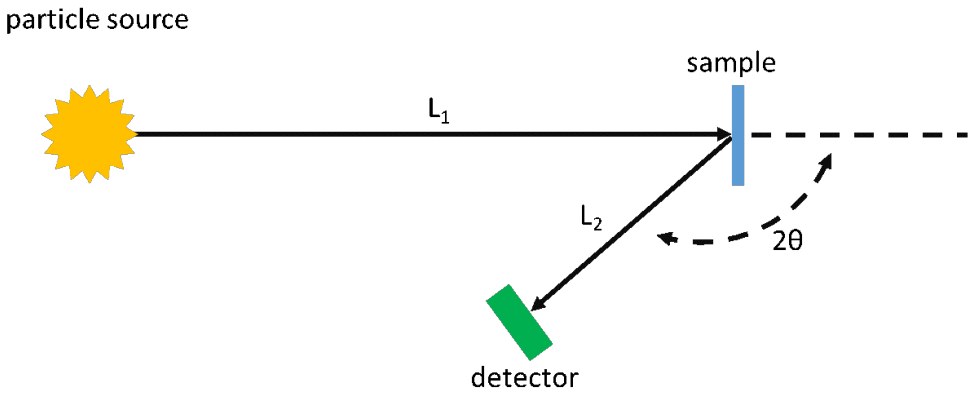

FIGURE 3.20: journey from target to detector

The total flight-path is therefore $L_1 + L_2$, with the scattering angle defined as 2θ. These values are known based on the instrument set-up. For diffraction experiments, having measured the time, t, to travel the flight-path, the wavelengths (λ) of the probing particle, and therefore the inter-atomic spacing, d, can be determined.

Given that velocity, v

$$v = \frac{L_1 + L_2}{t} \tag{3.5}$$

and using the two equations for energy, E,

$$E = \frac{1}{2}mv^2 \tag{3.6}$$

$$E = \frac{h^2}{2m\lambda^2} \tag{3.7}$$

where m is the mass of a neutron and h is Plank's constant. We can derive an expression for wavelength λ,

$$\lambda = \frac{h}{m}\frac{t}{L_1 + L_2} \tag{3.8}$$

with λ defined, we can use Bragg's law to find d.

$$d = \frac{\lambda}{2\sin 2\theta} \tag{3.9}$$

These values are important, as different elements (and isotopes/ions within elements) will lead to different scattering results. (72; 178)

In spectroscopy experiments, it is the inelastic scattering that is measured. This can be used to understand phase changes or diffusion processes in the material. As the probing particle interacts with the sample, its energy level changes, which is then detected by the detector. The spectra produced can be directly compared to photon spectroscopy (such as XPS or Raman). The transition energies, however, remain unchanged and it is only the intensity of peaks that differ. (179)

For X-ray scattering, the X-rays interact with the electron cloud of an atom (whereas for example neutrons interact with the nucleus). This results in scattering cross section for X-rays progressing with atomic number. X-rays interact strongly with the sample material, resulting in strong scattering intensities, however they do not penetrate deeply into a material, and thus often are used as a surface technique. Many X-ray scattering experiments take place in a vacuum environment, to minimise the X-rays scattering off particles in the air instead of the sample. When the X-rays are produced at high energies in a synchrotron, a vacuum is not always required, and bulk material properties can be seen. (180)

For the LDE experiment, the i11 beamline at Diamond Light Source was used.

3.4.2.2 X-ray Computed Tomography

X-ray computed tomography (or XRCT) is used to produced a 3D image of the sample. XRCT uses the basic concept of X-ray imagery in which the X-ray is passed through the sample, with the amount of X-rays being detected at the other side of the sample used to construct an image. However for XRCT, the sample is imaged at many angles and orientations to enable a 3D image to be built up of the sample. For the coin-cells imaged for the LDE experiment, the NXCT diondo d5 was used at the muvis centre at The University of Southampton. The scan and device parameters of the diondo d5 are shown in Figure 3.21.

X-ray Parameter:

Voltage [kV]:	250,000
Current [µA]:	60,000
Power [W]:	15,000
Filter:	Air

Detector Parameter:

Columns [px]:	3000
Columns [mm]:	417,000
Rows [px]:	3000
Rows [mm]:	417,000
Pixel-Binning:	1:1
Integration time [ms]:	540
Frame-Binning:	3
Capacitance [pF]:	1x1 1pF
Pitch [mm]:	0,139

Scan Parameter:

Mode:	CtMode
Number of Projections:	4500
ScanFieldExtensionHorizontal:	On
StopAndGo	Off
ScanFieldExtensionVertical:	Off
Rotation Mode:	Continuous Mode:
Image Type:	RAW
Scantime [HH:MM:SS]:	02:02:01

FIGURE 3.21: Scan parameters for the diondo d5 XRCT

Chapter 4

Life-cycle assessment of the aqueous aluminium-ion batteries

4.1 Motivation

This chapter explores the use of life cycle assessment, LCA, to understand the current position of the aq. Al-ion battery in terms of its environmental impacts - when compared to existing Li-ion technology and supercapacitors, and also as a baseline for improvement when developing this batter further. When using a low TRL (technology readiness level) product as the basis for an LCA, it gives the largest scope to alter the design direction with minimal cost. The results from this chapter will be used to inform the direction and scope of the investigations which take place in further chapters (Chapters 5, 6 and 7) and provide the over-arcing motivation for the battery development.

4.1.1 Research question for this chapter

The key questions this chapter aims to answer are:

- Can we produce an LCA for a low TRL battery?
- Can we use LCAs to understand potential use cases?
- Can we use LCAs to make informed design decisions?

4.1.2 Expected Results

Due to the TRL 4 of the lab-based aq. Al-ion battery, it is expected that the battery will have a higher environmental impact than COTS (commercial off the shelf) batteries to

which it is compared. This is not a negative result - but a result that will allow environmental impact goals to be set.

4.2 Scope of this LCA

The Al-ion battery assessed within this chapter is the state of art prior to undertaking this PhD. It is used as the baseline for the development that takes place during this PhD and within this thesis. This battery was developed by Holland (18).

4.2.1 Results and discussion

Using OpenLCA and the EUEF midpoint analysis, the impacts of production were assessed per functional kWh. The total impact in a variety of categories was calculated - discussed fully in Chapter 3. Table 4.1 shows the absolute values of each category per functional kWh, whereas Table 4.2 shows the results normalised and weighted to the product environmental footprint (PEF) suggested values (167) – which aim to quantify the impacts so that they can be compared to each other. The top five impact categories - taken as the categories with the highest normalised values, obtained from the data obtained in Table 4.2 are analysed further to identify their main contributors. These are, respiratory inorganics (6.74×10^{-7} kg PM2.5 eq.), resource use – energy carriers ($4.10 \times 10^{+1}$ MJ), minerals and metals (9.18×10^{-5} kg Sb eq.), climate change ($2.95 \times 10^{+0}$ kg CO_2 eq. overall) and acidification of water (1.76×10^{-2} Mole of H^+ eq.). These are presented graphically in Figure 4.1. The percentage impact contribution is provided for the production of: $AlCl_3$, copper battery casing, electrode substrate, KCl and 'other'. The category 'other' includes all other processes assessed during the impact assessment. (20)

TABLE 4.1: Impacts per functional kWh aqueous aluminium ion results (20)

Impact category	**Al-ion impacts per kWh**
Acidification terrestrial and freshwater [Mole of $H^+eq.$]	1.76×10^{-2}
Cancer human health effects [CTUh]	6.62×10^{-8}
Climate Change [kg CO_2 eq.]	$2.95\times 10^{+0}$
Climate Change (biogenic) [kg CO_2 eq.]	2.46×10^{-3}
Climate Change (fossil) [kg CO_2 eq.]	$2.95\times 10^{+0}$
Climate Change (land use change) [kg CO_2 eq.]	1.83×10^{-3}
Ecotoxicity freshwater [CTUe]	$1.91\times 10^{+0}$
Eutrophication freshwater [kg P eq.]	8.92×10^{-5}
Eutrophication marine [kg N eq.]	$4.11\times\times 10^{-3}$
Eutrophication terrestrial [Mole of N eq.]	4.45×10^{-2}
Ionising radiation - human health [kBq U235 eq.]	1.87×10^{-1}
Land Use [Pt]	$5.15\times 10^{+0}$
Non-cancer human health effects [CTUh]	5.73×10^{-7}
Ozone depletion [kg CFC-11 eq.]	4.50×10^{-7}
Photochemical ozone formation - human health [kg NMVOC eq.]	1.08×10^{-2}
Resource use, energy carriers [MJ]	$4.10\times 10^{+1}$
Resource use, mineral and metals [kg Sb eq.]	9.18×10^{-5}
Respiratory inorganics [kg PM2.5 eq.]	6.74×10^{-7}
Water scarcity [m^3 world equiv.]	7.50×10^{-1}

Figure 4.1 shows that the battery casing productions – which includes the mining of hydrocarbons through to the production of the plastic granulates – appears as a contributor to the main impacts. It is again worth mentioning that the assumption of casing mass was based off a Li-ion battery, and when using a lower mass for the casing, the impacts of this are reduced. Plastic is also highly recyclable, thus changing the input of the battery casing to a higher percentage recycled plastic would again reduce the impacts of this component. (20)

In terms of the copper contribution for the current collector, this could be reduced by looking into recycling methods at end of life (EoL), for Pb-acid batteries the recycling/reuse accounts for -21% of the overall impact (114). However, copper is not the only current collector option as there are many polymer or other metal foils which could be investigated for use in this cell. The choice for this component within the software was 'copper sheet', whereas for the production of CuHCF, 'copper mix' was used as they have different production methods (see **S1 f**or component breakdown). It is important to note, that the negative 'other' within the 'Resource use; minerals and metals' category is due to the CuHCF copper production, as it is assumed that for the CuHCF production 40% of the copper was from scrap or recycled sources. (20)

The impacts from the electrolyte cannot be reduced through a substitution, however recycling at EoL (end of life) will most likely play a role in reducing the overall impact. In terms of the aluminium, it has been shown that recycled Al uses 10% of the energy needed for primary production (69). It is important to bear in mind that there were many assumptions made within this analysis such as finding the appropriate production methods for branded products such as Nafion, as well as the Electrode substrate, and thus a more general descriptor was used – which may not have taken into account the key production processes and waste produced. Many assumptions were made on transport distances based on the locations of productive mines and manufacturing plants around the world – however these were in line with those recommended (and therefore used) in (23). The transportation methods, as well as the electricity sources used within production are assessed later in this chapter. However for the understanding of an initial baseline and to understand impacts of design changes, using values recommended in (23) is sufficient. (20)

TABLE 4.2: Normalised impacts per functional kWh aqueous aluminium ion results (20)

Impact category	**Value**
Resource use, mineral and metals	$\mathbf{1.28 \times 10^{-4}}$
Respiratory inorganics	$\mathbf{1.01 \times 10^{-4}}$
Climate Change	$\mathbf{8.44 \times 10^{-5}}$
Resource use, energy carriers	$\mathbf{5.59 \times 10^{-5}}$
Acidification terrestrial and freshwater	$\mathbf{2.1 \times 10^{-5}}$
Photochemical ozone formation - human health	1.36×10^{-5}
Eutrophication terrestrial	9.81×10^{-6}
Water scarcity	5.88×10^{-6}
Eutrophication marine	4.52×10^{-6}
Ionising radiation - human health	2.38×10^{-6}
Ozone depletion	1.30×10^{-6}
Eutrophication freshwater	1.03×10^{-6}
Land Use	3.25×10^{-7}

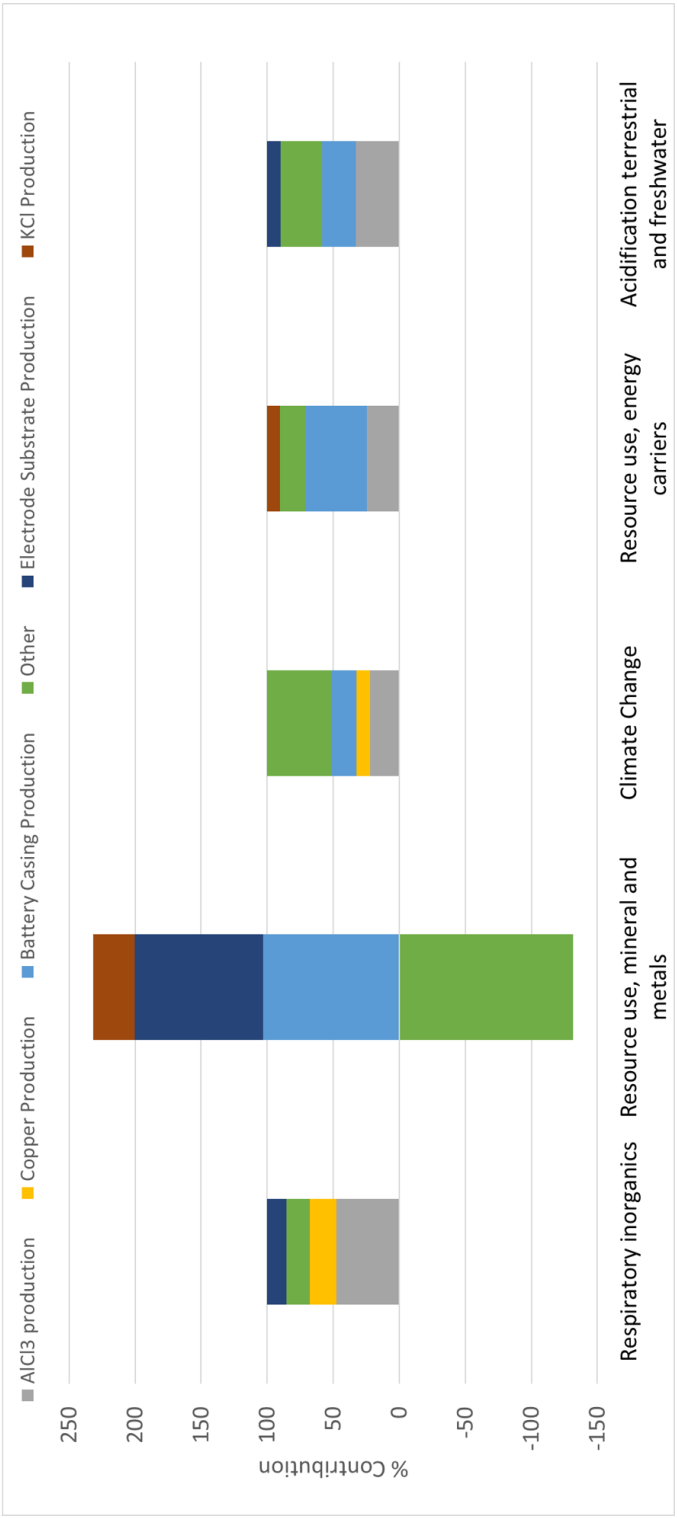

FIGURE 4.1: Top five impact categories from Al-ion cell LCA with their main contributors (20)

The lifecycle assessment has proven an excellent tool in understanding the current state of the aq. Al-ion battery. The results have shown where the battery can be improved (such as investigating different battery casing materials) to reduce overall envionmental impact. The LCA is not the only tool used to inform design. Overall TRL, ease of manufacture, cost and complexity will all impact on the final design if it is to be commercialised. By using the LCA as a starting point though, it ensures that environmental impacts remain the central driver of development. The LCA itself has limitations, as discussed already, such as the poor understanding and quantifying of nano-particles. Further, as this LCA was based on a low TRL design, therefore the manufacturing processes and inputs were based on examples given by (23), and may not reflect the actual manufacture. It is however, a useful tool to use in comparison to other energy storage devices, as discussed in the following sections. (20)

4.3 Case Study - use of Aq Al-ion technology in a dual energy storage system

This section specifically considers two case studies of dual energy storage systems (DESSs) discussed in the Chapter 2. The increase in car lifetime as well as the economic benefit of using DESS within electric vehicles have been shown (21). Here a city bus (example 10 in Table 2.1) and an electric vehicle (EV) modelled as a 1100 kg car (example 7 in Table 2.1) are used as examples, taking data from (157; 27)(26, 30). These DESSs have different output suggestions for the proportion of the high energy to high power ratio (HE: HP components) as well as the overall power and energy required. The city bus requires 150kW from the HP component, while the EV requires 19.9 kW. Therefore, a lifecycle assessment approach is used to analyse the environmental impacts of DESSs proposed for each case study; namely a Supercapacitor/Li-ion (SC/Li-ion) based on literature results reported. This section further evaluates the use of an aqueous Al-ion/Li-ion configuration as an emerging high power battery technology and compares the outputs. While the previous LCA in this chapter compared technologies per kWh or kW, the functional unit for this study is the full DESS for the lifetime of the vehicle, and therefore the functional unit is defined as such, using overall mass (in kg) to assess the environmental impacts. (21)

For this DESS analysis, values for the overall mass of the Al-ion battery are taken from the previous section (20), which is an assessment of a lab based, bench-top battery prototype. Therefore, the overall masses of the vehicles are likely unviable in this stage. The argument of this section is not to use the Al-ion battery as-is, but to argue that there is a use case for the battery, and to drive the design development of such a battery, such that we can realise these environmental benefits. This is not an assessment in isolation, and therefore should not be taken as such.

4.3.1 Results

Using OpenLCA (165) and the European Union's Environmental Footprint (EUEF) midpoint analysis (23), a cradle to gate analysis was performed. The fuel consumption and usage of the systems during the car's lifetime are not considered, only the procurement of raw materials and manufacturing of the energy storage systems are considered. The impacts of production for all required components (including replacement batteries) were assessed over 19 impact categories, including acidification, carcinogenic properties, climate impact, land usage, ozone impact and energy resource. Respiratory particulates are also calculated as part of the EUEF, however with regards to nano-particles (TiO_2 in the Al-ion and graphene in the SCs modelled are nano-powders) this assessment criteria is not fully accurate, as the calculations do not take into account nano-particulates currently, and therefore does not consider the full range of particulates produced during manufacture (181). For the purpose of this assessment, the main impact categories– climate change, acidification and resource use are presented in Tables 4.3 and 4.4, with the impacts shown graphically in Figure 4.2 for the city bus and Figure 4.3 for the EV. Full results for all impact categories are found at (182). For the SC/Li-ion case modelled, no replacements are needed and so BOL and EOL are plotted as a single value. The replacement of the Al-ion battery over the lifetime increases the environmental impacts, however they are still consistently lower than the equivalent Li-ion case. (21)

TABLE 4.3: Results of city bus case study for different ESSs for key environmental impacts. (21)

City Bus	Li-ion Only BOL	Li-ion Only EOL	SC/Li-ion BOL	SC/Li-ion EOL	Al-ion/Li-ion BOL	Al-ion/Li-ion EOL
Climate Change Impact [kg CO_2 eq.]	8,482	25,450	7,990	7,990	8,536	9143
Acidification [Mole of H^+ eq.]	31.09	93.26	29.32	29.32	33.25	41.62
Resource Use: Minerals and Metals [kg Sb eq.]	0.044	0.13	0.041	0.041	0.058	0.093
Resource Use: Energy Carriers [MJ]	96,050	288,100	93,230	93,230	99,180	117,900

Initially it is worth noting that the ratio of HP:HE in the DESSs described is different in both cases. The city bus has a mass ratio of $\tilde{1}$:1200 and the car has a mass ratio of $\tilde{1}$:131 for the SC: Li-ion. The differences in these outcomes are likely due to the driving use cases used to optimise the DESSs, and the likely different utilisations of a DESS, with the car using the HP for all high-power cases, and the bus for 'topping up' with the higher demand accelerations. (21)

When looking at environmental impacts, the results at BOL are within one order of magnitude for all the cases presented. Therefore, it is fair to say that for a vehicle with a short overall lifetime (defined as less than 5 years for the city bus, and less than $\tilde{5}$000 cycles for the EV), there is no strong environmental reason to use a DESS. Further, a DESS is often more expensive than using just one type of battery (142; 157; 183). Al-ion cells, although adding an appreciable mass to the DESS, have comparable environmental impacts per kW output to the SC. A reminder that the added mass was not factored into the vehicle lifetime data. The resulting environmental impacts are roughly the same to one significant figure across all BOL cases. When looking at resource use – the Al-ion/Li-ion seems the worst option for the low use case – however as this study does not take into account recycling and re-use – it is likely that

TABLE 4.4: Results of EV case study for different ESSs for key environmental impacts. (21)

City Bus	Li-ion Only BOL	Li-ion Only EOL	SC/Li-ion BOL	SC/Li-ion EOL	Al-ion/Li-ion BOL	Al-ion/Li-ion EOL
Climate Change Impact [kg CO_2 eq.]	3,740	7,486	3,752	3,752	4,541	5,399
Acidification [Mole of H^+ eq.]	13.72	27.44	13.76	13.76	19.06	24.66
Resource Use: Minerals and Metals [kg Sb eq.]	0.019	0.039	0.019	0.019	0.021	0.063
Resource Use: Energy Carriers [MJ]	42,390	84,770	42,940	42,940	54,380	67,090

the ease of recycling of Al-ion compared with Li-ion batteries (184) would lead to a more sustainable result – however this is beyond the scope of this study. (21)

We see the impact of the lifetime extension provided by the DESS when assessing the EOL results. This impact is shown most strongly with the SC/Li-ion DESS for both case studies. For the city bus example, at EOL, the SC/Li-ion would have just under a third the environmental impacts of the Li-ion only option. Specifically, looking at the climate change impact, for the Li-ion only option at end of life the emissions are around 25,446 kg CO_2 eq. compared to 7936 kg CO_2 eq. for the SC/Li-ion DESS. For the EV there is a $\tilde{5}$0% reduction in all impact categories reported. This reduction in impacts is mostly true for both the Al-ion/Li-ion EOL cases. The city bus case study shows that the Al-ion/Li-ion at EOL has 35% the emissions of the Li-ion EOL in climate change impacts, and 70% of Li-ion EOL's resource use (minerals and metals). This high use of minerals and metals comes from the contribution of the copper current collectors in the Al-ion cell, and while not considered within this study, the recycling and re-use of copper in the future would reduce this impact. For the EV case study, the resource use (minerals and metals) is higher for the Al-ion/Li-ion EOL than the Li-ion EOL, with 0.063 and 0.039 kg Sb eq. respectively. Overall, the impacts reported for the Al-ion/Li-ion EOL for the EV are slightly lower than that of the Li-ion only EOL case - climate change impact is 72% that of the Li-ion only case, while acidification is 90% that of the Li-ion only case. In this example we can see the impact

of the ratio of HP:HE and the difference it makes on the environmental output for the DESS. (21)

For the city bus case study, Al-ion could provide the HP component of a DESS in the future, as it provides similar environmental benefits to the SC but has the advantage of being cheaper, safer and easier to produce (20; 22). However, the electric vehicle assessed, with the higher reliance on the HP component would benefit environmentally from an SC/Li-ion DESS. For the EV example, it is useful to discuss what measures are needed to make the Al-ion/Li-ion DESS a viable environmental option, as this will inform future development of the technology. The first option is an increase in the lifetime of the Al-ion battery such that no replacements are needed over the vehicle lifetime – this would lead to the BOL = EOL results, as seen for the SC/Li-ion examples in both case studies. However, if this were not achievable, looking at the impact that is above that of Li-ion only – minerals and metals – we can inspect the data for the key contributor to this category. From the initial Al-ion LCA (20) we can see the key contributors are the copper current collector and the battery casing, made mainly from PEEK (polyether ether ketone). The battery casing for the Al-ion cell is Ĩ1% wt, compared to the SC and Li-ion casing, which are around 20% of the total mass. The casings for SC and Li-ion however are made of aluminium, a low impact metal with many established routes for production and recycling, which minimises the overall environmental impact of the case used. The copper current collectors, as mentioned previously, are assumed to be primary copper, a simple improvement in terms of the resource use here, is to switch to secondary (or recycled) copper for the current collectors, which will minimise the impact and have no design implications. Changing the copper source within the OpenLCA software to 75% recycled reduces the minerals and metals impact to 0.047 kg Sb eq. at EOL – still higher than the 0.39 kg Sb eq. for the Li-ion only EOL case. At 100% recycled copper the impact becomes 0.043 kg Sb eq. – at which point the next highest contributor takes over. (21)

Other options in terms of reducing the overall impact of the EV EOL case using Al-ion, would be to look at overall improvements in terms of the active material utilised within the batteries (22). As we are starting from a baseline of a lab-based prototype, there are many improvements that can be made here. Currently, only ṍ.6% of the mass of the battery is active material – the rest is support, binders, casing etc. However, within a fully commercial cell the active material is closer to 30% (185; 26). With a higher active material %, the overall amount of support materials reduces, which in turn reduces the environmental impacts. Maintaining the active material mass required of 66.24 kg for the Al-ion component. A 30% active material mass percentage in the Al-ion component reduces the overall mass of that component to 220.8 kg, and the impact of the minerals and metals resource category to 0.054 kg Sb eq. Combining this active material increase with 75% recycled copper for the current collectors, we

arrive at a value of 0.025 kg Sb eq. – below that of the Li-ion only EOL. These changes require the development of the Al-ion battery electrode, in order to accommodate and utilise more active material throughout the battery life and testing to ensure that the increased material loading does not degrade the battery performance. (21; 22)

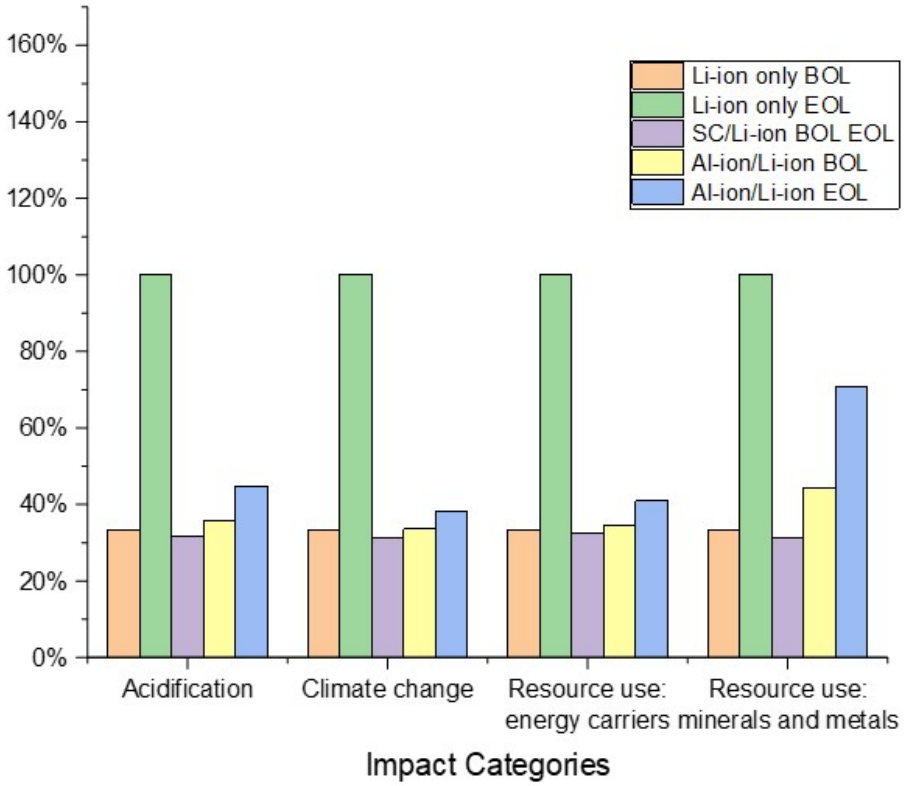

FIGURE 4.2: Impact categories scaled to EOL Li-ion for city bus (21)

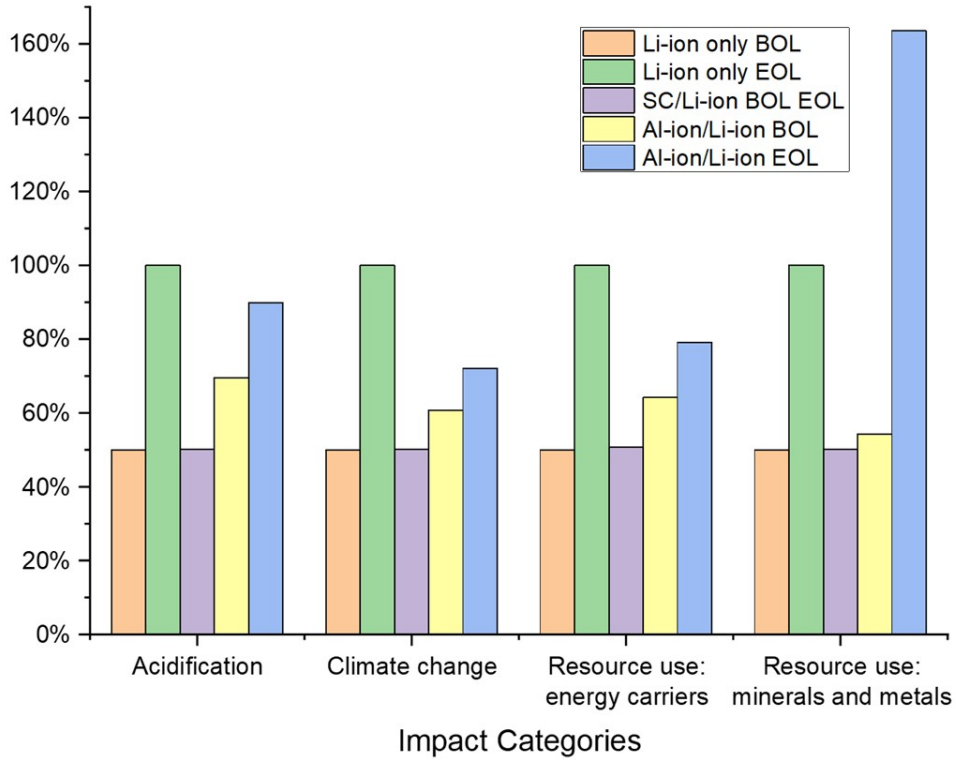

FIGURE 4.3: Impact categories scaled to EOL Li-ion for EV

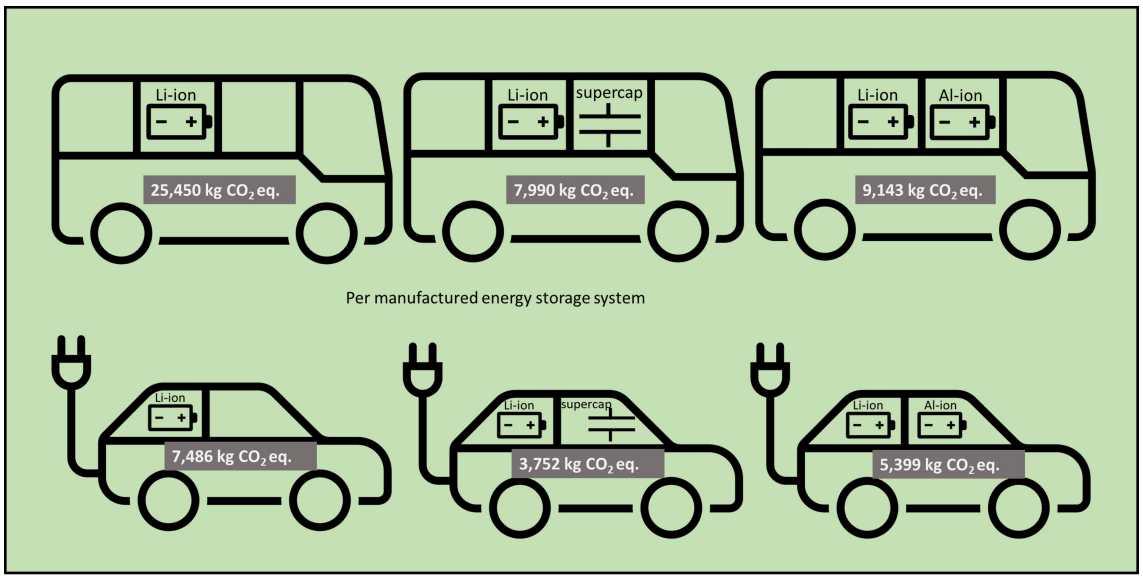

FIGURE 4.4: Summarised CO_2 impacts for ESS confgurations in city bus (upper) and EV (lower) per manufactured ESS

4.3.2 Sensitivity analysis

A key uncertainty within the analysis - apart from the mass implications - which are the subject of a sensitivity analysis include the transported distances of the raw materials (calculated in t*km with various transport methods in Tables 3.2, 3.4 and 3.3. A second uncertainty is the electricity mix used within the production. (21)

For the Li-ion components, the total transportation required comes to 1.55 t*km/kg for the battery pack, which is just under half of that for the aq. Al-ion battery – 3.59 t*km/kg for the battery pack. The Li-ion transportation assumes only lorries and trains, whereas the Al-ion transportation assumes lorries and barges are used. The supercapacitor paper does not list the transportation assumptions and none were used during the calculation of the overall impacts – as the overall mass of SCs was small it was assumed the transport impacts would be negligible. To evaluate the sensitivity of the analysis to transport, the CityBus BOL and EOL studies will be run with no transport for all three cases, and for double the current amount of assumed transportation, which will be compared with the original result in Figure 4.5 for BOL and Figure 4.6 for EOL. For all cases, the overall changes in the 19 impact categories are found in the supplementary data – with the range of change from ±0-10% of the baseline. The largest change seen in BOL is the acidification impact for Al-ion/Li-ion at 10% above the baseline (36.7 mol compared to 33.5 mol). The use of barge transport here and not for the Li-ion system is likely the key reason for this change. It is difficult to explicitly log every journey taken and with which vehicle for these studies. The ranges presented through this analysis do not change the overall take-aways from this study at EOL – with the SC/Li-ion and AL-ion/Li-ion cases still having reduced impacts over all categories compared to the Li-ion system – around a third of the Li-ion EOL values (apart from Al-ion/Li-ion resource use minerals and metals which is at two thirds that of the EOL Li-ion only). For the BOL cases however, the Al-ion/Li-ion system for acidification, climate change and fossil use, become more impactful when looking at the double transport assumption (by 4.66 mol, 477 kg CO_2 eq., and 8136 MJ respectively). Therefore, when looking at the BOL comparison, the Al-ion/Li-ion system may have higher environmental impacts than Li-ion only, with reduced impacts seen only after the lifetime of the vehicle. (21)

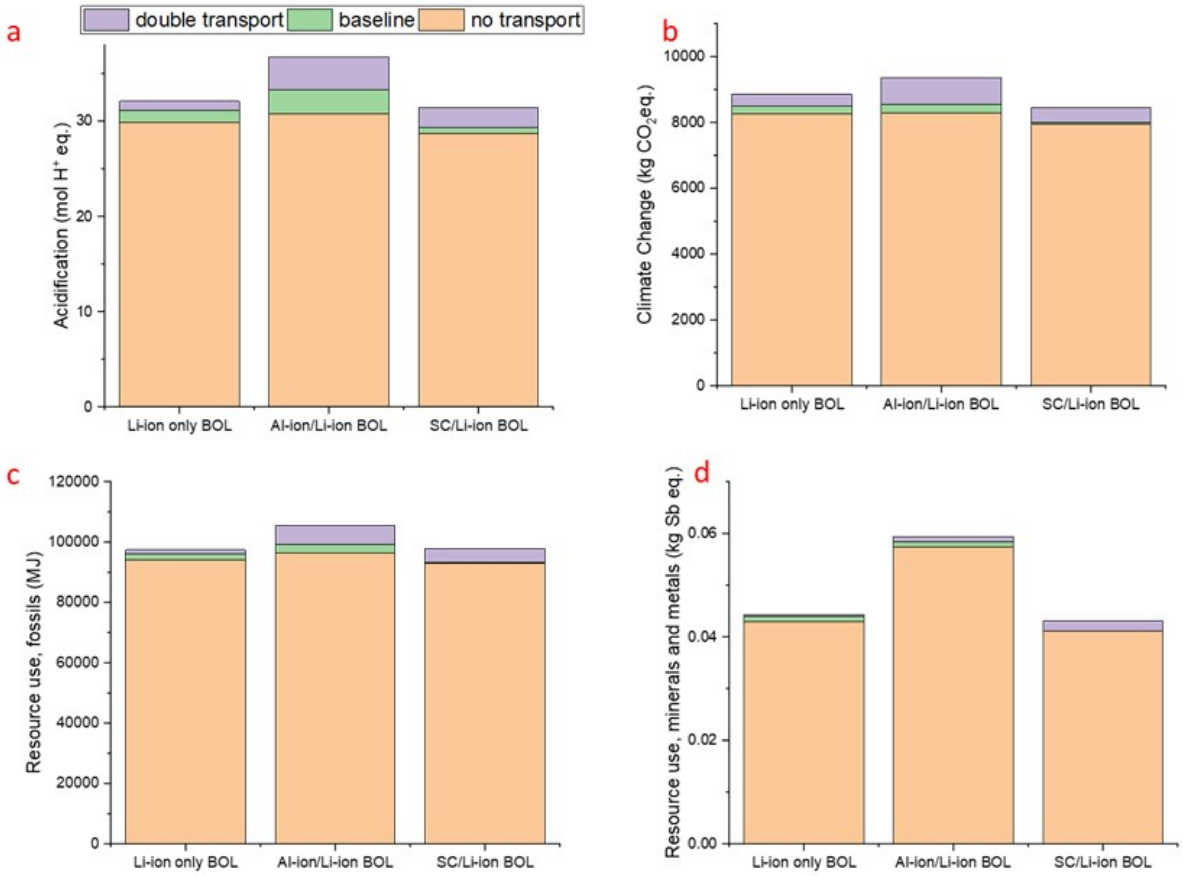

FIGURE 4.5: Sensitivity to transportation of raw materials for BOL city bus for a) acidification, b) climate change, c) fossil use and d) mineral and metal use (21)

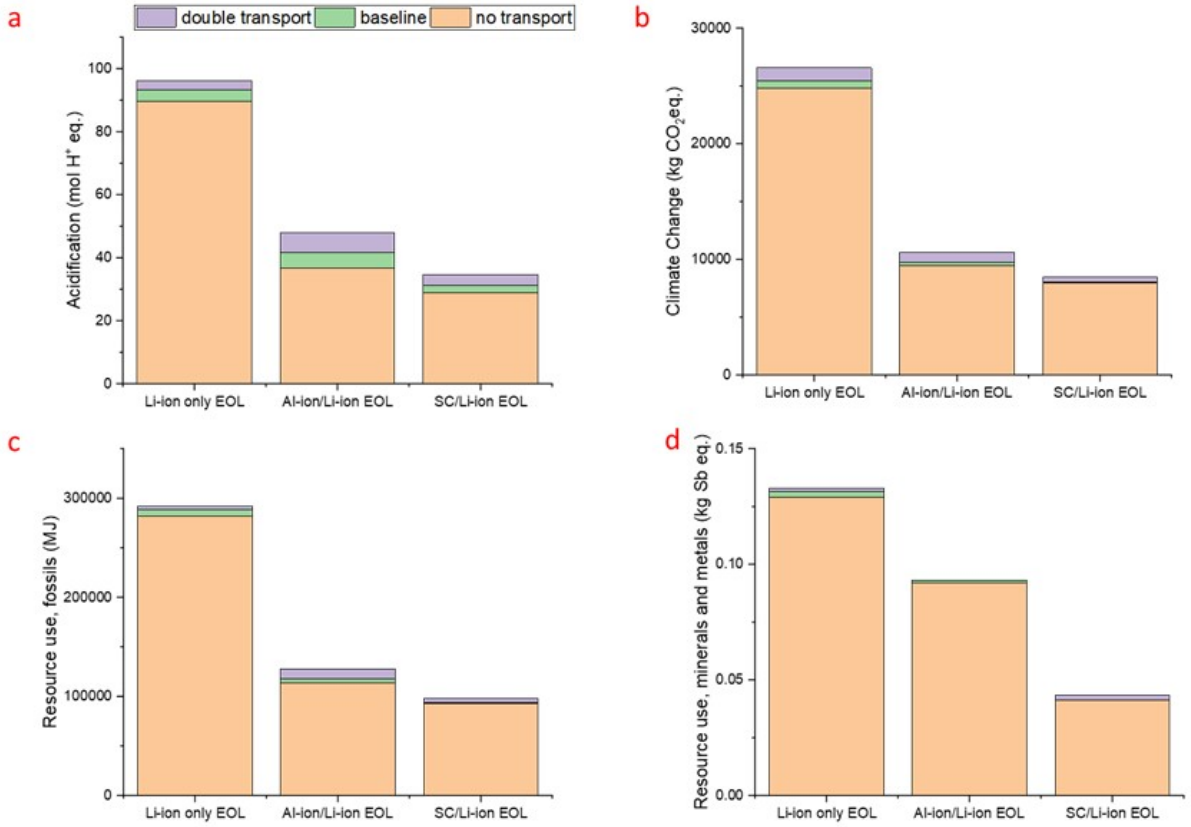

FIGURE 4.6: Sensitivity to transportation of raw materials for EOL city bus for a) acidification, b) climate change, c) fossil use and d) mineral and metal use

The electricity mix assumed for the baseline calculations is a mix of 80% renewable and 20% fossil fuel based. The BOL city bus cases underwent a sensitivity analysis, which looked at 100% renewable (wind powered) and 100% fossil fuel based (mixed). Figure 4.7 shows the results of this analysis, which for both the acidification and climate change impacts show that the renewable option has the least impact, with a 0-1% increase in impact when compared to the baseline. This is somewhat expected as the baseline is 80% renewable. Looking at the fossil fuel only option, the impacts increase by nearly 50% acidification (from 31.8 to 55.7 mol for Li-ion and from 29.3 to 56.6 mol for SC/Li-ion). The impacts on climate change increase by an order of magnitude – from 8,481 to 28,196 kg for Li-ion, and from 7,990 to 28,700 kg for SC/Li-ion. When looking at the Al-ion/Li-ion case though, the fossil fuel case increases the impacts substantially, placing it as the most impactful DESS with this electricity mix. For acidification it increases from 33 to 81 mol, and for climate change impacts, from 8,536 to 45,028 kg. This shows that the electricity use has a clear impact on these categories, and for the Al-ion/Li-ion case specifically, this must be chosen carefully in order to ensure the most sustainable outcome – considering that acidification is already a high impact category for the Al-ion/Li-ion case. (21)

When looking at the resource use - fossil fuels, the impacts are somewhat expected, with the use of fossil fuel-based electricity increasing this impact the most. The Al-ion/Li-ion DESS is again an outlier as the baseline case here has the least impact. The increases in impacts due to fossil fuel-based electricity match quite closely to the climate change impacts – with around 200% increase for Li-ion and SC/Li-ion, and around 400% increase from baseline for the Al-ion/Li-ion category. The minerals and metals impacts are interesting as for all three DESSs, the fossil fuel option is not the highest impact. However, the largest change from minimum to maximum impact in this category is only 5%, showing that electricity mix does not have a large impact on the overall resources used. (21)

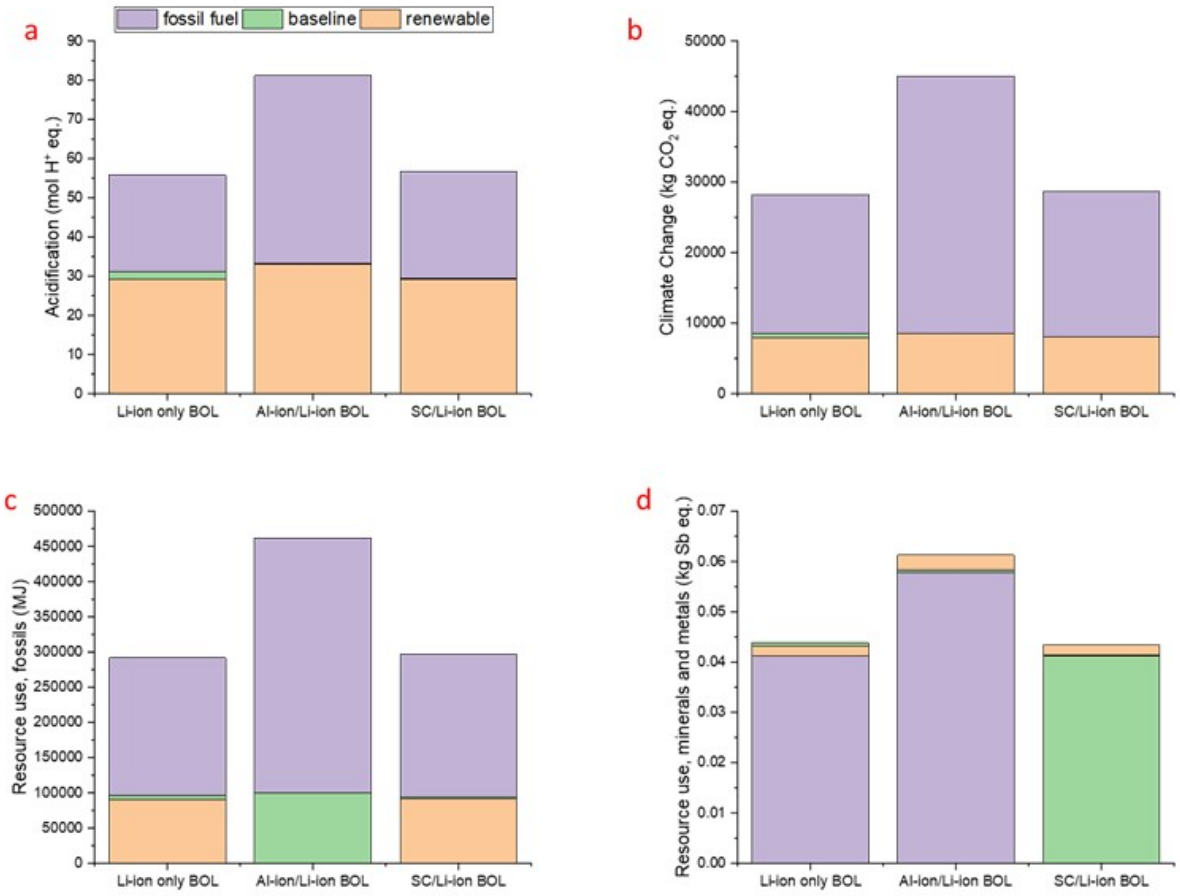

FIGURE 4.7: Sensitivity to electricity mix for BOL city bus for a) acidification, b) climate change, c) fossil use and d) mineral and metal use. (21)

4.3.3 Discussion on the DESS comparison

When assessing the environmental impacts of products, it is important to understand the limitations of the functional unit and approach used. For this case, the size of the ESSs were calculated and assessed based on values from literature. From looking

purely at the energy storage systems, using any DESS provides an environmental advantage in terms of the city bus assessed – but only over a long enough lifetime. This holds true even as Li-ion battery development extends the useful lifetime, since the DESS will always offer an advantage. However, for the electric car assessed, the SC/Li-ion had the least environmental impacts, with the Al-ion/Li-ion mostly reducing impacts compared to Li-ion only, except for the resource use of copper in the current collector. For vehicles with high mileage requirements over their lifetime, a SC/Li-ion DESS appears to have a clear environmental (and financial, since Li-ion batteries are expensive (36)) advantage at both HP:HE ratios. However, for short mileage requirements, the benefit may not be seen in the lifetime of the vehicle – but may still preserve the DESS for second life uses. This study does not take into account the growing field of second life uses for car batteries once they have reached 80% capacity and are no longer fit for their initial function. Grid storage and home-batteries for photovoltaics are applications that are currently being studied (186). A DESS would likely have a longer second-lifetime compared to a Li-ion ESS, however this has not yet been studied, and so using these energy storage systems in EVs may not just depend on the use in the EV, but over the whole lifetime of the DESS. This does add mass to the overall system – which is a non-trivial consequence. (21)

A limitation of this study is that the full electricity use and fuel-saving impacts are not taken into account over the vehicle's operational lifetime. This study only assesses a cradle-to-gate portion of the lifecycle. A further limitation is the Al-ion cells are still lab-based and therefore there are many assumptions made in this scale-up – which are discussed in this chapter and (20). Further uncertainties are introduced when modelling the use-case, such as electricity mixes, driving consistency and temperature ranges. Further, as illustrated in this study, and shown in Table 2.1, there is a vast range in the make-up of proposed DESSs (varying numbers of cells and supercapacitors, with varying overall performance needs) and the choice with the least environmental impact may depend on the overall design and use assumptions of the DESS. (21)

It is important to understand that the Li-ion battery pack and supercapacitors are already commercial technologies, compared to the Al-ion development stage. Given that the environmental improvements are already comparable with the SC DESS, this shows that there is potential for further improvements as the cell design develops, as shown with the EV example – increasing the active material and using recycled metals in the current collector (22). These are key areas of research that are strongly supported by this work. (21)

A further consideration in developing DESS systems is balancing operational requirements with environmental impact and safety. Environmental and safety aspects are linked to some degree in terms of the impact on acidification and climate change. Operational safety of DESS systems needs to incorporate a discussion of

control topologies, which is beyond the scope of this work. Using aqueous, non-toxic materials should provide advantages in reducing the likelihood and impact of thermal events and further work should be done in this area during the development of such systems. (21)

When looking at existing LCAs of Li-ion batteries, the functional units vary. For example Peters (24) evaluates the $kgCO_2$ eq. per Wh produced over the batteries lifetime – these specific comparisons are assessed within this chapter. Cossuta (28) reports on impacts per 5 capacitors, while the functional units of this study are per DESS. However, we can convert results into per kg values if we make some assumptions. For supercapacitors, the production phase states that 1.06E-1 $kgCO_2$ eq. are produced per 5 capacitors. Assuming the capacitor assessed is a Maxwell 5F capacitor (174), the mass of 5 capacitors is equal to 10 g. Within this study 4.32 kg SCs are required for the EV case – therefore based on (28), 45.7 $kgCO_2$ eq. would be produced. Based on (150), which looked at capacitors (not SCs) per kg, a capacitor produced 3.8 $kgCO_2$ eq., scaled to this study's 4.32 kg gives 16.5 $kgCO_2$ eq. Isolating the 4.32kg of SCs required for the EV in this study, the EUEF method used gives a total emission of 28.7 $kgCO_2$ eq. The value calculated in this study sits in between those it has been compared to, and there are many factors that can cause discrepancies, including the specific capacitors analysed are different, there are differences in transportation calculations and electricity mixes used in manufacturing, as well as the different calculation methods and software used. It is important therefore to understand these limitations when comparing LCA works and use them to understand trends and ranges to aid our design development. (21)

4.4 Competing with current technology

The results of the LCA performed in (20) can be used to set goals in terms of improvements required to become comparable with the current leading technology. One way of doing this is by increasing the functional energy density (see Eq. 3.1) so that the lifetime impacts reduce. (22)

We can do this in two ways; increasing the energy density of the cell itself over one discharge and/or increasing the number of cycles over the lifetime of the cell. If this can be achieved in tandem with development of more sustainable manufacturing practices then overall the environmental impacts can be reduced. Another metric of goal setting, is looking at how much the active material proportion of the design needs to be increased in order to meet the same environmental impacts. This would then reduce the overall mass of inactive materials, reducing environmental impact per kWh. This section will discuss using both methods to output evidence backed

development goals - based on competing with current Li-ion technology (per kWh) and capacitors (per kW). (22)

As values per kW are not available from Li-ion LCAs, this work will be performed for the per kWh FU. From (23), the values per kWh from cradle-to-gate for a variety of Li-ion designs are given, however they include the manufacture and production inputs - electricity, energy, and water. Therefore in order to compare fairly, the production of the Aq. Al-ion battery was added to the model based on values given by (23), and normalised to the kg output. The average values from the Li-ion batteries assessed were then taken from the (23) assessment. (22)

4.4.1 Competing on functional energy density

The methodology used to calculate the 'Competitive Functional Energy Density' is as follows:

For each impact category, the impact per kWh for the Al-ion cell and the average Li-ion cell are taken, using the equation

$$\frac{\text{Al-ion impact value}}{\text{Li-ion impact value}} = \frac{\text{Al-ion kg per functional kWh}}{\text{'Competitive' kg per functional kWh}} \tag{4.1}$$

the value for the 'Competitive Functional Energy Density' is calculated by

$$\text{'Competitive' Functional Energy Density} = \left(\frac{\text{Al-ion kg per functional kWh} \times \text{Li-ion impact value}}{\text{Al-ion impact value}}\right)^{-1} \tag{4.2}$$

and using Eq. 3.1, realistic values for the cycle life or discharge capacity can be inferred. (22)

For example, with overall CO_2, the average Li-ion impact is 6.45×10^{-1} kg CO_2 eq.(23), and the Al-ion (baselines) value is 4.93 kg CO_2 eq. Given the current value of Al-ion kg (of active material) per functional kWh is 0.038 kg kWh^{-1}, Eq. 4.2 becomes

$$\text{'Competitive' Functional Energy Density} = \left(\frac{0.038 \times 6.45 \times 10^{-1}}{4.93 \times 10^{+0}}\right)^{-1} \tag{4.3}$$

$$\text{'Competitive' Functional Energy Density} = 200.7 \text{kWh kg}^{-1} \tag{4.4}$$

With the current reported cycle life of 1750 (1), this would require a discharge capacity of 115 Wh kg^{-1} - a 10 times improvement in the current reported value. However, if we maintain the 15 Wh kg^{-1} discharge capacity, the cycle life requirement increases to 14,000 cycles. Although this seems large, the reported values for cycling CuHCF alone are 28,000 cycles ((102)), and 5000 for the TiO_2 electrode ((2)). The line in Figure

4.8, shows the parameter space for a 200 kWh kg^{-1} goal. Highlighted in this figure is the development space, the areas under the curve, where the current design sits presently, and the competitive space, above the curve, where the design would be competitive with Li-ion in terms of CO_2 emissions. (22)

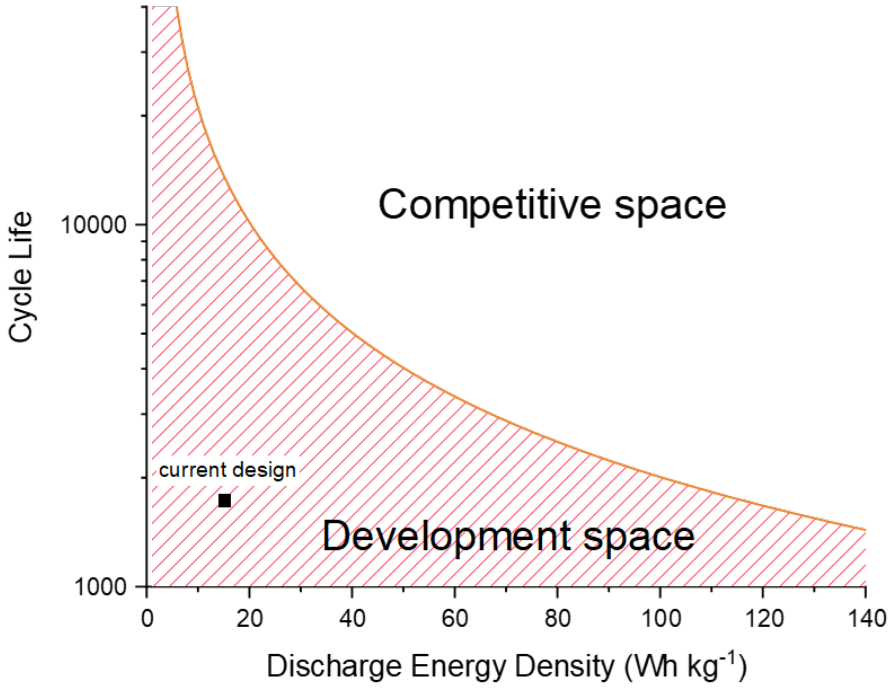

FIGURE 4.8: Competitive parameter space representing the functional energy density required to match Li-ion in CO_2 emissions, the line represents the 200 kWh CFED, with the space below being the development space, and the space above, where the design is environmentally competitive (22)

For each impact category, the competitive functional energy density will differ, and so this becomes a multi-faceted problem, with solutions dependent upon which impact is used to create the parameter space. Table 4.5 summarises the competitive functional energy density for each category. What is clear when looking at this table, is that the climate change competitive value is near the lower end of values, with results ranging from 130 kWh kg^{-1} for land use, to 7385 kWh kg^{-1} when looking at o-zone depletion. If we look closer at the o-zone value, and perform a similar calculation as we did for CO_2, we can see that either 4 kWh discharge capacity or 500,000 cycles would need to be achieved in order to meet this. These are quite optimistic, and probably unrealistic goals for this technology. Although the o-zone value is high, overall, the absolute impacts are low for o-zone depletion. (22)

It is more helpful to look at the competitive functional energy densities required for the five highest overall impact categories. These are respiratory inorganics, resource use, energy carriers and minerals and metals, climate change, and acidification of

water (20). The competitive functional energy densities required here, range from 200.7 (climate change) to 568.8 kg kWh^{-1} (respiratory inorganics). Taking the value 568.8 kWh kg^{-1}, again would mean 300 Wh kg^{-1} needed per discharge, or 38,000 lifetime cycles. However, as discussed before, the respiratory inorganics does not always take into account the use of nano-materials used, and so the value here may be higher than calculated (181). (22)

TABLE 4.5: Al-ion Competitive Functional Energy Density when compared with Li-ion values per kWh from (23) (22)

Impact category	**Al-ion Competitive Functional Energy Density (kWh kg^{-1})**
Acidification terrestrial and freshwater	321.4
Cancer human health effects	533.2
Climate Change	200.7
Ecotoxicity freshwater	383.1
Eutrophication freshwater	557.6
Eutrophication marine	311.4
Eutrophication terrestrial	330.8
Ionising radiation - human health	221.2
Land Use	130.8
Non-cancer human health effects	354.5
Ozone depletion	7,384.6
Photochemical ozone formation - human health	294.6
Resource use, energy carriers	227.7
Resource use, mineral and metals	274.3
Respiratory inorganics	568.8
Water scarcity	805.9

Looking more broadly at other reported LCA impacts for climate change (or global warming potential, GWP - depending on method used), a range of competitive functional energy densities can be calculated. GWP has been chosen because the majority of LCA or environmental impact analyses will include this, whereas other impact categories are less likely to be calculted or reported. Given that the climate change impact is a key impact for the aq. Al-ion cell, this decision seems pragmatic within the contraints of available data. (22)

Taking the values averaged in (24), for different cell chemistries (but all lithium ion) a wider picture can be drawn. Table 4.6 shows the resulting values. These are far higher than those calculated above from (23). The main reason for this, is that the studies averaged in Table 4.6 were all produced using slightly differing methodology, while they are all cradle-to-gate LCA analysis, the methodologies may have had an impact on the final reported impact.(22)

If we look at the averaged value for all the Li-ion chemistries listed in Table 4.6, the resulting Competitive Functional Energy Density is 1853 kWh kg^{-1}. To meet this goal

TABLE 4.6: Averaged Competitive Functional Energy Density for a variety of Li-ion chemistries - values taken from (24) (22)

Cell chemistry	**GWP [kg CO_2 eq.]**	**Al-ion Competitive Functional Energy Density [kWh kg^{-1}]**
Lithium Iron Phosphate - Carbon	0.078	1,671.9
Lithium Iron Phosphate - Lithium titanate	0.0251	5,168.8
Lithium Cobalt Oxide - Carbon	0.093	1,395.0
Manganese Spinel Oxide - Carbon	0.071	1,837.6
Nickel, Manganese, Cobalt - Carbon	0.086	1,515.6
Nickel, Aluminium, Cobalt - Carbon	0.068	1,904.8
Average	0.070	1853.0

for the Al-ion cell the lifetime would need to increase to around 120,000 cycles, or a discharge energy density of just over 1 kWh kg^{-1}. The parameter space presented here is most likely beyond the scope of Aqueous Al-ion technology. (22)

4.4.2 Capacitors and supercapacitors as a comparison

As discussed in the literature review, Chapter 2, it may be more insightful to use capacitor, or supercapcitor LCAs to set performance goals for this cell. Given that the Al-ion cell appears to behave similarly to a capacitor (85), and has a high power density of around 300 W kg^{-1}. If, again we aim to look at the climate change impacts (or global warming potential), there are two recent papers that can be used to set performance goals. Here, we will look at the impact per kW (the results per kWh $\times$ 0.053 as calculated earlier) - and so the equation to find the Competitive Functional Power Density is:

$$\text{'Competitive' Functional Power Density} = \left(\frac{\text{Al-ion kg per functional kW} \times \text{Capacitor impact value}}{\text{Al-ion impact value}}\right)^{-1} \tag{4.5}$$

which, in this case, becomes - substituting in equivalent values from (20),

$$\text{'Competitive' Functional Power Density} = \left(\frac{0.002 \times \text{Capacitor impact value}}{0.261}\right)^{-1} \tag{4.6}$$

This was used with the values from (28) and (150) to compare to supercapacitors and capacitors respectively - with the resulting competitive fuctional power density reported in Table **??**. The four capacitors were - Graphene Supercapacitor, Activated Carbon Supercapacitor, Multilayer Ceramic Capacitor (MLCC) and Tantalum

Electrolytic Capacitor (TEC). Values from (20) were used as they have adapted (28) values into the lifetime impact per kW. Values from (150) have also been adapted via the following method;

- Values were reported in impacts per kg in (150) for an MLCC and a TEC
- Energy per capacitor was calculated using $\frac{1}{2}CV^2$ where capacitance (C) is $1\mu F$, and V is the rated voltage provided by datasheets (16V for the MMLC and 25V for the TEC) (187; 188)
- Energy was converted into lifetime power by multiplying by the lifetime - given the lifetime testing for capacitors is 1000 hours (187; 188), this is the value assumed
- The lifetime power per capacitor was then multiplied by the number of capacitors reported in (150) used to calculate per kg impacts
- The resulting value here was the lifetime kW kg^{-1}, so taking the inverse gives kg kW^{-1}
- multplying the calculated kg kW^{-1} by the reported impacts in per kg provides the equivalent per kW impacts

(22)

TABLE 4.7: Averaged Competitive Functional Power Density for a variety of capacitors (22)

Capacitor type	**GWP [kg CO_2 eq.]**	**Al-ion Competitive Functional Energy Density [kW kg^{-1}]**
Graphene Supercapacitor (28)	2.53	51.6
Activated Carbon Supercapacitor (28)	1.05	124.3
Multilayer Ceramic Capacitor (150)	1.13	115.5
Tantalum Electrolytic Capacitor (150)	29.6	4.4

Given that the current value of Functional Power Density for the aq. Al-ion cell is 525 kW kg^{-1}, the design is already competitive environmentally with the reported capacitors. (22)

4.4.3 Competing on active material proportion

The work above provides support to goals for developing the aq. Al-ion cell. If looking at capacitors to enable a goal to be set - there is no need. This is encouraging

when placing the aq.Al-ion cell within its peers, but it does not provide a base for further development. Therefore, looking at the Li-ion technology as a baseline, and using the climate change impacts as the starting point, data from (23) would provide us with a realistic parameter space in which to improve performance. However, looking at the averaged data from over 16 Li-ion LCAs in (24), we would need to reach 150,000 lifetime cycles, or a discharge energy density of just over 1 kWh kg^{-1}. The methodology from (23) matches that of the initial aq. Al-ion LCA, and so we could say these goals are more realistic and practical. Although, it is always more interesting to attempt to meet the less practical goals, and by combining an increase in performance with an increase in % active material, the impractical goals may become feasible. (22)

As calculated earlier, the required mass of active material to calculate the per kWh impacts is 0.038 kg. When this value is input into the LCA model - the total mass of the battery assessed is 7 kg. This means that 0.5% of the battery is active material. Compared to Li-ion batteries, where the proportion of active material is often closer to 30% (26; 23). This value itself could be a valid goal for increasing active material to match that of Li-ion. However, if looking from an environmental perspective, the following methodology has been used. (22)

Using the baseline model, with the existing mass of 0.038 kg active material remaining constant, remaining supporting materials of polycarbonate electrode substrate, PEEK casing, copper current collector and electrolyte will be reduced in order to achieve 1%, 5%, 10%, 20% and 30% active material proportion. The manufacturing inputs of electricity and water will be scaled to the total calculated mass as before. The results will then be compared to those from (23; 24) in a similar manner to the previous section. Focusing on climate change (or GWP) impacts, due to availability of data, a 'goal space' of active material % will be derived, and discussed. This is a top-level assessment, and is only looking at the current design to provide a guideline idea of the point at which it becomes environmentally competitive with Li-ion, exploring options to increase the active material %, such as using carbon felts as the electrode substrate are explored theoretically in the next section, and empirically in Chapter 6. As with the functional energy density assessment, the production and manufacturing inputs have been added to the model to make a fair comparison with the Li-ion technology. Table 4.8 presents the resulting climate change impacts per functional kWh at different active material percentages. (22)

These resulting values of climate change impact can now be used in equation 4.2 to find the resulting competitive functional energy density required for differing % active material. Both the averaged values from (23) and (24) were used to create two parameter spaces - which are presented in Figures 4.9 and 4.10. Each line represents the competitive functional energy density for a given % active material, with the current reported values for the aq. Al-ion cell marked as a black square. If looking at Figure 4.9, the current aq. Al-ion cell sits on the 10% active material line. Therefore, if

TABLE 4.8: Resulting climate change per functional kWh impacts for different % active material for the aq. Al-ion battery (22)

% active material	Total Mass of Cell [kg]	Climate Change [kg CO2 eq.] per kWh
0.5	7	4.93
1	3.8	3.62
5	0.76	0.98
10	0.38	0.61
20	0.19	0.41
30	0.12	0.35

the performance of the cell remained the same, but the design changed such that we reach 10% active material, then the cell would be competitive with the Li-ion based on climate change impacts - according to (23). However, when looking at Figure 4.10, the current position of the aq. Al-ion is below the parameter space. Therefore a combination of performance improvement and increasing % active material is necessary to compete. If the discharge capacity remained the same, and cycle life increased to 10,000 - then we would require 30% active material to become competitive with this study. (22)

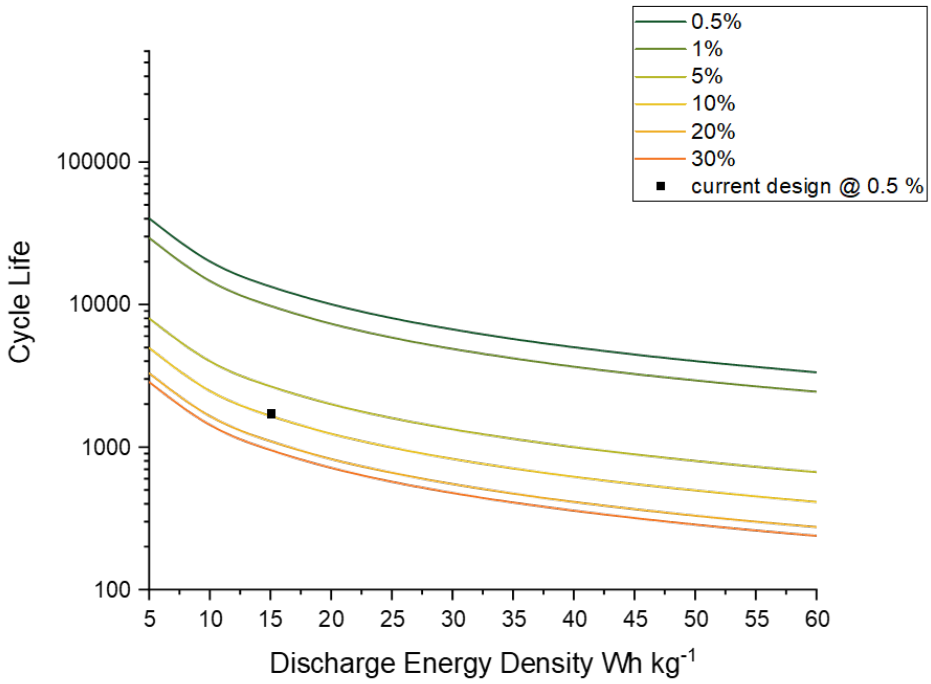

FIGURE 4.9: Competitive parameter space representing the functional energy density required to match Li-ion climate change impacts for a given % active material, compared to (23) (22)

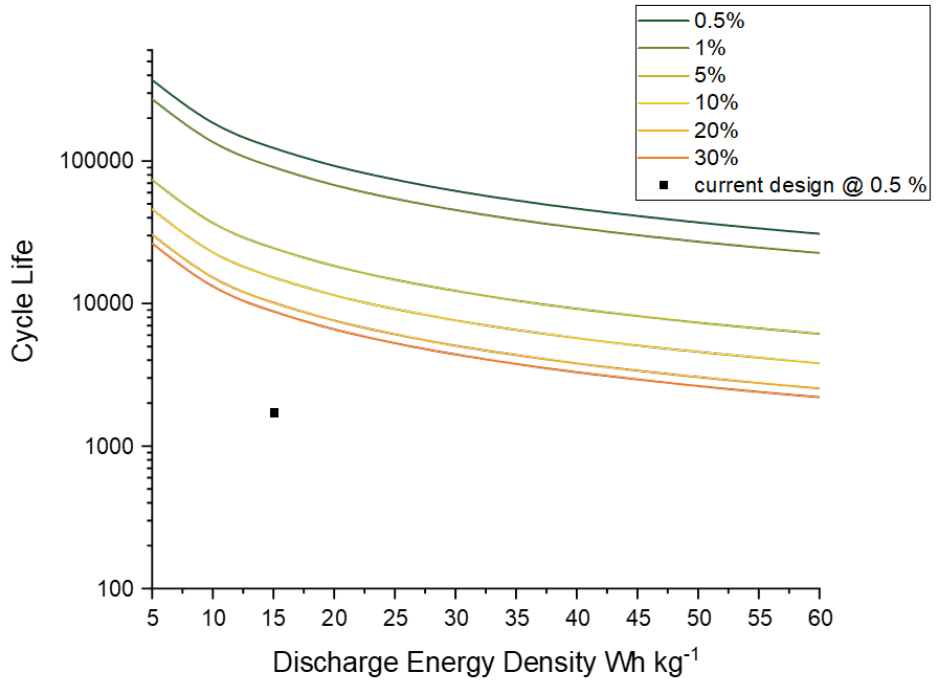

FIGURE 4.10: Competitive parameter space representing the functional energy density required to match Li-ion climate change impacts for a given percentage active material, compared to (24)

4.5 Increasing the utilisation of active material

Two ways to increase the utilisation of active material are; increase the amount of active material in the cell or reduce the amount of non-active material. One way of increasing the amount of active material is to use an electrode substrate with a higher surface area, so that more active material can adhere to the surface. (22)

4.5.1 Carbon felt as an electrode substrate

The use of carbon felt instead of the carbon fluoropolymer electrode substrate is an option discussed further in Chapter 6. The porous felt allows for increased electrode ink for the same surface area of electrode than the carbon fluoropolymer. Carbon felt obtained from sigracell when coated using the dip method was found to hold the most electrode ink per unit area, compared to other substrates and the spraying method. 62% wt. of the dipped electrode was of active material (TiO_2), compared to 12% wt. of the sprayed carbon fluoropolymer substrate used for the baseline discussed in (20; 1).(22)

The density of the felt is lower than that of the carbon fluoropolymer substrate, 0.0764 mg mm^{-3} compared to 1.65 g mm^{-3} (29), and the felt is thicker than the carbon

fluoropolymer (3.4 mm compared to 0.06 mm (29)). The mass of the carbon felt is added to that of the carbon fluoropolymer – as this is assumed to still be required within the cell. Overall, the mass of the substrate increases from 6000 mg to 8597.6 mg per electrode. Using this information, the mass of TiO_2 ink on a dipped carbon felt area of 100 ×100 mm was calculated as

$$\text{mass of substrate (2597.6 mg)} \times \text{percentage factor} = TiO_2 \text{ mass}$$
$$2597.6 \text{ mg} \times \tfrac{62}{38} = 4238.12 \text{ mg}$$

From this value, the amount of other electrode ink components were calculated as above, 9:0.5:0.5 TiO_2: carbon black: Nafion to create the dry mix mass of 4662 mg. Then isopropanol was calculated at 1:3 dry mix: isopropanol to arrive at the mass of the electrode ink as 18.6 g per cell. (22)

The same process was performed for the positive electrode, which has different proportions of active material in its ink (20). The total mass of the positive electrode ink was calculated as 9520.57 mg per cell. All other mass values and materials, such as the copper current collector, electrolyte, and battery casings remained the same. Overall, the mass distribution of electrodes chan ged, due to the increased proportions of electrode ink, with the positive electrode contributing 32% of overall mass, and the negative electrode 38%. Electrolyte, current collector, and battery casing mass contributions are 17%, 6% and 7% respectively. Figure 4.11 presents the updated mass distribution. When scaling the mass to meet 1 FU (functional kWh) this results in the total mass of the cell as 0.215 kg. The use of the carbon felt therefore decreases the amount of inactive material required, since the 0.038 kg active material remains constant. For this cell iteration, 0.177 kg of the cell is inactive, compared to the previous construction, where 6.9 kg inactive mass was required to support the active material. Increasing the active material percentage from 0.5% to 17%. Figure 4.11 presents the updated mass distribution, and Appendix B shows the breakdown of components and datasets used for the updated electrodes. At this value (17% active material), based on Figure 4.9, this design would be competitive with existing Li-ion technology. When looking at Figure 4.10, we could infer a lifetime goal of around 20,000 cycles to become competitive. The calculation used does not include the increased impact of the carbon felt itself - polyacrylonitrile fibres (PAN) and 56 MJ of electricity are required to create 1 kg of the felt from the PAN (189). However this example shows a design route that would be beneficial to the overall climate change impacts of the cell. (22)

4.5.2 Reducing inactive material - stainless steel coin-cell

As discussed in the following chapters, a closed coin-cell was developed. This introduced a separator into the LCI (life cycle inventory), and replaced the PEEK

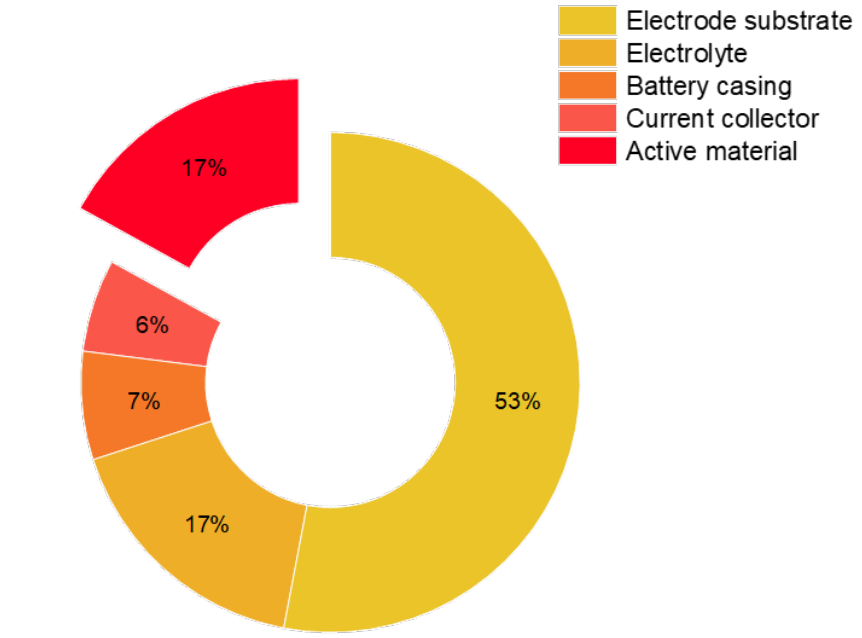

FIGURE 4.11: Cell component breakdown with CF substrate by % wt with active material highlighted (22)

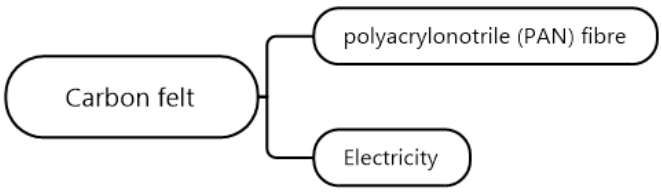

FIGURE 4.12: carbon felt production flow used in OpenLCA (22)

battery casing with stainless steel and PTFE coin-cell cases. This design removed the copper current collector, as the steel casing provides that capability. Appendix B shows the full material inventory. When taking all this into consideration the active material becomes 0.1% (see Figure 4.13), less than that for baseline cell. The volume of battery would therefore increase by five times to provide the same energy output, which may not be practical for many use-cases with limited space. However, the use of steel instead of PEEK as the battery casing does reduce environmental impacts across all categories as shown in Table 4.9. Going a step further, within the coin-cell, replacing the carbon-polymer substrate with carbon felt would increase the active material to 2% (see Figure 4.14). However, there are many practical aspects to

compressing the felt within the coin-cell which would require additional tests to confirm performance and ease of manufacture. Even so, assuming that the 1750 cycles at 15 Wh g^{-1}, the per kWh impacts are again an improvement on the baseline, and the coin-cell with carbon fluoropolymer electrode substrate. Having assessed these four options, it can be shown that the PEEK casing with carbon felt substrate increases the active material the most (to 17%), and reduces the environmental impacts across all categories. Carbon felt as an electrode substrate is discussed in Chapter 6. In the short term though, moving to a coin-cell based design would decrease the environmental impacts from the baseline - and feasibly - the manufacture of coin-cells is well known and reproducible. The development of a coin-cell is discussed in Chapter 3 and used for long duration testing in Chapter 7.

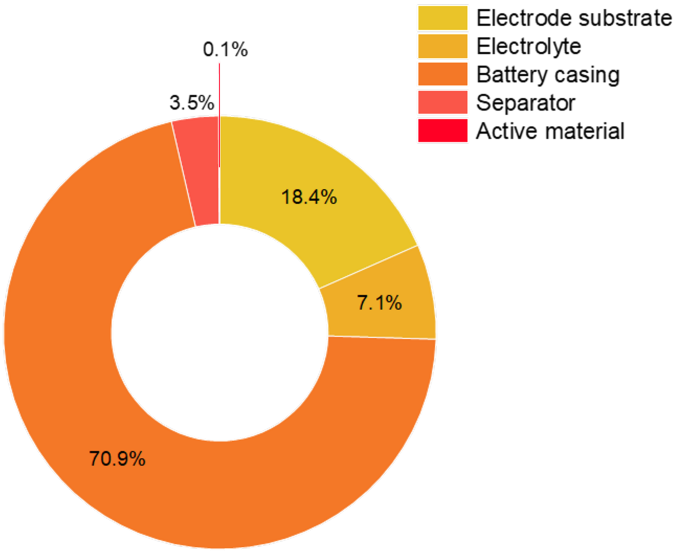

FIGURE 4.13: Coin cell component breakdown by % wt with active material highlighted

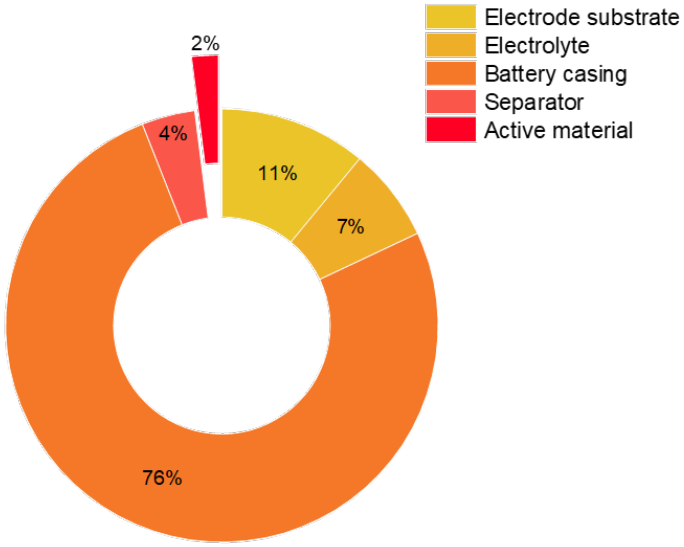

FIGURE 4.14: Coin cell component breakdown with CF substrate by % wt with active material highlighted

TABLE 4.9: per functional kWh aqueous aluminium ion results - not considering manufacturing steps

Impact category	**Al-ion baseline (carbon fluoropolymer substrate)**	**Al-ion CF (carbon felt substrate)**	**Coin Cell (carbon fluoropolymer substrate)**	**Coin cell (carbon felt substrate)**
Acidification terrestrial and freshwater [Mole of H+ eq.]	1.76×10^{-2}	4.55×10^{-4}	5.06×10^{-3}	3.46×10^{-3}
Cancer human health effects [CTUh]	6.62×10^{-8}	1.40×10^{-9}	1.56×10^{-8}	6.98×10^{-9}
Climate Change [kg CO2 eq.]	$2.95\times 10^{+0}$	7.00×10^{-2}	7.99×10^{-1}	3.49×10^{-1}

Continued on next page

Table 4.9 – *Continued from previous page*

Impact category	**Al-ion baseline (carbon fluoropolymer substrate)**	**Al-ion CF (carbon felt substrate)**	**Coin Cell (carbon fluoropolymer substrate)**	**Coin cell (carbon felt substrate)**
Climate Change (biogenic) [kg CO2 eq.]	2.46×10^{-3}	5.72×10^{-5}	9.81×10^{-4}	3.64×10^{-4}
Climate Change (fossil) [kg CO2 eq.]	$2.95\times 10^{+0}$	6.99×10^{-2}	7.96×10^{-1}	3.48×10^{-1}
Climate Change (land use change) [kg CO2 eq.]	1.83×10^{-3}	4.13×10^{-5}	1.17×10^{-3}	2.13×10^{-4}
Ecotoxicity freshwater [CTUe]	$1.91\times 10^{+0}$	5.18×10^{-2}	$5.42\times 10^{+0}$	$1.18\times 10^{+0}$
Eutrophication freshwater [kg P eq.]	8.92×10^{-5}	2.07×10^{-6}	4.08×10^{-5}	2.62×10^{-5}
Eutrophication marine [kg N eq.]	4.11×10^{-3}	1.05×10^{-4}	8.28×10^{-4}	3.50×10^{-4}
Eutrophication terrestrial [Mole of N eq.]	4.45×10^{-2}	1.14×10^{-3}	1.07×10^{-2}	3.67×10^{-3}
Ionising radiation - human health [kBq U235 eq.]	1.87×10^{-1}	4.24×10^{-3}	1.93×10^{-2}	1.37×10^{-2}
Land Use [Pt]	$5.15\times 10^{+0}$	1.14×10^{-1}	$2.55\times 10^{+0}$	7.22×10^{-1}

Continued on next page

Table 4.9 – *Continued from previous page*

Impact category	**Al-ion baseline (carbon fluoropolymer substrate)**	**Al-ion CF (carbon felt substrate)**	**Coin Cell (carbon fluoropolymer substrate)**	**Coin cell (carbon felt substrate)**
Non-cancer human health effects [CTUh]	5.73×10^{-7}	1.23×10^{-8}	3.48×10^{-7}	6.46×10^{-8}
Ozone depletion [kg CFC-11 eq.]	4.50×10^{-7}	1.61×10^{-8}	4.59×10^{-6}	6.02×10^{-7}
Photochemical ozone formation - human health [kg NMVOC eq.]	1.08×10^{-2}	2.72×10^{-4}	2.35×10^{-3}	1.18×10^{-3}
Resource use, energy carriers [MJ]	$4.10\times 10^{+1}$	$1.27\times 10^{+0}$	$1.21\times 10^{+1}$	$9.79\times 10^{+0}$
Resource use, mineral and metals [kg Sb eq.]	9.18×10^{-5}	3.85×10^{-6}	2.02×10^{-4}	8.21×10^{-6}
Respiratory inorganics [kg PM2.5 eq.]	6.74×10^{-7}	1.65×10^{-8}	1.48×10^{-7}	6.67×10^{-8}
Water scarcity [m^3 world equiv.]	7.50×10^{-1}	1.77×10^{-2}	6.09×10^{-1}	1.67×10^{-1}

4.6 Conclusion

LCA is a useful tool which can both assess the current environmental impacts of the battery, and help to guide the development of the design.

This chapter has highlighted the use of LCA for a low-TRL battery design and allowed it to be compared to state-of-the-art batteries and supercapacitors.

When compared to capacitors and supercapacitors, the aq. Al-ion battery is already environmentally competitive with respect to the global warming potential (CO_2 emissions) per lifetime kW. However, when comparing to the market leader in energy storage - the Li-ion battery with examples provided in (23) and (24), it is clear that the aq. Al-ion battery produces higher environmental impacts per kWh. As discussed, although the Al-ion battery behaves more like a capacitor, it is still useful to look at the current market leader for comparison. Using this baseline LCA in a real-world application of a DESS, for the electric vehicles assessed, the use of a DESS extended the energy system's overall lifetime and reduced the environmental impacts of the energy storage system, compared to a Li-ion Only ESS – apart from the Al-ion/Li-ion for the minerals and metals impact category, where it uses 163% that of the Li-ion only option within the EV. Overall however, the SC version of the DESS has lower environmental impacts. Given the SC assessed is commercially available, the mostly comparable results of the lab-based aqueous Al-ion technology is promising in terms of its potential sustainable development – with clear development directions such as using recycled copper and redesigning the battery casing being attainable options.

Based on improving total functional energy density, and increasing the active material proportion, a parameter space was created in which performance (i.e. cycle life and discharge energy density) and active material amount can be assessed together. Using this parameter space, we can see that the Al-ion battery is already competitive with capacitors and supercapacitors in its existing early development stage. Further, a design that equals the CO_2 emissions per kWh of Li-ion batteries can be set as a target.

From this parameter space created, performance based goals are set through the environmental impact perspective. Firstly the increase in active material is a clear target based on Figures 4.94.10. In order to achieve this goal, the reducing support material is evaluated practically by constructing a coin-cell in Chapter 5, as table 4.9 highlights the overall benefits of a coin-cell construction. Further, this target is investigated through increasing the utlisation of active material within the electrodes themselves through a carbon felt substrate (again as highlighted in Table 4.9) in Chapter 6. A target of increasing the cycle life of the cell is also set based on the work in this chapter. With Chapter 7 investigating degradation mechanisms within the cell in order to understand and mitigate these with further design developments.

Further to the goals set within the parameter space developed, there are other concerns that the LCA has highlighted, particularly through the case study of a DESS - the mass of the system - which will require reducing in future design iterations. However, this does fit the goal for increasing active material. By reducing supporting material and increasing the amount of active material within electrodes - this will reduce the mass of the overall battery design.

LCA has provided both the baseline understanding of the cell, and has provided further insight into the developments of the cell itself, allowing trialling of designs such as carbon felt or coin-cells in the software, before investing in the required materials.

Chapter 5

Initial validation of the aqueous Al-ion system and exploration of reducing support material through coin-cell casing

5.1 Motivation

This chapter describes the work performed assessing the baseline electrode design for the cell described in Chapter 4 and by Holland et al (1). The electrode ink components and ratios remain as described in Chapters 3 and 4, the electrolyte also remains as 1 M $AlCl_3$ + 1 M KCl in de-ionised water as per (1). Initial baseline cyclic voltammetry for the positive and negative electrodes are performed using a three electrode cell. These electrodes are then used to create a coin-cell for the aq. Al-ion system (1; 20). The research questions for this chapter are

- Can we reproduce the work of Holland et al.?
- Can we create a closed cell that cycles?
- Can we use LCA analysis to understand the environmental implications of this closed cell?

5.1.1 Expected Results

Based on the work of Holland et al (1; 102), it is expected that the flat, spray coated electrodes, made in the same method as (18) will perform as described in the

literature. This will confirm both the repeatability of the work and the validity of the methods used to produce the electrodes. Further, as the cell has not been tested in a closed design (i.e. a coin cell) before, it is expected that the performance with a separator material and likely build up of gas within the cell will impact the performance.

5.2 Confirmation of baseline activity of the electrodes

Electrodes were made using the method described in Chapter 3, the inks were spray coated onto a carbon-polymer substrate and cut to size to fit the aperture of a three-electrode cell. This set up was then used to perform cyclic voltammetry on the electrodes, to ascertain the electrochemical reactions taking place at the electrodes, as well as the repeatability.

5.2.1 TiO_2 negative electrode

The electrodes were weighed before and after the ink application. There was an average (from 5 samples) TiO_2 content of 3.8 mg on each electrode, given the overall average mass of the elctrode - 0.71 g - active material made up $\approx$ 0.55% of the electrode, on average. Initial CV sweeps from 0 V to -1.6 V (vs SCE) were performed to understand the full potential range at 5 mV s^{-1}, shown in Figure 5.1. There is clear hydrogen evolution from -1.5 V v SCE, and a flattening to 0 A current above -0.4 V v SCE. There are two small cathodic peaks at -0.6 and -0.2 V which were seen at subsequent cycles. On the reverse sweep there is a small peak at $\approx$0.7. The cause of these peaks is unknown, however they could be due to contamination in the set up (the electrode, electrolyte, or cleanliness of the cell), or other side reactions. The clear peaks of interest however are at -1.2 and -0.95 V v SCE. These values match well with the potential ranges in literature (illustrated in Figure 2.9). These peaks represent the redox reaction of Ti-ions, and so there is a reversible redox reaction occuring here.

Subsequent CV sweeps at varying scan ranges were thus performed between -0.7 and -1.4 V, as this is the area of interest for the TiO_2 electrode.

Four of the TiO_2 samples were scanned between 2 and 20 mV s^{-1}, with sample 3 also being scanned at 0.5 and 50 mV s^{-1}. These samples were all produced at the same time with the same ink and so variation is not expected between them. Graphs of these are presented in Figure 5.2. Peaks shift further away from each other as the scan rate increases, which can be seen in all plots. While the highest peaks seen were all found to be around -1.2 and -0.95 V v SCE, there were second peaks hinted at within the scans, however the exact shapes of the plots varied for each sample. Sample 4

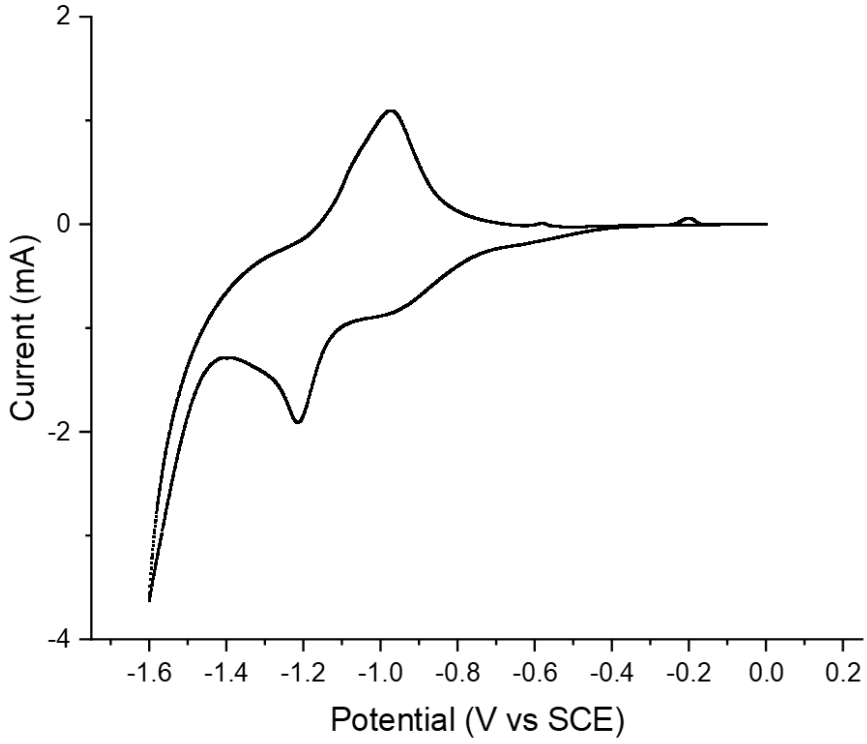

FIGURE 5.1: CV sweep of TiO_2 electrode in 1 M $AlCl_3$ + 1 M KCl at 5 mV s^{-1}

shows the two peaks the most strongly at all scan rates, on the forward sweep around -1.1 V and on the reverse sweep at around -1.0 V v SCE. Sample 1 shows broad peaks, and hints at secondary peaks in the forward sweep around -1.1 V, the second peak is clearer in the reverse sweep close to -1.0 V v SCE. Samples 2 and 3 show more distinct single peaks at the higher scan rates, with the suggested second peak in the reduction scan around -1.0 V v SCE. The lower scan rates (below 5 mV s^{-1}) for these samples begin to suggest a second peak in the forward sweep. There was also no sign of the small 'bump' seen at -0.6 V v SCE in Figure 5.1 in any subsequent scans.

The primary reaction seen have an average peak value of -1.1 V v SCE which matches well with the reported Ti^{3+}/Ti^{4+} redox pair's reaction potential of -0.96 v SCE(3) . The shape of the CVs in Figure 5.2 also appear somewhat stretched, showing a clear capacitance region between peaks. We can therefore assume that there are two mechanisms involved in this electrode - both the redox reaction and capacitive charge storage.

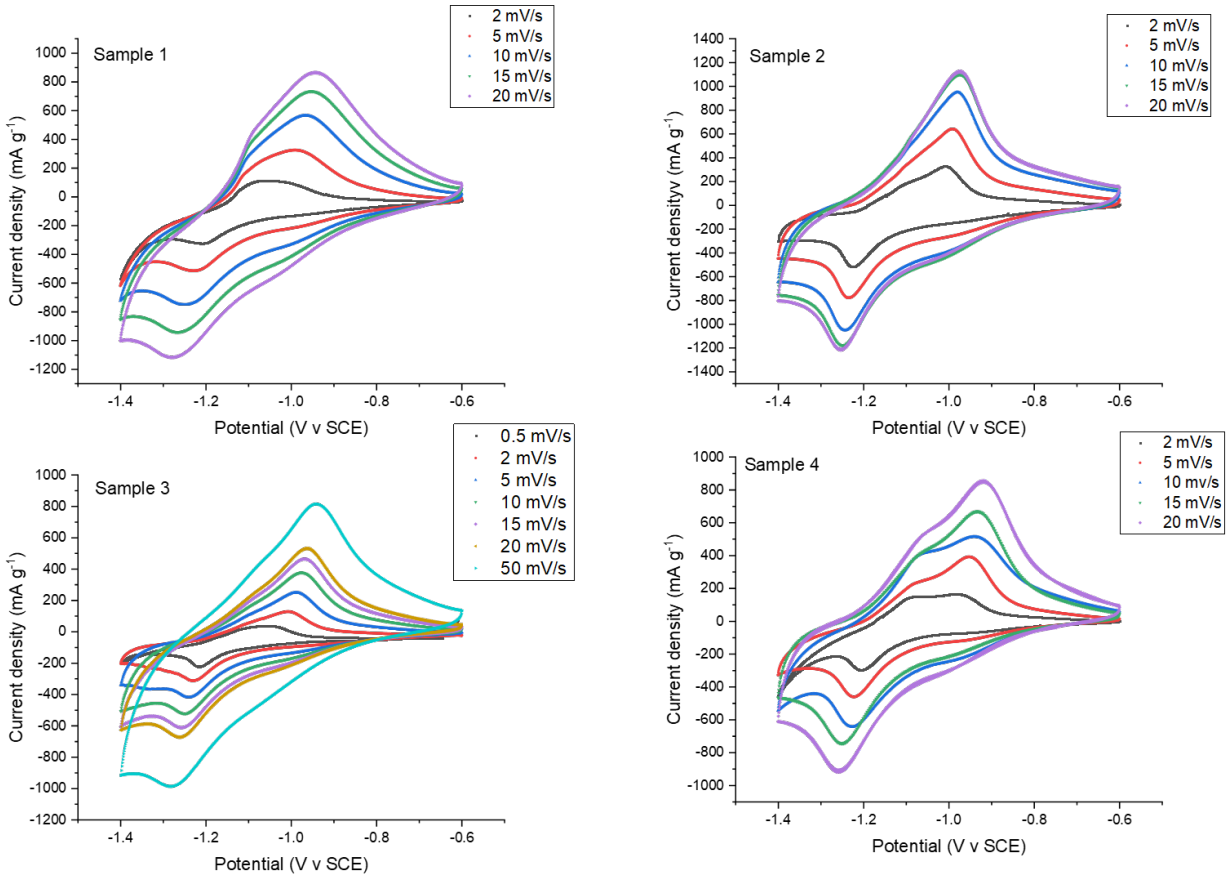

FIGURE 5.2: Cyclic voltammetry of four TiO_2 electrode samples in 1 M KCl + 1 M $AlCl_3$ varying between 0.5 mV s^{-1} and 50 mV s^{-1} sweep rates

Figure 5.3 shows the plot for Sample 3, which correlates to a diffusion controlled reversible reaction for the main peaks, based on the Randles-Sevcik equation 2.1. However, while there is a linear relationship shown, the intercept of the y-axis on this plot is not 0 for the negative sweep. It appears to be around -100 mAg^{-1}. This suggests that although we are seeing diffusion control reactions, that there is also the presense of non-faradaic charging - likely from a capacitive or adsorption reaction. The shape of the CVs do suggest a larger capacitive energy storage component, with a more rectangular center to the CV in-between the peaks.

We can calculate the diffusion coefficient given that, for our j_p of 1100 mA/g for the 20 mV/s sweep, we had an average of 3.3 mg TiO_2 on each sample. Therefore, with the $\approx$ 5 ml of electrolyte used, we can find that:

Variable	Value
Peak Current	0.00363 A
n	3
Area	0.000452 m^2
TiO_2 concentration	1502 mol/m^3
Scan rate	0.02 V/s
$\sqrt{Scanrate}$	0.1414

TABLE 5.1: Variabled for the Randles-Sevcik equation

Which gives us D = 7.3×10^{16} m^2 s^{-1}, when using the -1.3 A g^{-1} peak current density seen for the negative sweep, the diffusion coefficient becomes 1.02×10^{15} m^2 s^{-1}. This shows that the oxidation reaction is more efficient than the reduction as it has a smaller diffusion coefficient. These values are slightly higher than that calculated in (86) of around 10^{-20} m^2 s^{-1}, but sit within expected values. These values assume that 3 electrons are transferred in the reaction, with Al ions playing a role. If this were not the case, the diffusion would be slightly less efficient and the coefficient would be an order of magnitude less.

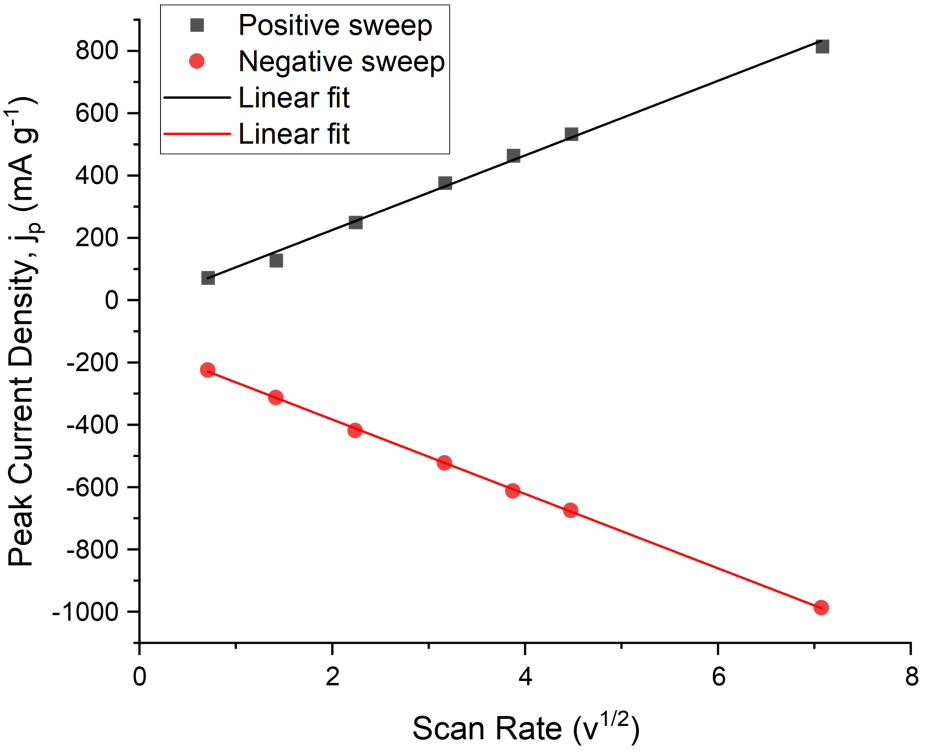

FIGURE 5.3: Peak current density vs the square root of the scan rate for the TiO_2 baseline electrode

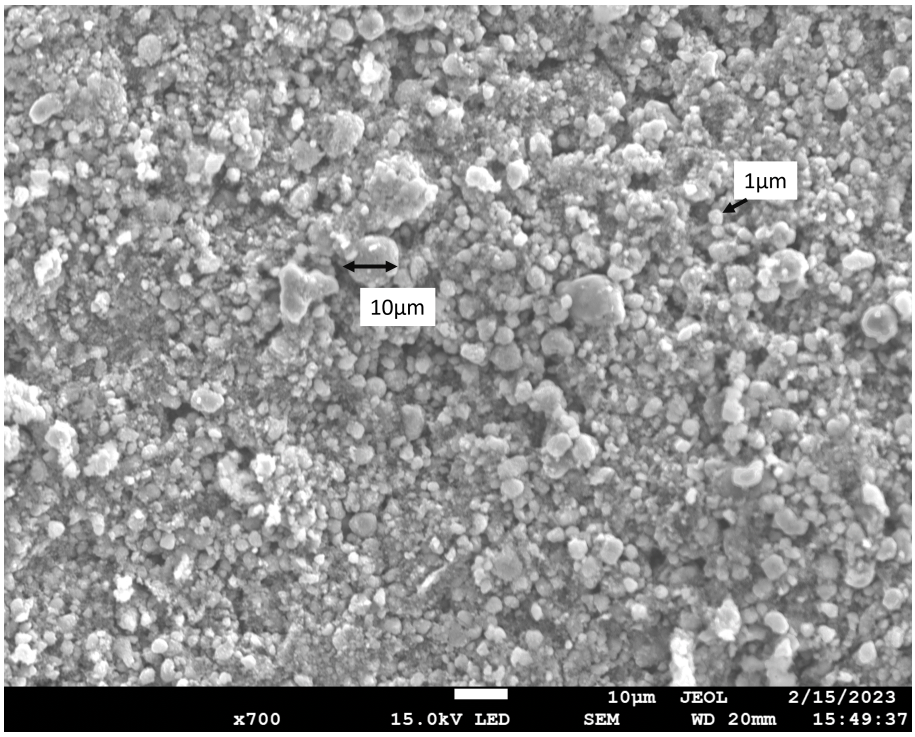

FIGURE 5.4: X700 magnification of TiO_2 surface on carbon fluoropolymer substrate

Using a SEM, the surface of the electrode was viewed. The TiO_2 particles are round, with varying sizes between about 1 - 10 μm.

Further, powder X-ray diffraction (PXRD) of the active material as obtained from Alfa Aesar and of the dried ink which had been powdered using a pestle and mortar were performed - see Figure 5.5. The TiO_2 anatase powder (Alfa Asar) initially had 13.1% rutile phase, but 100% anatase was seen in the ink sample. The Alfa Aesar package claimed 99.7% purity. The anatase powder used was first opened in 2011 and so over time, some of the powder may have transitioned to rutile, with existing contaminants acting as nucleation sites (this is unlikely given the high temperatures required for this transition to occur (around 600°C) (190). The transition can occur under visible light irradiation and is more likely to occur with contaminants present. Rutile is a far more stable phase, and so it is also unlikely that the phase transition occurred toward anatase during ink production and it is far more likely that the powder sampled for XRD was from a local concentration of rutile, while the powder used for making the ink was taken after the powder had been stirred.The analysis of this was done using the Rietveld method.

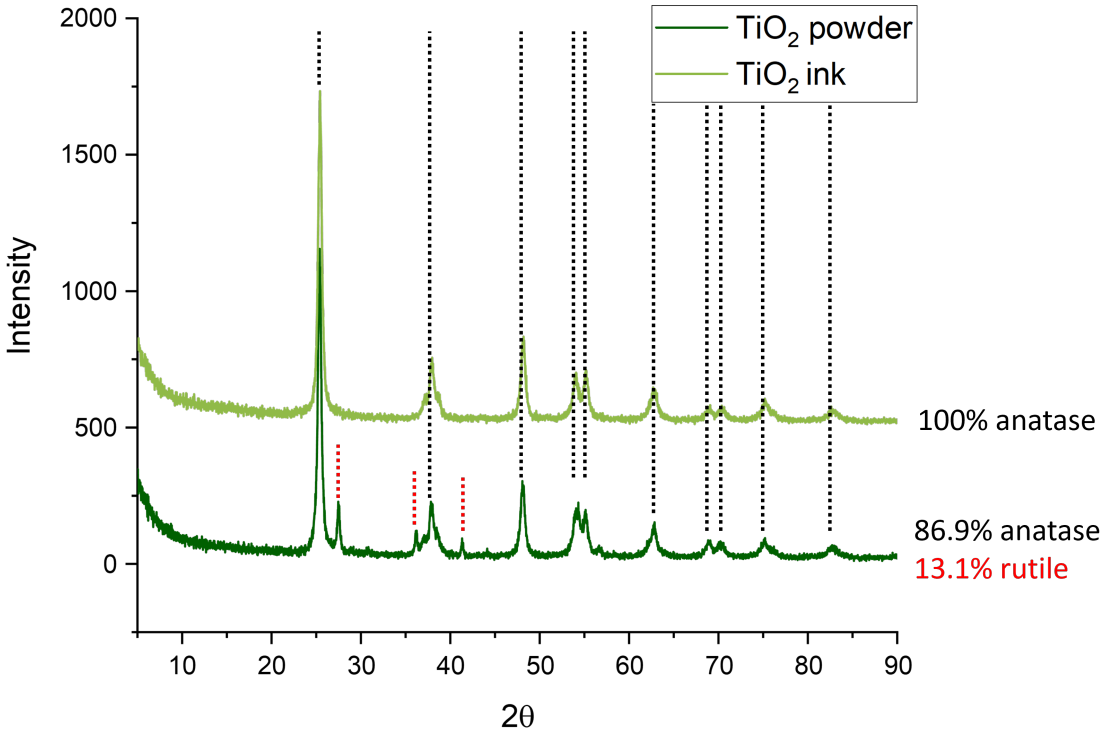

FIGURE 5.5: PXRD of TiO_2 powder, as a pure powder and when mixed in an ink

5.2.2 CuHCF positive electrode

The electrodes were weighed before and after the ink application. There was an average (from 5 samples) CuHCF content of 1.7 mg on each electrode, given the overall average mass of the electrode - 0.71 g - active material made up $\approx$ 0.25% of the electrode, on average.

The CuHCF initial sweep between 0.4 and 1.2 V at 20 mV s^{-1} shows distinct peaks at 0.62 and 0.83 V, as shown in Figure 5.6, which matches well with the literature (102). By averaging these values we find the half cell potential as 0.725 V v SCE. This matches closely with the half cell potential for CuCl - $Cu^{2+} + Cl^{-} + e^{-} \leftrightarrow CuCl$ = 0.78 V v SCE. Interestingly, this may suggest that the Cu in our CuHCF reacts with the chloride ions in the electrolyte.

We also know that $[Fe(CN)_6]^{3+} + e^{-} \leftrightarrow [Fe(CN)_6]^{4+} = 0.61V$ vs SCE, which is within the range of potentials which show activity in the half cell. Further CV scans from 0.5 to 50 mV s^{-1} were performed, with the results plotted in Figure 5.7. When further averaging the peaks for all sweeps performed, we find the half cell potential is 0.76 V which matches closer to our CuCl reaction. It has however been suggested that the Fe^{3+}/Fe^{2+} redox pair is at play, reacting with the K ion in the electrolyte. While not as obvious from the CV sweeps in this thesis – (102) found an average cell potential of 0.98 V v SCE for CuHCF cycled in just KCl - which matches closely the redox potential of 1 V v SCE for the Fe^{3+}/Fe^{2+} redox pair. Equation 5.1 shows the reversible reaction with the K^{+} that was proposed. However this may not be the whole story, and Cl may also be playing a part in the half cell reactions.

$$K_2CuFe^{3+}(CN)_6 + xK^{+} - xe^{-} \Longleftrightarrow K_{1+x}Cu[Fe^{2+}(CN)_6]_x[Fe^{3+}(CN)_6]_{1-x} \tag{5.1}$$

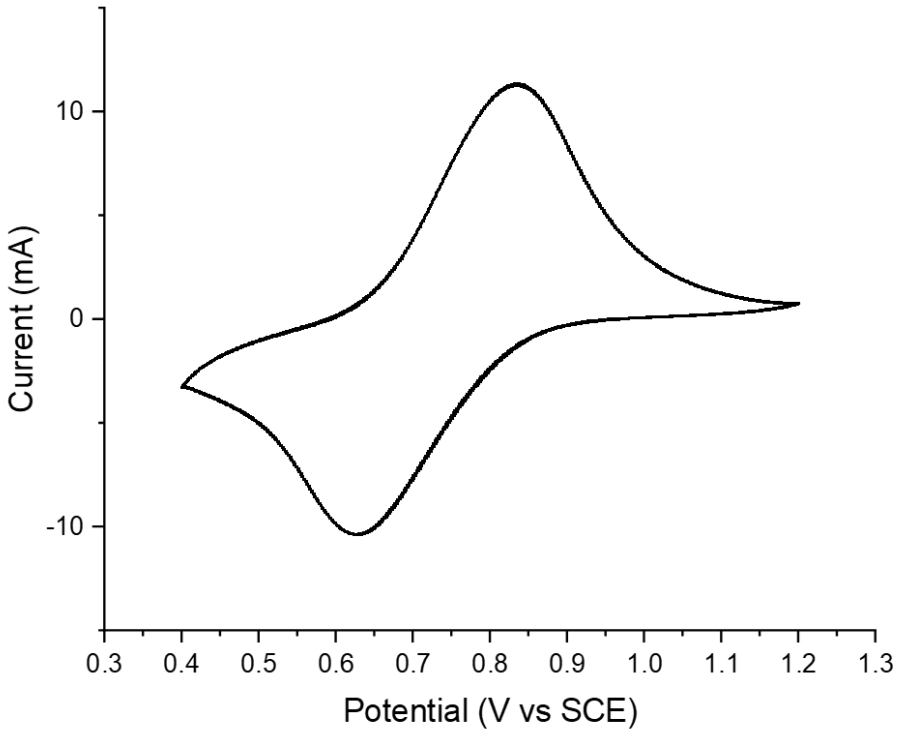

FIGURE 5.6: CV sweep of CuHCF electrode in 1 M $AlCl_3$ + 1 M KCl at 20 mV s^{-1}

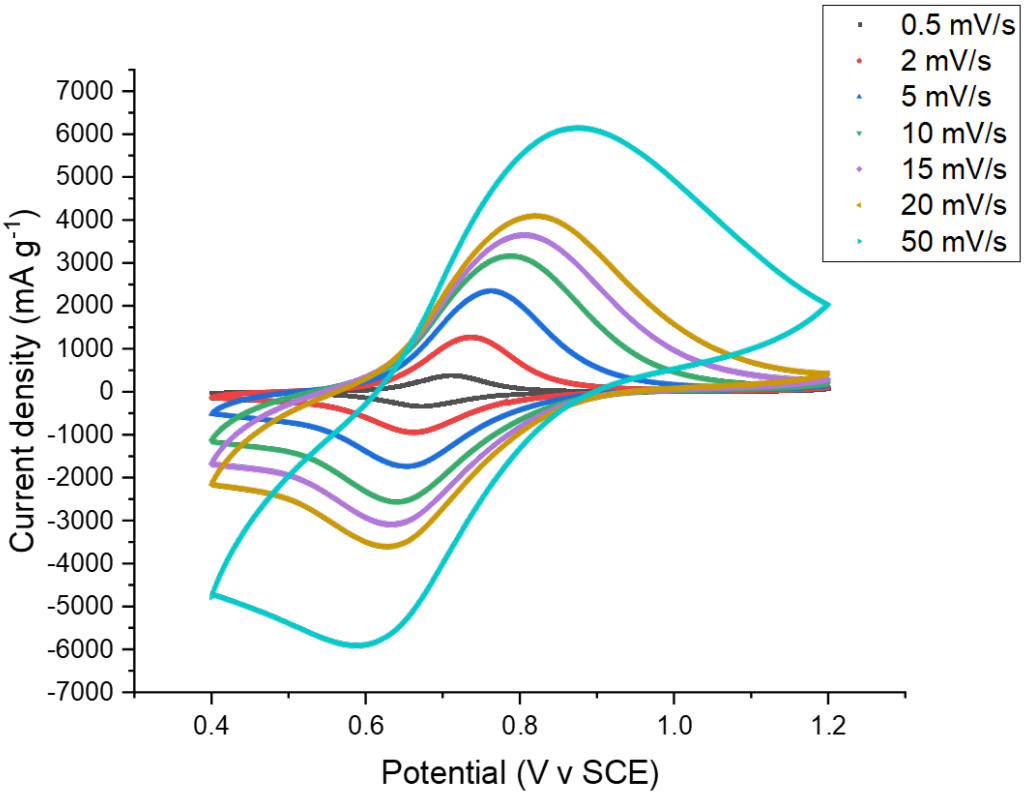

FIGURE 5.7: CV sweep of CuHCF electrode in 1 M $AlCl_3$ + 1 M KCl at 0.5 - 50 mV s^{-1}

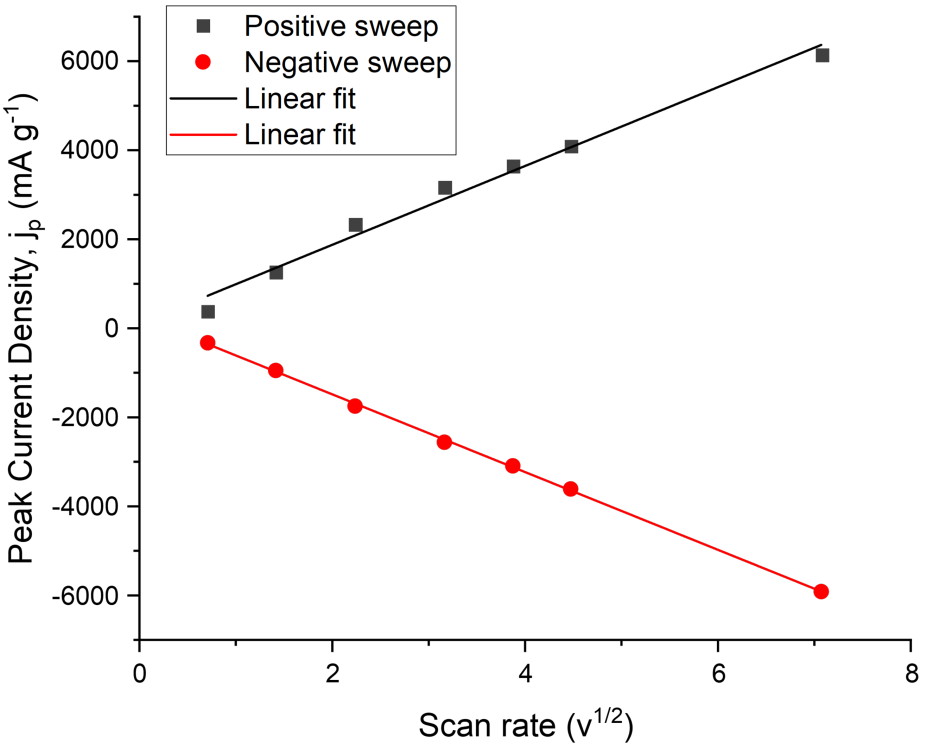

FIGURE 5.8: Peak current density vs the square root of the scan rate for the CuHCF baseline electrode

While there are many unknowns within this equation for the CuHCF electrode, by plotting the peak current density (j_p) against the square root of the scan rate (v) (Figure 5.8) we can see a linear relationship, which intercepts the y-axis at zero. This implies that there is a diffusion controlled, reversible redox reaction occurring. Using the Randles-Sevcik equation, the average mass of CuHCF on the electrodes (2.34 mg) we can calculate the diffusion coefficients for the 20 mV s^{-1} scan rate, as this scan rate was also chosen for the TiO_2 samples.

From our equation (Eq. 5.1), the number of electrons involved is an unknown (denoted as x in the equation) and so for simplicity we will assume only one electron is transferred as the Al ion is not involved in this reaction. This gives our diffusion coefficient at 1.52×10^{-9} m^2 s^{-1}. This value is the same for both oxidation and reduction, and is a higher value than that of the TiO_2. This makes sense as we know that some of the TiO_2 energy storage comes from capacitive charge transfer. Further, there is a lower concentration of CuHCF than TiO_2 (about a third lower) which impacts the diffusion as well. The value for the diffusion coeffient found matches well with values found for other small ions (such as K^+ and Cl^+) (76).

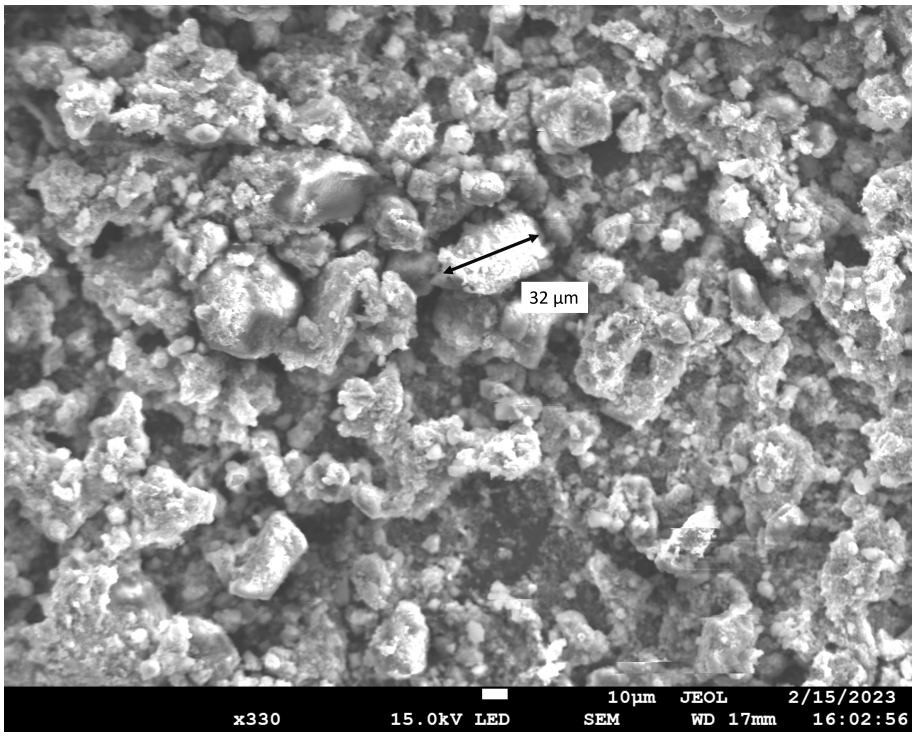

FIGURE 5.9: X330 magnification of CuHCF surface on carbon fluoropolymer substrate

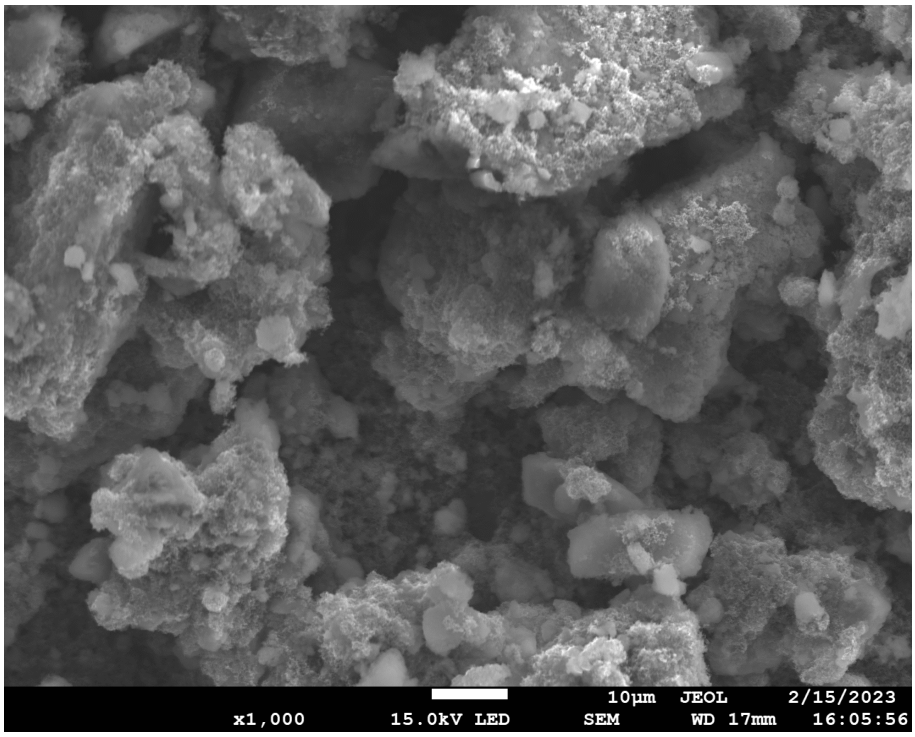

FIGURE 5.10: X1000 magnification of CuHCF surface on carbon fluoropolymer substrate

From SEM images of the surface of this electrode, the particles of CuHCF appear to have a 'fluffy' particle shape. It is hard to fully ascertain if these are separate particles

or one flowing mass with a textured surface. In Figure 5.9, a particle is picked out at 32 μm, however looking closer at X1000 magnification in Figure 5.10, it becomes harder to pick out individual particles, as the surface texture is rough and variable. Through PXRD the synthesised active material was confirmed as 100% CuHCF both as the pure active material and when within the electrode ink - shown in Figure 5.11.

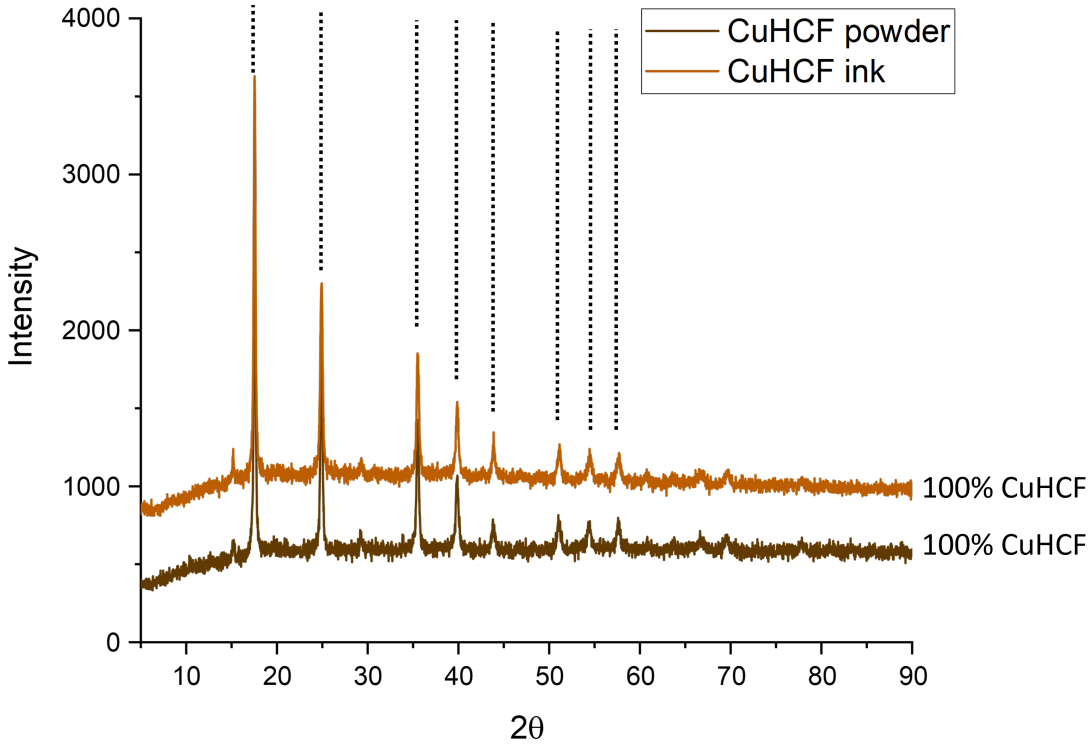

FIGURE 5.11: PXRD of CuHCF powder, as a pure powder and when mixed in an ink

5.3 Building a full cell in light of these findings

As stressed throughout Chapter 2, half cell experiments are a useful way to characterise and understand individual electrodes, but may not always translate into a working cell. Firstly, the cell would need to be balanced, ensuring that the right amount of active materials are present in the electrodes to allow for a full charge and discharge with no underutilised active material. With the goal of increasing the amount of utilised active material within a battery, the balancing needs to be right in order to prevent any waste. To do this, we must ensure that each electrode can accommodate (and give up) an equal number of Al ions in each charge cycle.

Our two average reaction potentials are 0.76 and -0.96 V v SCE. With the CuHCF cell having a capacity of 50 mAh g^1 and TiO_2 having a capacity of 14.5 mA h g^1 (18; 1), in

order to balance the cell we require a ratio of 2.44:1 TiO_2 :CuHCF. It is also useful to oversize the negative electrode to ensure that all material of the positive electrode is utilised.

From Chapter 4 we see the balanced values of active material for each electrode were 30.4 mg CuHCF and 76.5 mg TiO_2. That makes a ratio of 2.52:1 TiO_2:CuHCF. When looking at the current densities reached during the CV sweeps, the CuHCF densities were far higher (about 6 times) than that of the TiO_2 electrodes. This is reflected in the balancing seen above, however from these values it would be expected that 6 times more TiO_2 would be required to balance the full cell and reach the same total current on each electrode. This relationship however may not be so linear, since the active materials are ceramics, they have a high electrical resistance (for TiO_2 $10^{16}\Omega$ cm (191)). As thicker layers of active material build up there may be a reduction of electronic conductivity to the current collector. Therefore the ratio of 2.52:1, which has been proven in the literature (84; 18; 1) will be used when exploring the coin-cell design in the next section.

5.4 Cell design - Coin-cell development

Up to this point the Al-ion cell had been an open cell, the electrodes were separated by space filled with electrolyte as discussed in Chapter 1. As shown in Chapter 4 though, using this chemistry within a stainless steel coin-cell would reduce the overall environmental impacts if performance remains the same (in terms of discharge capacity and cycle life). The next section explores the practical implications of this design.

5.4.1 Separator material

Inside a coin-cell the electrodes would be compressed together and so a separator material is needed. Three separators were tested, to see which was the most compatible with the electrodes chosen. Cellulose filter paper, glass fibre filter paper, and a polymer separator paper were tested in coin-cells. Eleven cycles were performed at $\approx$ 833 mA g^{-1} based on the total active material, between 0.7 and 2.1 V. The high current density and voltage range used is similar to those in (18), and highlihhts the high power density of the battery. These three cells were constructed with electrodes, a layer of separator, and were then flooded with electrolyte, so that some overflowed as the cells were closed. These cells were not crimped fully, to allow any gas formed to escape through the seal, and allow for the separator material to be assessed in isolation of hydrogen formation.

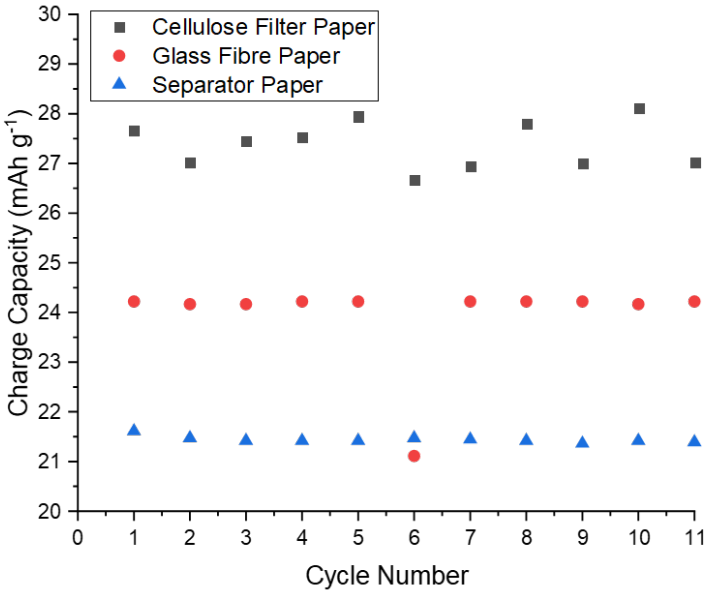

FIGURE 5.12: Charge capacity for three different separator materials over eleven cycles

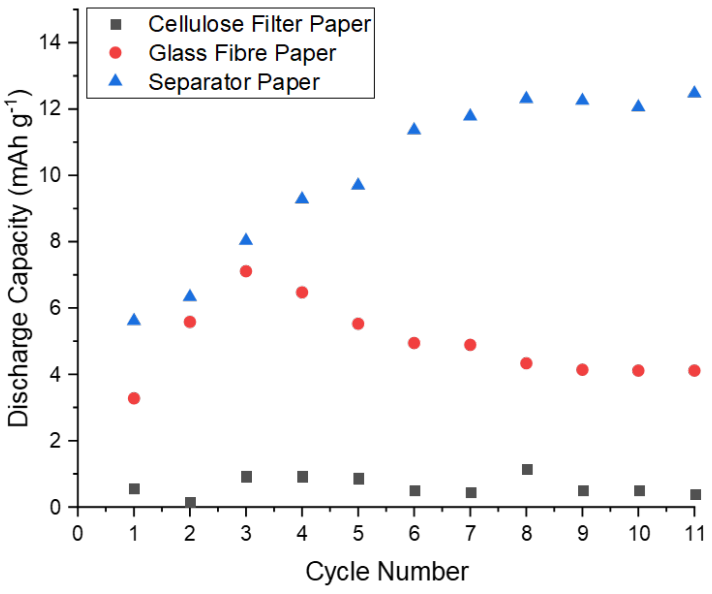

FIGURE 5.13: Discharge capacity for three different separator materials over eleven cycles

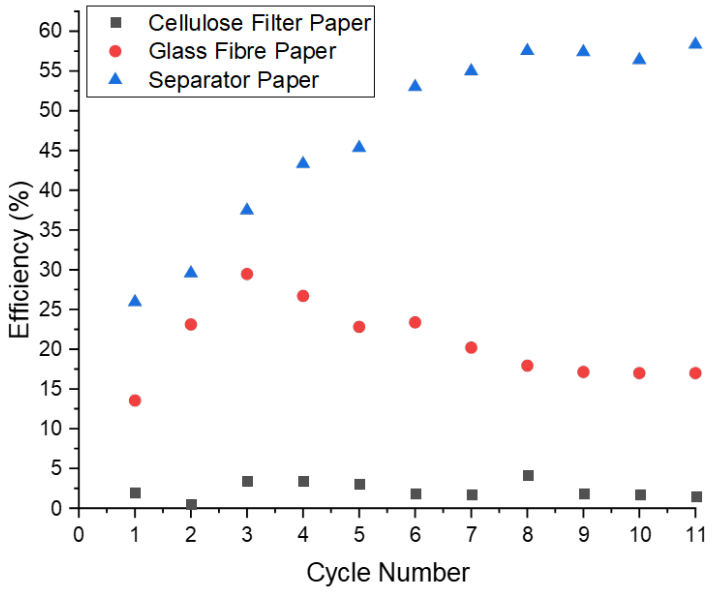

FIGURE 5.14: Efficiency for three different separator materials over eleven cycles

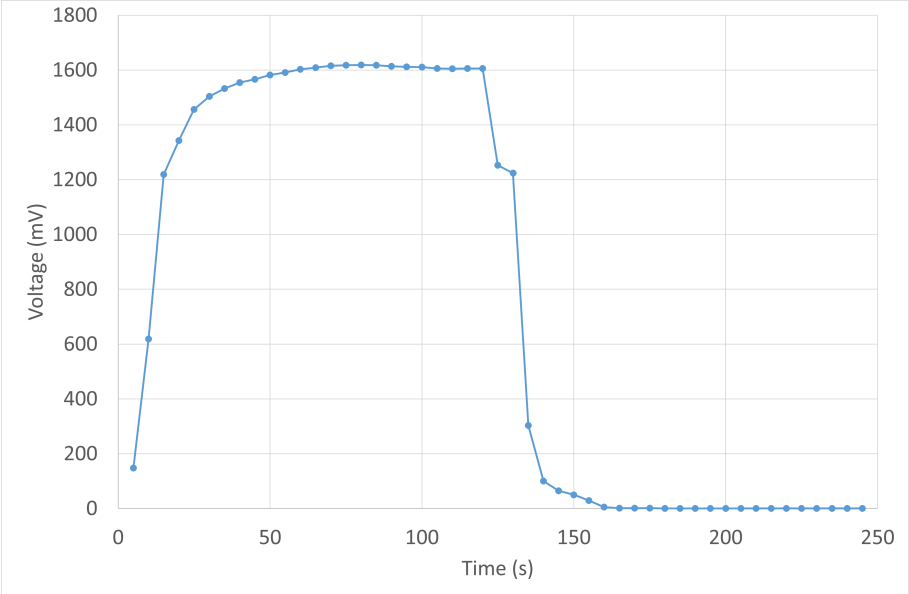

FIGURE 5.15: Separator Paper voltage profile for cycle 10

The charge capacity over these cycles are shown in Figure 5.12, where use of the Cellulose filter paper shows to have the highest capacity over the 11 cycles, although not consistent - as it varies between 26 - 28 mAh g^{-1}. For both the glass fibre and separator paper, the charge capacities are more consistent (charge 6 for the glass fibre is assumed an anomaly), with the glass fibre holding a charge of around 24 mAh g^{-1} and the separator paper of around 22 mAh g^{-1} over the cycles. When looking at the

discharge capacity (Figure 5.13) however, we see that the coin-cell with the cellulose paper drops to almost 0 mAh g^{-1} for all cycles. The glass fibre initially rises to 7.1 mAh g^{-1} at cycle 3, but then slowly declines to 4 mAh g^{-1} by cycle 11. The separator paper however slowly increases in discharge capacity and by cycle 11 seems to be settling at 12.5 mAh g^{-1} at 833 mA g^{-1} close to the reported 10 mAh g^{-1} at 333 mA g^{-1} for the open cell (1), but at a far higher current density. Figure 5.14 shows the overall efficiency of the three coin-cells. These follow a similar pattern to the discharge plots, with the cellulose paper close to 0%, the glass fibre settling at around 17% and the separator paper appearing to rise to 60% by the end of the eleventh cycle. While by no means an efficiency comparable to the near 100% reported in the literature (1), this result shows that for the coin-cell design, the separator paper provides the highest efficiency over the first 11 cycles, and so this design was taken forward for further cycling tests. The poor performance of the cellulose filter paper may be due to the material swelling or flaking when introduced to the aqueous electrolyte. The low efficiency could be due to the uncrimped nature of the cells, meaning the contact between the electrodes and separator is not ideal, and there is a higher resistive loss due to this.

Figure 5.15 shows the voltage profile of the separator paper coin-cell. The constant current discharge shows a small plateau of 5-10 seconds at 1.2 V before continuing the disharge curve. This matches the suspicion of a 2 stage discharge - potentially a combination of capacitive and redox reactions. The overall discharge took 40 seconds.

5.4.2 Carbon cement

To ensure continual contact between the coin-cell casing and the electrode material, the use of Leit-C carbon cement was considered as a means of increasing contact. Two cells were prepared, both using the separator paper, one with carbon cement used to fix the electrodes to the casing, and one without this. Both cells were then flooded with electrolyte, so that some overflowed as the cells were closed. Again, the cells were not fully crimped to allow for any gas formed to escape through the seal. Cells were cycled at 833 mA g^{-1}, between 0.7 and 2.1 V, continually until the discharge capacity reached half of that reported in (1) - 5 mAh g^{-1}. For the carbon cement containing cell, this was around 7050 cycles, see Figure 5.17. It should also be noted though, with this longer cycle life, there may have been additional performance degradation through electrolyte evaporation, since the cells were not crimped closed. Figure 5.16 compares discharge curves between the coin-cells with and without carbon cement. The starting voltage for both cells differs by 0.5 V - while they have both been charged with the same constant current this difference suggests that the contact resistance has reduced between the casing and the electrodes. Further, the plateau for the coin-cell with carbon cement is 0.2 V higher than that for the coin-cell

without. This again is an indication that the IR drop is reduced when using the carbon cement. Lastly, we can see the gradient of the discharge curve is less steep gradient than the coin-cell without carbon cement. With carbon-cement we may interprest some capacitive discharge given the linear section of 15 seconds of the discharge before it begins to turn. This is not clear for the coin-cell with carbon cement.

While the carbon cement coin-cell had the end of discharge limit at 0.5 V, from the shapes of these discharge curves we can conclude that using carbon cement reduces the contact resistance and will be used for future coin-cells.

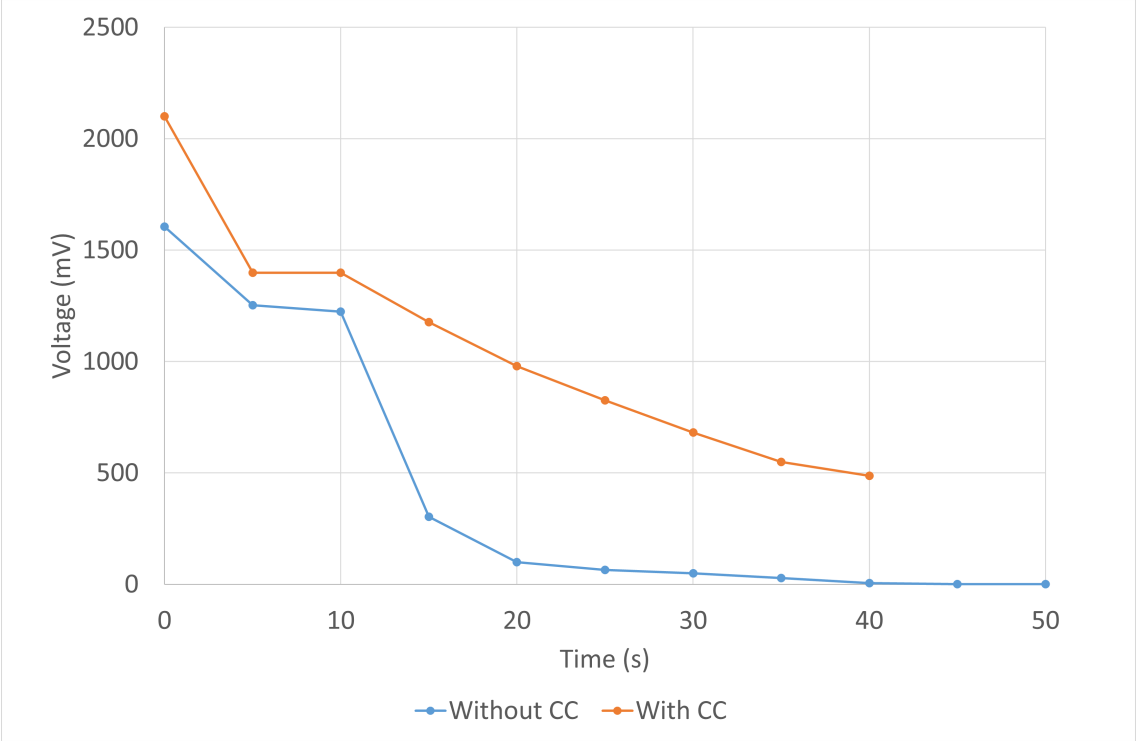

FIGURE 5.16: Discharge curves for with and without carbon cement 833 mA g^{-1} discharge

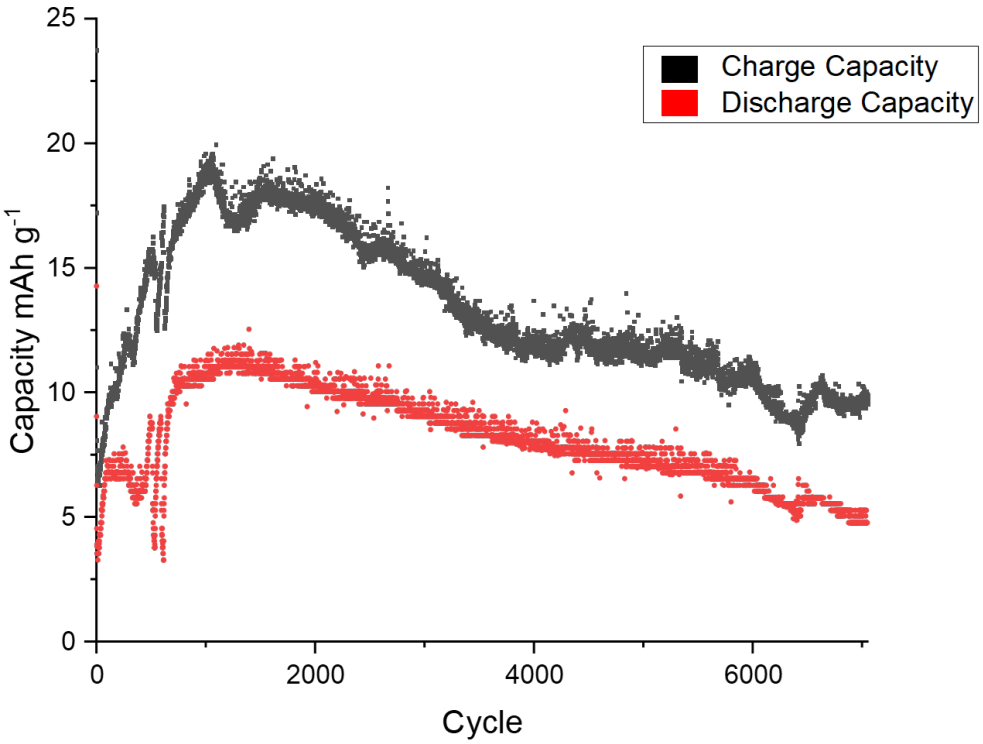

FIGURE 5.17: Charge and discharge capacity for the first 7050 cycles at 833 mA g^{-1} for cell with carbon cement

Based on these results, using carbon cement appears to increase the contact between the electrode and current collector (casing), which in turn has increased the cycle life reported for the cell. The conductive carbon cement has lowered the contact resistance between the electrode and the surface of the coin cell by ensuring they are adhered through - ensuring contact between these surfaces in an uncimped cell. The functional energy density (FED) of this coin-cell is 63.4 kWh (given the voltage range of 1.4 V). This is 2.4 times more than the lab based initial design. We create a new competitive functional energy density, CFED, for our coin-cell to be environmentally competitive on climate change with the average Li-ion values from Chapter 4. In the following equation, value for the Al-ion impact value is that found for the coin cell in 4, and not that of the initially analysed cell. We find from Eq. 4.2

$$\text{'Competitive' Functional Energy Density} = \left(\frac{\text{Al-ion kg per functional kWh} \times \text{Li-ion impact value}}{\text{Al-ion impact value}}\right)^{-1} \tag{5.2}$$

$$\text{'Competitive' Functional Energy Density} = \left(\frac{0.038 \times 0.645}{0.799}\right)^{-1} \tag{5.3}$$

$$\text{'Competitive' Functional Energy Density} = 32.6\text{kWh kg}^{-1} \tag{5.4}$$

By redrawing our parameter space, this coin-cell is in the competitive space. This is where lifetime performance provides reduced climate change impacts compared to Li-ion - see Figure 5.18.

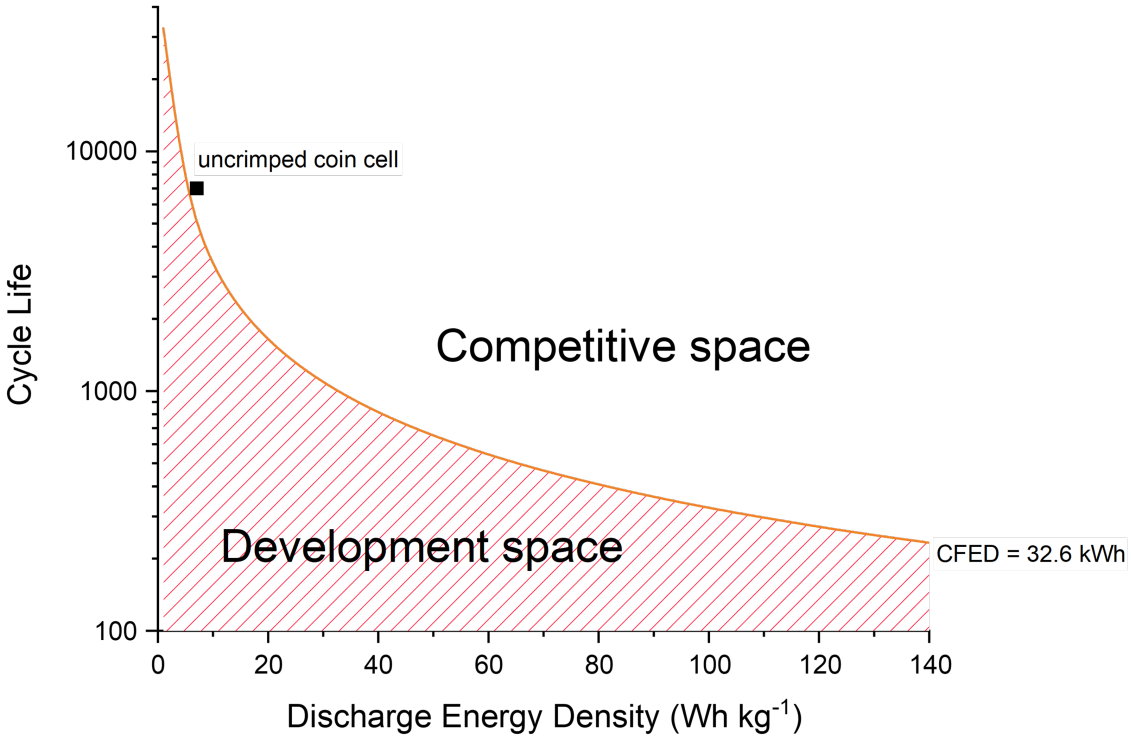

FIGURE 5.18: Competitive parameter space representing the functional energy density required to match Li-ion in CO_2 emissions for the uncrimped coin-cell, the line represents the 32.6 kWh CFED, with the space below being the development space, and the space above, where the design is environmentally competitive

5.4.3 Closed cells

Once the cells were crimped closed, the cycling regime described above (0.7 -2.1 V at $\approx$ 833 mA g^{-1}) was performed. However it was clear from initial cycles that the capacity was not reaching that measured of the uncrimped cell. Further, the cell itself bloated and burst open during cycling at this regime - suggesting gas build up during cycling. Figures 5.20 and 5.21 shows the pristine coin-cell, and after it had burst in operation. This is unacceptable behaviour for the cell. In order to reduce the formation of gas within the coin-cell, the voltage range was reduced, and cells were cycled at different voltage limits to observe the capacity changes.

Using fully crimped cells, any gas formed during cycling would remain as bubbles within the cells. Evidence of gas formation may appear both through observations of a sealed (crimped) cell, and of its cycling performance. Physically the cell may bloat slightly, or bubbles of electrolyte may be present around the crimped seal. In terms of performance, increased gas within the cell may bubble on electrode surfaces, reducing overall surface area of active material available, reducing the cell's capacity, the capacity fade may therefore occur quicker than in an open cell, as the gas bubble increases with each cycle.

FIGURE 5.19: Pristine and bloated coin-cell diagram

FIGURE 5.20: Pristine cell

FIGURE 5.21: Burst cell

Ultimately, a coin-cell is therefore not the optimum design if we want to work at the widest available voltage range - an open cell or cell with a valve to allow for gas release would be the best choice. However, to understand how the cell changes and degrades over its lifetime, using in-situ measurements at DLS (Diamond light source), a closed cell is required to allow such measurements to be taken. Thus, although the optimum performance of the cell may not be realised in a closed coin-cell, it is still important to finalise the design and safe cycling regime in order to perform long duration XRD analysis - see Chapter 7.

Cells were cycled between the following ranges to understand the cut-off for the upper limit in which gas formation was minimal, while still allowing for capacity storage.

- 0.8- 2.1 V
- 0.8-1.7 V
- 0.8-1.5 V

using a constant voltage charge to ensure that the voltage did not overshoot the upper limit set. The discharge current was 250 mA g^{-1}, again to ensure a slower discharge and less chance of overshooting the voltage limit. Measurements of coin-cells were taken before and after 1000 cycles were performed, to measure the bloating. The results are presented in Table 5.2. Values of the centre (C) and edge (E) of the cell were taken, as shown in Figure 5.19. Cells cycled to 2.1 V and 1.7 V showed an increase in the C and E measurements and appeared bloated (increase of 0.93 mm for 2.1 V and 0.64 mm for the 1.7 V cell at the centre). The cells cycled to 1.5 V did not appear to have bloated after 1000 cycles, with measurements varying by 0.01 mm from the original measurements. Therefore the choice to cycle between 0.8 - 1.5 V for the LDE was made, as this will allow the cells to cycle continually and will eliminate the gas as a degradation mechanism within the cell. Final coin-cell construction methodology is shown in Chapter 3.

TABLE 5.2: Coin-cell voltage range and bloat measurements

Voltage range [V]	**Initial C [mm]**	**Initial E [mm]**	**Final C [mm]**	**Final E [mm]**
0.8-2.1	3.12	3.10	4.05	4.02
0.8 -1.7	3.11	3.10	3.75	3.53
0.8-1.5	3.09	3.10	3.10	3.11

5.5 Conclusion

The electrochemistry for the aq. Al-ion cell was validated through CV sweeps of the individual electrodes, which showed peaks which matched with the reported data described in Chapter 2. Further, through using a coin-cell, an appropriate separator paper was identified, and a cell was cycled with 7050 cycles above 7 Wh discharge energy. By looking back at Chapter 4, the resulting 63.4 kWh FED shows environmental improvements through this change of support material and casing, and pushes the design into the competitive space in terms of CO_2 emissions. The use of a closed, crimped coin-cell highlighted the issue of gas formation, which needs investigating and mitigating in order to continue with a closed cell design. Alternatively, a vented cell similar to the Pb-acid design, could be used to enable a higher working voltage range to be met. This of course would need to be undertaken alongside a new LCA to fully understand the impacts of this casing design.

Chapter 6

Investigating carbon felt electrodes and active material utilisation

6.1 Motivation

Increasing the utilisation of the active material within the electrodes will increase the overall capacity and energy storage of the cell. This in turn reduces the proportion of inactive material, which then reduces the environmental footprint of the design, as discussed in Chapter 4. The use of porous substrates (here, carbon felt) was therefore chosen to assess the following research questions

- how the use of carbon felt impacts the performance of the cell
- how evenly this ink dispersed within the bulk of the felt, and
- whether compression of the felt can be utilised to further increase diffusivity and performance

6.1.1 Expected results

Based on the understanding from the LCA work in Chapter4 it is expected that the overall capacity of individual electrodes will be increased due to the higher loading of active material on the porous substrate. The increased surface area provided by the carbon felt will allow more of the active material to be in contact with the electrolyte - while the carbon fibres provide a conductive link to the current collector.

6.2 Methods of increasing material utilisation

There are many ways to increase the utilisation of active materials in electrodes. For example, using smaller particles, such as nano-particles will increase the available surface area of the active material and can therefore increase overall utilisation. This was shown in (2) where 5 nm TiO_2 was compared to 25 nmn particles within the aq. Al-ion system. Although this is a viable option for TiO_2, the cost of manufacturing these particles is high compared to the larger alternatives - both financially and environmentally - with the understanding of nano-particles still not fully quantifiable by LCA methods (see Chapter 4). Further, this solution works only where nano-powders are available. For the CuHCF, as this is made in the lab - there is no guarantee that nano-particules are made (see Chapter 5 for SEM images of the powders).

Increasing the surface area of active material available to the electrolyte can be done in more sustainable ways. Using an electrode substrate with a rougher texture will increase the overall coated area. In addition, a 3D matrix which can be impregnated with active material will further increase the available surface area both on top and within the electrode itself. Textiles have been explored for such a substrate, both for the wearable applications of batteries, and also for the ability for each strand within the textile to be coated with the active material (192).

Therefore a carbon felt material has been chosen as a means of increasing the overall surface area of active material in contact with the electrolyte. Using carbon felt as a substrate provides the conductive pathways between the fibres. Polyacrylonitrile (PAN)-based carbon felt was purchased from SGL, Germany. Table 6.1 summarises key information on the felt, taken from the data sheet (29). This particular felt, GFD 2.5, was chosen due to its low resistance and high porosity - as well as the ease of procurement.

TABLE 6.1: Summary of procured carbon felts from SGL carbon, values taken from datasheet (29)

Property	**GFD 2.5**
Bulk Density	0.09 g cm^{-2}
Nominal Thickness	2.5 mm
BET Surface area	0.4 m^2 g^{-1}
Through Resistance	$< 5\ \Omega$ mm
% Open Pores	94%
Virgin	Y

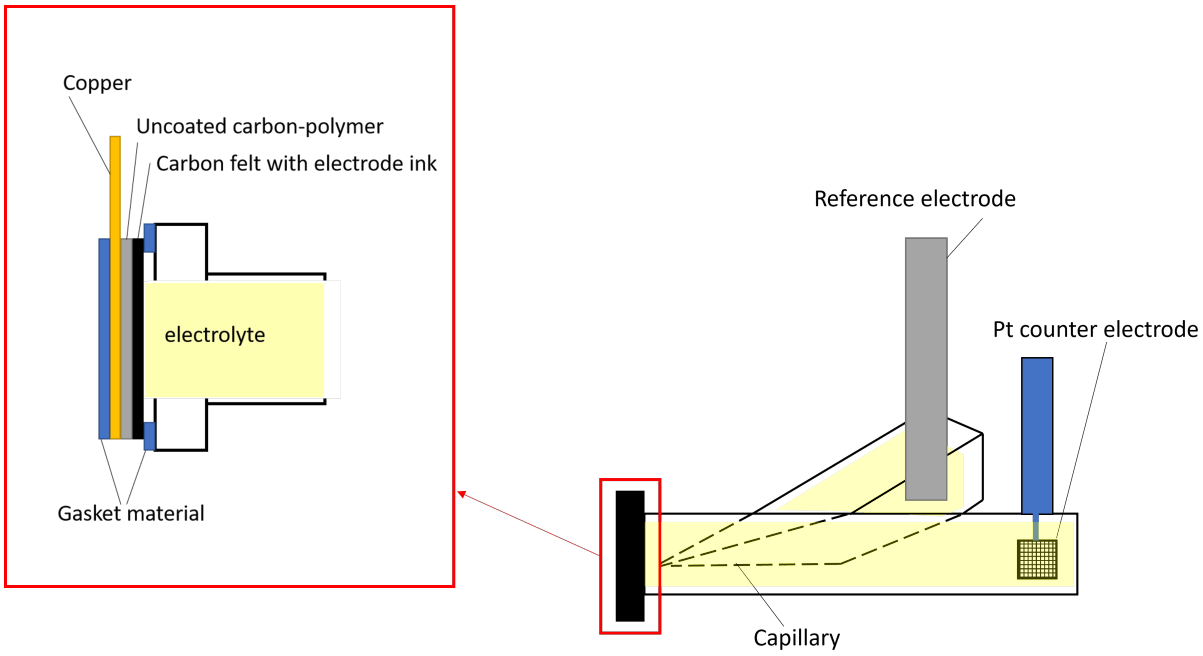

FIGURE 6.1: Diagram of three cell electrode with carbon felt substrate

6.3 Electrochemical performance of the carbon felt electrodes

The electrodes were prepared as described in Chapter 3 and set up in a three-electrode cell with a Pt counter electrode and SCE reference electrode. Initial CV sweeps were taken to confirm the electrochemical activity matched those found in Chapter 5, followed by galvanostatic charge discharge (GCD) measurements for a variety of active material densities and current densities. A sample of active material densities were then chosen (low, mid and highest performing) to characterise at a range of temperatures and compression.

6.3.1 Electrochemical measurements of the positive carbon felt electrode - CuHCF

The CV for the 2.5 mg cm^{-2} shows peaks that are shifted and slightly broader compared those found in Chapter 5 Figure 5.7 for the positive electrode. For the 50 mV s^{-1} sweep shown in Figure 6.2, the negative peak is at 0.3 V, and the positive peak at 1.05 V v SCE (compared to 0.62 V v SCE and 0.92 V v SCE respectively). This may be due to the 3D nature of the carbon felt, creating a small range of potentials within the thickness of the electrodes as they are at different distances and have different routes to where the voltage is applied at the back surface - and so the 'real' potential experienced by the electrode may not be the instantaneous one being applied. With the initial 2D electrodes, this was not of consideration.

6.3.1.1 Initial assessment of active material densities

The Galvanostatic charge-discharge (GCD) measurements were taken three times at each current density for each electrode sample, the results of which are plotted in Figure 6.3. The initial observation from these measurements is that the lower the density of active material, the higher the discharge capacity - which initially seems counter-intuitive. The peak capacity for the 2.5 mg cm^{-2} is 287.3 mAh g^{-1}, whereas for the 29.9 mg cm^{-2} is 18.2 mAh g^{-1}. This would suggest that for the higher concentrations of active material, much of it is not utilised. For the lower concentrations, there would be a thinner layer of active material on the carbon felt fibres, which implies that it may be a primarily surface reaction taking place. Another reason for this might be that the charge transfer resistance is lower for thinner layers of CuHCF (193), and so having thicker layers would in fact hamper the conductance through the whole electrode - with these thin layers over the felt fibres, this would be improved. Figure 6.11b shows the thick layers of CuHCF between the carbon fibres for the high loading sample. Further, when comparing these results to previous work using a flat, carbon fluoropolymer electrode substrate, the maximum discharge

capacity recorded is nearly ten times higher (36 mAh g^{-1} @ 1000 mA g^{-1} (102) compared to 259 mA h g^{-1}@ 1256.8 mA g^{-1} for the 2.5 mg cm^{-2} sample at a similar current density discharge). The various GCD results for the 2.5 mg cm^{-2} sample are shown in Table 6.2.

After testing an electrode through 30 discharges, it was noted that the electrolyte had a yellow hue - this corresponded to (102), finding that Fe^{3+} was present in the used electrolyte. This matches with the proposed reaction involving Fe^{3+}/Fe^{2+} redox pairs and suggests that one of the reactions occurring may be irreversible and therefore leaves Fe^{3+} in the electrolyte over time, potentially degrading the electrode and limiting its useful lifetime.

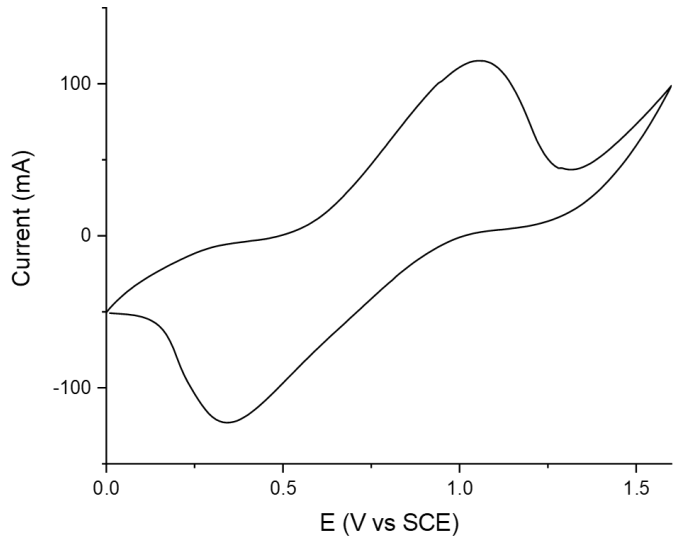

FIGURE 6.2: Cyclic voltammogram for CuHCF carbon felt electrode at 2.5 mg cm^{-2} in 1 M $AlCl_3$ + 1 M KCl, 50 mV s^{-1}

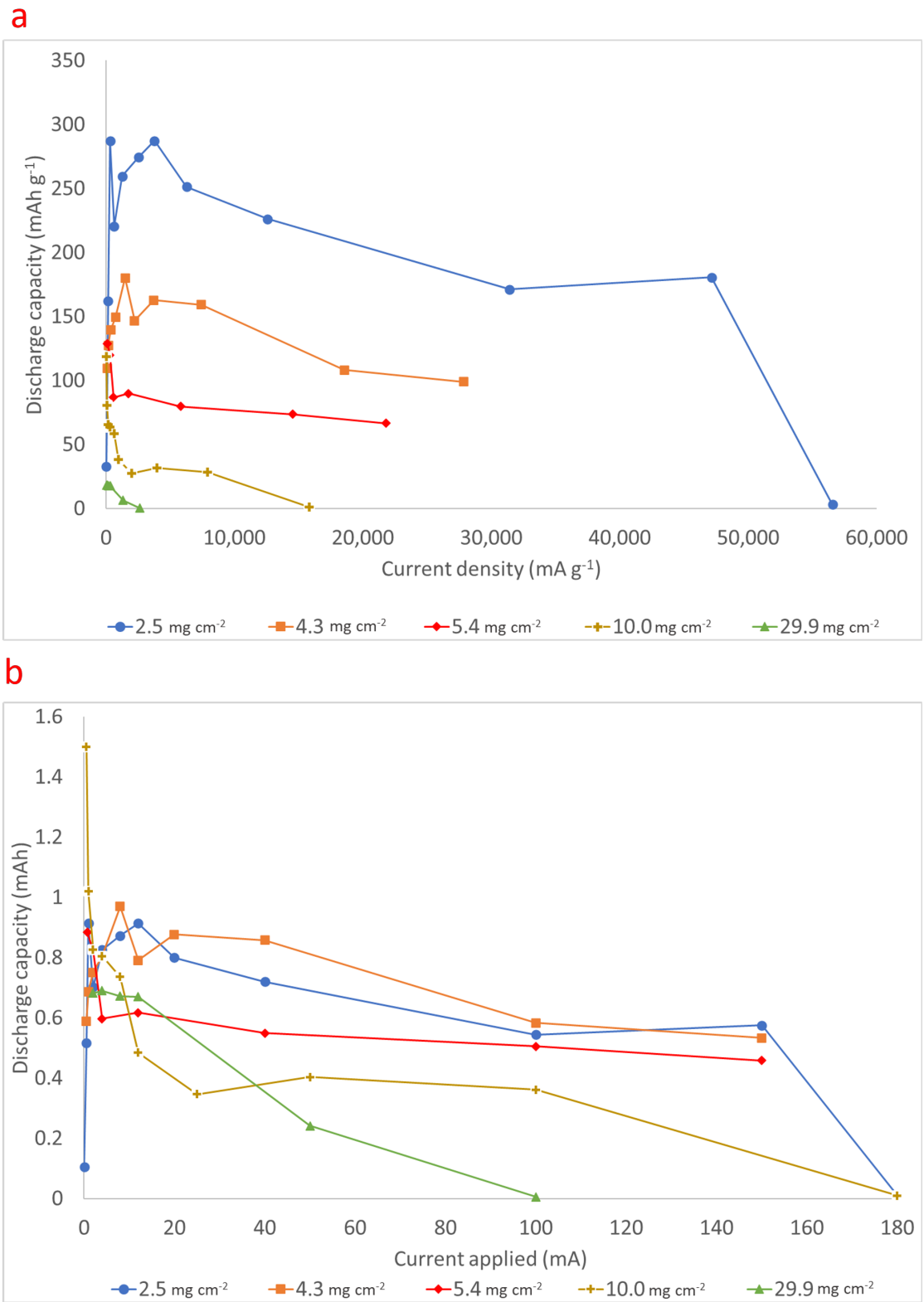

FIGURE 6.3: Discharge capacities at a variety of current densities (a) and for the actual current applied (b) for the carbon felt electrode with varying values of active material (from 2.5 - 29.9 mg cm^{-2}) for CuHCF electrode in 1 M $AlCl_3$ + 1 M KCl

TABLE 6.2: Summary of discharge capacities (average) for varying current density discharges for the CuHCF carbon felt electrode with 2.5 mg cm^{-2} density of active material

Current density [mA g^{-1}][a]	**Discharge capacity [mAh g^{-1}]**[a]
15.7	33.0
157.1	162.0
314.2	287.3
628.4	220.5
1,256.8	259.5
2,513.5	274.4
3,770.3	287.2
6,283.8	251.4
12,567.6	226.2
31,419.0	171.1
47,128.5	180.7

[a] based on the pre-soaked measured CuCHF mass

6.3.2 Electrochemical measurements of the negative carbon felt electrode - TiO_2

The CV for the 30.1 mg cm^{-2} shows broader peaks compared to those found in Chapter 5 for the negative electrode. For the 50 mV s^{-1} sweep shown in Figure 6.5, the negative peak is at -1.2 V v SCE, and the positive peak at -0.93 V v SCE, which is comparable to those in in Figure 5.2.

6.3.2.1 Initial assessment of active material densities

The GCD measurements were taken three times at each current density for each electrode sample, the results of which are plotted in Figure 6.5. Much like the CuHCF samples discussed above, the lower the density of active material the higher the discharge capacity. The peak capacity for the 1.81 mg cm^{-2} is 205.0 mAh g^{-1}, whereas for the 30.1 mg cm^{-2} is 6.1 mAh g^{-1}. Table 6.3 shows the results for the 1.81 mg cm^{-2} active material density sample. Again, as with the CuHCF electrodes, this suggests that for the higher concentrations of active material, much of it is not utilised. Looking at the scanning electron microscope (SEM) images for the high concentration of active material (Figure 6.11a) much of the active material is in contact with itself but not in contact with the carbon fibres. Given the active material itself is not very electrically conductive (electrical resistivity around $10^{16}\Omega$ cm (191) compared to $< 0.005\Omega$ cm of the carbon fibres (29)) these thicker layers would in fact hamper the conductance through the whole electrode - with thin layers over the felt fibres, this would be improved - see Figure 6.12. While there is carbon black in the electrode ink which aids in conduction - the thin layers and carbon fibres are clearly boosting this further.

Further, when comparing these results to previous work using a flat, carbon fluoropolymer electrode substrate, the maximum discharge capacity seen is about four times higher (15 mAh g^{-1} @ 4,000 mA g^{-1} (84) compared to 61.10 mA h g^{-1}@ 4,700 mA g^{-1} for the 2.77 mg cm^{-2} sample at a similar current density discharge).

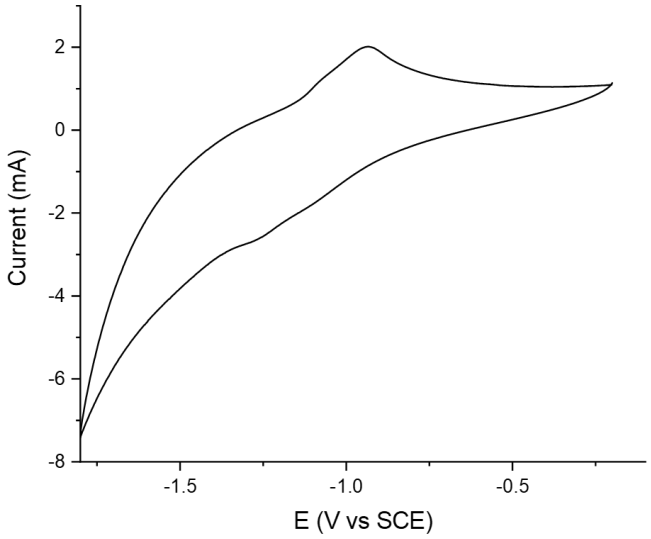

FIGURE 6.4: Cyclic voltammogram for TiO_2 carbon felt electrode at 30.1 mg cm^{-2} in 1 M $AlCl_3$ + 1 M KCl, 50 mV s^{-1}

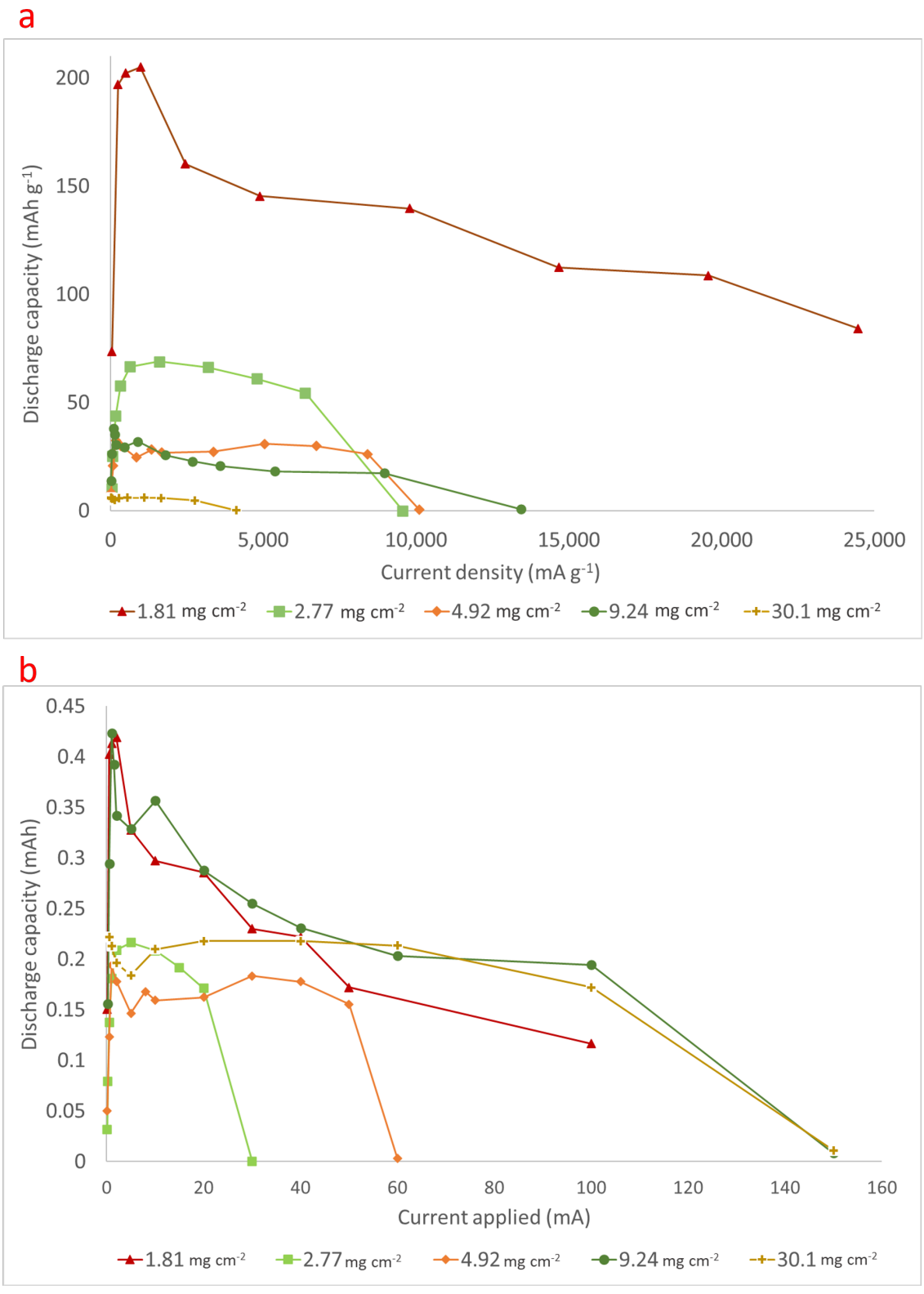

FIGURE 6.5: Discharge capacities at a variety of current densities(a) and as the absolute current applied (b) for the carbon felt electrode with varying values of active material (from 1.81 - 30.1 mg cm^{-2}) for TiO_2 electrode in 1 M $AlCl_3$ + 1 M KCl

TABLE 6.3: Summary of discharge capacities (average) for varying current density discharges for the TiO_2 carbon felt electrode with 1.81 mg cm^{-2} density of active material

Current density [mA g^{-1}][a]	**Discharge capacity [mAh g^{-1}]**[a]
48.9	73.7
244.5	196.9
489.0	202.2
978.1	205.0
2,445.2	160.3
4,890.5	145.4
9,780.9	139.6
14,671.4	112.5
19,561.8	108.7
24,452.3	84.2
48,904.5	57.1

[a] based on the pre-soaked measured TiO_2 mass

6.3.3 Further characterisation of the TiO_2 carbon felt electrode

To optimise the performance of the electrodes, new electrodes were manufactured with the goal loading of 1.81 mg cm^{-2}. Due to the nature of manufacturing, a range of loadings between 1.63 and 3.2 mg cm^{-2} were produced. The 3.2 mg cm^{-2} was chosen to undergo further characterisation tests. These included CV sweeps and discharge capacity measurements at further temperatures (20, 25, 30, 35, 40, 45 and 50°C). The CV sweeps were performed at 50 mV s^{-1}, and discharge capacity measured at 1 A g^{-1}.

The initial 100 cycles were performed at 20°C to allow for full wetting of the electrode, and to check the discharge capacity was in line with what was reported above. Cyclic

voltammetry was taken of the pristine electrode, and after 100 cycles as shown in Figure 6.6. The pristine CV shows the expected reactions at -0.9 and -1.32, which are also seen (although less prominently and with a wider range) in the 100 cycle CV. However there is also another reaction with peaks at 0.52 and 0.63 present in the pristine reaction, which disappears after the 100 cycles. This extra reaction is likely a reason for the initial increased discharge capacity seen, before the stabilised phase. The CV after 100 cycles is smoother, which as discussed above is more expected for the 3D electrode. There is likely a small range of potentials within the thickness of the electrode, and so the 'real' potential experienced by the electrode may not be the instantaneous one being applied.

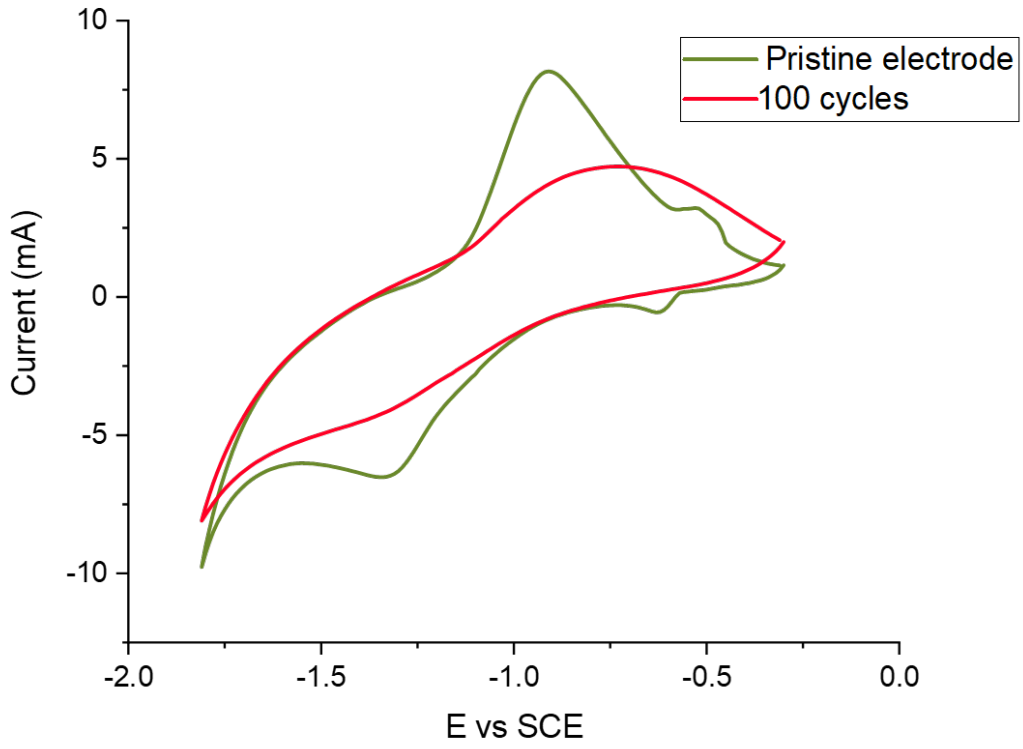

FIGURE 6.6: Pristine and 100 cycle CV for TiO_2 carbon felt electrode in 1 M $AlCl_3$ + 1 M KCl at 50 mV s^{-1} with a TiO_2 loading of 3.2 mg cm^{-2}

After the initial 100 cycles at 20°C, 20 cycles were performed at each temperature after the temperature had stabilised as discussed in Chapter 3. Figure 6.7 shows the discharge capacity, efficiency and temperature for this test. There is a clear jump in capacity from 44.8 mAh g^{-1} at 20°C to the stabilised discharge capacity at 25°C to 59.6 mAh g^{-1}. This capacity remains stable up to 40°C, where it jumps to 64.2 mAh g^{-1}. At 50°C the capacity appears to drop slightly back to 62.9 mAh g^{-1}. This drop may be due to the adhesive used to secure the three-electrode cell losing some of its

effectiveness at this high temperature. To complete the test, the cell was discharged at 20°C again, expecting results to match the initial 44.8 mAh g^{-1} discharge capacity. While it did drop to 52.7 mAh g^{-1}, the capacity remained high. Potentially the initial increase in temperature to 25°C helped increase the wetting of the electrode, and once the capacity increased, it was maintained.

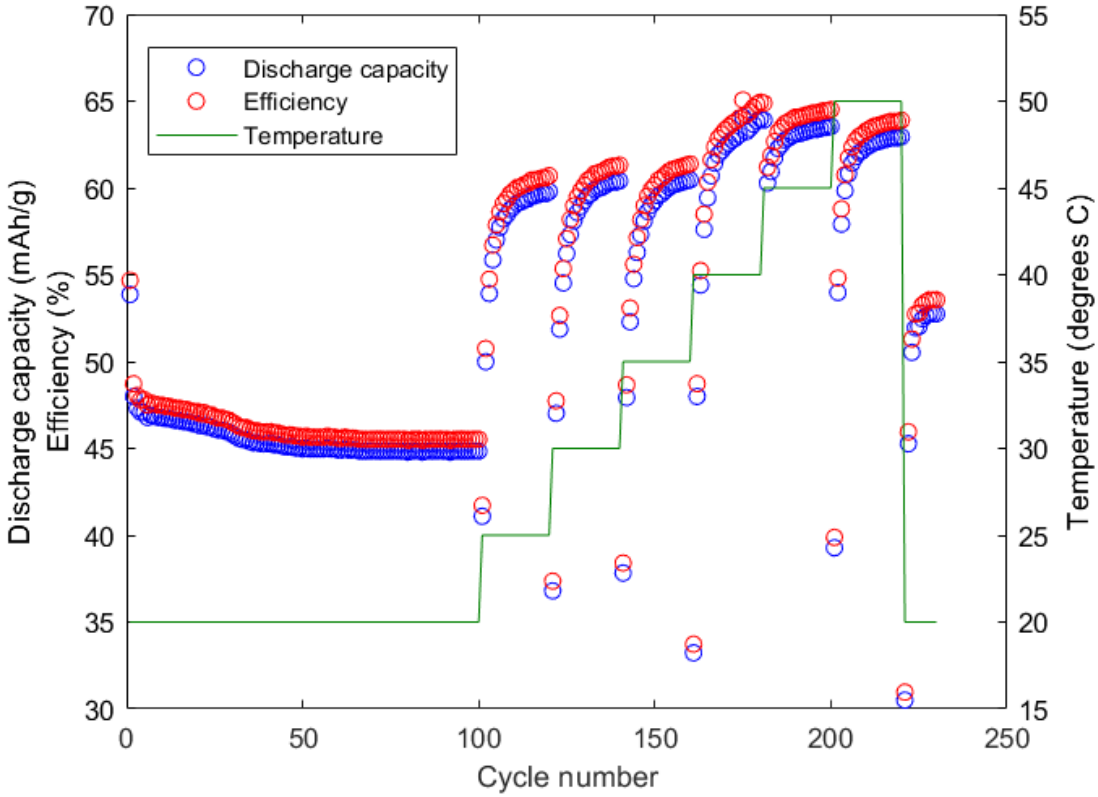

FIGURE 6.7: Discharge capacity and efficiency for TiO_2 carbon felt electrode in 1 M $AlCl_3$ + 1 M KCl at 1 A g^{-1} with a TiO_2 loading of 3.2 mg cm^{-2} at temperatures 20-50°C

6.4 Where the carbon felt fits in terms of environmental impact - assessing the parameter space

This is promising for the future development of carbon felts as an electrode substrate for this cell. In terms of the environmental impact, with this increased discharge capacity, it is likely that the functional energy density (FED) of a carbon felt based aq. Al-ion battery would be increased. The parameter space for the carbon felt cell (with the same support material as the lab based initial design) with respect to climate change is, from Eq. 4.2

$$\text{'Competitive' Functional Energy Density} = \left(\frac{\text{Al-ion kg per functional kWh} \times \text{Li-ion impact value}}{\text{Al-ion impact value}}\right)^{-1} \tag{6.1}$$

$$\text{'Competitive' Functional Energy Density} = \left(\frac{0.038 \times 0.645}{0.11}\right)^{-1} \tag{6.2}$$

$$\text{'Competitive' Functional Energy Density} = 4.49\text{kWh kg}^{-1} \tag{6.3}$$

If we redraw our parameter space for this value and estimate an achievable discharge capacity, we can create a target lifetime for the carbon felt cell. Based on the maximum seen discharge capacity from both electrodes, we assusme 200 mAh g^{-1} capacity, for a 1.4 V discharge range that would provide a discharge capacity of 280 Wh kg^{-1}. Taking our value for climate change impact from Chapter 4, for the assessment of a carbon felt based battery, we can now redraw the parameter space. From Figure 6.8, we would only need our carbon felt cell to perform 16 cycles to compete with Li-ion on climate change impacts. This estimate however is full of a key untested assumption - that the carbon felt cell will work as a system. However, if the cell can be optimised using a carbon felt substrate, the environmental impacts will be greatly reduced.

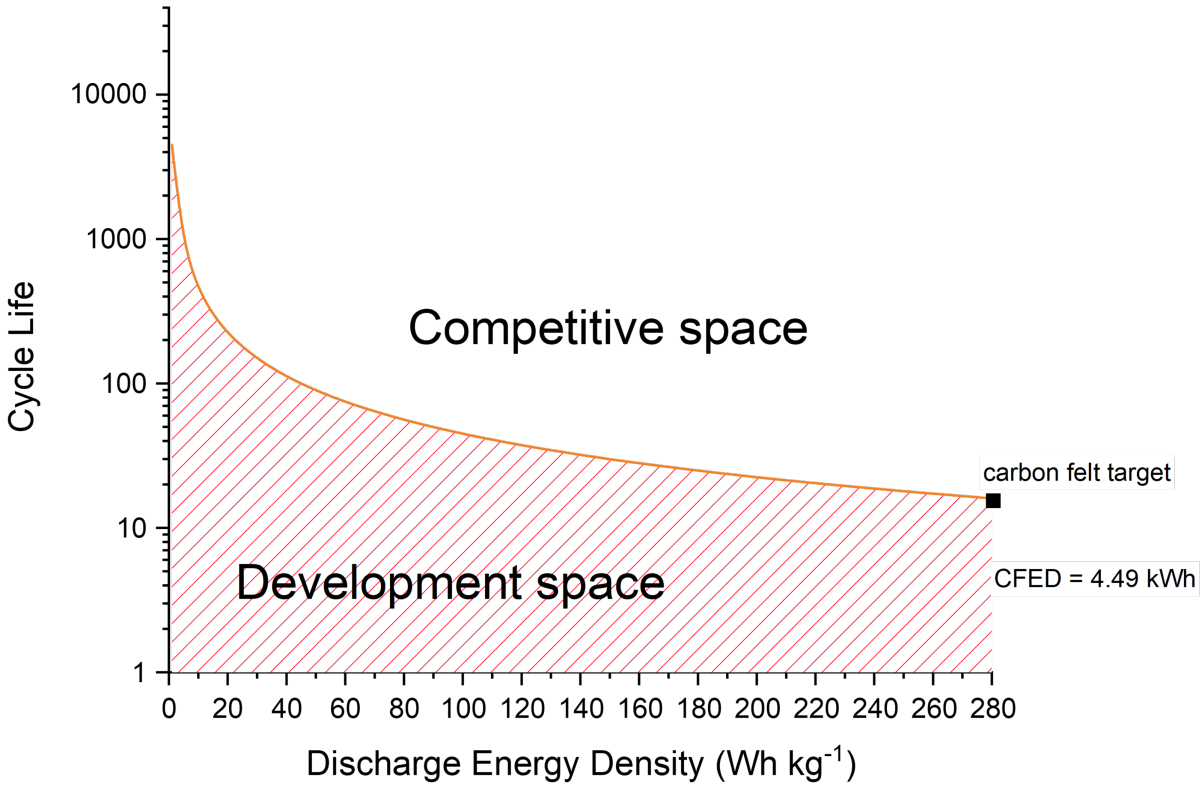

FIGURE 6.8: Competitive parameter space representing the functional energy density required to match Li-ion in CO_2 emissions for the carbon felt, lab-based cell, the line represents the 4.49 kWh CFED, with the space below being the development space, and the space above, where the design is environmentally competitive

6.5 Imaging the carbon felt

6.5.1 Scanning Electron Microscope ink dispersal measurements within the carbon felt electrodes.

A SEM (Scanning Electrode Microscope) was used to probe both the surface and internal deposition. The samples imaged for Figures 6.10, 6.12, 6.11 and 6.13 were not cycled after imaging due to contamination introduced in the imaging processs. The samples were mounted to a fitting using conductive tape (see Figure 6.9) and loaded into the SEM. Initial images of the virgin felt were taken to provide a baseline from which to compare the other samples. Figure 6.10a shows a $\times 25$ magnification, the individual carbon fibres are clearly visible and tangled, with anisotropic distribution. There are many pores visible within the sample. Figure 6.10b shows a close up image of one fibre at $\times 7000$ magnification, four fibres were investigated at this magnification

and the image appears representative. The fibre has clear grooves along its length, with some unknown particles (assumed dust or contamination) flecked on it.

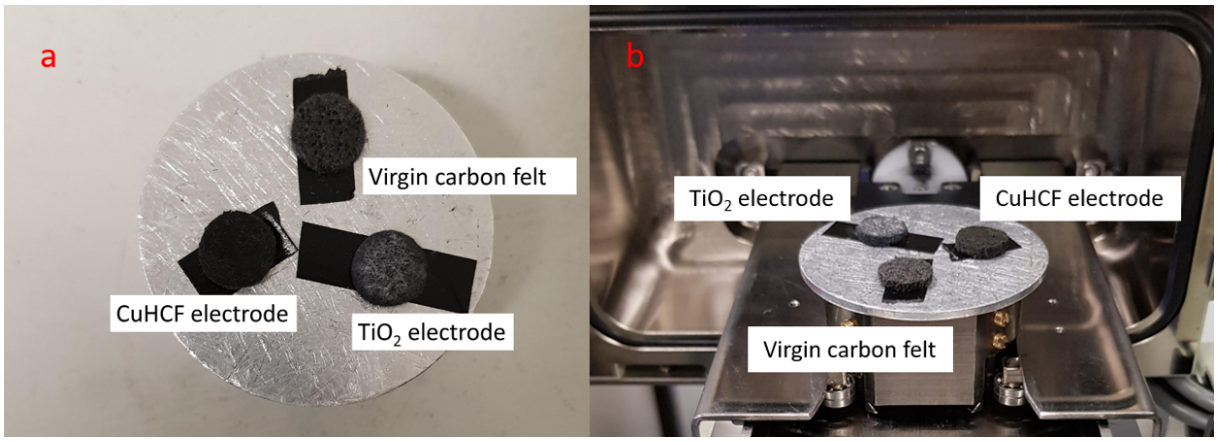

FIGURE 6.9: Carbon felt samples a) mounted and b) fitted in the SEM

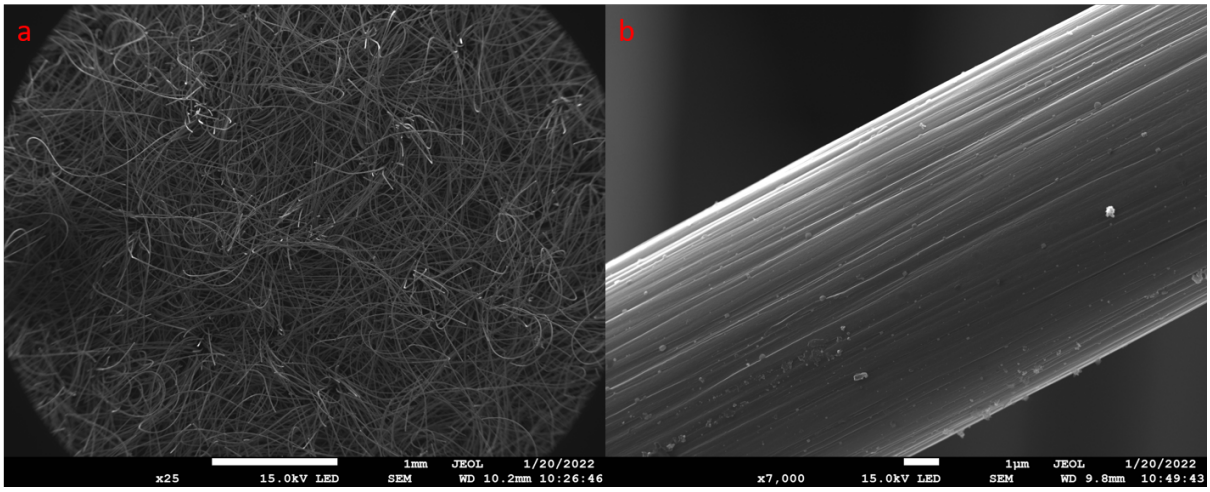

FIGURE 6.10: SEM image of virgin carbon felt a) $\times$25 and b) $\times$7000 magnification

The two electrode samples were compared at a magnification of $\times$250, shown in Figure 6.11. There is an obvious difference in terms of the active material shape, distribution and adhesion within the carbon felt. The TiO_2 in Figure 6.11a appears to have formed balls of around 5-7 microns, which have adhered to each other between the carbon fibres. The dark pores appear mainly filled with these balls, but there are still a few voids - showing where there was no ink adhesion. It is clear to make out the individual carbon fibres, as the TiO_2 has not adhered onto the fibres themselves, but between them, with a few examples of fibres with one or two 'balls' attached. The copper hexacyanoferrate (CuHCF) however appears to have adhered both to the fibres and in between them with it difficult to fully see the individual carbon fibres on Figure 6.11b. There is no clear particle shape at this magnification, with the active material appearing fluffy and cloud-like, with one or two small voids (black) visible in

the top left of the image - the ink, at least from this image, looks well dispersed throughout. Further magnified images of individual fibres are shown for the TiO_2 electrode in Figure 6.12, there is a thin coating of particles clinging around some grooves of the carbon fibre. For the CuHCF close up, Figure 6.13, a thicker, again almost fluffy, distribution can be seen adhered to the fibre. On further magnification of the CuCHF fibre, it was difficult to produce a focussed image, hence the lower magnification of $\times$7000 compared to the TiO_2 fibre ($\times$25,000).

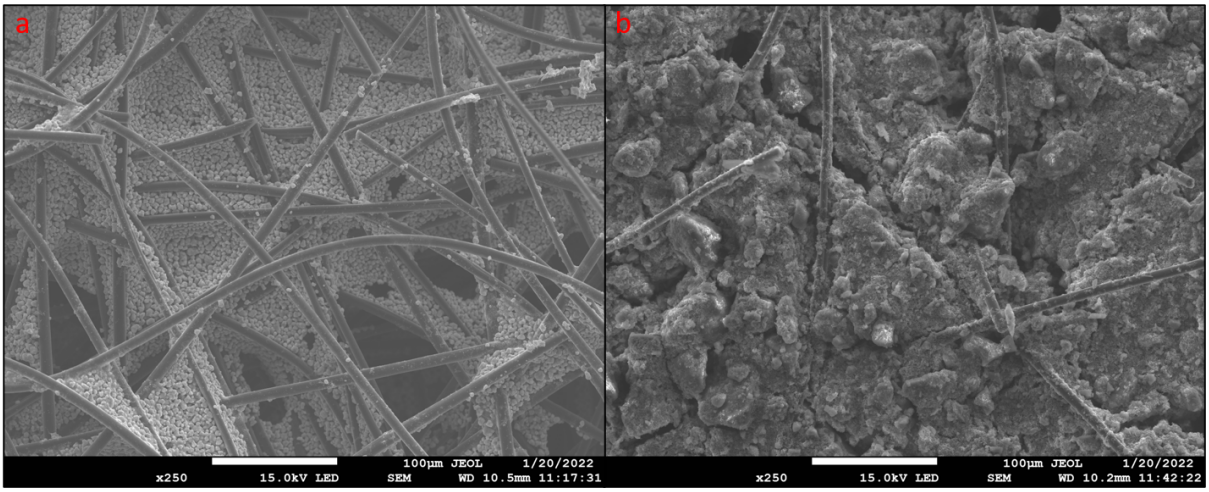

FIGURE 6.11: SEM image of carbon felt electrodes at $\times$250 magnification. a) TiO_2 electrode (30.1 mg cm^{-2}) b) CuHCF electrode (29.9 mg cm^{-2})

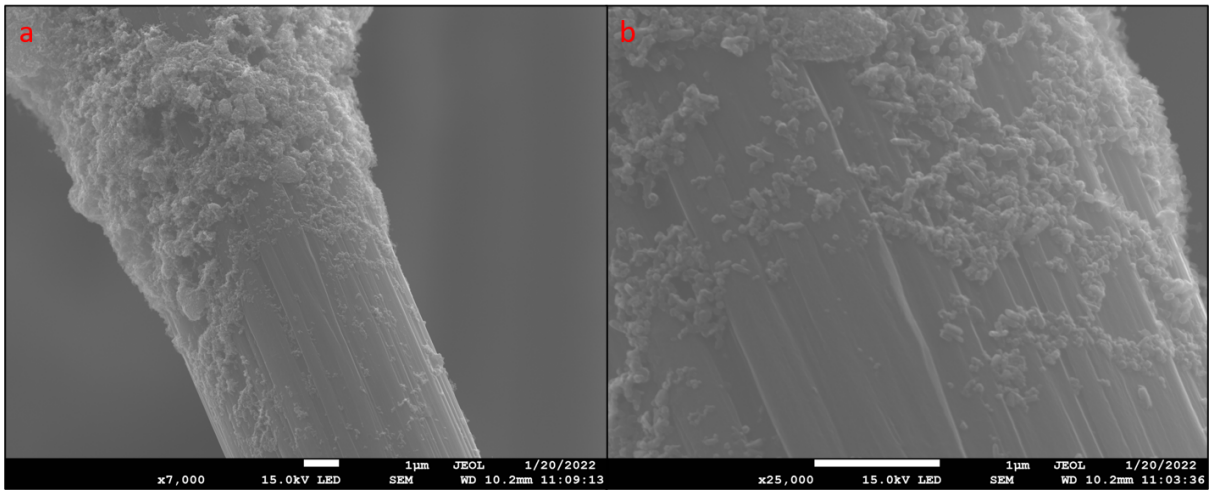

FIGURE 6.12: SEM image of TiO_2 carbon fibre (2.8 mg cm^{-2}), a) $\times$7000 and b) $\times$25,000 magnification

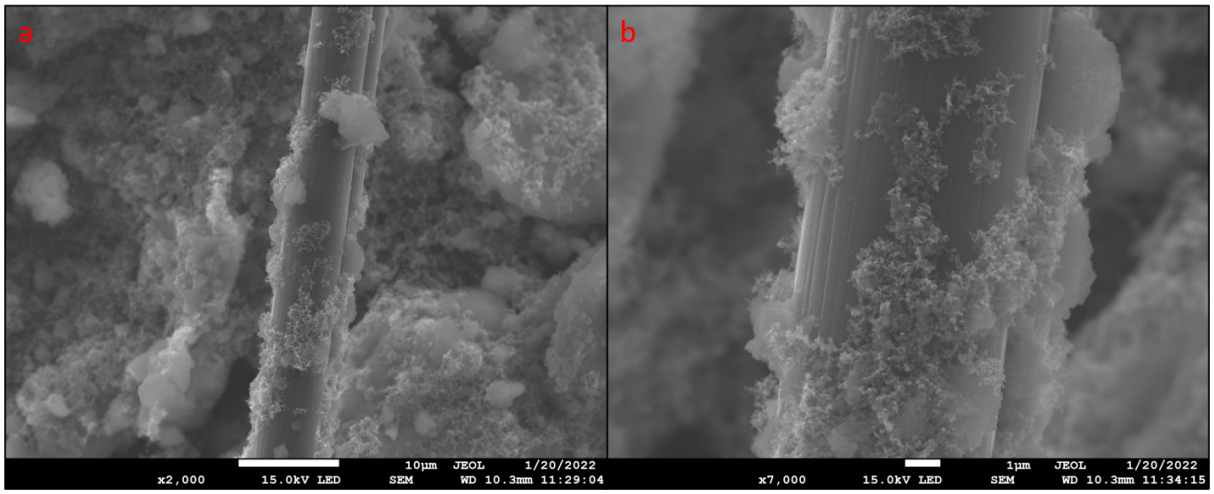

FIGURE 6.13: SEM close up of CuHCF carbon fibre (2.6 mg cm^{-2}), a) $\times$2000 and b) $\times$7000 magnification

6.5.2 Scanning Electron Microscope post-cycling measurements within the carbon felt electrodes.

The CuCHF electrodes showed cracks in the material after cycling. Figure 6.14 shows the 2.5 mg cm^{-2} sample after it had been cycled through the discharge capacities highlighted in the previous sections. The cracks are about 0.1 and 0.5 microns thick, and vary in length up to 20 microns. Figure 6.14b shows various cracks, and near the bottom of the image there are cracks which have joined up into each other. This may be a result of the material breaking down after cycling, and may be related to the Fe found in the electrolyte after the cycling occurred.

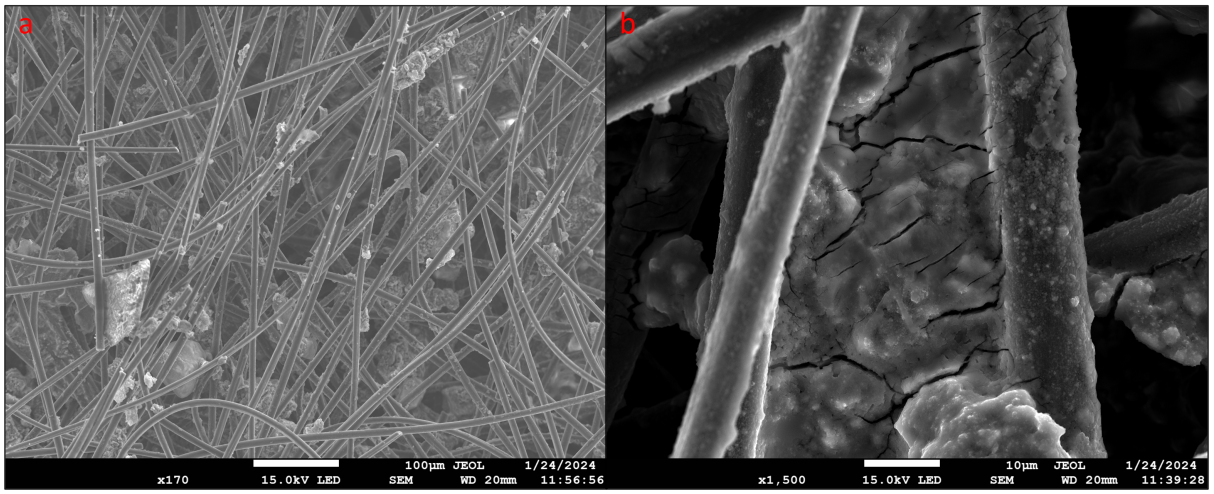

FIGURE 6.14: SEM close up of 2.51 mg cm^{-2} CuHCF carbon fibre electrode after cycling, a) $\times$170 and b) $\times$1500 magnification

There seem to be no cracks in the cycled TiO_2 carbon felt electrode. Figure 6.15 shows the 2.77 mg cm^{-2} electrode after cycling though the discharge capacities in the previous sections. The individual balls of material which sit between the fibres have merged into a more amorphous material. This could be a coating of one of the Ti-A-O compounds that were found in Chapter 7, or it could also be salts from the electrolyte which have adhered to the TiO_2 when the sample dried.

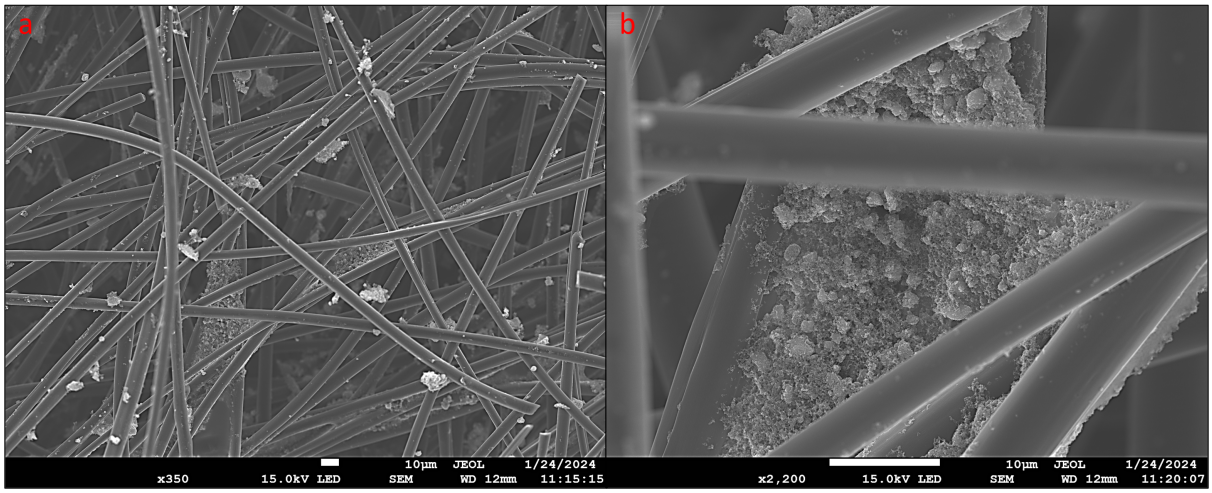

FIGURE 6.15: SEM close up of 2.77 mg cm^{-2} TiO_2 carbon fibre electrode after cycling, a) $\times$350 and b) $\times$2200 magnification

These cycled carbon felts were then washed in de-ionised water and dried in ambient conditions overnight. The resulting SEM images show that the remaining material within both electrodes had mainly washed away, which was reflected in the PXRD (below). We can also see a potential breakdown in the carbon felt itself on the TiO_2 electrode (Figure 6.17) which would require further investigation to ensure that carbon felt breakdown will not be a cause of performance degradation. CuHCF washed SEM images are shown in Figure 6.16.

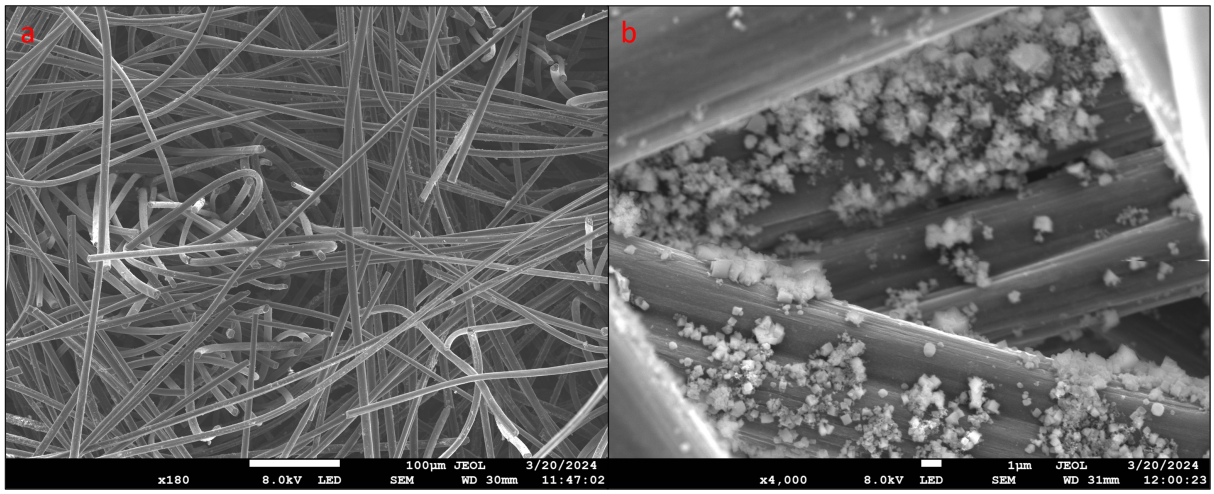

FIGURE 6.16: SEM close up of 2.51 mg cm^{-2} CuHCF carbon fibre electrode after cycling, washing, and drying, a) $\times$180 and b) $\times$4000 magnification

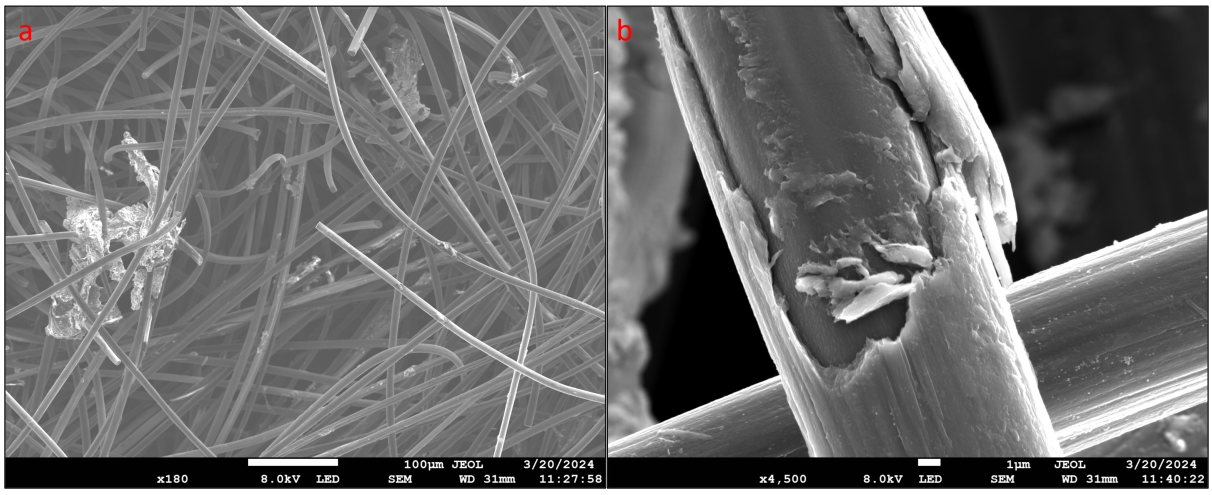

FIGURE 6.17: SEM close up of 2.77 mg cm^{-2} TiO_2 carbon fibre electrode after cycling, washing, and drying a) $\times$180 and b) $\times$4500 magnification

Powdered X-ray diffraction (PXRD) of both electrodes (washed, dried and ground with a pestle and mortar) after cycling, showed no evidence of any active material. This is likely due to the very low amount of active material within the electrodes which may have been washed off during the washing process. Further, while carbon does not diffract strongly, the main component in the powder was the carbon felt, as the remaining ink could not be separated from the felt. Copper Chloride, CuCl was picked up on both the electrodes. This may be from a parasitic reaction with the copper in the current collector and the chlorine in the electrolyte. If this were only present on the CuHCF electrode we could assume it was from the copper within the CuHCF itself. But as it is present on both it must be due to the current collector used. We know the half cell equation:

$$Cu^{2+} + Cl^{-}e^{-} \leftrightarrow CuCl = 0.78 \text{ V v SCE}$$

this reaction was occuring within the CuHCF electrode. However the TiO_2 electrode was not exposed to these potentials. Given CuCl is not soluble in water, washing the electrodes prior to the grinding and PXRD would likely leave only the CuCl, given the active materials were in fact soluble. See Figures 6.18 and 6.19.

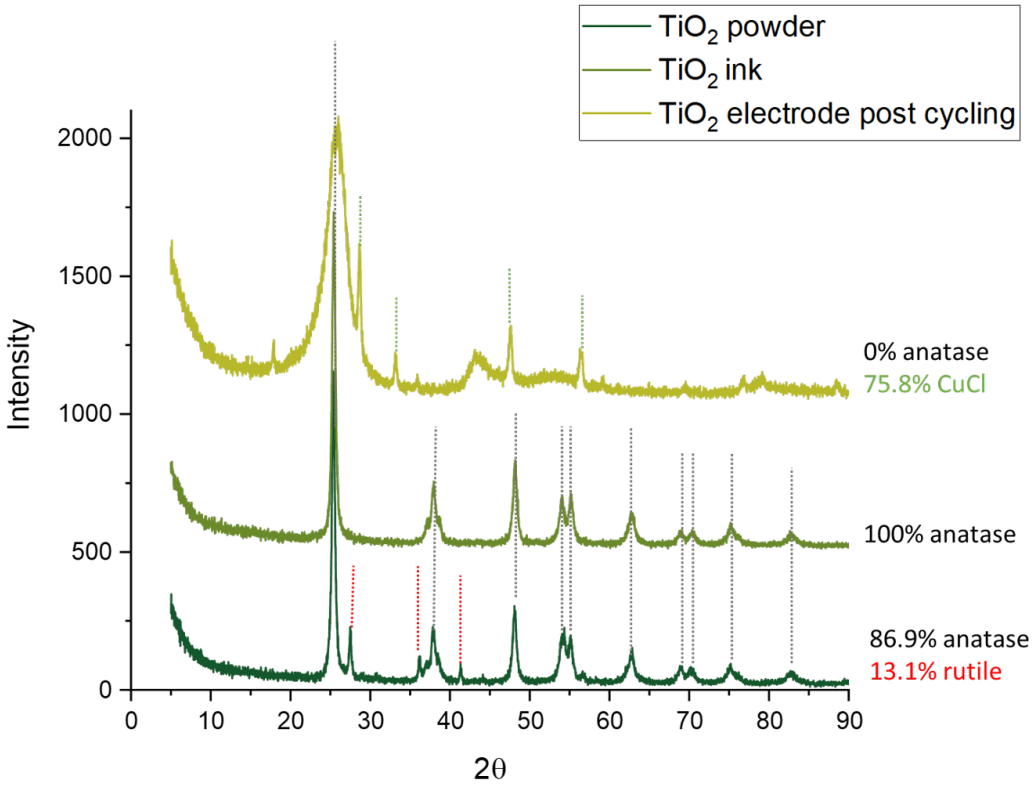

FIGURE 6.18: PXRD of TiO_2 powder, as a pure powder, when mixed in an ink and as a powdered cycled electrode

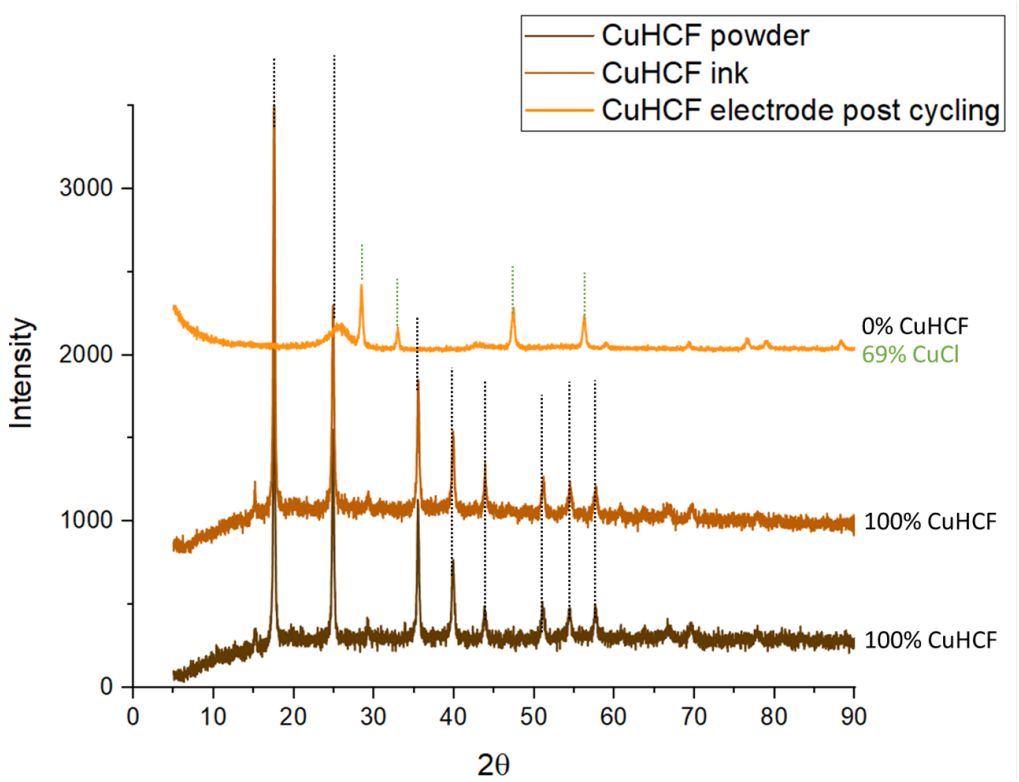

FIGURE 6.19: PXRD of TiO_2 powder, as a pure powder, when mixed in an ink as a powdered cycled electrode

SEM images have their limitations, as they can only show the surface layer of the electrodes, however the carbon felt is porous throughout its bulk, and so the SEM may not have revealed the full ink dispersion. The use of X-ray Computed Tomography (XCT), allows a 3D reconstruction of the electrode, and thus can be used to assess distribution of the active material throughout the carbon felt.

6.6 Compression, diffusivity and conductivity through the carbon felt electrodes

To fully utilise the active material within the carbon felt, the amount which it is compressed between the current collector and separator material is an important parameter to assess. While the felt is uncompressed, the pores within the electrode are full of electrolyte, ensuring all surfaces are in contact throughout the electrode, allowing a high diffusion of ions - however, while uncompressed the conduction between the carbon fibres to the current collector will be limited by the number of contacts made between fibres. As the felt is compressed, the pore space reduces and so there will be less electrolyte overall within the electrode - but contact between the carbon fibres will be increased, thus improving the conduction through the electrode. If the electrode in entirely compressed - i.e. no pore space for electrolyte, this is

essentially a flat electrode and only the very outer layer will be able to react with the electrolyte. At the other extreme, if the electrode is so uncompressed as to inhibit contact between carbon fibres, there will be no conduction through the bulk, and only the fibres physically touching the current collector will act as an electrode. Between these two extremes will be a parameter space where the diffusion of ions and conduction of electrons varies with compression. The experiment at DIAD, used a compression rig, and took XCT scans at 7 different stages of compression, in order to ascertain this parameter space, and find an optimum compression for overall electrode (and thus battery) performance. It is expected that this value may be different for each electrode. Once this compression has been found, the results can feed into the design of an optimised cell, taking into account the carbon felt characterisation work on active material loading. (25)

6.6.1 Optimising active material loading on the carbon felt electrode

The results presented below are part of an ongoing analysis in collaboration with James Le Houx, Diamond Light Source and The Faraday Institution. The analyses were performed to obtain the plots shown in Figures 6.20 were performed by Le Houx.

The below shows a plot of the diffusivity and conductivity for virgin felt (i.e. carbon felt without any active material). Imaging was also taken of the carbon felt electrodes (TiO_2 and CuHCF) dry and within electrolyte, to fully understand the interplay between the electrode conductivity and ion diffusivity. This is ongoing work and the initial results already suggest that there needs to be at least some compression to provide conductivity (at 0 N we see 0.03 conductivity) whereas there is always ion diffusivity even at full compression (0.11 diffusivity at 6.7 N compression). The compression of the carbon felts during the experiments above has been constant, the felt was compressed to 1 mm in order to accommodate it within the three electrode cell. This would be equivalent to 1.64 N for the TiO_2 (where the diffusivity dominates strongly) and 2.47 N for the CuHCF electrodes - still with diffusivity dominating, but with a higher proportion of bulk transfer taking place through conductivity. Increasing compression further, which as we can see will increase conductivity of the electrode, may also provide more contact between active material and the carbon fibres, and therefore increase the utilisation of the electrodes with a higher active material density. This work will be crucial in optimising the design of the overall cell to ensure maximum utilisation of material and minimum environmental impact.

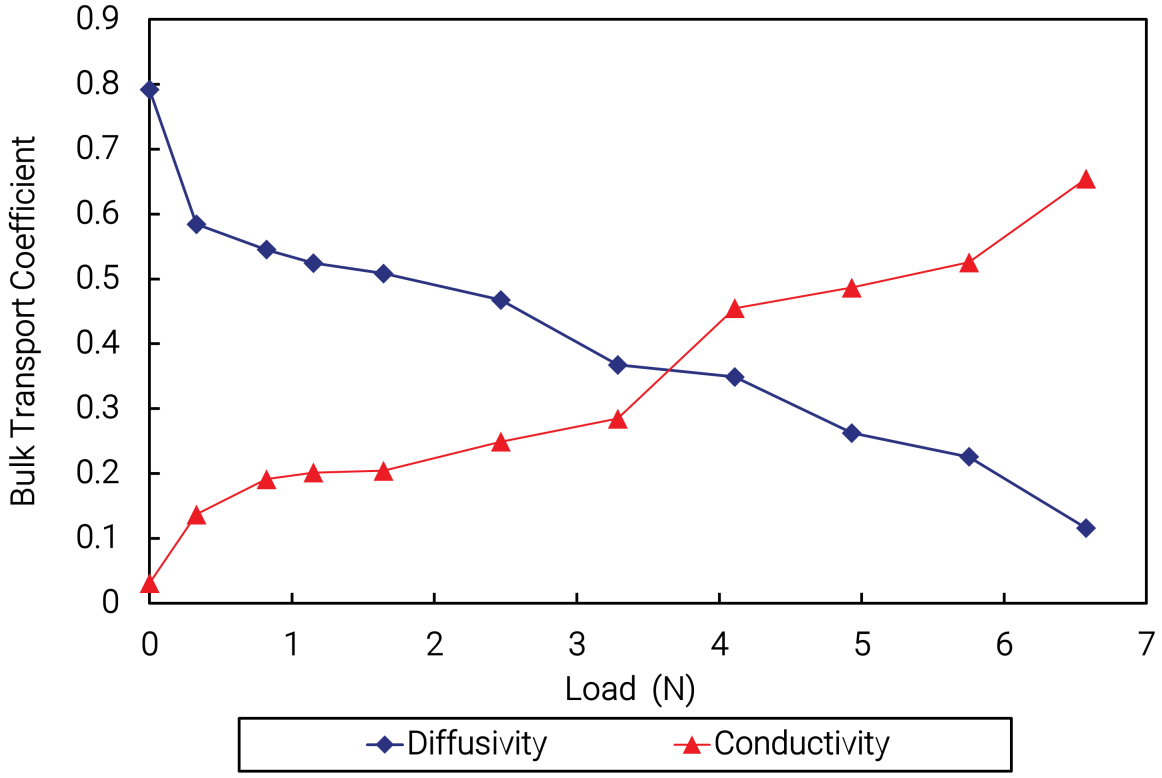

FIGURE 6.20: Plot of relationship between diffusivity within the electrode pore space and the electrical conductivity of the virgin carbon felt substrate (25)

6.7 Conclusions

This section has taken the goal of increasing the utilisation of active material percentage within the cell, and looked at carbon felt as a substrate for the electrode ink. In doing so, the amount of active material within the electrode was increased from ≈3% to ≈62% (around 30 mg cm^{-2} active material). While this showed an increased discharge capacity compared to the flat electrode, the active material was not fully utilised. Further investigations into the active material density within the carbon felts revealed the 'less is more' trend - a lower active material density ensured that more of it was utilised. For CuHCF, a maximum discharge capacity of 287.2 mAh g^{-1} was seen, while for the TiO_2 electrode, a maximum discharge capacity of 205.1 mAh g^{-1} was found. Based on this work, a new CFED of just 4.49 kWh has been calculated which provides a target cycle life of 16 cycles of a full cell developed using carbon felts. This is a relatively low target compared to cycle lives discussed in Appendix A and thus likely to be met in future. Further optimisation of the electrodes was explored through varying temperature of the TiO_2 electrode, with more investigations needed to fully understand the role of temperature in both wetting the electrodes and the impact on discharge capacity.

Further, the collaboration with DLS in looking at the role of compression on the performance of the electrodes has produced a top-level parameter space so far. However, as this work only considers a dry virgin carbon felt, there is more work to be done analysing the data collected from the electrodes with active material within them, and while wetted with electrolytes to fully understand the impact on compression here. This is an ongoing analysis and the resulting data will instruct future design of carbon felt half-cells, and aid in the development of a working carbon-felt full cell.

Chapter 7

Long duration study into the changes and degradation of the aqueous aluminium-ion battery as coin-cells

7.1 Motivation

Fully understanding the behaviour of the cell over its lifetime is important in designing a battery with a long cycle life. This includes optimising both design and use of the cell to limit or mitigate degradation and thus extend the useful life of the cells. In terms of sustainability - a longer lifetime will reduce the environmental impacts per kW (or kWh) as highlighted in Chapter 4.

Previous neutron diffraction work on the TiO_2 electrode has shown that after 5000 cycles, negligible change was found in the lattice parameters (2). This particular study took a pristine electrode and an electrode that had been cycled, and performed ex-situ analysis. The ex-situ analysis included the washing of the electrodes, the scraping of the active material and grinding it into a powder prior to diffraction. These processes may wash off soluble new phases, may relax any stresses within the matrix, and therefore may not provide a full picture. This process may also introduce contamination to the sample.

This chapter describes a long duration experiment which involves in-situ and operando measurements while the cell is cycling. Taking measurements throughout the lifetime of the cell, without requiring the destruction of the cell, will reveal the degradation mechanisms. This experiment has been performed on a Li-ion cell which revealed bulk fatigue mechanisms (194).

The Long Duration Experiment (LDE) beamline at Diamond Light Source (DLS) can accept coin-cells, with only a small modification - a laser-thinned window in the casing - which means the battery is representative of a real life application. The LDE was run from April 2022 to March 2023, with only one cell, an open circuit cell (A3), remaining within the beamline for that full duration.

7.2 Research question

Within this chapter, the key research questions being answered are:

- Does in-situ XRD tell us anything about the degradation mechanisms of the aq. Al-ion battery
- Does cycling regime impact the degradation mechanisms?

7.3 Experiment design and expectations

The long duration experiment (LDE) is active on beamline i11 of DLS. This facility consists of many LDEs on a table which are subject to weekly X-ray diffraction (XRD) readings. The average wavelength during the experiment was: 1.496 Å and the average energy was 15 keV.

Using the LDE, the change in lattice parameters of the TiO_2 and CuHCF electrodes, arising from Al^{3+} interaction within the materials, as a function of charge regime over cycle life will be investigated, correlating the structural changes and performance changes of the cells. Thus, this experiment required cells be kept at ambient conditions, stored at 0% SoC (state of charge) to provide any calendar degradation over time and act as a 'baseline'.

A range of cycling regimes enable the isolation of specific degradation mechanisms and changes to be seen based on the cell use over time. Further, an additional cell at 90% SoC with a constant trickle charge will be investigated to understand the stresses on the material in a constant charged state. In practical use, the cell may be constantly held at this state prior to being discharged as needed.

7.3.1 X-Ray diffraction variables

Within the LDE, electrode materials will be investigated over a 1 and 48 degree 2θ range as previous experimentation has shown that all significant Bragg peaks will be contained within this range (195). The measurements were taken during a resting state

for the cells, and for cells in regime b), a brief rest period (4 hours) was introduced prior to measurements being taken, to ensure all cells were in the same charge state.

7.3.2 Expected Results

It was expected that evidence of change or degradation corresponding with a reduced performance of the cells would follow one or more of the following predictions.

- Lattice expansion (or contraction) due to accommodation of Al^{3+} ions over time, with a concomitant reduction in cell capacity as electrode degrades (Figure 7.1a).
- The formation of new Al-Ti-O phases within the negative electrode materials (Al_2TiO_5 and $Al_2Ti_7O_{15}$ have previously been observed (5)), limiting the available ions for charge transfer and reducing overall capacity over time (Figure 7.1c).
- Broadening of the Bragg peaks over time, indicating reduction in particle size of the active materials, resulting from a variety of changes including: lattice expansion/contraction cycles, phase transformation, increased particle stress/strain, hydroxide formation or binder/supporting material decomposition. Detailed analysis of Bragg, background and electrochemical data allow exact mechanisms to be elucidated.
- Sharpening of Bragg peaks may also be seen - due to zone refinement or growth in particles.
- Changes in peak intensities indicating preferential growth of the materials or the creation of non-stoichiometric phases resulting from Al^{3+} inclusion (Figure 7.1b) or hydroxide formation.

Depending on the changes in the Bragg peaks over time, there may be more specific experiments designed to fully understand the situation, as illustrated by the potential for both sharpening and broadening of peaks depending on different mechanisms.

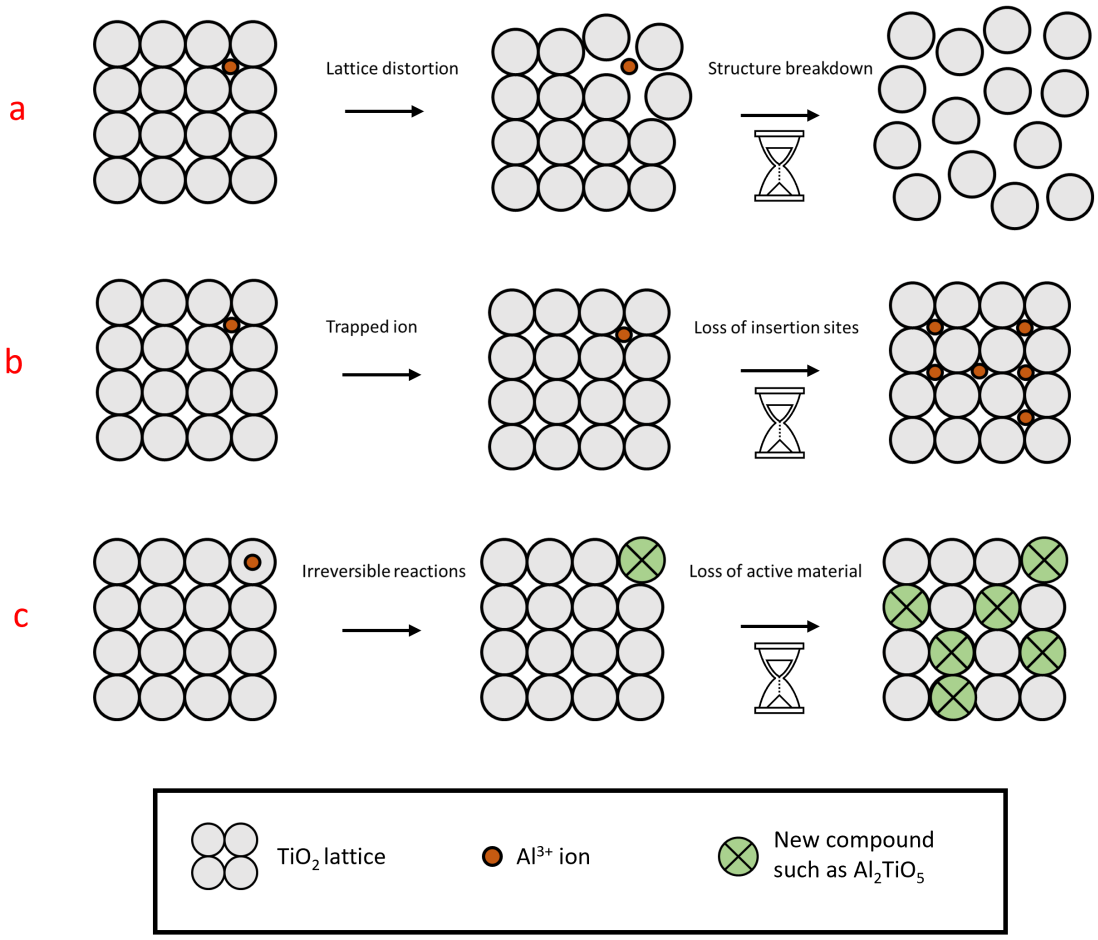

FIGURE 7.1: Illustration of potential electrode degradation mechanisms over time, showing a) lattice distortion, b) trapped ions and c) formation of new phases through irreversible reactions

Cells were prepared as developed in Chapter 5 and described in Chapter 3, using the laser thinned cases provided by DLS. Figure 7.2 shows the exploded view of the cell, with Figure 7.3 an image of a crimped cell used for testing.

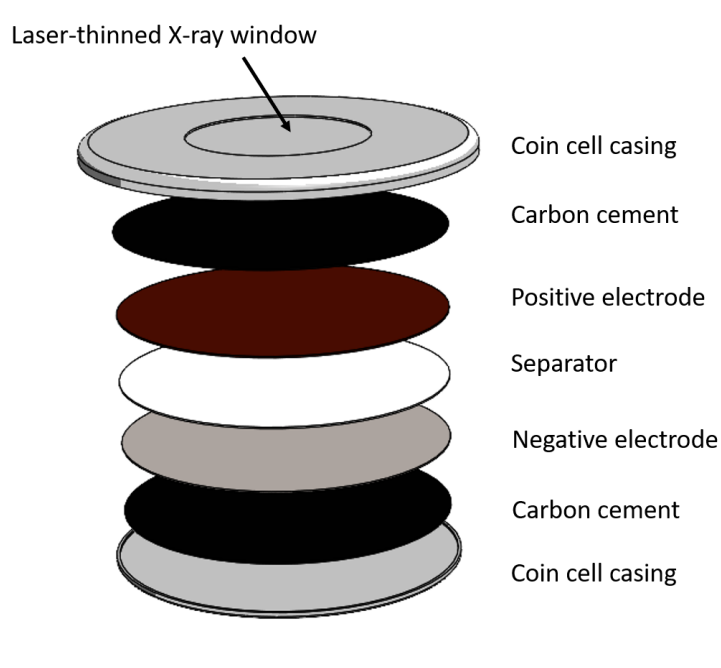

FIGURE 7.2: Exploded coin-cell diagram

FIGURE 7.3: Crimped cell with laser thinned window on case

7.4 Cycling Regime at the LDE

The initial regimes in the LDE are

- 1 cell at OCV (open circuit voltage)
- 1 cell at constant voltage 1.4 V

- 2 cells on charge regime a)
- 2 cells on charge regime b)

Charge regime a) is as follows

1. constant voltage charge at 1.4 V
2. constant current discharge at 250 mA g^{-1} (equivalent to about 1 mA) to 0.8 V
3. loop 1-2 50 times
4. rest for 12 hours
5. loop 1-4 for entirety of test

Charge regime b) is as follows

1. constant voltage charge at 1.4 V
2. constant current discharge at 250 mA g^{-1} to 0.8 V
3. loop 1-2 for entirety of test

The key difference between regime a) and b) is whether a rest period is introduced. This is primarily to allow measurements to be taken at shorter cycle intervals for regime a), however the resting may have an impact on the full cycling life of the coin-cell which can inform usage recommendations for lifetime extension.

7.5 Results and Discussion

7.5.1 Unit cells and coin-cells

A note on syntax. The term cell, as in coin-cell, is used to describe the battery that is being tested within the LDE. The term cell as in unit cell, is used to describe the crystal structure of the material being measured via XRD (i.e the TiO_2 and CuHCF). Throughout this chapter the two types of cell will be discussed, and will be explicitly described as either the coin-cell or unit cell to avoid confusion.

7.5.2 Initial XRD results from the aq. Al-ion coin-cells

There is difficulty in fully fitting all peaks and patterns within the diffraction measurements, this is due to both the number of phases present in the coin-cell, and the distance from the detector of each phase.

Phases within the coin-cell include (but may not be limited to)

- Nafion
- Carbon
- Steel
- Polyvinyl flouride (PVDF)
- CuHCF
- anatase TiO_2
- rutile TiO_2

Specific phases, such as the steel and PVDF, appear at two distinct distances from the detector, and so the diffraction pattern appears twice for each phase, slightly shifted. This is easily identified for the steel as it has an intense peak, and is illustrated in Figure 7.4 (top). Given that the PVDF and carbon (graphite) also appear at two distinct distances from the detector, there are many doubled peaks, making resolving the main phases of interest (TiO_2 and CuHCF) difficult. Further, as shown in Figure 7.4 (bottom), there are peaks which have many possible phases (illustrated using slashes above the peak), which mainly fall above 13°. Therefore the main peak fitting and analysis was done using only 2θ values below 13°, where the overlapping peaks, as well as the intense steel peaks are minimised. Unless stated otherwise, any reference to TiO_2 is the anatase phase. Further, it should be noted that the peaks seen at 2.8° on all diffraction patterns are an artefact of the scan calibration itself and is not relevant to the analysis.

There was difficulty in fitting both Nafion and the PVDF, as they were purchased specific products and their exact make-up is unknown. Given the multi-phase nature of this sample, the main focus of fitting initially was on the anatase TiO_2 and CuHCF. Peaks (below 13°) for these two phases are as follows; For CUHCF, there were resolvable peaks at 4.7°, 5.5°, 7.8°, 9.1° and 11.1°. For the anatase TiO_2, resolvable peaks are at 8.0°, 11.6°, 11.8° and 12.1°. The anatase phases are difficult to view apart from at 8.0° - however there may also be the contribution of a PVDF phase here. Figure 7.5 highlights these phases.

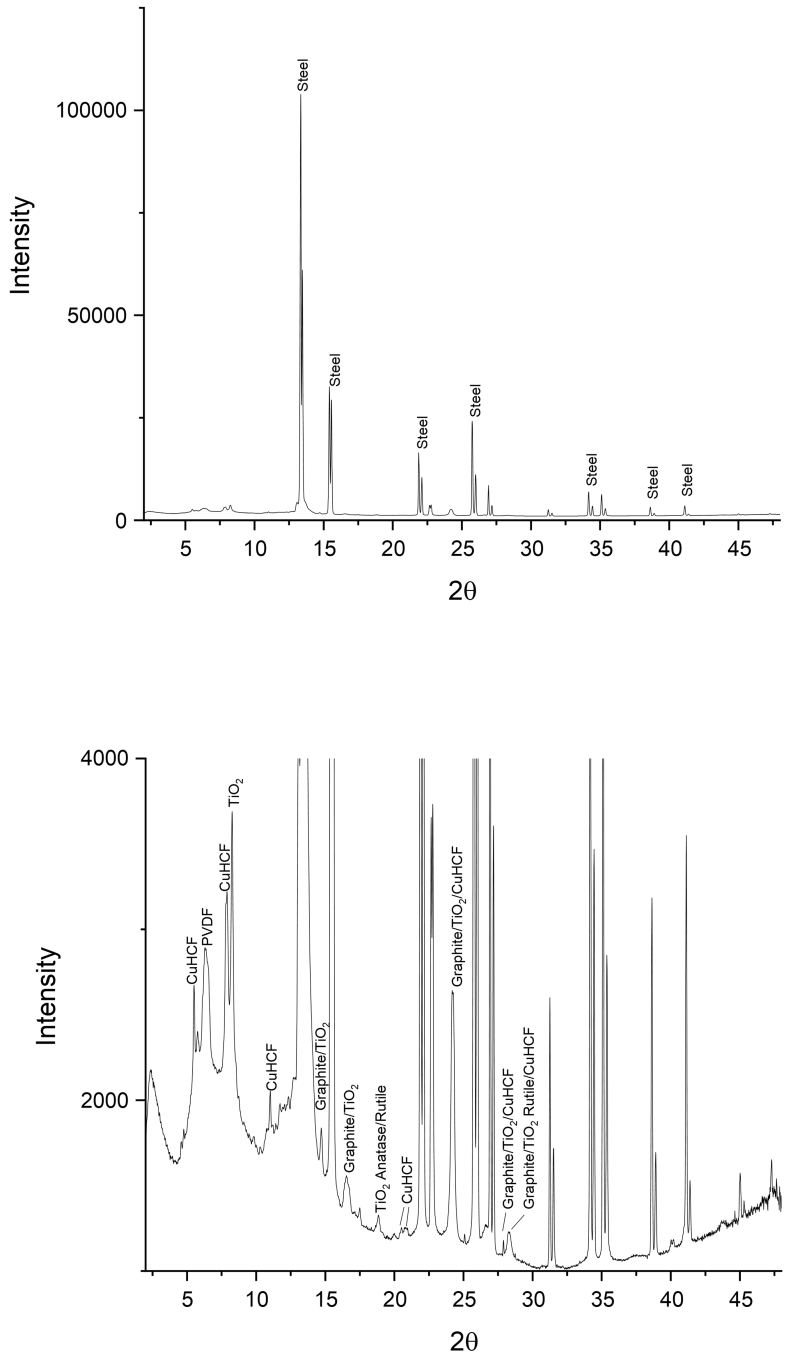

FIGURE 7.4: Full diffraction pattern of pristine coin-cell, highlighting the steel double peaks (top), and a zoomed in version up to intensity=4000 (bottom) showing potential overlapping peaks

7.5.3 Coin-Cell cycling and diffraction results

Due to the nature of manufacture of the coin-cells (small batch, hand-made, lab-based), there is slight variability introduced and differences in the final composition of each coin-cell. It was therefore expected that not all the coin-cells would perform as expected. Therefore only a select few coin-cells could be analysed within the LDE, producing a smaller dataset than desired, but revealing interesting information about the workings of the coin-cell over time.

7.5.3.1 Regime a) Coin Cell C2 and C1 cycling and diffraction results

Coin-cell C2 was subject to regime a), with rest periods every 50 cycles. The discharge capacities measured across the lifetime of the coin-cell is shown in Figure 7.6a. These discharge capacities are lower than was measured in Chapter 5, by about ten times (12 mAh g^{-1} was achieved here) due to the smaller voltage range applied (to account for gassing). The lowest discharge capacity measured was 0.21 mAh g^{-1}, based on the total mass of active material (TiO_2 + CuCHF). The highest discharge capacity seen is 1.22 mAh g^{-1} at cycle 3502. The profile of discharge capacities over cycle number does not follow the expected trend. One would expect the discharge capacity to start high, stabilise for many cycles and then slowly drop. However, coin-cell C2 had an erratic first 100 cycles, with a drop in capacity around cycle 200. This then rises to a somewhat stable 0.75 mAh g^{-1} average, up to cycle 2000, where a steady rise in capacity is seen to $\approx$1 mAh g^{-1}. Here the capacity appears to remain stable until the 4500th cycle, where there is a drop in capacity to 0.78mAh g^{-1} until cycle 5500. Here the capacity begins dropping slowly to 0.56 mAh g^{-1} at 7100. Following this there is a sharp decrease in capacity and the cell reaches end of life at cycle 7784 . There are many reasons that could explain the erratic behaviour - the current (Amp) range on the Arbin monitor was set too high for the first 100 cycles, and so this explains the erratic measurements before this was noticed and corrected. This does not explain the drop around cycle 200 though, there may have been power issues at the facility around certain cycles. This may be an artifact of the coin-cell itself, a building up of a passivisation layer, or gas forming within the coin-cell. It may also have taken many cycles for the electrodes to become fully wetted and therefore utilised. Representative cycles throughout the cell life were be assessed in terms of discharge performance and diffraction data to understand these performance changes fully over cycle life. These cycles illustrated in Figure 7.6b are 0, 300, 2200, 2500, 2900, 3300, 5000, 5500, 6200. For cycles 500-1600 Diamond Light Source was in a shutdown and no measurements were taken. A broad peak appears around cycle 2200 at 3.5°, either a transformed version of the narrow peak seen in cycles 0 and 300, or the narrow peak is being hidden by the new broad one. This broad peak increases in intensity as the cycling continues. The CuHCF peak at 7.9° is visible on cycles 0 and 300, however as the cycle number

increases, this peak intensity lowers, and perhaps broadens, however this is difficult to see next to the 8.03° TiO_2 peak, which appears unchanged throughout the diffraction measurements. Further, the CuHCF peak at 11° increases in intensity and broadens as cycling continues. At cycle 5000, a second peak appears at 10.9° - this corresponds with the drop in capacity seen around cycle 4500 (unfortunately we only have XRD from cycle 3300 and 5000 to show this before and after). This 10.9° peak continues to grow and broaden. At the end of the coin-cells life, shown in Cycle 7700, the 10.9° peak has grown sharper in intensity than the CuHCF peak at 11°. The TiO_2 peaks at 8.03° and 12° appear unchanging throughout the cycling of the coin-cells.

The growing peak at 10.9° corresponds with the compound Al_2TiO_5 (230), which has been seen in other studies cycling TiO_2 electrodes (196; 5). However this is the only peak present that corresponds with Al_2TiO_5 in the XRD measurements.

A broadening peak suggests that the particle size is reducing, which would make more surface area available for electrochemical reactions, and could explain the increased performance over time - if the 3.5° and 11° are both attributed to CUHCF. The unchanging TiO_2 peaks suggest there is little interaction or change within the bulk of the material, further indicating that the reaction here may be a surface reaction, with little impact on the lattice over time.

Cycle 200 for coin-cell C2 was 4 seconds, with a resulting discharge capacity of 0.296 mAh g^{-1}, given the total mass of active material of 4.01 mg. By cycle 4000 the discharge capacity is 0.923 mAh g^{-1} with a 16 second discharge time. From Figure 7.6(c-f), it is clear that not just the discharge time is changing as cycles increase, but the peak current - seen at the start of the charging step - reduces over time.

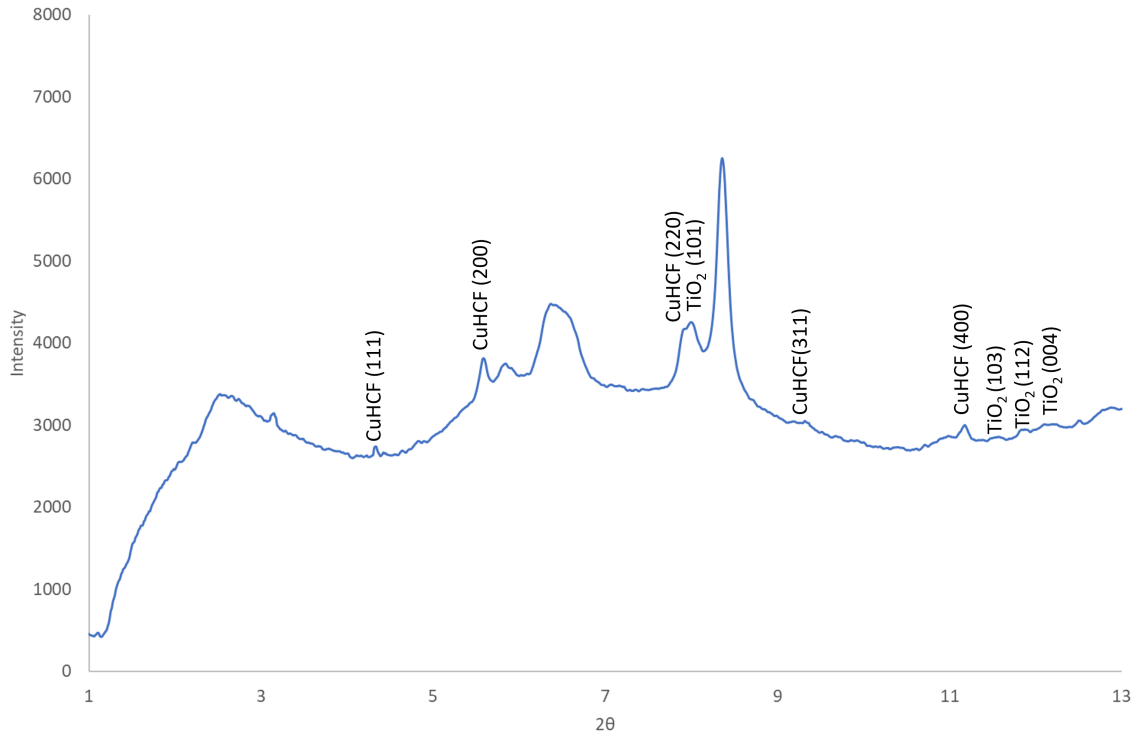

FIGURE 7.5: Full diffraction pattern of pristine coin-cell C2, highlighting TiO_2 and CuHCF peak locations.

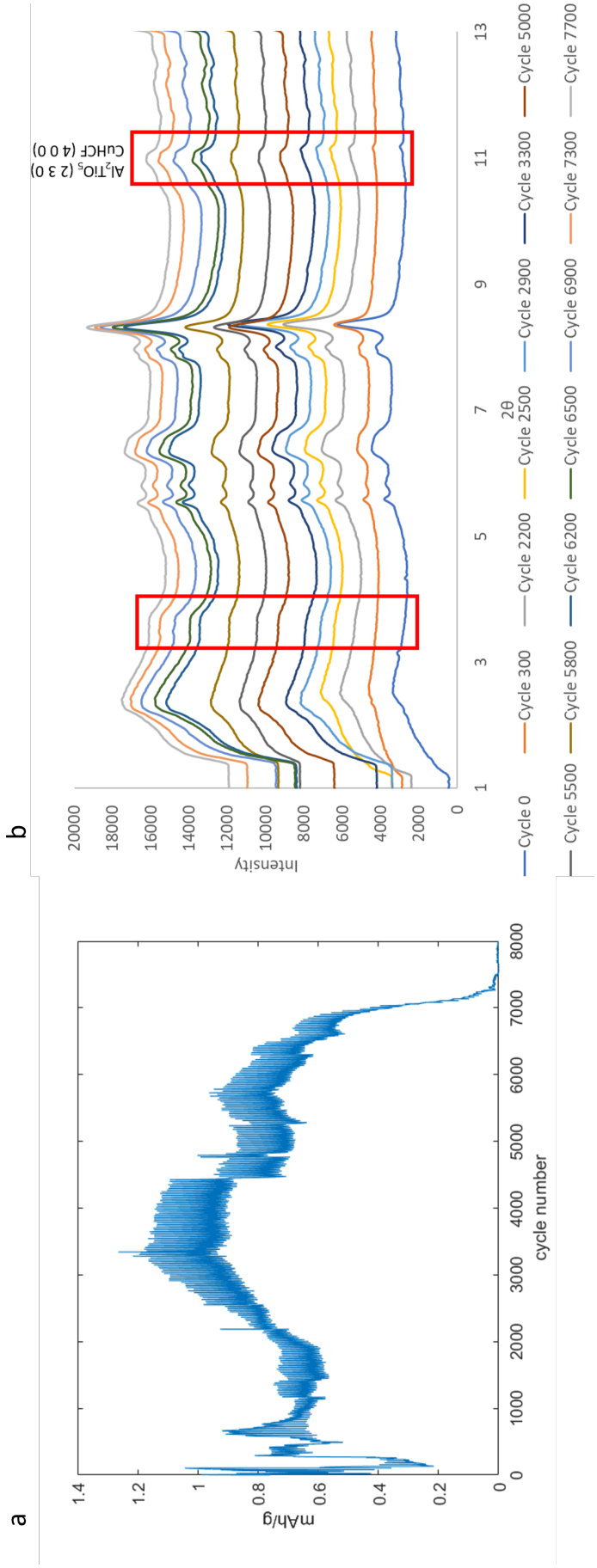

FIGURE 7.6: a)Discharge capacity for Coin-cell C2, b) diffraction data for coin-cell C2 at varying cycles for 2θ 2°-13°, with points of interest highlighted

Coin-cell C1 lasted 313 cycles overall, which were completed in seven days. The discharge capacity and XRD for begining and end of life are shown in Figure 7.7. From an initial discharge capacity of 1.76 mAh g^{-1}, the capacity falls gradually until cycle 313. After each rest period, the initial discharge capacity is increased compared to the following 49 cycles. This was also seen in coin-cell C2 - suggesting that a rest period allows for an increased capacity. Although the lifetime was far shorter for this cell, the diffraction data at end of life shows the same broadening of peaks for CuHCF at 7.9°, suggesting a similar mechanism is involved here. This phenomenon is not seen for the other CuHCF peaks. For cell C1, the peak at 10.3° is present for cycle 0, which was unidentified in the data fitting, which disappeared completely by cycle 313 - this perhaps was a contaminant which may be responsible for the short lifetime seen.

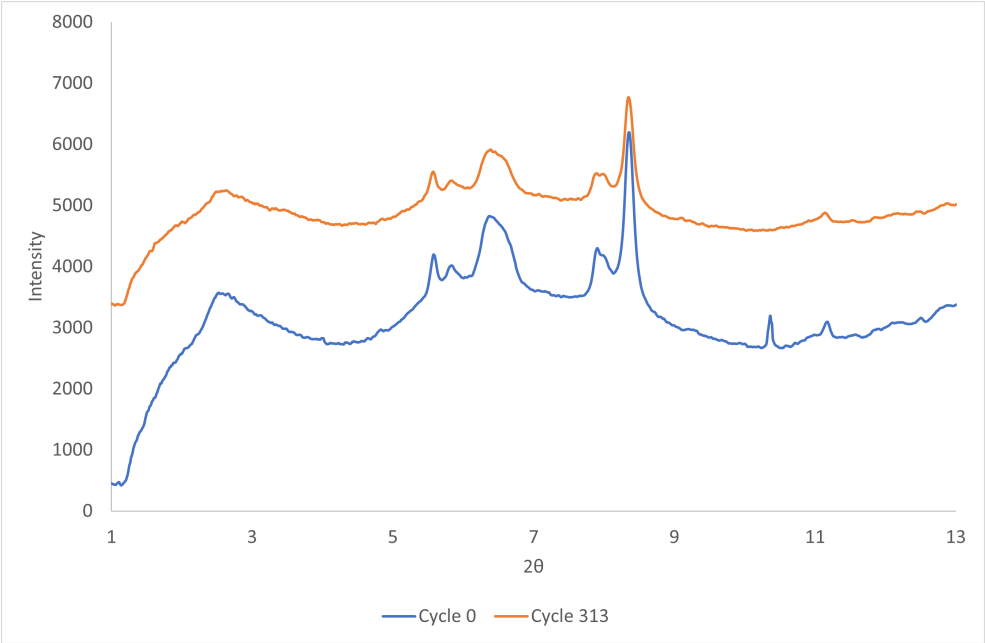

FIGURE 7.7: Coin-cell C1 XRD data over the 313 cycle lifetime

7.5.3.2 Regime b) Coin Cell C4 (and C3) cycling and diffraction results

Coin-cell C4 was subject to regime b), with continual cycling, and no rest periods. The discharge capacities measured across the lifetime of the coin-cell is shown in Figure 7.8. The initial discharge measured for the coin-cell is completed over 12 seconds, with a discharge capacity of 0.82 mAh g^{-1}, based on the total mass of active material (TiO_2 + CuCHF). From here the capacity drops and by cycle 100 is less than 0.2 mAh g^{-1}. Cycle 228 shows a peak (0.47 mAh g^{-1}) which then declines linearly to cycle 848.

The lifetime of 848 cycles was completed in 2 days, and therefore as XRD measurements are taken weekly, there were only beginning of life and end of life measurements taken - meaning any changes within the lifetime of the coin-cell may

have been undetected. Figure 7.9 shows the beginning and end of life diffraction data - which are unchanged. This may suggest that a rest period within the use of the battery allows for the required changes within the CuHCF material (becoming more amorphous, as seen in the section above). Of course, it may also be due to the manufacturing process, introduced contaminants, or a drying out of the electrolyte. Looking at the peaks around 11°, there is a broad peak forming to the left of the CuHCF peak - which matches that seen for coin-cell C2 - the Al_2TiO_5 (2 3 0) compound. This is evidence that there might be a loss in active material due to the formation of this compound - and therefore a reduction in capacity. If we compare the lifetime of this coin-cell to that of the one tested in the lab, where over 7000 cycles were completed in a 'no rest' regime, we can see further evidence that the coin-cell manufacture may be to blame. However it is useful to note that the coin-cells were not crimped closed, and were cycled at a higher rate, with a larger voltage range - and so direct comparison is not possible.

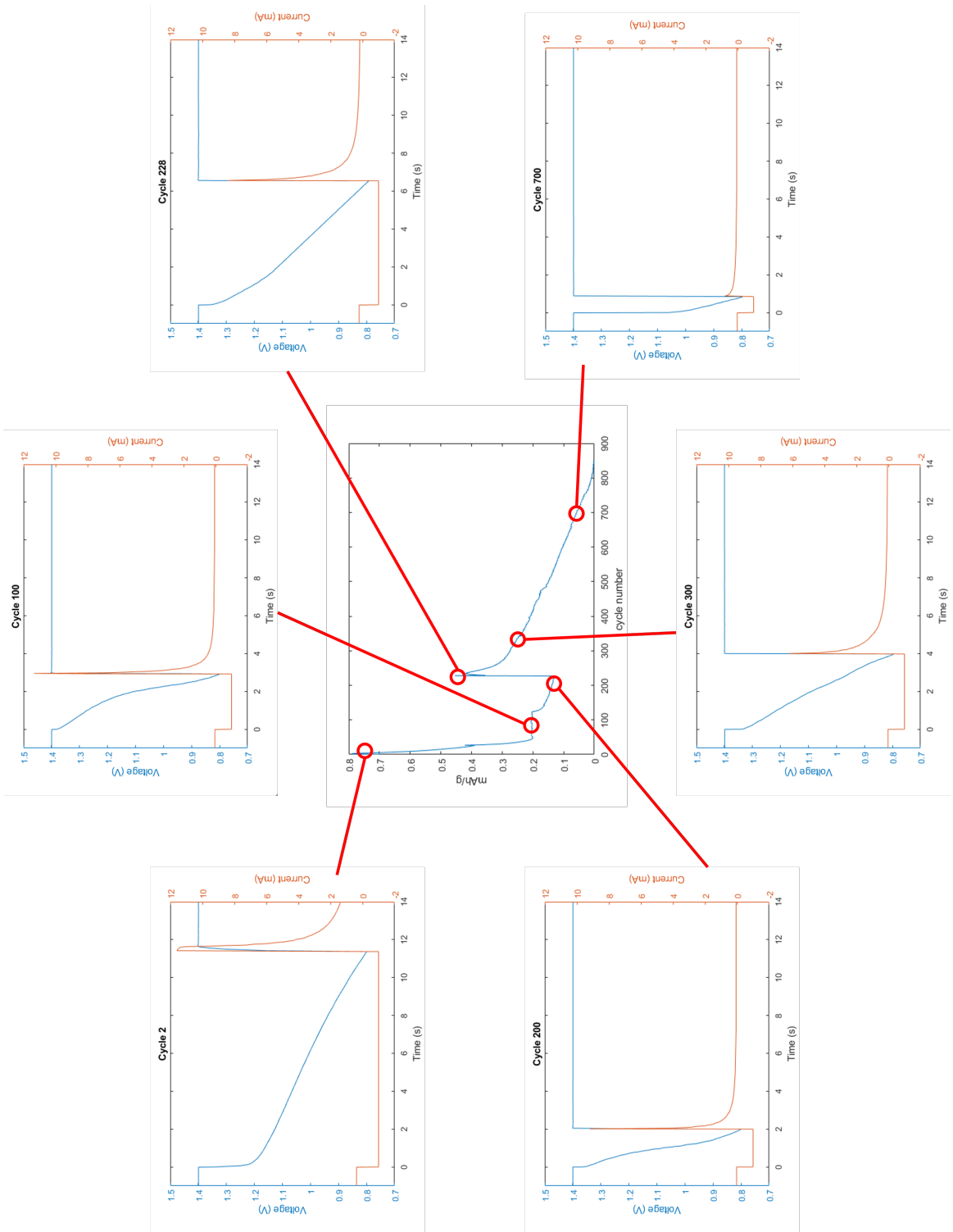

FIGURE 7.8: Discharge capacity for Coin-cell C4 with cycles 2, 100, 200, 228, 300 and 700 highlighted and the voltage/current plot of those cycles

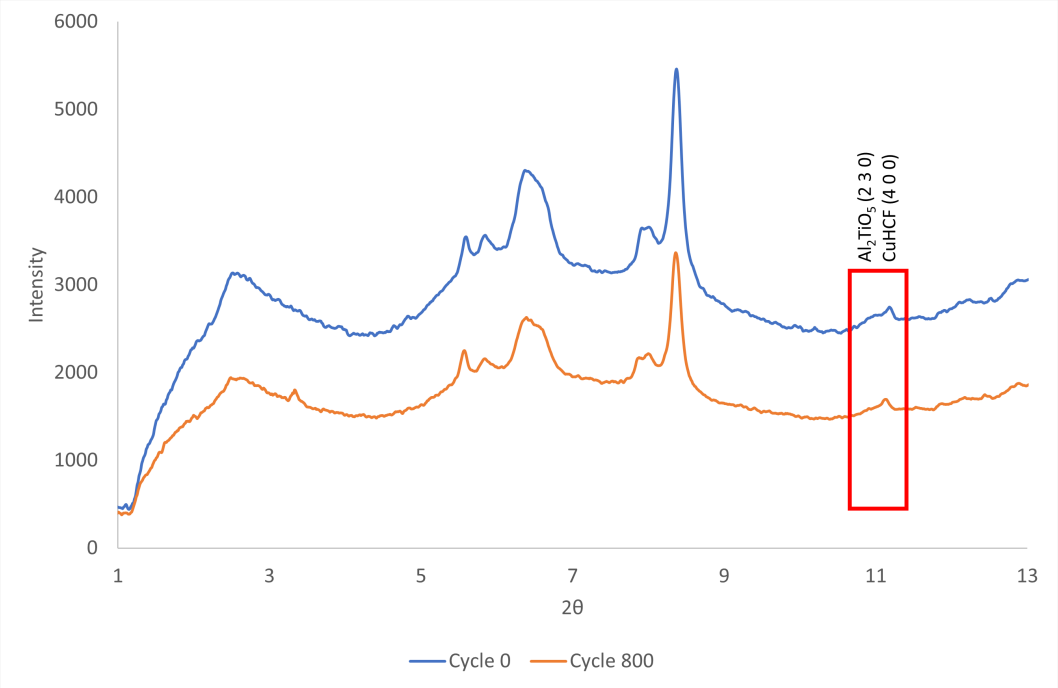

FIGURE 7.9: XRD data from coin-cell C4 for beginning and end of life

Unfortunately, coin-cell C3, which was also on regime b) had 0 capacity for all cycles performed. However it still held a voltage of 1.4 V during the constant voltage charge regime, then instantly dropped to 0 V during discharge. This extreme cycling (although not useful for battery life itself) did still show an interesting development with the XRD measurements. There are growing peaks around 8.9° and 12.5° - which corresponds to TiO_2 in the rutile phase - as highlighted in Figure 7.10. There is also evidence of a growing peak at 19.8° which also matches rutile (310). Therefore it is likely that this phase was either contaminating the cell to begin with and grew with time, or that the large voltage differentials applied to the coin-cell created the right conditions for this phase to form.

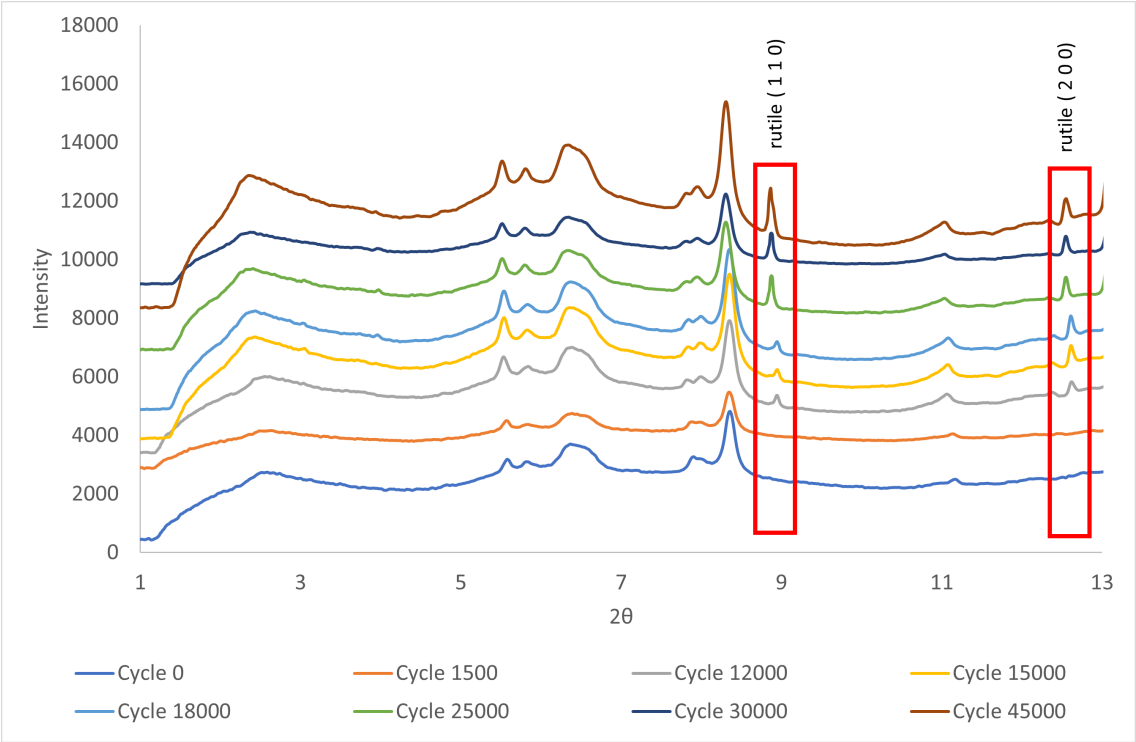

FIGURE 7.10: XRD data from coin-cell C3 for cycles up to 45000

7.5.3.3 Open Circuit Coin-cell - A3

Coin-cell A3 was initially cycled 10 times, 1.4 - 0.8 V, matching the regimes of a) and b), then left open circuit throughout the experiment. This was done to see if the changes found through XRD were due to the cycling regime of the coin-cells, or an artefact of the cell materials over time. The April 2022 measurements from Figure 7.11 were taken prior to the initial 10 cycles, and all other subsequent measurements were taken at open circuit voltage. Unfortunately, the coin-cell monitoring did not record any data prior to June 2022, and was faulty between June 26th and October 10th 2022 - therefore the complete picture of self discharge and open circuit voltage is not available. However, from the data shown in 7.11(top), the coin-cell appears to reach an open circuit voltage of around 0.2 V which is maintained between June and November, which then proceeds to decay to 0 V by January 2023. The most striking change seen in the XRD data is at 6.4° where a sharp peak begins appearing in January 2023 - this matches a corresponding sharpening close to the TiO_2 peak at around 8°. Both these peaks correspond to the Al-Ti-O compound $Al_2Ti_7O_{15}$. The May 2022 show peaks of interest at 9.09° and 12.52° - which correspond to the rutile crystal structure of TiO_2 - these peaks are not present in the initial measurements, and appear to slowly flatten as time proceeds.

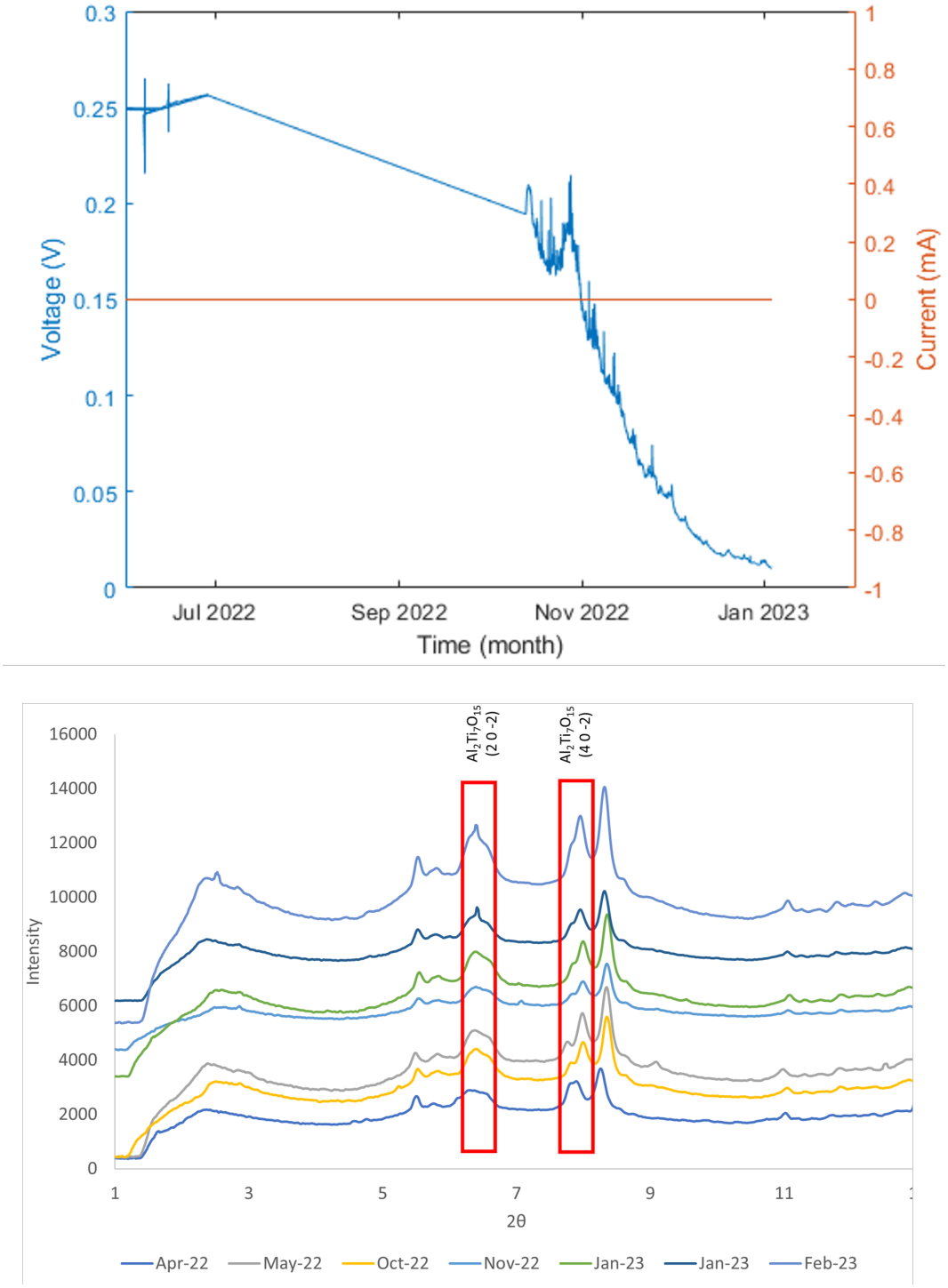

FIGURE 7.11: Voltage/current (top) and XRD data (bottom) from coin-cell A3 in open circuit conditions between April 2022-March 2023

7.5.4 Full Charge Coin Cell - C5

Coin-cell C5 underwent the initial 10 cycles, 1.4 - 0.8 V, matching the regimes of a) and b), then set to constant voltage at 1.4 V throughout the experiment. The XRD shows a growing a shifting left of CuHCF peak over time at 11° - but no evidence of a rutile phase growing within the cell. The changing peak of the CuHCF were also seen in the other coin-cells tested - and this could be due to lattice accommodation of Al ions. Further, the separation of the TiO_2 and CuHCF peaks around 8° is present, similar to that seen in cell C2 and C3. These changes are shown in Figure 7.12.

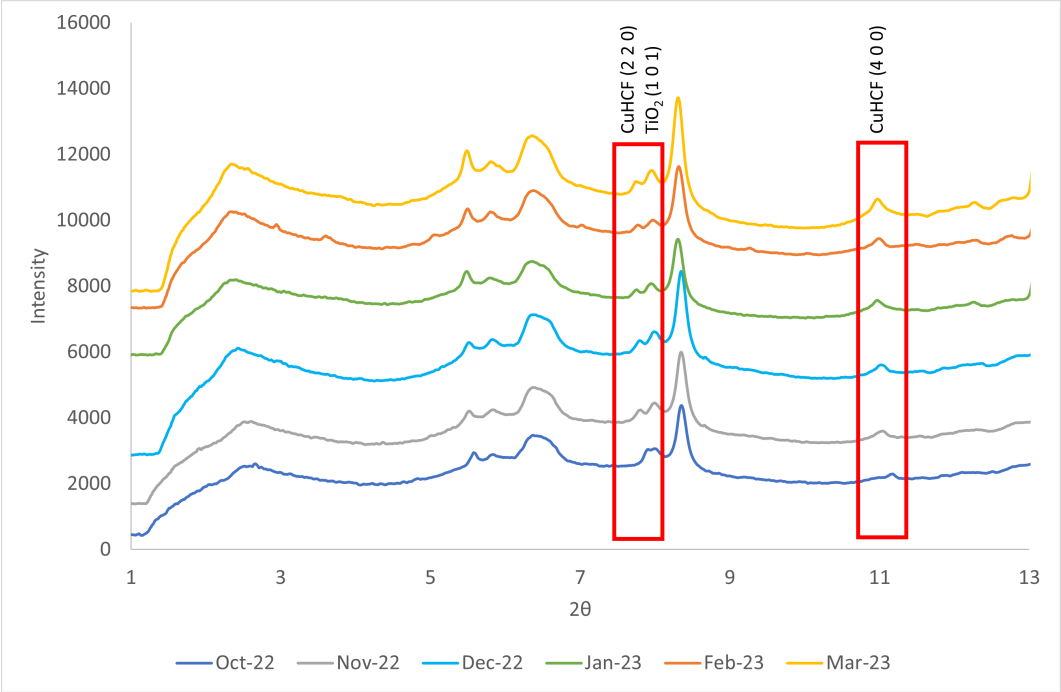

FIGURE 7.12: XRD of coin-cell C5, held at 1.4 V constantly between Octover 2022 and March 2023

7.6 X-ray Computed Tomography

The following section shows the XRCT (X-ray Computed Tomography) taken at the muvis facility at The University of Southampton using the diondo d5. 3D scans were taken of all coin-cells after their duration in the LDE, and compared to a scan of a pristine cell - as made. The coin-cells were scanned at an angle, to allow for the X-rays to penetrate the thinner areas of the steel casing. Due to the double thickness of the steel around the crimped area, the images produced are of the central section of the coin-cells, and not the full coin-cell. These scans help to identify the extent and location of bloating within the cells that were cycled at different regimes.

Figure 7.13 shows the pristine cell, as made, with the different sections labelled. It is difficult to fully make out the different sections of the coin-cell, and there are no obvious gaps between the layers, this cell is fully crimped and there has been no bloating.

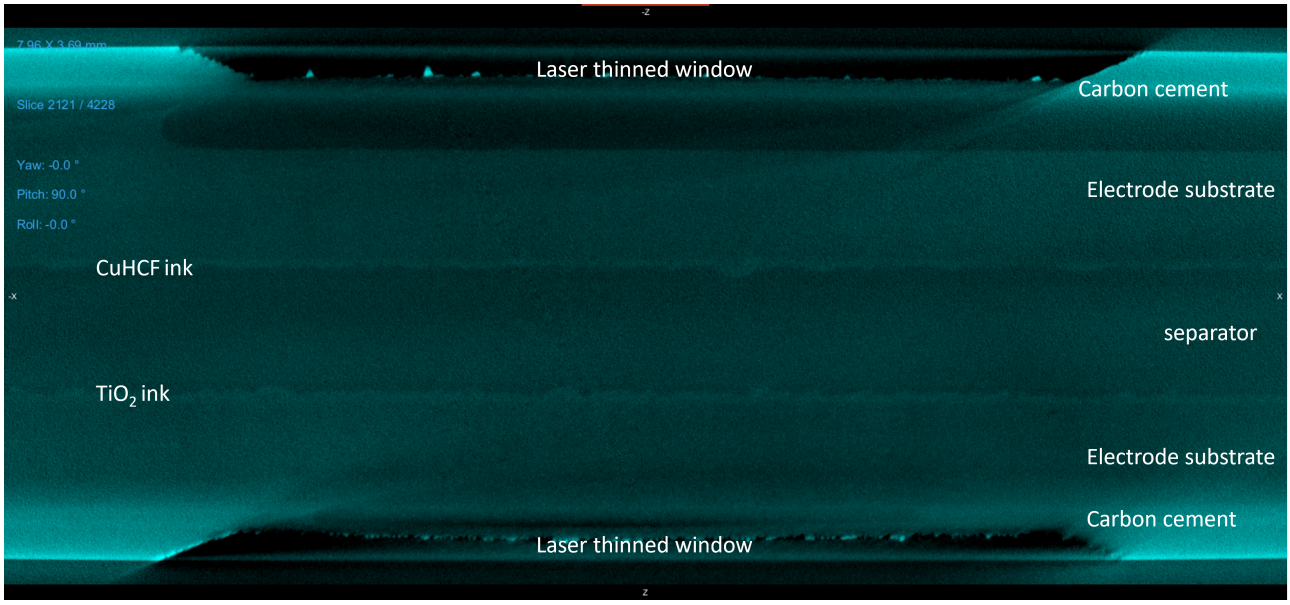

FIGURE 7.13: Pristine Cell CT scan

Both cells that were cycled with regime a) - with a rest period every 50 cycles are shown in Figure 7.14, with cell C1 above and C2 below. Unfortunately the full cell C1 was not captured during the scan, however the gaps between the separator and electrodes was captured. The C1 cell which completed 313 cycles overall showed bloating both at the casing edge and between electrodes and separator. The largest gap between the positive casing and the electrode substrate is 0.76 mm. Around the separator the larger distance (0.12 mm) seen for the positive electrode-separator gap suggests that the gassing is higher with the CuHCF reactions. Looking at cell C2, which completed 7784 cycles shows gaps between all layers within the coin-cell. The largest gaps at the casing side again are near the positive casing (0.89 mm) as well as the distance between the separator and positive electrode (0.33 mm). In this image too we can see the electrode ink clearly, with most of it showing as adhering to the electrode substrate, but with some delamination sen to the left of the 0.33 mm measurement label in Figure 7.14. This again suggests that the main gassing was occurring around the positive electrode.

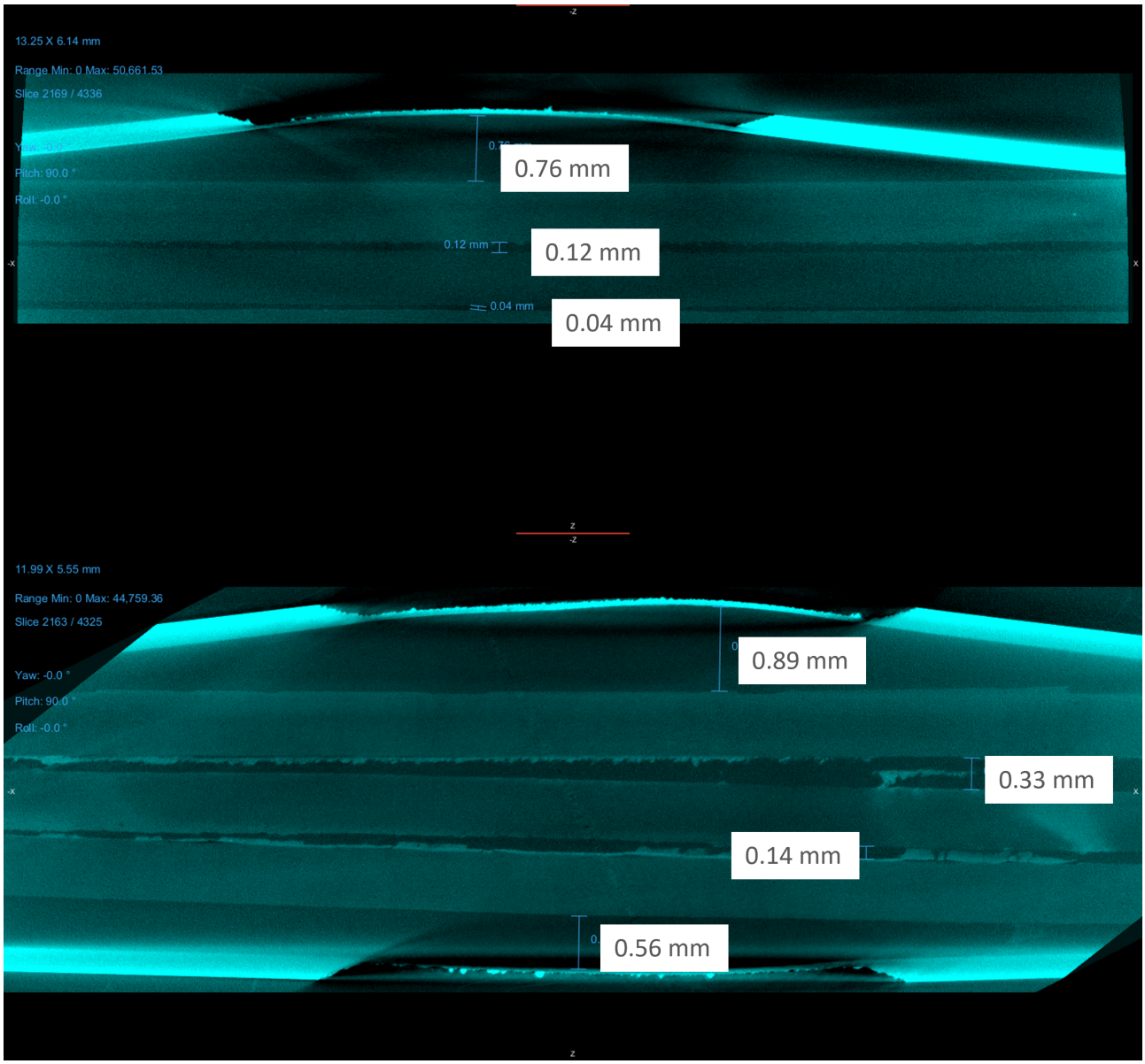

FIGURE 7.14: CT scan of coin-cells cycled with Regime a), C1 above and C2 below

The two cells that cycled on regime b) (C3 and C4) had no rest periods. The CT scans are shown in Figure 7.15. Coin-cell C3 did not maintain any capacity during cycling, but did cycle between the voltages of 1.4 - 0 V for 45,000 cycles. There is evidence of some bloating on this coin-cell, however unlike the cells C1 and C2, the gaps are larger on the negative electrode side - 0.22 mm between the separator and electrode, and 0.28 mm between the casing and electrode substrate. This may be evidence of the rutile phase of the TiO_2 growing here. On coin-cell C4 the overall bloating seen is minimal, with the maximum gap being between the negative electrode and separator (0.12 mm). This coin-cell was cycled for the shortest amount of time in total (2 days, 848 cycles) which may contribute to the reduced overall gassing. The evidence of Al-Ti-O compounds found on the XRD scans for this cell may also be contributing to the

slightly larger gap on the negative side of the coin-cell, there may have been some side reactions here which produced gas.

From looking at both regime a and b cells, it appears as though the coin-cell can tolerate the gassing on the CuHCF side more than that on the TiO_2 side. In terms of understanding the exact charge transfer mechanism, it would make sense that the redox reaction on the CuHCF electrode is more likely to produce gas than the potential surface or pseudocapacitive reactions at the TiO_2 electrode.

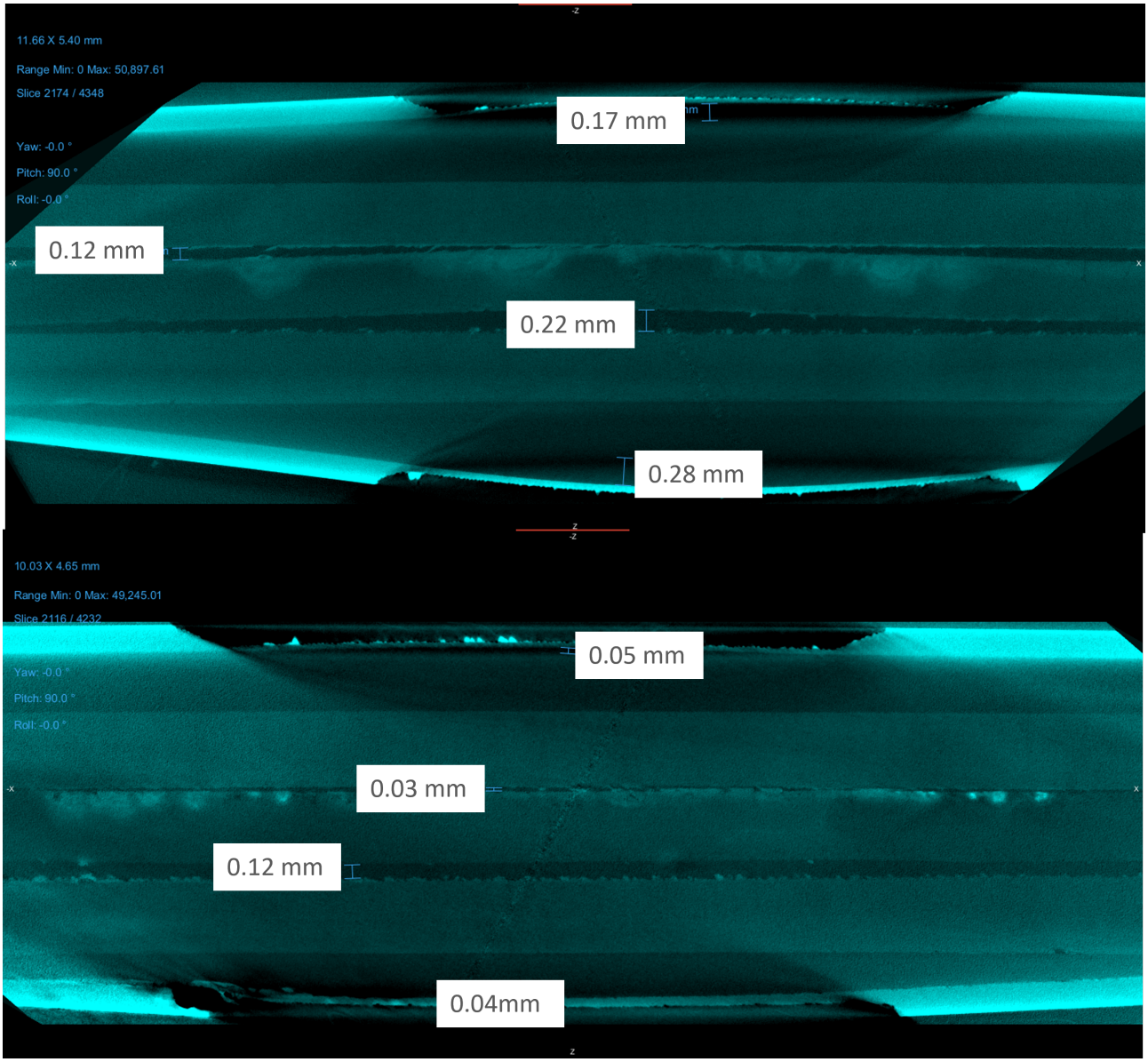

FIGURE 7.15: CT scan of coin-cells cycled with Regime b), C3 above and C4 below

Coin-cell C5 was held at 1.4 V continually, the CT scan shown in Figure 7.17 indicates that while there was some bloating at the negative electrode-case interface (0.16 mm), the gaps between the separator and electrodes are small - 0.06 mm and 0.08 mm at the

negative and positive interfaces respectively. Coin Cell A3, which was held open circuit for the duration of the experiment. This cell showed a growth in Al-Ti-O phases over time, potentially leading to a drop in open circuit voltage to 0 V after 10 months. The growth of these new compounds may have contributed to the larger gap between the negative electrode and the separator (0.13 mm) shown in Figure 7.16, and the slight gap of 0.06 mm between the electrode and negative case.

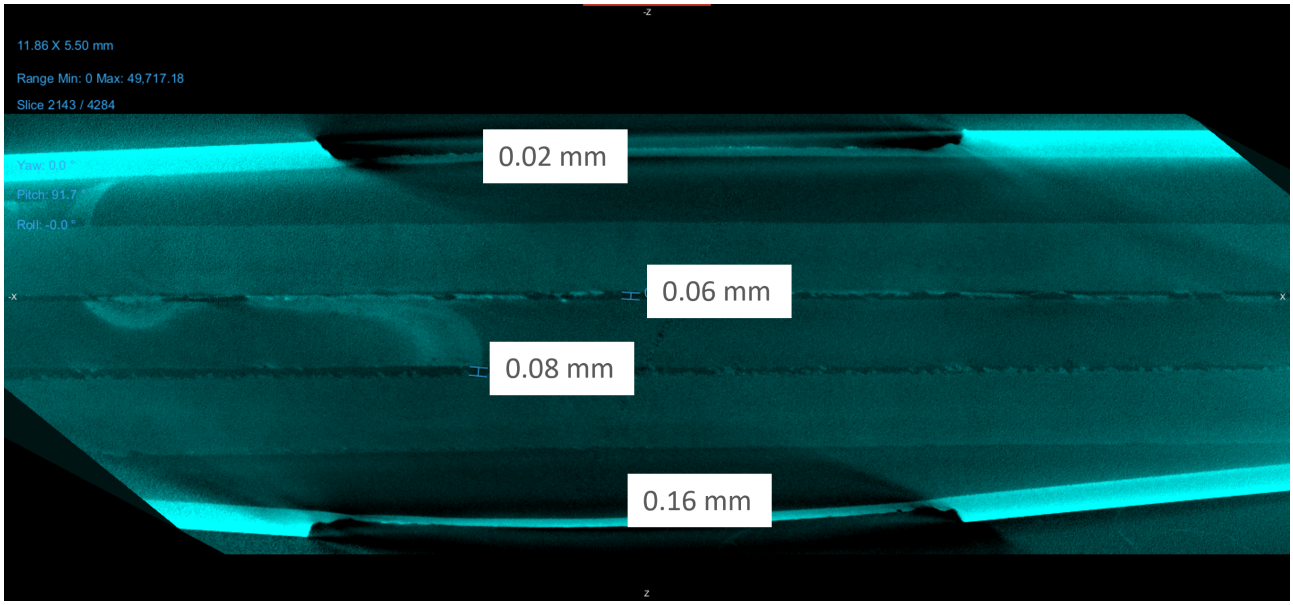

FIGURE 7.16: CT scan of coin-cell C5 post cycling

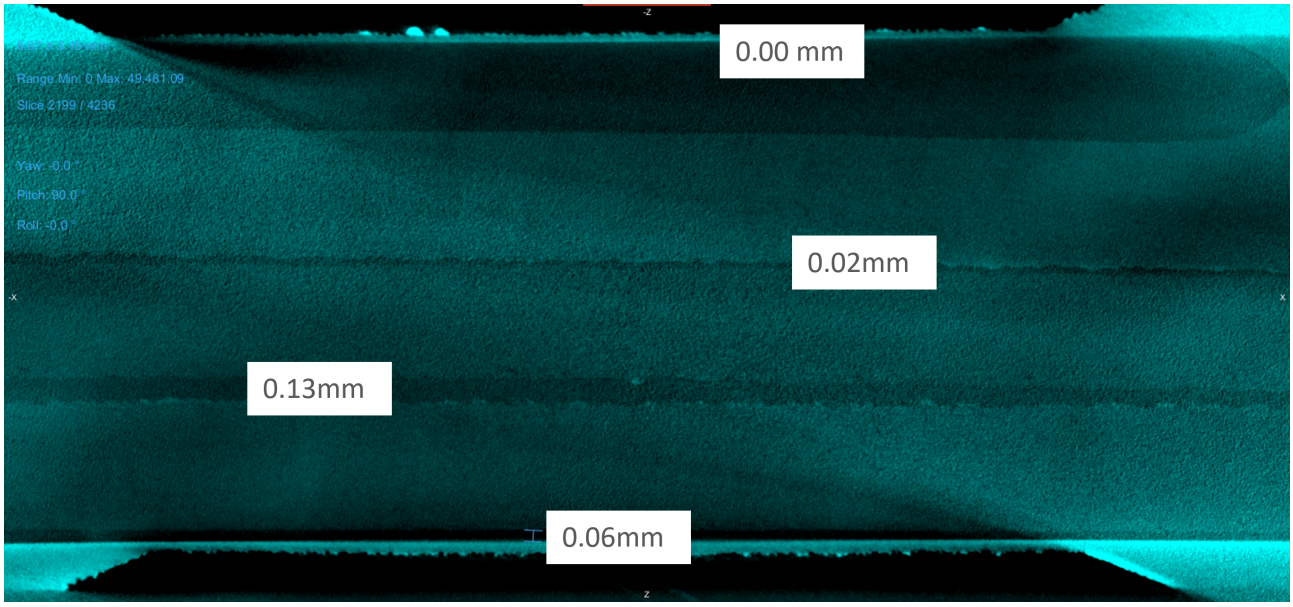

FIGURE 7.17: CT scan of coin-cell A3 post cycling

TABLE 7.1: Summary of outcomes from the long duration experiment at Diamond Light Source

Coin-cell no.	Regime	Total cycles	Highest discharge capacity	XRD comment	CT scan
C1	a	313	1.76 $mAhg^{-1}$	slight broadening and left shifting in CuHCF peaks, contaminant at 10.3°	0.92 mm main areas of bloating on CuHCF side of cell
C2	a	7784	1.21 $mAhg^{-1}$	potential growth of Al_2TiO_5, and/or CuHCF left shifting and broadening	1.92 mm most bloating seen overall, with main areas on CuHCF side of cell
C3	b	45000	0.00 $mAhg^{-1}$	rutile present and peak gowing sharply over time	0.79 mm minimal bloating, largest gap between TiO_2 and casing
C4	b	848	0.82 $mAhg^{-1}$	no change seen	0.24 mm minimal bloating
C5	1.4 V	10	n/a	left shifting of CuHCF peaks	0.32 mm minimal bloating, largest gap between TiO_2 and casing
A3	OCV	10	n/a	growth of $Al_2Ti_7O_{15}$ phase shown over time	0.21 mm least bloating overall, largest gap between TiO_2 and casing

7.7 Discussion and Conclusions

This chapter highlights the difficulties of preparing and measuring batteries both in-situ and operando - yet it also highlights the importance of doing so to fully understand the inner workings of the battery over time. Overall, none of the cells prepared performed as expected, with very low reversible capacities being found. 1 mAh g^{-1} was the 'high' reversible capacity found. This is likely due to the low voltage range in which the cells were cycled, not allowing sufficient potentials for charge and discharge to occur. However this is not the only reason. The cells may not have been well balanced to begin with. While care was taken during manufacturing, the accuracy of the spray coating and low masses may have contributed to this. Two key differences to highlight between what was seen in Chapter 5 with over 7000 cycles being performed is that the cells initially were not crimped which allowed any generated gas to escape, and that the cells were instantly placed on a cycling regime. For the LDE there was a week between the construction of the cells and the setting up of the experiment.

This chapter has also highlighted the difficulty in working with a multi-phase sample for XRD, with stainless steel and PVDF phases showing higher intensity than the phases we are interested in, limiting the analysis to a small range of 2θ values. However, some conclusions can still be drawn.

There is a lack of change in TiO_2 lattice over time, which matches with previous findings (2). However there is evidence of Al-Ti-O compounds becoming more present over time which would reduce available active material within the TiO_2 electrode and therefore reduce capacity over time. This is seen strongly in coin-cell C2 - the highest/most consistent cycling cell - with evidence of Al_2TiO_5, as well as in coin-cell C4, when both coin-cells are at the end of their lifetime. Further, evidence of another compound, $Al_2Ti_7O_{15}$, is suggested in A3 - the cell at constant rest. The evidence of rutile crystal structures within the failed coin-cell (C3), shows the importance of manufacturing with high purity anatase TiO_2 to ensure we understand if rutile is a contaminant that causes failure or a product of a certain mode of cell failure. Rutile TiO_2 was not seen in any of the cells which completed full cycles, including A3 and C5 which completed ten cycles prior to their testing conditions.

When looking at the CuHCF, the broadening and left shifting of peaks was seen in cells C1, C2 and C5. These features suggest the particle sizes reducing or becoming amorphous. As cell C5, held at 1.4 V constantly also shows this broadening, it would indicate that particle strain increasing is a likely cause of this due to accommodation of Al^{3+}.

The bloating of the coin-cells was assessed with CT scans. The bloating of the cells has two-fold implications. With bloating between layers, the contact between them reduces, which reduces the overall area available for electrochemical or pseudocapacitive reactions. We would expect the largest bloated areas to have the lowest overall capacity and cycle life. However, as the bloating is a result of gasses produced from either a redox or parasitic reaction, more bloating would be present in a cell that has a higher capacity or more cyles. It is difficult to ascertain which of these mechanisms was in play, as we only have scans from the end of life and were not able to CT scan the cells throughout the lifetime testing. In future, it would be useful to perform both CT and XRD scans in tandem, in order to ascertain when the bloating begins and map that to the overall performance and phase changes within the cell.

Looking at Table 7.1 we can see that the coin-cells on regime a) show the highest amount of bloating overall. Coin-cell C2, the best overall performing coin-cell, has the largest bloating overall. It was expected that coin-cell A3 would show no or little change in terms of gas production, but this study suggests even at OCV there are parasitic reactions occurring. It is encouraging to see that 7784 cycles were successfully performed for coin-cell C2 (with around 7000 of stable capacity),

matching closely the number of cycles seen in the open coin-cell from Chapter 5 - and over 5 times that seen in Holland's work (84).

The link between the rutile phase and the environment in which it grows and inhibits charge storage is an interesting area of further research highlighted from this chapter - and previously discussed in literature (2). Do we know if this rutile phase develops due to failure, or if the presence of the rutile phase itself is the cause of the failure? In future, it would be useful to re-design a cell using a casing material that does not diffract so strongly as stainless steel, and plan to perform CT scans of the cells at multiple times during the cycling to view where the bloating starts within the cell and how it migrates over time. XRD measurements of both charged and discharged states would also provide additional information, although this can be difficult to perform due to the differing cycling regimes and limited time in which to collect sample measurements. Further, given the low voltage range and therefore capacity of the coin-cells cycled, realistic use cases were not performed. Fitting the cell with a valve or using a different cell design would allow for the full voltage to be reached, but may not be compatible with the synchrotron. The operando, in-situ approach to understanding cell changes over time is a complex approach, however it has provided insights into the mechanisms of this cell and with refinement can show more in the future.

Chapter 8

Conclusions and future work

The work in this thesis followed a methodology which prioritises the environmental impact of the end product to inform the design and development directions of an aqueous aluminium-ion battery. By starting with a life-cycle assessment, key performance improvements which were linked to reducing overall CO_2 emissions of the battery were found. Firstly, ensuring the utilisation and amount of active material was of a higher percentage of the overall battery mass, and secondly, by increasing the overall cycle life of the battery itself.

LCA has been an excellent tool in both providing a baseline for the current environmental impacts of the design, and exploring the environmental impacts of design changes. An overall assessment of the functional energy density of the battery over its lifetime allowed a parameter space to be created in which batteries could be compared - see Figure 4.8. Further, by using the model built to assess impacts, the different support materials and electrode substrates were tweaked, to understand the overall environmental impacts of design changes to the overall battery. It was found that by increasing the active material utilisation, which effectively reduces the mass of the support material required, a reduction in environmental impact is seen. Alongside increasing the cycle life of an individual battery, this was found to reduce the overall impacts of an individual battery over it's lifetime. While the chapter exploring LCA focused on the quantitative outputs, it is difficult to 'put a number' on reduced environmental impacts, due to how many assumptions are required when assessing the theoretical production of a lab-based cell . However, the overall trends and conclusions taken from this assessment are strong.

The LCA model was then used for an assessment of a practical application of the aq. Al-ion battery. By understanding the environmental impacts of a Dual Energy Storage System (DESS) within electric vehicles, the argument for diversifying our energy storage solutions is made abundantly clear. The economic benefits for DESS is already largely reported, owing mainly to the increased usable lifetime of the system. By

analysing both an EV car and bus, as BESS and DESS, the environmental impacts were clear - over the lifetime of the electric vehicle, the environmental impacts are reduced by about a third when using a DESS.This is true whether the high power component is a traditional supercapacitor or the aq. Al-ion battery. This has implications for further development of the aq. Al-ion battery, as the environmental impacts will reduce as this battery design is developed. Taking into account the uncertainties around raw material acquisition and transportation, as well as the electricity sources used in manufacturing, the DESS still shows to be the most environmentally sustainable option for our long life electric vehicles.

The LCA has proven vital in allowing future design directions to be assessed, such as coin cell design or using carbon felts as the electrode substrate. Creating a new metric of competitive functional energy density (CFED) allows design goals to be created that serve the environmental impacts and the performance of the batteries. The LCA should continue to be seen as a tool that can be used at all stages of design development, to pin-point environmental impacts and evaluate options for improving them. This is something that needs to be widely utilised in the energy storage industry to ensure we are not just meeting performance targets, but environmental ones too.

An aspect of increasing active material percentage is reducing the amount of support material. This includes use of thinner metallic casing, such as the coin cell example explored in Chapter 4, and developed practically in Chapter 5. While using an un-crimped coin cell, over 7000 cycles were completed with an overall functional energy density of 63.4 kWh - pushing this cell into the competitive space in terms of CO_2 emissions compared to Li-ion. However on crimping closed the coin cell, it was clear that gassing was an issue for a closed cell - and so to operate a coin cell successfully with this chemistry, the voltage range would need reducing, reducing the FED. Future work should look into including valves or additives to minimise the build-up of gas within the cells.

In taking further direction from LCA, using carbon felts to increase the amount and utilisation of active material was studied. This was not a linear improvement, as was assumed with the initial LCA. Increasing the amount of active material did not necessarily increase the specific discharge capacity when using carbon felt electrode substrates. Ensuring that the active material is fully utilised is not a simple problem to solve. There are many factors at play and an overall parameter space involving the felt porosity, active material loading and compression must be created, as well as taking temperature into account. As was noted, higher discharge capacities were seen with lower loadings of active material, which were impacted by potential surface reactions, low bulk conductance of the ceramic active materials, and the compression of the electrode. Further, balancing the cell will also need to be considered and a full cell needs to be evaluated. But if looking back to Chapter 4, it may be possible to meet a

competitive functional energy density with carbon felt electrodes - given the high discharge capacities found in the half cells.

Further exploration of how the aq. Al-ion cell changes over its lifetime was performed via a long duration experiment at DLS. While there was no obvious trend seen across all of the coin-cells, it's clear that rutile phases of TiO_2 within the electrodes inhibit performance of the battery dramatically. Further, it appears that over time there may be a new layer which forms over the TiO_2 electrode, as A-Ti-O compounds, which have been seen in previous studies. The CuHCF was found to have broader peaks over the lifetime of the battery, suggesting particles becoming smaller, or amorphous, and potentially leading to the increase of battery capacity during cycling. Overall, this experiment has helped understand some of the processes during the lifetime of the battery, but has also highlighted the difficulty in analysing multi-phase XRD for in-situ operando cells.

To answer the initial research question - Can we use environmental impacts to drive the design of a sustainable battery? Yes. We can and we must. Using LCA is one example of a tool that is vital to ensure that the goal of a sustainable future, of 'net zero', is met. We can create a parameter space in which both the cycle life, energy density and an environmental impact (in our case CO_2) are considered - see Figures 4.8, 5.18 and 6.8. This ensures that we develop our battery technology alongside an understanding of all the environmental impacts and not focus purely on performance improvements to meet customer or industry demands. The focus for enhanced performance must go hand-in-hand with reducing environmental impacts. This thesis has shown that by starting with the environment in mind, we can gain understanding to improve the battery performance without sacrificing our planet.

While this thesis has answered the initial research questions - there are many aspects that would be pertinent to revisit and reflect on. It should be noted that this work was carried out during the covid-19 pandemic and, as such, access to laboratories and facilities was limited for the first year of the PhD Given this, the experimental work did not have sufficient time to fully develop and provide clear answers. The carbon felt electrodes were investigated in terms of active material density. However experiments in terms of cycle life were not performed, nor was there time to balance these cells and create a fully cycling cell. The evidence of CuCl on the felts after cycling should have been investigated further, with different current collectors (or even relying on the carbon felt itself to provide this) investigated to eliminate the parasitic reactions and understand how to limit any others. The investigations into how all of this interplays with the compression of the felt itself were also fascinating, however it may have been too early to start exploring this as there were many questions left half-answered. The downside of the time-limited PhD and academic curiosity is that we cannot answer every question we have, and that by investigating, new questions, not answers, tend to be the outcome.

This thesis has highlighted that an open cell or valved design will be the best topography for this aq. Al-ion system. But as already stated, the key highlight of this thesis is that we can use LCA to develop our batteries in a more sustainable way.

Appendix A

Aqueous aluminium energy storage tables

TABLE A.1: Negative electrode materials and mechanism assumptions

Electrode material	Half or full cell	Electrolyte	Specific capacity	Coulombic efficiency	Cycles performed	Capacity fade	Mechanism assumption	Ref.
TiO_2 nanotubes	Half cell	1M $AlCl_3$	75 mA h g^{-1} @ 4 mA cm^{-2}	90% [a]	14	Not discussed	Intercalation into TiO_2. Speculation of Ti^{4+}/Ti^{3+} redox couple	(3)
TiO_2 nanotube array	Half cell	Various combinations of NaCl + $Al_2(SO_4)_3$	75 mA h g^{-1} @ 4 mA cm^{-2}	Not discussed	Not discussed	Not discussed	Ti^{4+}/Ti^{3+} redox couple, speculation of Cl^- assistance in Al^{3+} insertion	(4)
TiO_2 nanosphere	Half cell	1M $AlCl_3$	180 mA h g^{-1} @ 50 mA g^{-1}	90% [a]	30	6%	Not discussed	(89)
TiO_2 anatase nanopowder	Half cell	1M $AlCl_3$ + 1M KCl	15.6 mA h g^{-1} @ 2.85 mA g^{-1}	99%	5000	15%a	Speculation on pseudocapacitive behaviour of Al and TiO_2	(2)
TiO_2 anatase nanopowder	Half cell	1M $AlCl_3$ + 1M KCl	15 mA h g^{-1} @ 40 A g^{-1}	100% a	Not discussed	Not discussed	Pseudocapacitive behaviour of Al and TiO_2	(84)

Continued on next page

Table A.1 – *Continued from previous page*

Electrode material	**Half or full cell**	**Electrolyte**	**Specific capacity**	**Columbic efficiency**	**Cycles performed**	**Capacity fade**	**Mechanism assumption**	**Ref.**
TiO_2 anatase nanopowder	Full cell with CuHCF positive electrode	1M $AlCl_3$ +1 M KCl	10 mA h g^1 @ 333 mA g^1	90%	1750	7%	Al^{3+} surface adsorption or intercalation	(1; 18)
TiO_2 Rutile nanopowder	Half cell	1M $AlCl_3$	29.4 mA h g^{-1} @0.5 A g^{-1}	89.8%	50	23% [a]	Al^{3+} insertion in preference to the hydrogen evolution. Different long term behaviour to anatase noted	(87)
TiO_2 graphene	Half cell	Various $AlCl_3$ (0.011M) $Al2(SO_4)_3$ (0.5M) $Al(NO_3)_3$ (1M)	50 mA h g^{-1} @6.25 A g^{-1} for 0.25 M $AlCl_3$ electrolyte	Not discussed	120 with 0.25 M $AlCl_3$ electrolyte	50% [a]	Graphene minimised resistance for charge carriers in the TiO_2, and enhanced insertion into electrode. Possibility of crystal phase transition of TiO_2 to aluminium titanate.	(5)

Continued on next page

Table A.1 – *Continued from previous page*

Electrode material	**Half or full cell**	**Electrolyte**	**Specific capacity**	**Columbic efficiency**	**Cycles performed**	**Capacity fade**	**Mechanism assumption**	**Ref.**
graphene-TiO_2 nanocomposite	Half cell	0.5M $AlCl_3$	54 mA h g^{-1} @6.25 A $^{-1}$	Not discussed	20%	Capacity increased during cycles	reversible crystal phase transition of TiO_2 to aluminium titanate	(195)
TiO_2 anatase nanopowder	Full cell with graphene positive electrode	1 M $AlCl_3$	40 mA h g^{-1} @ 1 mA cm^{-2}	Not discussed	1000	38% [a]	Not discussed	(117)
T-Al (Al pre-treated with chloroaluminate melts)	Full cell with MnO_2 positive electrode	2M $Al(CF_3SO_3)$ 2M $Al(CF_3SO_3)_3$ + 0.1 M $Mn(CF_3SO_3)_2$	168 mA h g^{-1} @100 mA g^{-1} 100 mA h g^{-1} @ 500 mA g^{-1}	100% [a]	40 100	Not discussed	Plating and stripping of Al on surface Al ions stripped from the anode may react with electrolyte and form a complicated product rich in Al and electrolyte components.	(91)

Continued on next page

Table A.1 – *Continued from previous page*

Electrode material	Half or full cell	Electrolyte	Specific capacity	Columbic efficiency	Cycles performed	Capacity fade	Mechanism assumption	Ref.
T-Al	Full cell with Birnessite MnO_2 positive electrode	2M ($Al(OTF)_3$)	350 mA h g^{-1} @100 mA g^{-1}	Not discussed	30	88%	Plating and stripping of Al on the surface	(121)
		2M ($Al(OTF)_3$) + 0.5 M $MnSO_4$	554 mA h g^{-1} @ 100 mA g^{-1}		65	42%		
T-Al	Full cell with MnO_2 positive electrode	5M ($Al(OTF)_3$)	467 mA h g-1@ 0.01 mA cm^{-1}	80%[a]	65	42%[a]	Plating and stripping of Al on the surface	(92)
Al foil	Full cell with Bi_2O_3 positive electrode	1M $AlCl_3$	103 mA h g^1 @ 0.5 Ag^{-1}	99%	70		Not discussed for Al	(119)

Continued on next page

Table A.1 – *Continued from previous page*

Electrode material	Half or full cell	Electrolyte	Specific capacity	Columbic efficiency	Cycles performed	Capacity fade	Mechanism assumption	Ref.
MoO_3	Half cell	1M $Al(NO_3)_3$	308 mA h g^{-1} @ 1 A g^{-1} 232 mA h g^{-1} @ 8 mA g^{-1}		Not discussed	Not discussed	Reversible intercalation of Al^{3+} between MoO_3 nanobelts	(100)
MoO_3	Full cell with $VOPO_4$ positive electrode	Gelatin-polyacryylamide hydrogel	88 mA h g^{-1} @ 6 A g^{-1}	100%a	2800 @ 1 A g^{-1}	13.8%	As above	(100)
MoO_3	Half cell	1M $AlCl_3$	680 mA h g^{-1} @ 2.5 A g^{-1}	99%[a]	350	75%[a]	Reversible diffusion-controlled intercalation, with high Al^{3+} trapping in the first cycle	(6)

Continued on next page

Table A.1 – *Continued from previous page*

Electrode material	**Half or full cell**	**Electrolyte**	**Specific capacity**	**Columbic efficiency**	**Cycles performed**	**Capacity fade**	**Mechanism assumption**	**Ref.**
MoO_3 nanowire	Half cell	1M $AlCl_3$	300 mA h g^{-1} @ 3 A g^{-1}	89%	400	10%	Hexagonal crystal structure of electrode allows easy intercalation. Redox pair Mo^{6+}/Mo^{5+} and Mo^{5+}/Mo^{4+}	(197)
Al	Full cell with V_2O_5 positive elctrode	2M $Al(OTF)_3$	186 mA h g^{-1} @ 40 mA g^{-1}	Not discussed	50	89% (35% with Nafion barrier on V_2O_5 electrode)	Not discussed for Al	(107)
Ppy coated MoO_3	Full cell with CuHCF positive electrode	PVA-$Al(NO_3)_3$ hydrogel	30 mA h g^{-1} @ 200 mA g^{-1}	Not discussed	100	16.8%	Not discussed	(60)

Continued on next page

Table A.1 – *Continued from previous page*

Electrode material	Half or full cell	Electrolyte	Specific capacity	Columbic efficiency	Cycles performed	Capacity fade	Mechanism assumption	Ref.
Al foil	Full cell with KNCHF positive electrode	5M $Al(CF_3SO_3)_5$	46.5 mA h g^{-1} @ 20 mA g^{-1}	100%[a]	500	43%[a]	Plating and stripping, with Ni acting as a catalyst to create an unstable interface	(99)
Zn-Al alloy	Full cell with MnO_2 positive electrode	2M $Al(OTF)_3$	700[a] mA h g^{-1} @ 100 mA g^{-1}	100%[a]	80	35%[a]	Plating and stripping of Al, Zn substrate providing protection from passivation layer growth and Al providing shielding from Zn dendrite growth.	(96)

[a] values estimated from graph data

TABLE A.2: Positive electrode materials and mechanism assumptions

Electrode material	Half or full cell	Electrolyte	Specific capacity	Coulombic efficiency	Cycles performed	Capacity fade	Mechanism assumption	Ref.
Vanadium pentoxide xerogel (xero- V_2O_5)	Half cell	1M $AlCl_3$	120 mA h g^{-1} @ 60 mA g^{-1}	Not discussed	12	38%[a]	Al ions and water molecules co-intercalate into V_2O_5. Proton exchange in the V_2O_5 interlayers may also be occurring. This is a diffusion-controlled process.	(103)
$FeVO_4$ nanorods	Half cell	1M $AlCl_3$ + ammonium hydroxide	350 mA h g^{-1} @ 60 mA g^{-1}	Not discussed	20	85%[a]	Complex reversible Al^{3+} insertion/reaction mechanism and poor insertion kinetics. Converting lattice of electrode	(105)

Continued on next page

Table A.2 – *Continued from previous page*

Electrode material	**Half or full cell**	**Electrolyte**	**Specific capacity**	**Columbic efficiency**	**Cycles performed**	**Capacity fade**	**Mechanism assumption**	**Ref.**
Bronze-type vanadium oxide (VO_2 – B) holey nanobelts	Half cell	5M $Al(TOf)_3$	234 mA h g^{-1} @ 150 mA g^{-1}	100%[a]	1000 @ 1 A g^{-1}	0.228	H^+ and Al^{3+} co-intercalation	(106)
Vanadium Phosphate ($VOPO_4$)	Half cell	1M $Al(NO_3)_3$	115 mA h g^{-1} @ 1 A g^{-1} 64mA h g^{-1} @ 6 A g^{-1}	Not discussed	Not discussed	Not discussed	Intercalation of Al^{3+} accompanied by V^{5+}/V^{4+} and V^{4+}/V^{3+} reduction	(100)
Vanadium Phosphate ($VOPO_4$)	Full cell with MoO_3 negative electrode	Gelatin-polyacryylamide hydrogel	88 mA h g^{-1} @ 6 A g^{-1}	100%[a]	2800 @ 1 A g^{-1}	13.8%	as above	(100)

Continued on next page

Table A.2 – *Continued from previous page*

Electrode material	**Half or full cell**	**Electrolyte**	**Specific capacity**	**Columbic efficiency**	**Cycles performed**	**Capacity fade**	**Mechanism assumption**	**Ref.**
V_2O_5 nanorods	Full cell with Al negative electrode	2M Al(TOf)$_3$	186 mA h g^{-1} @ 40 mA g^{-1}	74%[a] (100%[a] with Nafion barrier)	50	89% (35% with Nafion barrier)	Al reacting at the surface while protons intercalate into the electrode	(107)
CuHCF	Half cell	1M $AlCl_3$ + 1M KCl	35 mA h g^{-1} @ 1 A g^{-1}	100%	28000	25% with various current densities	Not fully discussed, but suggestions of Fe dissolution into electrolyte.	(**?**)
CuHCF	Full Cell with TiO_2 negative electrode	1M $AlCl_3$ + 1M KCl	10 mA h g^{-1} @ 333 mA g^{-1}	90%	1750	7%	Discussion of K^+ intercalation alongside Al^{3+}	(1)

Continued on next page

Table A.2 – *Continued from previous page*

Electrode material	Half or full cell	Electrolyte	Specific capacity	Columbic efficiency	Cycles performed	Capacity fade	Mechanism assumption	Ref.
CuHCF nanoparticles	Half cell	0.5M $Al_2(SO_4)_3$	75.75 mA h g^{-1} @ 50 mA g^{-1}	Not discussed	400 @ 400 mA g^{-1}	25.6%	Reduction of Fe^{3+} to Fe^{2+} was observed during discharge both in K and non K containing nanoparticles	(198)
CuHCF	Half cell	1M $Al(NO_3)_3$	50 mA h g^{-1} @ 500 mA g^{-1}	Not discussed	Not discussed	Not discussed	Reduction of Fe^{3+} to Fe^{2+} was observed during discharge	(60)
	Full cell with MoO_3 negative electrode	PVA- $Al(NO_3)_3$ hydrogel	30 mA h g^{-1} @ 200 mA g^{-1}	Not discussed	100	16.8%		
$FeFe(CN)_6$	Half cell	5M $Al(OTF)_3$ (WISE)	116 mA h g−1 @ 150 mA g^{-1}	99%	100	39%	Primarily Al^{3+} intercalation, suggests there may also be some K^+ and proton insertion	(113)

Continued on next page

Table A.2 – *Continued from previous page*

Electrode material	Half or full cell	Electrolyte	Specific capacity	Columbic efficiency	Cycles performed	Capacity fade	Mechanism assumption	Ref.
$K_2CoFe(CN)_6$	Half cell	1M $Al(NO_3)_3$	50 mA h g^{-1} @ 0.1 A g^{-1}	95%	1600	24%	Al^{3+} intercalation, and redox couples of Co^{3+}/Co^{2+} and Fe^{3+}/Fe^{2+}	(112)
KNHCF	Full cell with Al foil	5M $Al(CF_3SO_3)_5$	46.5 mA h g^{-1} @ 20 mA g^{-1}	100%	500	43%[a]	Al^{3+}intercalation, and redox couples of $Ni^{3+}/Ni^{2+}$and Fe^{3+}/Fe^{2+}	(99)
MnO_2	Full cell with T-Al negative electrode	2M $Al(CF_3SO_3)$	168 mA h g^{-1} g @100 mA g^{-1}	100%[a]	40	50%[a]	Two phase reaction with soluble Al phase forming on surface of electrode, along with an amorphous MnO_2 layer	(91)
		2M $Al(CF_3SO_3)_3$ + 0.1M $Mn(CF_3SO_3)_2$	100 mA h g^{-1} @ 500 mA g^{-1}		100	Not discussed		

Continued on next page

Table A.2 – *Continued from previous page*

Electrode material	Half or full cell	Electrolyte	Specific capacity	Columbic efficiency	Cycles performed	Capacity fade	Mechanism assumption	Ref.
Birnessite MnO_2	Full cell with T-Al negative electrode	2M $Al(OTF)_3$ + 0.5M $MnSO_4$	554 mA h g^{-1}@ 100 mA g^{-1}	100%a	65	42%	Three step process, Mn^{2+} dissolves into electrolyte on first discharge, on first charge forms layer with Al on electrode surface and this is then reversibly deposited/stripped over subsequent charges.	(93)
Cryptomelane MnO_2 nanowires	Half cell	1M $Al(NO_3)_3$	109 mA h g^{-1} @ 20 mA g^{-1}	Not discussed	60	38%	Al^{3+} intercalation, replacing the K-ions within the lattice, and Mn^{4+}/Mn^{3+}, Mn^{3+}/Mn^{+} redox pairs within the cathode. No structural changes of the nanowires.	(115)

Continued on next page

Table A.2 – *Continued from previous page*

Electrode material	**Half or full cell**	**Electrolyte**	**Specific capacity**	**Columbic efficiency**	**Cycles performed**	**Capacity fade**	**Mechanism assumption**	**Ref.**
Magnesium doped MnO_2 nanorods	Half cell	1M $Al(NO_3)_3$	Not discussed	Not discussed	Not discussed	Not discussed	Diffusion controlled Al insertion, Mn^{4+}/Mn^{3+}, Mn^{3+}/Mn^{+} redox pairs, as well as surface pseudocapacitive storage	(116)
Mn_3O_4	Full cell with Al negative electrode	5M $Al(OTF)_3$ (WISE)	467 mA h g^{-1} @ 0.01 mA cm^{-2}	80%[a]	65	42%	Dissolution of Mn^{2+} into electrolyte and formation of amorphous layer alongside Al^{3+} intercalation	(92)
MnO_2	Full cell with Zn-Al negative electrode	2M $Al(OTF)_3$	700a mA h g^{-1} @ 100 mA g^{-1}	100%[a]	80	35%[a]	Al^{3+} intercalation and redox reactions of Mn^{4+}/Mn^{3+}, Mn^{3+}/Mn^{+}	(96)

Continued on next page

Table A.2 – *Continued from previous page*

Electrode material	Half or full cell	Electrolyte	Specific capacity	Columbic efficiency	Cycles performed	Capacity fade	Mechanism assumption	Ref.
Graphite from 4B pencil sketch	Full cell with TiO_2 negative electrode	1M $AlCl_3$	40 mA h g^{-1} @ 1 mA cm^{-}	Not discussed	1000	38%[a]	Al^{3+} insertion/extraction, expansion of graphite interlayers during this process resulting in cracking of the electrode.	(117)
Graphite with carbon nano particle deposition	Half cell	1M $AlCl_3$	157 mA h g^{-1} @ 1A g^{-1}	Not discussed	3500 @ 50 A g^{-1}	0%	Capacitive surface storage	(118)
Bi_2O_3	Full cell with Al negative electrode	1M $AlCl_3$	1130 mA h g^{-1} @ 1.5 A g^{-1}	99%[a]	70	98%[a]	Alloying between Al-Bi, and interfacial charge separation – pseudo capacitive storage.	(119)

Continued on next page

Table A.2 – *Continued from previous page*

Electrode material	**Half or full cell**	**Electrolyte**	**Specific capacity**	**Columbic efficiency**	**Cycles performed**	**Capacity fade**	**Mechanism assumption**	**Ref.**
WO_3	Half cell	1M $AlCl_3$	100 mA h g^{-1} @ 1.5 A g^{-1}	$< 80\%$	100	Increased capacity to 210 mA h g^{-1}	Intercalation of Al^{3+}	(101)
		0.5M $Al_2(SO_4)_3$	90 mA h g^{-1} @ 1.5 A g^{-1}	80%	100	Increased capacity to 185 mA h g^{-1}		
$Na_3V_2(PO_4)_3$	Half cell	0.1M $AlCl_3$	120 mA h g^{-1} @ 60 mA g^{-1}	Not discussed	20	50%[a]	Combination of surface capacitive storage and intercalation of Al^{3+}	(199)

[a] values estimated from graph data

TABLE A.3: Aluminium-ion based supercapacitors

Electrode materials	Electrolyte	Capacitance	Specific energy	Specific power	Specific capacity	Cycles performed	Fade	Charge storage	Ref.
CuFe-PBA and activated carbon (AC) – asymmetrical	1 M $Al(NO_3)_3$	Not given	13 Wh kg^{-1}	Not given	37 mAh g^{-1} @ 1 C	1000	Specific capacity fade: 10%	Uncertainty as to whether it is pseudocapacitive or purely EDLC	[122]
MnO_2 and Al doped TiO_2 nanotube arrays	1 M $AlCl_3$	554 F g^{-1} @ 10 mV s^{-1}	105.9 Wh kg^{-1}	1.02 kW kg^{-1}	Not given	Not given	Not given	Introduction of Al^{3+} into the TiO_2 lattice increase charge carrier density. MnO_2 maintains high energy density at high power densities	[121]

Continued on next page

Table A.3 – *Continued from previous page*

Electrode Materials	Electrolyte	Capacitance	Specific energy	Specific power	Specific capacity	Cycles performed	Fade	Charge storage	Ref.
V_2O_5 Mesoporous Carbon – symmetrical	1 M $Al_2(SO_4)_3$	290 F g^{-1} @ 0.5 A g^{-1}	18 Wh kg^{-1}	147 W kg^{-1}	Not given	10,000	Specific capacitance fade: 12%	EDLC provided by the carbon, and additional surface redox reactions from Al^{3+} adsorption and V^{5+}/V^{4+} redox couple	[69]
Oxygen rich porous graphene	1 M $AlCl_3$	230 F g^{-1} @ 5 A g^{-1}	Not given	Not given	63.8 mAh g^{-1} @ 5 A g^{-1}	10,000	Specific capacitance fade: 7.4%	EDLC and potential adsorption/desorption	[55]
PEDOT:PSS on carbon cloth substrate and activated carbon	Unknown concentration $Al_2(SO_4)_3$	265 F g^{-1} @ 0.2 A g^{-1}	43.2 Wh kg^{-1}	265 W kg^{-1}	51 mAh g^{-1} @ 100 mA g^{-1}	Not given	Not given	Reduction of charge transfer resistance compared to other cation salts	[123]

Continued on next page

Table A.3 – *Continued from previous page*

Electrode Materials	Electrolyte	Capacitance	Specific energy	Specific power	Specific capacity	Cycles performed	Fade	Charge storage	Ref.
$W_{18}O_{49}$ nanowires (NWs)-reduced graphene oxide (rGO) and rGO	1 M $AlCl_3$	365.5 F g^{-1}@1Ag^{-1}	28.5 Wh kg^{-1}	751 W kg^{-1}	Not given	12,000	3.30%	Intercalation of Al^{3+}	[124]

Appendix B

Life cycle inventory for aqueous aluminium cell

B.1 Baseline LCI

TABLE B.1: LCI baseline from Chapter 4

Material/ Process	PEFCR Geographical reference	PEFCR Dataset name	Dataset used	Year	Unit	Value	Related process
Electrode General							
Polycarbonate	EU-28+EFTA	Polycarbonate granulate (PC)	GaBi ts	2018	mg	2	Polycarbonate (PC) granulate, production mix, at plant, Technology mix, dipenyl carbonate route and phosgene route, 1.20–1.22 g cm^3
Polyvinyl Fluoride	WORLD	Polyvinyl Fluoride	Gabi ts	2018	mg	2	Polyvinyl fluoride, production mix, at plant, polymerisation of vinyl fluoride, 1.77 g cm^3

Continued on next page

Table B.1 – *Continued from previous page*

Material/ Process	PEFCR Geographical reference	PEFCR Dataset name	Dataset used	Year	Unit	Value	Related process
Copper	EU-28+EFTA	Copper Sheet	Gabi ts	2018	mg	10	Copper sheet, single route, at plant, melting and mechanical treatment (fabrication), 8.92 g cm^3
Alcohol	EUR	Alcohol ether sulphate (petro based)	ecoinvent 3.2	2015	mg	1.7	Alcohol ether sulphate (petro based) production, production mix, at plant, technology mix, 100% active substance
Hydrogen Fluoride	EUR	Hydrogen Fluoride	ecoinvent 3.2	2015	mg	1.7	hydrogen fluoride production, production mix, at plant, technology mix, 100% active substance
Chlorine Dioxide	GLO	Chlorine Dioxide	ecoinvent 3.2	2015	mg	1.7	chlorine dioxide production, production mix, at plant, technology mix, 100% active substance

Continued on next page

Table B.1 – *Continued from previous page*

Material/ Process	PEFCR Geographical reference	PEFCR Dataset name	Dataset used	Year	Unit	Value	Related process
Tetrafluoroethane	GLO	Tetrafluoroethane	ecoinvent 3.2	2015	mg	1.7	tetrafluoroethane production, production mix, at plant, technology mix, 100% active substance
Carbon Black	RER	Carbon black, general purposes	ecoinvent 3.2	2015	mg	6.8	Carbon black, general purposes production, production mix, at plant, technology mix, 100% active substance
Propanol	EUR	isopropanol	ecoinvent 3.2	2015	mg	357	isopropanol production, production mix, at plant, technology mix, 100% active substance
Positive Electrode							

Continued on next page

Table B.1 – *Continued from previous page*

Material/ Process	PEFCR Geographical reference	PEFCR Dataset name	Dataset used	Year	Unit	Value	Related process
Ferrous Chloride	EUR	Iron chloride	ecoinvent 3.2	2015	mg	2	Iron (II) chloride production, production mix, at plant, technology mix, 100% active substance
Hydrogen Cyanide	N/A	Hydrogen Cyanide	N/A	N/A	mg	2	could only be modelled as am emission so production not taken into account
Potassium carbonate	EUR	Potassium carbonate	ecoinvent 3.2	2015	mg	2	potassium carbonate production, production mix, at plant, technology mix, 100% active substance
Calcium hydroxide	EUR	Calcium hydroxide	ecoinvent 3.2	2015	mg	2	Calcium hydroxide production, production mix, at plant, technology mix, 100% active substance

Continued on next page

Table B.1 – *Continued from previous page*

Material/ Process	PEFCR Geographical reference	PEFCR Dataset name	Dataset used	Year	Unit	Value	Related process
Chlorine	N/A	Chlorine	N/A	N/A	mg	2	could only be modelled as am emission so production not taken into account
Copper	EU+EFTA	Copper mix, primary+secondary, from CFF	PEFCR	2019	mg	9	CFF Copper - LCI
Nitric Acid	EUR	Nitric Acid	ecoinvent 3.2	2015	mg	9	Nitric acid production, production mix, at plant, technology mix, 100% active substance
Negative Electrode							

Continued on next page

Table B.1 – *Continued from previous page*

Material/ Process	PEFCR Geographical reference	PEFCR Dataset name	Dataset used	Year	Unit	Value	Related process
TiO_2	EUR	titanium dioxide	ecoinvent 3.2	2015	mg	75.45	titanium dioxide production, production mix, at plant, technology mix, 100% active substance
Electrolyte							
$AlCl_3$	GLO	Aluminium Chloride	ecoinvent 3.2	2015	mg	5	aluminium chloride production, production mix, at plant, technology mix, 100% active substance
KCL	EU-28+3	Potassium chloride as K2O at plant EU−28+3 S	Quantis	2015	mg	5	Potassium chloride, at plant, as K2O, per kg K2O

Continued on next page

Table B.1 – *Continued from previous page*

Material/ Process	PEFCR Geographical reference	PEFCR Dataset name	Dataset used	Year	Unit	Value	Related process
deionised water	EUR	deionised water	ecoinvent 3.2	2015	mg	50	De-ionised water production, production mix, at plant, technology mix, 100% active substance
Battery Casing							
Plastic casing	EU-28	Plastic granulate (unspecifiec)	GaBi ts	2012	mg	60	Plastic granulate secondary (low metal contamination), production mix, at plant, from post-consumer plastic waste, via grinding, metal separation, washing, pelletization, plastic waste with low metal fraction
Charger							

Continued on next page

Table B.1 – *Continued from previous page*

Material/ Process	PEFCR Geographical reference	PEFCR Dataset name	Dataset used	Year	Unit	Value	Related process
Charger	GLO	Charger EPTA	Recharge/ts	2010-2012	mg	1.49E-04	taken from reference (23)
Manufacturing							
Power electrode	EU-27	Electricity grid mix	GaBi 6 ts	2011	MJ	1.01E-02	taken from reference (23)
Power cell forming	EU-27	Electricity grid mix			MJ	3.04E-04	taken from reference (23)
Power battery assembly	EU-27	Electricity grid mix			MJ	2.53E-07	taken from reference
Tap Water	EU-27	Tap water	GaBi 6 ts	2012	kg	2.78E-03	taken from reference (23)
Hydrochloric Acid	DE	Hydrochloric acid mix (100%)	GaBi 6 ts	2012	kg	1.15E-04	taken from reference (23)

Continued on next page

Table B.1 – *Continued from previous page*

Material/ Process	PEFCR Geographical reference	PEFCR Dataset name	Dataset used	Year	Unit	Value	Related process
Nitric Acid	EU-27	Nitric acid (98%)	GaBi 6 ts	2012	kg	0.00E+00	taken from reference (23)
deionised water	EU-27	Water (deionised)	GaBi 6 ts	2012	kg	0.00E+00	taken from reference (23)
Waste water treatment	EU-27	Municipal waste water treatment (sludge incineration)	GaBi 6 ts	2012	kg	2.99E-03	taken from reference (23)
Transport							

Continued on next page

Table B.1 – *Continued from previous page*

Material/ Process	**PEFCR Geographical reference**	**PEFCR Dataset name**	**Dataset used**	**Year**	**Unit**	**Value**	**Related process**
Land Transport	EU-28+3	Transport	GaBi ts	2012	kg*km	0.1966	Articulated lorry transport, Euro 4, Total weight 32 t (without fuel), consumption mix, to consumer, diesel driven, Euro 4, cargo, more than 32t gross weight / 24,7t payload capacity
Sea Transport	EU-28+3	Transport	GaBi ts	2012	kg*km	1.00831	Barge, consumption mix, to consumer, technology mix, diesel driven, cargo, 1500 t payload capacity - ROW w/o EU-28+3

B.2 Additional carbon felt input LCI

TABLE B.2: Additional materials added to LCI for carbon felt electrode substrate

Material/ Process	PEFCR Geographical reference	PEFCR Dataset name	Dataset used	Year	Unit	Value	Related process
Battery Casing							
PAN	EU-28	polyacrylonitrile fibres (PAN)	GaBi ts	2012	kg	1	Polyacrylonitrile fibres (PAN), production mix, at plant, from acrylonitrile and methacrylate, PAN without additives
Electricity	EU-28	polypropylene granulate (PP)	GaBi ts	2011	MJ	56	taken from reference (23)

Note that a total of 2597 mg of carbon felt was used for each electrode

B.3 Additional coin cell input LCI

TABLE B.4: Battery casing materials used for coin-cell casing

Material/ Process	PEFCR Geographical reference	PEFCR Dataset name	Dataset used	Year	Unit	Value	Related process
Battery Casing							
Stainless Steel	EU-28	Steel sections	GaBi ts	2012	g	2	Steel sections, including recycling, production mix, at plant, blast furnace route / electric arc furnace route, 1kg
PTFE ring	EU-28	polypropylene granulate (PP)	GaBi ts	2012	g	0.05	Polypropylene granulate (PP), production mix, at plant

Note that the copper current collector was not included in this inventory

Appendix C

Contribution to Exploring Time as a Resource for Wellness in Higher Education - Overwork is not evidence of passion

Below is the chapter contribution made to a forthcoming book exploring wellbeing in academia. While not directly related to this thesis, it was an important piece of work for me. Over the years academia has lost many great people to suicide, and I have personally lost a close friend who was unable to finish their PhD. I truly hope that we can all work to make academia a more inclusive, compassionate and sustainable place to work.

C.1 Abstract

While working in higher education we are told that it is a vocation, that we are driven by passion. While true, this is often used as an excuse to underpay, especially PhD students and those on casual contracts. It is used to justify the expectations to go 'above and beyond' their contracted duties. Passion and drive are weaponised to ensure those in higher education overwork and are made to lose out financially, emotionally, and mentally when they take time for themselves. In this chapter, the term passion will be explored, the ways in which it has been weaponised will be

discussed, and a way forward will be proposed. The chapter will end with reflection questions for PhD students, staff, and senior staff in higher education that should be seen as jumping off points for making real change and ensuring the passion stays alive for those at their institution.

C.2 Introduction

While working in higher education we are told that it is a vocation, that we are driven by passion. While true, this is often used as an excuse to underpay, especially PhD students and those on casual contracts. It is used to justify the expectations to go 'above and beyond' contracted duties. This chapter explores what it means to weaponise our passion and how it has created a culture of overwork. As the topics discussed throughout this book are nuanced, words can have subtly different meanings and loadings. Therefore, this chapter begins with some definitions. The hope is that this chapter is understood as it was intended, that it is clear, concise, free from ambiguity – and a tool that enables reflection, action, and change. This chapter is specifically about the UK higher education and focuses on academic research and teaching staff as well as students.

The Collins dictionary states "If you have a passion for something, you have a very strong interest in it and like it very much" (201). In this chapter, I would also expand this definition to encompass enthusiasm, excitement, and motivation. This can be applied to work in many ways: the topic we study (enthusiastic to learn and talk about our topic); the environment within which we work (motivated to exist in the academic culture, in our office; excited to talk to other people, to socialise, to be part of something collective); and the way in which we work (driven to change or foster strong relationships, support networks, inclusive understanding). The passion itself is often a strong internal driver for the things we do and brings us joy, as well as satisfaction within our lives.

When thinking of overwork, it can be split into both the practical and personal. Practically, overworking means working for more hours than you are either contracted to or have agreed (internally or externally) to. Personally, overwork can be seen as working at the detriment to other factors within your life (neglecting to eat properly, nurture relationships, look after our health), regardless of how many hours that is for. Personal overwork can be applied to both the time worked, as well as the emotional and mental component to overwork. If we work to the extent that we are too fatigued, distressed, or otherwise mentally overwhelmed that we cannot do the things in our lives that we both need and want to do – then we are overworking. We may only spend three hours on a piece of work, but if the topic is difficult, draining, or distressing, this may be too much time, we may be overworking and be unable to

cope for the rest of that day. In Figure C.1, I provide my illustration of how overwork can present itself. We see overwork in academia encouraged through the culture and the contracts within which we work. It is interesting to note that the practical examples are often the addition of actions and extra responsibility, and the personal examples are a decrease in actions, and avoidance of certain responsibilities (such as having to cancel medical appointments). Throughout this chapter, both practical and personal overwork will be discussed and will be identified as such.

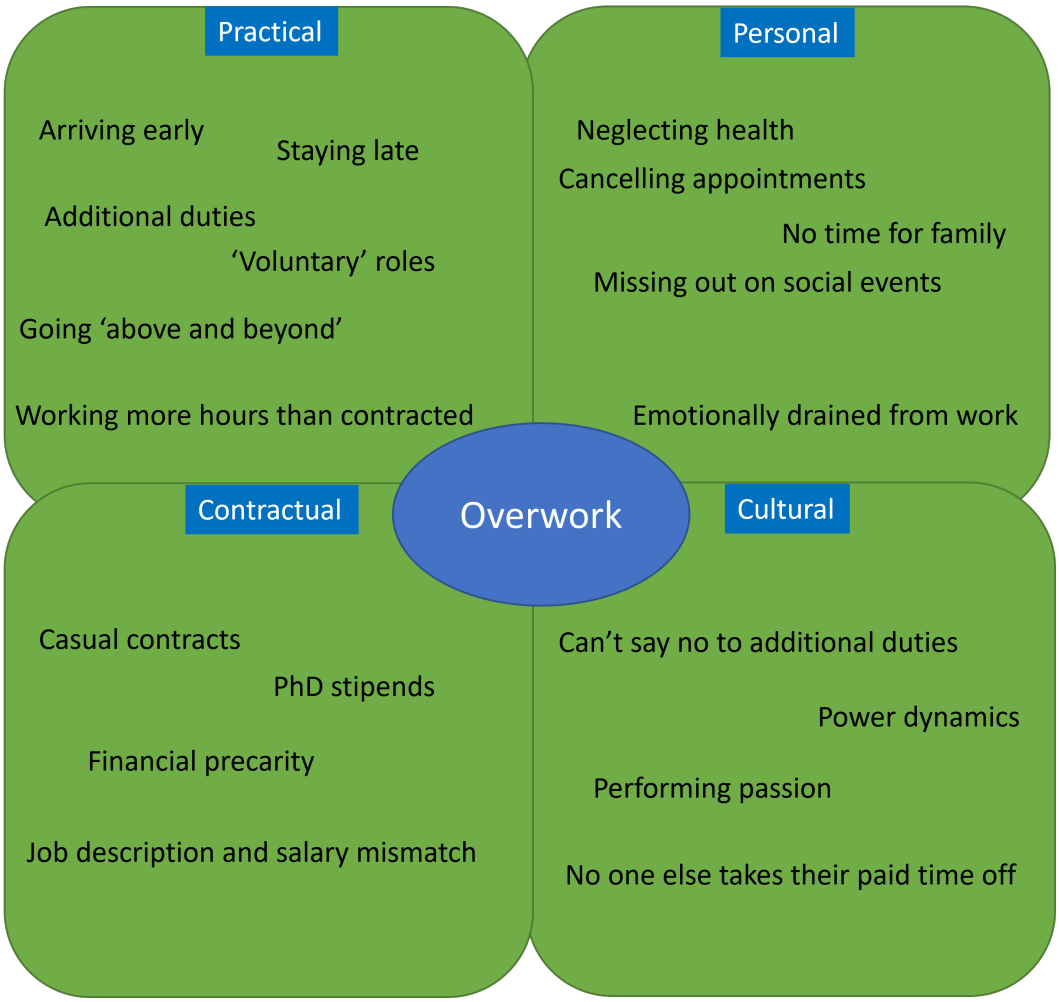

FIGURE C.1: Ways in which overwork can present itself

In more recent years, self-care has been seen as nice-to-haves, a warm bubble bath or a pamper session. However, the core meaning of self-care and its inception is based in the Black community, as it relates to meeting your basic health and wellbeing needs by yourself and within your community (202). Self-care refers to the maintenance elements of our day-to-day, looking after yourself that only you can do. This includes brushing your teeth, staying hydrated, following up on medical needs, and sorting out your financials. Treating yourself to nice things is great for wellbeing, but in this chapter, that is not what self-care refers to.

C.3 Exploring Academic Overwork

C.3.1 The Culture, Power Dynamics, and Overwork

Within any life situation, there are power structures. An employer and employee, a supervisor and supervisee, a manager, and their direct reports. It is also prudent to note that privilege outside of the workplace structure can bring power dynamics into the workplace, and academia too – popular and unpopular people, gender, race, sexuality, disabilities, social status, and even accents can all play into power structures and create dynamics which work to weaponise 'passion' and encourage overwork in an academic environment. The well-known adage of 'publish or perish' within academia further illustrates the pervasiveness of continual overworking. If an academic is not writing and publishing academic articles (which is often in addition to the research and teaching they do – practical overwork), then their career will stagnate (203).

Further, academia for researchers is full of competition. Competing for funding, grants, and awards. Being continually made to compete for these to maintain your job causes anxiety, fear, and overwork, impacting mental health and wellbeing. If your job depends on you securing a grant – you will work and work to ensure you get that grant (204). Unfortunately, though, there is always something new to bid or apply for. So, this competitive undercurrent drives those in academia to push themselves more and more to be eligible for these awards. Within the constraints of grant applications and awards, future contractual overwork is often planned right into the request. Grant applications are costed based on the work required,then, through reviews, these valid costs are often deemed too expensive – the cost needs to reduce to get the funding. So, two posts become one, or roles are merged, principal researcher time is reduced, etc. If this grant is thus awarded, the contracts created and the expectation from everyone will already be 'above and beyond' what has been asked for – which is exactly what the academic culture makes acceptable. An ouroboros of overworked academic researchers.

The culture within the academic environment has been fostered with a historical, stereotypical worker in mind: The male academic, who is able to work long hours on their passions and intrigues with a wife at home looking after the children and the housework, who organises everything else so the male academic can focus on work. Although the demographics of the academy have changed (only slightly with 70% of professors in the UK identify as being male (205)), and academics often have many other responsibilities in their life on top of their research – those at the top, and those setting the standards, are often from the generation of 'kept men', and while these men do not recognise their privilege, they are in a position to demand the same working ethic as was expected of them. This expectation has a hidden support

network embedded, support which many minoritised groups do not have. Therefore, many academics feel pressure to overwork, pressure to neglect their family, friends, caring responsibilities, and self-care, resulting in personal overwork, due to the culture. This pressure, whether it translates to neglect, can lead to increased anxiety. The pressure leads to guilt – both for neglecting their life outside research, and for not working enough on their research. When the power dynamics at play create an environment that takes 'passion' and morphs it into anxiety, we create an academic on the verge of burnout, unable to reach their potential and unable to truly enjoy their passion for research (206).

From X (formally Twitter) – which is itself a small, biased, sample – many examples of overwork culture have been shared. One tweeter discussed that while on maternity leave, they still worked on and submitted a paper, both they and their supervisor thought nothing of it. Later, when interviewed by the ATHENA Swan group (an organisation dedicated to ensuring inclusion and diversity), the committee were shocked that they were expected to work while on leave, although it is not uncommon (207)). Another tweeter shared how they were often told that if you were passionate enough about the work, you won't experience burnout – yes, an academic deciding not to consult studies on how burnout manifests. Many shared how they found themselves working late, checking emails on weekends, and shared a general sense of unease when they were not working. Another tweeter told the story of a supervisor 'showing off' about their sleeping habits (only sleeping once every 48 hours) and how they were surprised when this was met with concern, not congratulations.

Many academics can revel in these identities, love to struggle through and see it as a rite of passage, or a badge of honour. They see it as their hard work being rewarded and that others should be doing the same. There is a toxicity in this view, as it only serves the few who survive, and those who do not make it, cannot take it, leave academia and so their voices are no longer heard. Those who see overwork as passion are the ones who stay in academia; subconsciously or otherwise, they want to re-create the conditions they succeeded in. If you make the game 'easier', create a less hostile culture, their win may feel less meaningful. This only serves to perpetuate the culture that you must overwork to succeed. Instead of asking 'who isn't in the room anymore, who left quietly and overwhelmed?', we continue to listen to those who survive through academia, while they claim they are thriving.

C.3.2 Contractual Overwork for Staff

In calling out the culture as a means of weaponising passion and encouraging overwork, universities and other institutions can easily dismiss this as specific to certain research groups or individuals and argue it is not a problem that exists at the higher levels. However, when we look at specific use of contracts (specifically in the

UK), we can see that the written voice of these institutions also creates a culture of overworking. Over the last decade, there has been an increase in casual contracts for academics. This reduces the amount of full-time, salaried positions and replaces them with a culmination of smaller part-time fixed term positions to deliver very specific pieces of work. Over 66% of academic research staff and 45% of teaching staff are on these casual contracts in UK universities in 21/22 (205).

The University and Colleges Union (UCU) in the UK reports four key costs of casualisation – findings 3 and 4, lack of agency, and an inability to project into the future are major factors in causing overwork (208). The financial precarity these contracts put people in, in addition to the stress involved in delivering work in a short period of time, strips people of their passion for the job and renders people tired, burnt-out, continually anxious for their future, and no longer able to find job satisfaction through their passions.

An example job listing posted on March 2023 at a top British university is for a 9-hour-a-week role lecturing in Hindi studies. This role requires four hours of teaching per week, with five hours remaining for preparing lectures, preparing coursework, marking work, organising tutorials, writing reports on student progress, preparing and delivering examinations including oral exams, conducting research in order to meet scholarship and professional development targets, as well as admin, office hours, serving on faculty committees and taking part in open days. Reading through the job description, you'd be forgiven for thinking that it sounds like an impossible amount of work given the contracted time, and you would be right. Imagine an academic requiring four such roles, potentially at different institutions, to make a full-time salary. This is contractual practical overwork; the role itself is asking for more time than it will pay for.

Even within full-time, open-ended contracts – the overwork is pervasive. The means of calculating workload often do not consider many duties. Mentoring, outreach, activism, time spent doing peer review, and often paper writing itself are not considered but are expected of academic staff. Thanks to the overwork culture baked into the system, this overwork is seen as normal. During 2019, the UCU participated in 'Action short of Strike (ASOS)'; this was defined as doing only what their contracted role was, for the time it was contracted for. To many people outside of academia, this does not sound like ASOS at all, it sounds like how many people behave at work. As a response to the ASOS, many universities threatened pay deductions, specifically for refusing to reschedule anything that was missed during ASOS (209). The huge disruption caused by ASOS at universities is proof that overwork is baked into the contracts and is expected by many academics. Here, we see that the underlying culture and expectation of academia being a passion-driven vocation creates contracts that do not fully list the duties, because why wouldn't someone want to go above and beyond for something they are passionate about?

Often, the small benefits within our contracts that aim to give balance, such as paid time off, are not used. This is where culture takes precedent over the contracts, where the culture of practical and personal overwork lead to helpful contractual terms being unused. The implied view that if one is motivated and satisfied by their research, they shouldn't need time off. This can be seen as competitive suffering, the need to perform overworking, to show dedication to the job. Where most of a contract encourages overwork, having time off stipulated is counter intuitive, and often seen as a test, not a right.

C.3.3 Postgraduate Students, Research, and Overwork

In the UK, the annual stipend given to a PhD researcher in 2023 from UKRI (UK research and innovation) is £17,688. UKRI is the largest funder of PhD stipends in the UK, funding around 8000 studentships every year. This amount equates to about £340 a week, and, assuming a PhD researcher works 37 hours on their PhD each week, they are being paid £9.18 per hour – below minimum wage for the UK. Assuming a PhD researcher in the UK is worth about £15 per hour, they should be working about 22 hours a week and spend the rest of their time on other paid work. But how many of us know a full-time PhD researcher who spends 22 hours a week on their work. A 2005 in-depth study of postgraduate researchers in Oxford found that "28% spend 30 or less hours a week on their research, 43% spend between 31 and 45 hours, and 29% spend more than 45 hours a week on their research" (210). Further, this study found that those who spent less time on their research also felt less supported by their department and in their work. We would not expect that PhD students are valuing themselves below minimum wage – and they are not. The same study found that those who spent more than 30 hours a week on research saw their research as better than those who worked less. Therefore, working for more hours equates to a perceived increase in research value but an actual decrease in their hourly wage. This all shows quite clearly that however you look at it, PhD researchers in the UK are undervalued and overworked.

The PhD is meant to be an introduction into academic life, into research, academic writing, teaching, and, I suppose, the overwork culture. During a PhD, the student must keep a good relationship with their supervisor, as this is the person who approves your work and can help shape your future within the field. Because of this power dynamic at play, PhD students will find it hard to say no to their supervisor when new aspects of work are suggested, or when additional work is proposed. Often, a PhD student may find themselves supporting their supervisor in work unrelated to their project, be that in helping masters students or providing research and experimentation. This is done in addition to the work required for the PhD project and creates extra pressure on the student. Saying no to a supervisor may

damage the relationship but will free up time to work on the PhD. Saying yes to a supervisor will improve the personal relationship, will show that you are passionate about the field of work, not just your PhD work. However, your own research, your personal life, and general wellbeing may suffer. The UK produced 26,980 PhDs in 21/22 (205), while many of them won't pursue further academic jobs, for those that do, the competition is fierce, and PhDs often find there are at least 250 applicants per job. Therefore, all the extra work, 'above and beyond' experience and other proof of passion feels necessary to have a chance at an academic career. But a career based on the unhealthy overworking ethic cannot be sustainable.

Those undertaking postgraduate roles also have practical overwork baked into their stipend agreements, setting students up to expect to be paid for a fraction of the work they do. This makes postdoctoral jobs acceptable within a framework of overwork. We see further that student advisors, who themselves were brought up in the same culture, see no issue demanding yet more work and unrelated work from their students – further squeezing the capacity of the student and leading them to neglect their self-care and wellbeing. PhD students have a high rate of depression and suicide in the UK with 40% of PhD students at risk of suicide (211), and many cite the pressure to continually be working and performing passion as a major driver. Increased levels of anxiety and depression for PhD students was also found for those spending more time on their research per week (over 41 hours) (212). This culture is harming passionate academics. We need to change.

C.4 The Author's Perspective

We don't all have the same 24 hours in a day. As a disabled PhD candidate, I experience that first hand. I need to manage my energy, my symptoms, and of course, my work. I live with dissociative identity disorder (DID), I have chronic migraines, nerve damage, and I am autistic. These are all called invisible disabilities since they are not apparent at first glance. However, I can assure you they are not invisible to me.

One key impact of being disabled is that my time becomes limited. I lose time through medical appointments, through having migraines, through dissociating. I lose time through having to chase down medical tests or prescriptions. I lose time through needing to rest and recover from dissociative episodes. I also lose time talking to the university disability offices, requesting accommodations, chasing those accommodations, and complaining about my accommodations and access needs not being met – something felt by many disabled academics(213). I also lose time talking about being disabled in academia and being disabled in STEM, because I feel guilty if I do not take these opportunities, as discussed earlier. Therefore, the amount of work I can do is time-limited for me. This does not stop me feeling pressure to work more,

and even when I do push myself and overwork – I still work far less than many other PhD students. I struggle with this. In December 2020, my medication was unavailable, so I took two weeks off sick with debilitating anxiety and withdrawal symptoms. I felt guilty, I started thinking that a PhD wasn't for someone like me, that I would never make it in academia. I was lucky in that my supervisor was (and continues to be) supportive. We set long-term goals so that I do not feel pressured to get everything done at once. This doesn't always help – because I see other students, other researchers. I see them coming in on weekends to do experiments or staying late at the office reading paper after paper. Something I cannot do, something I know isn't sustainable for them, and yet something I feel jealous of, and guilty about.

On average, I spend about 30 hours a week on my PhD. It feels strange admitting that, like admitting a huge crime, making a terrible confession. I know if I push myself to work for longer hours, I risk my health but that doesn't stop the continual thoughts that I should be doing more. Heck, I'm writing this book chapter when my main research area is in batteries and energy storage. I am working on this because it is important, and because I am passionate about this topic – I am falling into the exact same way of thinking that this chapter presents. I exist within the overwork culture of the academy, I have internalised it, and in that, you get to read this chapter. Is that irony? I'm not sure. Is it okay? Probably not. Will it continue? Yes. Because my drive and motivation to make a difference in this space has led me to work for free, on a topic not related to my PhD.

C.5 Conclusions, Reflections, and Calls to Action

The exploitation of passion transforms it into anxiety – the motivation and drive to perform is still there but it no longer comes from a place of excitement but a place of fear. The fear that others will not view them as passionate enough, that they are not performing their passion as well as others in their field (214). But for passion to truly be explored and realised, for our wellbeing to be supported through our work, all other aspects of our lives need to be supported too. Creating an environment of overwork causes people to resent what they previously loved, leading to guilt and shame and a feeling of "I should be enjoying this, I'm spending all my time on a topic I am passionate about". This leads to burnout, mental health issues, and the loss of brilliant, brilliant people from academia. Please use the reflection questions in C.1 to help process this chapter and what you can do.

TABLE C.1: Reflection questions for reducing overwork in academia

For everyone	Look at the figure for this chapter, do you recognise any of this in yourself?
	Can you talk to your peers (students, colleagues) about how you're feeling?
	Have you noticed your mood is tied to your work? Do you feel guilt when you are not working?
	Do you feel safe to talk to your supervisor/manager about this? If not, do you have someone you can talk to about this?
	Can you do less? Can you cut part of your project and still produce good work?
	Are you passionate about your topic? What do you need to help find that passion?
	How much time do you spend doing voluntary or additional roles?
	Are you neglecting yourself? Your wellbeing and your self-care?
For staff	Does your contract reflect the work you do and the time you spend doing it? Do you know who to talk to if not?
	Are you taking your paid time off? If not, why not? Can you book something off now, even a half day?
	Are your colleagues on casual contracts? If so, how can you support them?
	Are you expecting your students to overwork? Are you assuming passion based on the time they spend working?
	Do you or your colleagues have marginalised identities? How can you be supported or support others to limit overwork?
For senior staff	Why are you reading this book, this chapter? What did you want to get out of it?
	Do you know how many members of staff are on casual contracts?
	How do you calculate workload for staff? How can you take account of 'extra duties'?
	Do you encourage others to take their paid time off?
	Do you judge staff based on their working hours, perceived passion and eagerness to go 'above and beyond'?
	Are you asking for even more from your minoritised staff?
	How can you change the culture in your organisation?

References

[1] A. Holland, R. D. McKerracher, A. Cruden, and R. G. A. Wills, "An aluminium battery operating with an aqueous electrolyte," *Journal of Applied Electrochemistry*, vol. 48, no. 3, pp. 243–250, 2018. https://doi.org/10.1007/s10800-018-1154-x.

[2] A. W. Holland, R. McKerracher, A. Cruden, and R. G. A. Wills, "Tio2 nanopowder as a high rate, long cycle life electrode in aqueous aluminium electrolyte," *Materials Today Energy*, vol. 10, pp. 208–213, 2018. https://doi.org/10.1016/j.mtener.2018.09.009.

[3] S. Liu, J. J. Hu, N. F. Yan, G. L. Pan, G. R. Li, and X. P. Gao, "Aluminum storage behavior of anatase tio2 nanotube arrays in aqueous solution for aluminum ion batteries," *Energy & Environmental Science*, vol. 5, no. 12, pp. 9743–9746, 2012. https://doi.org/10.1039/C2EE22987K.

[4] Y. Liu, S. Sang, Q. Wu, Z. Lu, K. Liu, and H. Liu, "The electrochemical behavior of cl- assisted al3+ insertion into titanium dioxide nanotube arrays in aqueous solution for aluminum ion batteries," *Electrochimica Acta*, vol. 143, pp. 340–346, 2014. https://doi.org/10.1016/j.electacta.2014.08.016.

[5] H. Lahan, R. Boruah, A. Hazarika, and S. K. Das, "Anatase tio2 as an anode material for rechargeable aqueous aluminum-ion batteries: Remarkable graphene induced aluminum ion storage phenomenon," *The Journal of Physical Chemistry C*, vol. 121, no. 47, pp. 26241–26249, 2017. https://doi.org/10.1021/acs.jpcc.7b09494.

[6] H. Lahan and S. K. Das, "Al3+ ion intercalation in moo3 for aqueous aluminum-ion battery," *Journal of Power Sources*, vol. 413, pp. 134–138, 2019. https://doi.org/10.1016/j.jpowsour.2018.12.032.

[7] D. Chao, W. Zhou, F. Xie, C. Ye, H. Li, M. Jaroniec, and S.-Z. Qiao, "Roadmap for advanced aqueous batteries: From design of materials to applications," *Science Advances*, vol. 6, p. 4098, 2020. https://doi.org/10.1126/sciadv.aba4098.

[8] G. A. Elia, K. V. Kravchyk, M. V. Kovalenko, J. Chacón, A. Holland, and R. G. A. Wills, "An overview and prospective on al and al-ion battery technologies," *Journal of Power Sources*, vol. 481, p. 228870, 2021. https://doi.org/10.1016/j.jpowsour.2020.228870.

[9] L. Suo, O. Borodin, T. Gao, M. Olguin, J. Ho, X. Fan, C. Luo, C. Wang, and K. Xu, ""water-in-salt" electrolyte enables high-voltage aqueous lithium-ion chemistries," *Science*, vol. 350, no. 6263, p. 938. https://doi.org/10.1126/science.aab1595.

[10] H. Pan, Y. Shao, P. Yan, Y. Cheng, K. S. Han, Z. Nie, C. Wang, J. Yang, X. Li, P. Bhattacharya, K. T. Mueller, and J. Liu, "Reversible aqueous zinc/manganese oxide energy storage from conversion reactions," *Nature Energy*, vol. 1, no. 5, p. 16039, 2016. https://doi.org/10.1038/nenergy.2016.39.

[11] L. Jiang, Y. Lu, C. Zhao, L. Liu, J. Zhang, Q. Zhang, X. Shen, J. Zhao, X. Yu, H. Li, X. Huang, L. Chen, and Y.-S. Hu, "Building aqueous k-ion batteries for energy storage," *Nature Energy*, vol. 4, no. 6, pp. 495–503, 2019. https://doi.org/10.1038/s41560-019-0388-0.

[12] H. Gao and J. B. Goodenough, "An aqueous symmetric sodium-ion battery with nasicon-structured na3mnti(po4)3," *Angewandte Chemie International Edition*, vol. 55, no. 41, pp. 12768–12772. https://doi.org/10.1002/anie.201606508.

[13] H. Zhang, K. Ye, S. Shao, X. Wang, K. Cheng, X. Xiao, G. Wang, and D. Cao, "Octahedral magnesium manganese oxide molecular sieves as the cathode material of aqueous rechargeable magnesium-ion battery," *Electrochimica Acta*, vol. 229, pp. 371–379, 2017. https://doi.org/10.1016/j.electacta.2017.01.110.

[14] S. Gheytani, Y. Liang, F. Wu, Y. Jing, H. Dong, K. K. Rao, X. Chi, F. Fang, and Y. Yao, "An aqueous ca-ion battery," *Advanced Science*, vol. 4, no. 12, p. 1700465, 2017. https://doi.org/10.1002/advs.201700465.

[15] Z. Hu, Y. Guo, H. Jin, H. Ji, and L.-J. Wan, "A rechargeable aqueous aluminum–sulfur battery through acid activation in water-in-salt electrolyte," *Chemical Communications*, vol. 56, no. 13, pp. 2023–2026, 2020. https://doi.org/10.1039/C9CC08415K.

[16] H. Qin, Z. P. Song, H. Zhan, and Y. H. Zhou, "Aqueous rechargeable alkali-ion batteries with polyimide anode," *Journal of Power Sources*, vol. 249, pp. 367–372, 2014. https://doi.org/10.1016/j.jpowsour.2013.10.091.

[17] L. Yu and G. Z. Chen, "Redox electrode materials for supercapatteries," *Journal of Power Sources*, vol. 326, pp. 604–612, 2016. https://doi.org/10.1016/j.jpowsour.2016.04.095.

[18] A. Holland, *Development and characterisation of an aqueous aluminium-ion battery*. Thesis, 2018. https://eprints.soton.ac.uk/455972/.

[19] A. Afif, S. M. H. Rahman, A. Tasfiah Azad, J. Zaini, M. A. Islan, and A. K. Azad, "Advanced materials and technologies for hybrid supercapacitors for energy storage – a review," *Journal of Energy Storage*, vol. 25, p. 100852, 2019. https://doi.org/10.1016/j.est.2019.100852.

[20] N. Melzack, R. Wills, and A. Cruden, "Cleaner energy storage: Cradle-to-gate life cycle assessment of aluminum-ion batteries with an aqueous electrolyte," *Front. Energy Research*, vol. 9, no. 290, 2021. https://doi.org/10.3389/fenrg.2021.699919.

[21] N. Melzack, R. Wills, and A. Cruden, "An environmental perspective on developing dual energy storage for electric vehicles - a case study exploring al-ion vs. supercapacitors alongside li-ion," *Front. Energy Research*, vol. 11, 2024. DOI={https://doi.org/10.3389/fenrg.2023.1266670}.

[22] N. Melzack, "Advancing battery design based on environmental impacts using an aqueous al-ion cell as a case study," *Sci Reports*, vol. 12, no. 1, 2022. https://doi.org/10.1038/s41598-022-13078-4.

[23] C. Siret, J. Tytgat, T. Ebert, and M. Mistry, "Product environmental footprint category rules for high specific energy rechargeable batteries for mobile applications," *The Advanced Rechargeable and Lithium Batteries Association*, 2018.

[24] J. F. Peters, M. Baumann, B. Zimmermann, J. Braun, and M. Weil, "The environmental impact of li-ion batteries and the role of key parameters – a review," *Renewable and Sustainable Energy Reviews*, vol. 67, pp. 491–506, 2017. https://doi.org/10.1016/j.rser.2016.08.039.

[25] J. Le Houx, N. Melzack, N. Aslani, A. James, H. Dehyle, A. Leonardi, M. Pimblott, O. King, R. Wills, and S. Ahmed, "Optimising the compression ratio of a carbon felt electrode through image-based modelling for an aqueous al-ion battery," *In draft*, 2024.

[26] J. F. Peters and M. Weil, "Providing a common base for life cycle assessments of li-ion batteries," *Journal of Cleaner Production*, vol. 171, pp. 704–713, 2018. https://doi.org/10.1016/j.jclepro.2017.10.016.

[27] M. Song, H. Tan, D. Chao, and H. J. Fan, "Recent advances in zn-ion batteries," *Advanced Functional Materials*, vol. 28, no. 41, p. 1802564, 2018. https://doi.org/10.1002/adfm.201802564.

[28] M. Cossutta, V. Vretenar, T. A. Centeno, P. Kotrusz, J. McKechnie, and S. J. Pickering, "A comparative life cycle assessment of graphene and activated

carbon in a supercapacitor application," *Journal of Cleaner Production*, vol. 242, p. 118468, 2020. https://doi.org/10.1016/j.jclepro.2019.118468.

[29] "Sigracell battery felts tds bf.01," tech. rep., SGL Carbon, 2019. Available online https://www.sglcarbon.com/en/markets-solutions/material/sigracell-battery-felts/.

[30] N. Melzack, R. G. A. Wills, and A. J. Cruden, "Enhanced discharge capacity in carbon felt electrodes for aqueous aluminium-ion half-cells," *In draft*, 2024.

[31] N. Melzack and R. Wills, "A review of energy storage mechanisms in aqueous aluminium technology," *Front. Chemical Engineering*, vol. 4, 2022. https://doi.org/10.3389/fceng.2022.778265.

[32] D. Wu, X. Li, X. Liu, J. Yi, P. Acevedo-Peña, E. Reguera, K. Zhu, D. Bin, N. Melzack, R. G. A. Wills, J. Huang, X. Wang, X. Lin, D. Yu, and J. Ma, "2022 roadmap on aqueous batteries," *Journal of Physics: Energy*, vol. 4, no. 4, p. 041501, 2022. https://doi.org/10.1088/2515-7655/ac774d.

[33] "Climate change 2014: Mitigation of climate change," report, International Panel on Change, 2014. https://www.ipcc.ch/site/assets/uploads/2018/02/ipcc_wg3_ar5_full.pdf.

[34] W. Tang, Y. Zhu, Y. Hou, L. Liu, Y. Wu, K. P. Loh, H. Zhang, and K. Zhu, "Aqueous rechargeable lithium batteries as an energy storage system of superfast charging," *Energy & Environmental Science*, vol. 6, no. 7, pp. 2093–2104, 2013. https://doi.org/10.1039/C3EE24249H.

[35] "Climate change act 2008," tech. rep., UK Government. Available online https://www.legislation.gov.uk/ukpga/2008/27/contents.

[36] D. Larcher and J. M. Tarascon, "Towards greener and more sustainable batteries for electrical energy storage," *Nature Chemistry*, vol. 7, no. 1, pp. 19–29, 2015. https://doi.org/10.1038/nchem.2085.

[37] "Uk energy statistics, q1," tech. rep., Department for Business Energy and Industrial Strategy, 2019. Available online https://assets.publishing.service.gov.uk/media/5d149fcded915d324443ba6e/Press_Notice_June_19.pdf.

[38] "National grid open day," *Presentation*, 2010.

[39] A. Castillo and D. F. Gayme, "Grid-scale energy storage applications in renewable energy integration: A survey," *Energy Conversion and Management*, pp. 885–894, 2014. url:101016/jenconman201407063.

[40] "Electric vehilces and infrastructure: Briefing paper," report, House of Commons Library, 2020. Available online https://commonslibrary.parliament.uk/research-briefings/cbp-7480/.

[41] "Uk battery strategy," government document, Department for Business and Trade, UK Government, 2023. Available online https://www.gov.uk/government/publications/uk-battery-strategy.

[42] M. Shahjalal, P. K. Roy, T. Shams, A. Fly, Chowdhury, J. Islam, M. R. Ahmed, and K. Liu, "A review on second-life of li-ion batteries: prospects, challenges, and issues," *Energy*, vol. 241, p. 122881, 2022. https://doi.org/10.1016/j.energy.2021.122881.

[43] A. Alhamali, M. E. Farrag, G. Bevan, and D. M. Hepburn, "Review of energy storage systems in electric grid and their potential in distribution networks," in *2016 Eighteenth International Middle East Power Systems Conference (MEPCON)*, pp. 546–551, 2016. https://doi.org/10.1109/MEPCON.2016.7836945.

[44] K. Liu, Y. Liu, D. Lin, A. Pei, and Y. Cui, "Materials for lithium-ion battery safety," *Science Advances*, vol. 4, no. 6, p. eaas9820, 2018. https://doi.org/10.1126/sciadv.aas9820.

[45] T. M. Gür, "Review of electrical energy storage technologies, materials and systems: challenges and prospects for large-scale grid storage," *Energy & Environmental Science*, vol. 11, no. 10, pp. 2696–2767, 2018. https://doi.org/10.1039/C8EE01419A.

[46] G. Ressler, "Application of system safety engineering processes to advanced battery safety," *SAE International Journal of Engines*, vol. 4, no. 1, pp. 1921–1927, 2011. http://www.jstor.org/stable/26278269.

[47] A. D. Ballantyne, J. P. Hallett, D. J. Riley, N. Shah, and D. J. Payne, "Lead acid battery recycling for the twenty-first century," *Royal Society Open Science*, vol. 5, no. 5, p. 171368, 2018. https://doi.org/10.1098/rsos.171368.

[48] L. Souyang, J. Huang, H. Wang, J. Liu, and M. Zhu, "Progress of hydrogen storage alloys for ni-mh rechargeable power batteries in electric vehicles: A review," *Materials Chemistry and Physics*, vol. 200, pp. 164–178, 2017. 1https://doi.org/10.1016/j.matchemphys.2017.07.002.

[49] X. Luo, J. Wang, M. Dooner, and J. Clarke, "Poverview of current development in electrical energy storage technologies and the application potential in power system operation," *Applied Energy*, vol. 137, pp. 511–536, 2015. https://doi.org/10.1016/j.apenergy.2014.09.081.

[50] A. Eftekhari and P. Corrochano, "Electrochemical energy storage by aluminum as a lightweight and cheap anode/charge carrier," *Sustainable Energy Fuels*, vol. 1, no. 6, pp. 1246–1264, 2017. https://doi.org/10.1039/C7SE00050B.

[51] P. A. Christensen, P. A. Anderson, G. D. J. Harper, S. M. Lambert, W. Mrozik, M. A. Rajaeifar, M. S. Wise, and O. Heidrich, "Risk management over the life cycle of lithium-ion batteries in electric vehicles," *Renewable and Sustainable Energy Reviews*, vol. 148, p. 111240, 2021. https://doi.org/10.1016/j.rser.2021.111240.

[52] F. Larsson, S. Bertilsson, M. Furlani, I. Albinsson, and B.-E. Mellander, "Gas explosions and thermal runaways during external heating abuse of commercial lithium-ion graphite-licoo2 cells at different levels of ageing," *Journal of Power Sources*, vol. 373, pp. 220–231, 2018. https://doi.org/10.1016/j.jpowsour.2017.10.085.

[53] "Energy storage technology and cost characterization report," report, US Department of Energy, 2019. Available online https://energystorage.pnnl.gov/pdf/PNNL-28866.pdf.

[54] C. P. Grey and J. M. Tarascon, "Sustainability and in situ monitoring in battery development," *Nature Materials*, vol. 16, no. 1, pp. 45–56, 2017. https://doi.org/10.1038/nmat4777.

[55] H. Zhang, X. Liu, H. Li, I. Hasa, and S. Passerini, "Challenges and strategies for high-energy aqueous electrolyte rechargeable batteries," *Angewandte Chemie International Edition*, vol. n/a, no. n/a, 2020. https://doi.org/10.1002/anie.202004433.

[56] L. Suo, O. Borodin, Y. Wang, X. Rong, W. Sun, X. Fan, S. Xu, M. A. Schroeder, A. V. Cresce, F. Wang, C. Yang, Y.-S. Hu, K. Xu, and C. Wang, ""water-in-salt" electrolyte makes aqueous sodium-ion battery safe, green, and long-lasting," *Advanced Energy Materials*, vol. 7, no. 21, p. 1701189, 2017. https://doi.org/10.1002/aenm.201701189.

[57] J. O. G. Posada, A. J. R. Rennie, S. P. Villar, V. L. Martins, J. Marinaccio, A. Barnes, C. F. Glover, D. A. Worsley, and P. J. Hall, "Aqueous batteries as grid scale energy storage solutions," *Renewable and Sustainable Energy Reviews*, vol. 68, pp. 1174–1182, 2017. https://doi.org/10.1016/j.rser.2016.02.024.

[58] H. J. Gores, J. Barthel, S. Zugmann, D. Moosbauer, M. Amereller, R. Hartl, and A. Maurer, *Liquid Nonaqueous Electrolytes*. Handbook of Battery Materials, 2011. https://doi.org/10.1002/9783527637188.ch17.

[59] F. Gray and M. Armand, *Polymer Electrolytes*, pp. 627–656. Wiley Online Books, 2011. https://doi.org/10.1002/9783527637188.ch18.

[60] P. Wang, Z. Chen, Z. Ji, Y. Feng, J. Wang, J. Liu, M. Hu, H. Wang, W. Gan, and Y. Huang, "A flexible aqueous al ion rechargeable full battery," *Chemical Engineering Journal*, vol. 373, pp. 580–586, 2019. https://doi.org/10.1016/j.cej.2019.05.085.

[61] R. M. Dell, "Aqueous electrolyte batteries," *Philosophical Transactions: Mathematical, Physical and Engineering Sciences*, vol. 354, no. 1712, pp. 1515–1527, 1996. http://www.jstor.org/stable/54631.

[62] C. Yang, J. Chen, T. Qing, X. Fan, W. Sun, A. von Cresce, M. S. Ding, O. Borodin, J. Vatamanu, M. A. Schroeder, N. Eidson, C. Wang, and K. Xu, "4.0 v aqueous li-ion batteries," *Joule*, vol. 1, no. 1, pp. 122–132, 2017. https://doi.org/10.1016/j.joule.2017.08.009.

[63] T. P. Narins, "The battery business: Lithium availability and the growth of the global electric car industry," *The Extractive Industries and Society*, vol. 4, no. 2, pp. 321–328, 2017. https://doi.org/10.1016/j.exis.2017.01.013.

[64] T. Prior, P. A. Wäger, A. Stamp, R. Widmer, and D. Giurco, "Sustainable governance of scarce metals: The case of lithium," *Science of The Total Environment*, vol. 461-462, pp. 785–791, 2013. https://doi.org/10.1016/j.scitotenv.2013.05.042.

[65] P. Maxwell, "Transparent and opaque pricing: The interesting case of lithium," *Resources Policy*, vol. 45, pp. 92–97, 2015. https://doi.org/10.1016/j.resourpol.2015.03.007.

[66] B. Huang, Z. Pan, X. Su, and L. An, "Recycling of lithium-ion batteries: Recent advances and perspectives," *Journal of Power Sources*, vol. 399, pp. 274–286, 2018. https://doi.org/10.1016/j.jpowsour.2018.07.116.

[67] R. E. Ciez and J. F. Whitacre, "Examining different recycling processes for lithium-ion batteries," *Nature Sustainability*, vol. 2, no. 2, pp. 148–156, 2019. https://doi.org/10.1038/s41893-019-0222-5.

[68] CRC, ed., *Abundance of Elements in The Earth's Crust and in The Sea*, pp. 14–17. 97 ed., 2016-2017.

[69] L. Butterwick and G. D. W. Smith, "Aluminium recovery from consumer waste—i. technology review," *Conservation Recycling*, vol. 9, no. 3, pp. 281–292, 1986. https://doi.org/10.1016/0361-3658(86)90018-4.

[70] U. Government, "U.s. geological survey, mineral commodity summaries," report, 2020. Available online https://www.usgs.gov/centers/national-minerals-information-center/mineral-commodity-summaries.

[71] S. K. Das, S. Mahapatra, and H. Lahan, "Aluminium-ion batteries: developments and challenges," *Journal of Materials Chemistry A*, vol. 5, no. 14, pp. 6347–6367, 2017. https://doi.org/10.1039/C7TA00228A.

[72] R. I. Smith, S. Hull, M. G. Tucker, H. Y. Playford, D. J. McPhail, S. P. Waller, and S. T. Norberg, "The upgraded polaris powder diffractometer at the isis neutron source," *Review of Scientific Instruments*, vol. 90, no. 11, p. 115101, 2019. https://doi.org/10.1063/1.5099568.

[73] N. Melzack, R. G. A. Wills, A. J. Cruden, and M. Owen-Jones, "Enhanced discharge capacity in carbon felt electrodes for aqueous aluminium-ion half-cells," in *ECS 245th meeting*, 2024. https://doi.org/10.13140/RG.2.2.22413.76001.

[74] R. C. Massé, C. Liu, Y. Li, L. Mai, and G. Cao, "Energy storage through intercalation reactions: electrodes for rechargeable batteries," *National Science Review*, vol. 4, no. 1, pp. 26–53, 2017. https://doi.org/10.1093/nsr/nww093.

[75] V. Bagotsky, *Fundamentals of Electrochemistry*. The ECS Series of Texts and Monographs, Wiley, 2005.

[76] CRC, ed., *Thermochemistry,Kinetics, Electrochemistry and Solution Chemistry*. 102 ed., 2021.

[77] L. Guan, L. Yu, and G. Z. Chen, "Capacitive and non-capacitive faradaic charge storage," *Electrochimica Acta*, vol. 206, pp. 464–478, 2016. https://doi.org/10.1016/j.electacta.2016.01.213.

[78] X. Zheng, C. Han, C.-S. Lee, W. Yao, C. Zhi, and Y. Tang, "Materials challenges for aluminum ion based aqueous energy storage devices: Progress and prospects," *Progress in Materials Science*, vol. 143, p. 101253, 2024. https://doi.org/10.1016/j.pmatsci.2024.101253.

[79] Y. Luo, X. Yang, C. Wang, A. Fraser, H. Zhang, X. Sun, and X. Li, "Advanced metal anodes and their interface design toward safe metal batteries: A comprehensive review," *Progress in Materials Science*, vol. 139, p. 101171, 2023. https://doi.org/10.1016/j.pmatsci.2023.101171.

[80] Y. Liu, G. He, H. Jiang, I. P. Parkin, P. R. Shearing, and D. J. L. Brett, "Cathode design for aqueous rechargeable multivalent ion batteries: Challenges and opportunities," *Advanced Functional Materials*, vol. 31, no. 13, 2021. https://doi.org/10.1002/adfm.202010445.

[81] S.-y. Liu, S. Ye, C. Li, G. Pan, and X. Gao, "Rechargeable aqueous lithium-ion battery of tio2/limn2o4 with a high voltage," *Journal of The Electrochemical Society*, vol. 158. https://doi.org/10.1149/2.094112jes.

[82] S. Sang, Y. Liu, W. Zhong, K. Liu, H. Liu, and Q. Wu, "The electrochemical behavior of tio2-ntas electrode in h+ and al3+ coexistent aqueous solution," *Electrochimica Acta*, vol. 187, pp. 92–97, 2016. https://doi.org/10.1016/j.electacta.2015.11.021.

[83] T. Koketsu, J. Ma, B. J. Morgan, M. Body, C. Legein, W. Dachraoui, M. Giannini, A. Demortière, M. Salanne, F. Darurlze, H. Groult, O. J. Borkiewicz, K. W. Chapman, P. Strasser, and D. Dambournet, "Reversible magnesium and aluminium ions insertion in cation-deficient anatase tio2," *Nature Materials*, vol. 16, no. 11, pp. 1142–1148, 2017. https://doi.org/10.1038/nmat4976.

[84] A. W. Holland, A. Cruden, A. Zerey, A. Hector, and R. G. A. Wills, "Electrochemical study of tio2 in aqueous alcl3 electrolyte via vacuum impregnation for superior high-rate electrode performance," *BMC Energy*, vol. 1, no. 1, p. 10, 2019. https://doi.org/10.1186/s42500-019-0010-9.

[85] B. D. Smith, R. G. A. Wills, and A. J. Cruden, "Aqueous al-ion cells and supercapacitors — a comparison," *Energy Reports*, vol. 6, pp. 166–173, 2020. https://doi.org/10.1016/j.egyr.2020.03.021.

[86] W. Tang, J. Xuan, H. Wang, S. Zhao, and H. Liu, "First-principles investigation of aluminum intercalation and diffusion in tio2 materials: Anatase versus rutile," *Journal of Power Sources*, vol. 384, pp. 249–255, 2018. https://doi.org/10.1016/j.jpowsour.2018.02.088.

[87] T. Zhao, M. Ojeda, J. Xuan, Z. Shu, and H. Wang, "Aluminum storage in rutile-based tio2 nanoparticles," *Energy Procedia*, vol. 158, pp. 4829–4833, 2019. https://doi.org/10.1016/j.egypro.2019.01.712.

[88] Y.-S. Kim, K. D. Harris, B. Limoges, and V. Balland, "On the unsuspected role of multivalent metal ions on the charge storage of a metal oxide electrode in mild aqueous electrolytes," *Chem. Sci.*, vol. 10, pp. 8752–8763, 2019. http://dx.doi.org/10.1039/C9SC02397F.

[89] M. Kazazi, P. Abdollahi, and M. Mirzaei-Moghadam, "High surface area tio2 nanospheres as a high-rate anode material for aqueous aluminium-ion batteries," *Solid State Ionics*, vol. 300, pp. 32–37, 2017. https://doi.org/10.1016/j.ssi.2016.11.028.

[90] M. Kazazi, Z. A. Zafar, M. Delshad, J. Cervenka, and C. Chen, "Tio2/cnt nanocomposite as an improved anode material for aqueous rechargeable aluminum batteries," *Solid State Ionics*, vol. 320, pp. 64–69, 2018. https://doi.org/10.1016/j.ssi.2018.02.034.

[91] Q. Zhao, M. J. Zachman, W. I. Al Sadat, J. Zheng, L. F. Kourkoutis, and L. Archer, "Solid electrolyte interphases for high-energy aqueous aluminum

electrochemical cells," *Science Advances*, vol. 4, no. 11, p. eaau8131, 2018. https://doi.org/10.1126/sciadv.aau8131.

[92] C. Wu, S. Gu, Q. Zhang, Y. Bai, M. Li, Y. Yuan, H. Wang, X. Liu, Y. Yuan, N. Zhu, F. Wu, H. Li, L. Gu, and J. Lu, "Electrochemically activated spinel manganese oxide for rechargeable aqueous aluminum battery," *Nature communications*, vol. 10, no. 1, pp. 73–73, 2019. https://doi.org/10.1038/s41467-018-07980-7.

[93] S. He, J. Wang, X. Zhang, J. Chen, Z. Wang, T. Yang, Z. Liu, Y. Liang, B. Wang, S. Liu, L. Zhang, J. Huang, J. Huang, L. A. O'Dell, and H. Yu, "A high-energy aqueous aluminum-manganese battery," *Advanced Functional Materials*, vol. 29, no. 45, p. 1905228. https://doi.org/10.1002/adfm.201905228.

[94] T. Dong, K. L. Ng, Y. Wang, O. Voznyy, and G. Azimi, "Solid electrolyte interphase engineering for aqueous aluminum metal batteries: A critical evaluation," *Advanced Energy Materials*, vol. 11, no. 20, p. 2100077, 2021. https://doi.org/10.1002/aenm.202100077.

[95] Q. Hao, F. Chen, X. Chen, Q. Meng, Y. Qi, and N. Li, "Bi-functional poly(vinylidene difluoride) coated al anodes for highly rechargeable aqueous al-ion batteries," *Electrochimica Acta*, vol. 421, p. 140495, 2022. https://doi.org/10.1016/j.electacta.2022.140495.

[96] C. Yan, C. Lv, L. Wang, W. Cui, L. Zhang, K. N. Dinh, H. Tan, C. Wu, T. Wu, Y. Ren, J. Chen, Z. Liu, M. Srinivasan, X. Rui, Q. Yan, and G. Yu, "Architecting a stable high-energy aqueous al-ion battery," *Journal of the American Chemical Society*, vol. 142, no. 36, pp. 15295–15304, 2020. https://doi.org/10.1021/jacs.0c05054.

[97] Q. Ran, H. Shi, H. Meng, S.-P. Zeng, W.-B. Wan, W. Zhang, Z. Wen, X.-Y. Lang, and Q. Jiang, "Aluminum-copper alloy anode materials for high-energy aqueous aluminum batteries," *Nature Communications*, vol. 13, no. 1, p. 573, 2022. https://doi.org/10.1038/s41467-022-28238-3.

[98] Q. Ran, S.-P. Zeng, M.-H. Zhu, W.-B. Wan, H. Meng, H. Shi, Z. Wen, X.-Y. Lang, and Q. Jiang, "Uniformly mxene-grafted eutectic aluminum-cerium alloys as flexible and reversible anode materials for rechargeable aluminum-ion battery," *Advanced Functional Materials*, vol. 33, no. 1, p. 2211271, 2023. https://doi.org/10.1002/adfm.202211271.

[99] Y. Gao, H. Yang, X. Wang, Y. Bai, N. Zhu, S. Guo, L. Suo, H. Li, H. Xu, and C. Wu, "The compensation effect mechanism of fe–ni mixed prussian blue analogues in aqueous rechargeable aluminum-ion batteries," *ChemSusChem*, vol. 13, no. 4, pp. 732–740, 2020. https://doi.org/10.1002/cssc.201903067.

[100] P. Wang, Z. Chen, H. Wang, Z. Ji, Y. Feng, J. Wang, J. Liu, M. Hu, J. Fei, W. Gan, and Y. Huang, "A high-performance flexible aqueous al ion rechargeable battery with long cycle life," *Energy Storage Materials*, vol. 25, pp. 426–435, 2020. https://doi.org/10.1016/j.ensm.2019.09.038.

[101] H. Lahan and S. K. Das, "Reversible al3+ ion insertion into tungsten trioxide (wo3) for aqueous aluminum-ion batteries," *Dalton Transactions*, vol. 48, no. 19, pp. 6337–6340, 2019. https://doi.org/10.1039/C9DT00844F.

[102] A. Holland, H. Kimpton, A. Cruden, and R. Wills, "Cuhcf as an electrode material in an aqueous dual-ion al3+/k+ ion battery," *Energy Procedia*, vol. 151, pp. 69–73, 2018. https://doi.org/10.1016/j.egypro.2018.09.029.

[103] J. R. González, F. Nacimiento, M. Cabello, R. Alcántara, P. Lavela, and J. L. Tirado, "Reversible intercalation of aluminium into vanadium pentoxide xerogel for aqueous rechargeable batteries," *RSC Advances*, vol. 6, no. 67, pp. 62157–62164, 2016. https://doi.org/10.1039/C6RA11030D.

[104] L. Znaidi, N. Baffier, and M. Huber, "Synthesis of vanadium bronzes mxv2o5 through sol-gel processes i - monoclinic bronzes (m = na, ag)," *Materials Research Bulletin*, vol. 24, no. 12, pp. 1501–1514, 1989. https://doi.org/10.1016/0025-5408(89)90161-X.

[105] S. Kumar, R. Satish, V. Verma, H. Ren, P. Kidkhunthod, W. Manalastas, and M. Srinivasan, "Investigating fevo4 as a cathode material for aqueous aluminum-ion battery," *Journal of Power Sources*, vol. 426, pp. 151–161, 2019. https://doi.org/10.1016/j.jpowsour.2019.03.119.

[106] Y. Cai, S. Kumar, R. Chua, V. Verma, D. Yuan, Z. Kou, H. Ren, H. Arora, and M. Srinivasan, "Bronze-type vanadium dioxide holey nanobelts as high performing cathode material for aqueous aluminium-ion batteries," *Journal of Materials Chemistry A*, vol. 8, no. 25, pp. 12716–12722, 2020. https://doi.org/10.1039/D0TA03986A.

[107] Q. Zhao, L. Liu, J. Yin, J. Zheng, D. Zhang, J. Chen, and L. A. Archer, "Proton intercalation/de-intercalation dynamics in vanadium oxides for aqueous aluminum electrochemical cells," *Angewandte Chemie International Edition*, vol. 59, no. 8, pp. 3048–3052, 2020. https://doi.org/10.1002/anie.201912634.

[108] L. Chen, J. L. Bao, X. Dong, D. G. Truhlar, Y. Wang, C. Wang, and Y. Xia, "Aqueous mg-ion battery based on polyimide anode and prussian blue cathode," *ACS Energy Letters*, vol. 2, no. 5, pp. 1115–1121, 2017. https://doi.org/10.1021/acsenergylett.7b00040.

[109] B. Kong, J. Tang, Z. Wu, J. Wei, H. Wu, Y. Wang, G. Zheng, and D. Zhao, "Ultralight mesoporous magnetic frameworks by interfacial assembly of

prussian blue nanocubes," *Angewandte Chemie International Edition*, vol. 53, no. 11, pp. 2888–2892, 2014. https://doi.org/10.1002/anie.201308625.

[110] C. D. Wessells, S. V. Peddada, M. T. McDowell, R. A. Huggins, and Y. Cui, "The effect of insertion species on nanostructured open framework hexacyanoferrate battery electrodes," *Journal of The Electrochemical Society*, vol. 159, no. 2, pp. A98–A103. https://doi.org/10.1149/2.060202jes.

[111] M. Xia, X. Zhang, T. Liu, H. Yu, S. Chen, N. Peng, R. Zheng, J. Zhang, and J. Shu, "Commercially available prussian blue get energetic in aqueous k-ion batteries," *Chemical Engineering Journal*, vol. 394, p. 124923, 2020. https://doi.org/10.1016/j.cej.2020.124923.

[112] Y. Ru, S. Zheng, H. Xue, and H. Pang, "Potassium cobalt hexacyanoferrate nanocubic assemblies for high-performance aqueous aluminum ion batteries," *Chemical Engineering Journal*, vol. 382, p. 122853, 2020. https://doi.org/10.1016/j.cej.2019.122853.

[113] A. Zhou, L. Jiang, J. Yue, Y. Tong, Q. Zhang, Z. Lin, B. Liu, C. Wu, L. Suo, Y.-S. Hu, H. Li, and L. Chen, "Water-in-salt electrolyte promotes high-capacity fefe(cn)6 cathode for aqueous al-ion battery," *ACS Applied Materials Interfaces*, vol. 11, no. 44, pp. 41356–41362, 2019. https://doi.org/10.1021/acsami.9b14149.

[114] S. Liu, G. L. Pan, G. R. Li, and X. P. Gao, "Copper hexacyanoferrate nanoparticles as cathode material for aqueous al-ion batteries," *Journal of Materials Chemistry A*, vol. 3, no. 3, pp. 959–962, 2015. https://doi.org/10.1039/C4TA04644G.

[115] J. Joseph, J. Nerkar, C. Tang, A. Du, A. P. O'Mullane, and K. Ostrikov, "Reversible intercalation of multivalent al3+ ions into potassium-rich cryptomelane nanowires for aqueous rechargeable al-ion batteries," *ChemSusChem*, vol. 12, no. 16, pp. 3753–3760, 2019. https://doi.org/10.1002/cssc.201901182.

[116] J. Joseph, J. F. S. Fernando, M. A. Sayeed, C. Tang, D. Golberg, A. Du, K. Ostrikov, and A. P. O'Mullane, "Exploring aluminum-ion insertion into magnesium-doped manjiroite (mno2) nanorods in aqueous solution," *ChemElectroChem*, vol. n/a, no. n/a, 2020. https://doi.org/10.1002/celc.202001408.

[117] S. Nandi, H. Lahan, and S. K. Das, "A proof of concept for low-cost rechargeable aqueous aluminium-ion batteries," *Bulletin of Materials Science*, vol. 43, no. 1, p. 26, 2019. https://doi.org/10.1007/s12034-019-1988-9.

[118] K. Mohanapriya and N. Jha, "Hierarchically hybrid nanostructure of carbon nanoparticles decorated graphene sheets as an efficient electrode material for supercapacitors, aqueous al-ion battery and capacitive deionization," *Electrochimica Acta*, vol. 324, p. 134870, 2019. https://doi.org/10.1016/j.electacta.2019.134870.

[119] S. Nandi and S. K. Das, "An electrochemical study on bismuth oxide (bi2o3) as an electrode material for rechargeable aqueous aluminum-ion battery," *Solid State Ionics*, vol. 347, p. 115228, 2020. https://doi.org/10.1016/j.ssi.2020.115228.

[120] M. Tian, R. Li, C. Liu, D. Long, and G. Cao, "Aqueous al-ion supercapacitor with v2o5 mesoporous carbon electrodes," *ACS Applied Materials Interfaces*, vol. 11, no. 17, pp. 15573–15580. https://doi.org/10.1021/acsami.9b02030.

[121] M. Krishnamoorthy and N. Jha, "Oxygen-rich hierarchical porous graphene as an excellent electrode for supercapacitors, aqueous al-ion battery, and capacitive deionization," *ACS Sustainable Chemistry Engineering*, vol. 7, no. 9, pp. 8475–8489, 2019. https://doi.org/10.1021/acssuschemeng.9b00233.

[122] H. A. Andreas, "Self-discharge in electrochemical capacitors: A perspective article," *Journal of The Electrochemical Society*, vol. 162, no. 5, pp. A5047–A5053, 2015. https://doi.org/10.1149/2.0081505jes.

[123] M. Haque, Q. Li, A. D. Smith, V. Kuzmenko, P. Rudquist, P. Lundgren, and P. Enoksson, "Self-discharge and leakage current mitigation of neutral aqueous-based supercapacitor by means of liquid crystal additive," *Journal of Power Sources*, vol. 453, p. 227897, 2020. https://doi.org/10.1016/j.jpowsour.2020.227897.

[124] B. W. Ricketts and C. Ton-That, "Self-discharge of carbon-based supercapacitors with organic electrolytes," *Journal of Power Sources*, vol. 89, no. 1, pp. 64–69, 2000. https://doi.org/10.1016/S0378-7753(00)00387-6.

[125] B. E. Conway, W. G. Pell, and T. C. Liu, "Diagnostic analyses for mechanisms of self-discharge of electrochemical capacitors and batteries," *Journal of Power Sources*, vol. 65, no. 1, pp. 53–59, 1997. https://doi.org/10.1016/S0378-7753(97)02468-3.

[126] A. Lewandowski, P. Jakobczyk, M. Galinski, and M. Biegun, "Self-discharge of electrochemical double layer capacitors," *Physical Chemistry Chemical Physics*, vol. 15, no. 22, pp. 8692–8699, 2013. https://doi.org/10.1039/C3CP44612C.

[127] J. Niu, W. G. Pell, and B. E. Conway, "Requirements for performance characterization of c double-layer supercapacitors: Applications to a high

specific-area c-cloth material," *Journal of Power Sources*, vol. 156, no. 2, pp. 725–740, 2006. https://doi.org/10.1016/j.jpowsour.2005.06.002.

[128] S. Fletcher, V. J. Black, and I. Kirkpatrick, "A universal equivalent circuit for carbon-based supercapacitors," *Journal of Solid State Electrochemistry*, vol. 18, no. 5, pp. 1377–1387, 2014. https://doi.org/10.1007/s10008-013-2328-4.

[129] S. Devese and T. Nann, "Suppressed self-discharge of an aqueous supercapacitor using earth-abundant materials," *Journal of Electroanalytical Chemistry*, vol. 871, p. 114307, 2020. https://doi.org/10.1016/j.jelechem.2020.114307.

[130] A. Lewandowski, P. Jakobczyk, M. Gnat, and E. Rudnicka, "Heat generated during electrochemical double-layer capacitor "self-discharge"," *Journal of Applied Electrochemistry*, vol. 44, no. 5, pp. 551–554, 2014. https://doi.org/10.1007/s10800-014-0665-3.

[131] W. Zhong, S. Sang, Y. Liu, Q. Wu, K. Liu, and H. Liu, "Electrochemically conductive treatment of tio2 nanotube arrays in alcl3 aqueous solution for supercapacitors," *Journal of Power Sources*, vol. 294, pp. 216–222, 2015. https://doi.org/10.1016/j.jpowsour.2015.06.052.

[132] "Iso 14040:2006 environmental management — life cycle assessment — principles and framework," *International Organization for Standardization*, 2006.

[133] G. Jonker and J. Harmsen, *Chapter 4 - Creating Design Solutions*, pp. 61–81. Amsterdam: Elsevier, 2012. https://doi.org/10.1016/B978-0-444-53846-8.00004-4.

[134] D. Caro, *Carbon Footprint*, pp. 252–257. Oxford: Elsevier, 2019. https://doi.org/10.1016/B978-0-12-409548-9.10752-3.

[135] M. Maczka, M. Guzik, M. Mosiałek, M. Wojnarowska, P. Pasierb, and T. Nitkiewicz, "Life cycle assessment of experimental al-ion batteries for energy storage applications," *Science of The Total Environment*, vol. 912, p. 169258, 2024. https://doi.org/10.1016/j.scitotenv.2023.169258.

[136] M. A. Salgado Delgado, L. Usai, L. A.-W. Ellingsen, Q. Pan, and A. Hammer Strømman, "Comparative life cycle assessment of a novel al-ion and a li-ion battery for stationary applications," *Materials*, vol. 12, no. 19, 2019. https://www.mdpi.com/1996-1944/12/19/3270.

[137] X. Xia and P. Li, "A review of the life cycle assessment of electric vehicles: Considering the influence of batteries," *Science of The Total Environment*, vol. 814, p. 152870, 2022. https://doi.org/10.1016/j.scitotenv.2021.152870.

[138] S. Verma, G. Dwivedi, and P. Verma, "Life cycle assessment of electric vehicles in comparison to combustion engine vehicles: A review," *Materials Today: Proceedings*, vol. 49, pp. 217–222, 2022. https://doi.org/10.1016/j.matpr.2021.01.666.

[139] T. Feng, W. Guo, Q. Li, Z. Meng, and W. Liang, "Life cycle assessment of lithium nickel cobalt manganese oxide batteries and lithium iron phosphate batteries for electric vehicles in china," *Journal of Energy Storage*, vol. 52, p. 104767, 2022. https://doi.org/10.1016/j.est.2022.104767.

[140] M. J. Lencwe, S. P. D. Chowdhury, and T. O. Olwal, "Hybrid energy storage system topology approaches for use in transport vehicles: A review," *Energy Science Engineering*, vol. 10, no. 4, pp. 1449–1477, 2022. https://doi.org/10.1002/ese3.1068.

[141] A. Ostadi and M. Kazerani, "A comparative analysis of optimal sizing of battery-only, ultracapacitor-only, and battery–ultracapacitor hybrid energy storage systems for a city bus," *IEEE Transactions on Vehicular Technology*, vol. 64, no. 10, pp. 4449–4460, 2015. https://doi.org/10.1109/TVT.2014.2371912.

[142] T. Zhu, R. Lot, R. G. A. Wills, and X. Yan, "Sizing a battery-supercapacitor energy storage system with battery degradation consideration for high-performance electric vehicles," *Energy*, vol. 208, p. 118336, 2020. https://doi.org/10.1016/j.energy.2020.118336.

[143] R. S. Sankarkumar and R. Natarajan, "Energy management techniques and topologies suitable for hybrid energy storage system powered electric vehicles: An overview," *International Transactions on Electrical Energy Systems*, vol. 31, no. 4, p. e12819, 2021. https://doi.org/10.1002/2050-7038.12819.

[144] L. Zhang, X. Hu, Z. Wang, F. Sun, J. Deng, and D. G. Dorrell, "Multiobjective optimal sizing of hybrid energy storage system for electric vehicles," *IEEE Transactions on Vehicular Technology*, vol. 67, no. 2, pp. 1027–1035, 2018. https://doi.org/10.1109/TVT.2017.2762368.

[145] Z. Song, H. Hofmann, J. Li, X. Han, and M. Ouyang, "Optimization for a hybrid energy storage system in electric vehicles using dynamic programing approach," *Applied Energy*, vol. 139, pp. 151–162, 2015. https://doi.org/10.1016/j.apenergy.2014.11.020.

[146] V. B. Venkateswaran, D. K. Saini, and M. Sharma, "Environmental constrained optimal hybrid energy storage system planning for an indian distribution network," *IEEE Access*, vol. 8, pp. 97793–97808, 2020. https://doi.org/10.1109/ACCESS.2020.2997338.

[147] T. Zhu, R. Lot, and R. G. A. Wills, "Optimization of dual energy storage system for high-performance electric vehicles," in *2018 IEEE Vehicle Power and Propulsion Conference (VPPC)*, pp. 1–6. https://doi.org/10.1109/VPPC.2018.8604961.

[148] J. Sanfélix, M. Messagie, N. Omar, J. Van Mierlo, and V. Hennige, "Environmental performance of advanced hybrid energy storage systems for electric vehicle applications," *Applied Energy*, vol. 137, pp. 925–930, 2015. https://doi.org/10.1016/j.apenergy.2014.07.012.

[149] L. A. Ellingsen, A. Holland, J.-F. Drillet, W. Peters, M. Eckert, C. Concepcion, O. Ruiz, J.-F. Colin, E. Knipping, Q. Pan, R. G. A. Wills, and G. Majeau-Bettez, "Environmental screening of electrode materials for a rechargeable aluminum battery with an alcl3/emimcl electrolyte," *Materials*, vol. 11, no. 6, 2018. https://doi.org/10.3390/ma11060936.

[150] L. Smith, T. Ibn-Mohammed, S. C. L. Koh, and I. M. Reaney, "Life cycle assessment and environmental profile evaluations of high volumetric efficiency capacitors," *Applied Energy*, vol. 220, pp. 496–513, 2018. https://doi.org/10.1016/j.apenergy.2018.03.067.

[151] M. Sperling and T. Kivela, "Concept of a dual energy storage system for sustainable energy supply of automated guided vehicles," *Energies*, vol. 15, no. 2, 2022. https://doi.org/10.3390/en15020479.

[152] Maxwell, "2.7 v 350 f ultracapacitor cell," 2019. Available online https://www.mouser.co.uk/pdfDocs/27V350F_ds_3002974-EN1.pdf.

[153] Panasonic, "Lithium ion ncr18650b," 2012. Available online https://www.imrbatteries.com/content/panasonic_ncr18650b-2.pdf.

[154] J. Ruan, Q. Song, and W. Yang, "The application of hybrid energy storage system with electrified continuously variable transmission in battery electric vehicle," *Energy*, vol. 183, pp. 315–330, 2019. https://doi.org/10.1016/j.energy.2019.06.095.

[155] C. Zheng, Y. Wang, Z. Liu, T. Sun, N. Kim, J. Jeong, and S. W. Cha, "A hybrid energy storage system for an electric vehicle and its effectiveness validation," *International Journal of Precision Engineering and Manufacturing-Green Technology*, 2021. https://doi.org/10.1007/s40684-020-00304-5.

[156] L. C. A. Silva, J. J. Eckert, M. A. M. Lourenço, F. L. Silva, F. C. Corrêa, and F. G. Dedini, "Electric vehicle battery-ultracapacitor hybrid energy storage system and drivetrain optimization for a real-world urban driving scenario," *Journal of the Brazilian Society of Mechanical Sciences and Engineering*, vol. 43, no. 5, p. 259, 2021. https://doi.org/10.1007/s40430-021-02975-w.

[157] X. Lu and H. Wang, "Optimal sizing and energy management for cost-effective pev hybrid energy storage systems," *IEEE Transactions on Industrial Informatics*, vol. 16, no. 5, 2020. https://doi.org/10.1109/TII.2019.2957297.

[158] A. Mamun, Z. Liu, D. M. Rizzo, and S. Onori, "An integrated design and control optimization framework for hybrid military vehicle using lithium-ion battery and supercapacitor as energy storage devices," *IEEE Transactions on Transportation Electrification*, vol. 5, no. 1, pp. 239–251, 2019. https://doi.org/10.1109/TTE.2018.2869038.

[159] H. H. Eldeeb, A. T. Elsayed, C. R. Lashway, and O. Mohammed, "Hybrid energy storage sizing and power splitting optimization for plug-in electric vehicles," *IEEE Transactions on Industry Applications*, vol. 55, no. 3, pp. 2252–2262, 2019. https://doi.org/10.1109/TIA.2019.2898839.

[160] J. Shen, S. Dusmez, and A. Khaligh, "Optimization of sizing and battery cycle life in battery/ultracapacitor hybrid energy storage systems for electric vehicle applications," *IEEE Transactions on Industrial Informatics*, vol. 10, no. 4, pp. 2112–2121, 2014. https://doi.org/10.1109/TII.2014.2334233.

[161] A. Ciroth, "Ict for environment in life cycle applications openlca — a new open source software for life cycle assessment," *The International Journal of Life Cycle Assessment*, vol. 12, no. 4, p. 209, 2007. https://doi.org/10.1065/lca2007.06.337.

[162] B. Steubing, G. Wernet, J. Reinhard, C. Bauer, and E. Moreno-Ruiz, "The ecoinvent database version 3 (part ii): analyzing lca results and comparison to version 2," *The International Journal of Life Cycle Assessment*, vol. 21, no. 9, pp. 1269–1281, 2016. https://doi.org/10.1007/s11367-016-1109-6.

[163] G. Wernet, C. Bauer, B. Steubing, J. Reinhard, E. Moreno-Ruiz, and B. Weidema, "The ecoinvent database version 3 (part i): overview and methodology," *The International Journal of Life Cycle Assessment*, vol. 21, no. 9, pp. 1218–1230, 2016. https://doi.org/10.1007/s11367-016-1087-8.

[164] "Gabi software system and database for life cycle engineering," 2015.

[165] A. Ciroth, C. Di Noi, T. Lohse, and M. Srocka, "openlca 1.10, comprehensive user manual," report, GreenDelta, 2020.

[166] N. Otte, "Freshwater ecotoxicity as an impact category in life cycle assessment," report, European Centre for Ecotoxicology and Toxicology of Chemicals, 2016. https://www.ecetoc.org/report_27/summary/.

[167] J. Potocnik, "Commission recommendation of 9 april 2013 on the use of common methods to measure and communicate the life cycle environmental

performance of products and organisations text with eea relevance," *Official Journal of the European Union*, vol. 56, 2013. https://doi.org/10.3000/19770677.L_2013.124.eng.

[168] Sigracell, "Speciality graphites for energy storage," 2016.

[169] J.-Y. Choi, D. J. Lee, Y. M. Lee, Y.-G. Lee, K. M. Kim, J.-K. Park, and K. Y. Cho, "Silicon nanofibrils on a flexible current collector for bendable lithium-ion battery anodes," *Advanced Functional Materials*, vol. 23, no. 17, pp. 2108–2114, 2013. https://doi.org/10.1002/adfm.201202458.

[170] W. Liu, J. Sang, L. Chen, J. Tian, H. Zhang, and G. Olvera Palma, "Life cycle assessment of lead-acid batteries used in electric bicycles in china," *Journal of Cleaner Production*, vol. 108, pp. 1149–1156, 2015. https://doi.org/10.1016/j.jclepro.2015.07.026.

[171] H. C. Kim, T. J. Wallington, R. Arsenault, C. Bae, S. Ahn, and J. Lee, "Cradle-to-gate emissions from a commercial electric vehicle li-ion battery: A comparative analysis," *Environmental Science & Technology*, vol. 50, no. 14, pp. 7715–7722, 2016. https://doi.org/10.1021/acs.est.6b00830.

[172] J. Matheys, W. Van Autenboer, J.-M. Timmermans, J. Van Mierlo, P. Van den Bossche, and G. Maggetto, "Influence of functional unit on the life cycle assessment of traction batteries," *The International Journal of Life Cycle Assessment*, vol. 12, no. 3, p. 191, 2007. https://doi.org/10.1065/lca2007.04.322.

[173] G. Majeau-Bettez, T. R. Hawkins, and A. H. Strømman, "Life cycle environmental assessment of lithium-ion and nickel metal hydride batteries for plug-in hybrid and battery electric vehicles," *Environmental Science Technology*, vol. 45, no. 10, pp. 4548–4554, 2011. https://doi.org/10.1021/es103607c.

[174] Maxwell, "2.7v 5f ultracapacitor cell bcap0005 p270 s01," 2013. Available online https://maxwell.com/wp-content/uploads/2021/08/2_7_5F_ds_3001974_datasheet.pdf.

[175] Maxwell, "3.0 v 150 f ultracapacitor cell," 2019.

[176] N. Elgrishi, K. J. Rountree, B. D. McCarthy, E. S. Rountree, T. T. Eisenhart, and J. L. Dempsey, "A practical beginner's guide to cyclic voltammetry," *Journal of Chemical Education*, vol. 95, no. 2, pp. 197–206, 2018. https://doi.org/10.1021/acs.jchemed.7b00361.

[177] R. Pynn, "Neutron scattering a primer," 1990. Available online 12/2020 https://www.ncnr.nist.gov/summerschool/ss17/pdf/NeutronScatteringPrimer.pdf.

[178] J. J. Biendicho, M. Roberts, C. Offer, D. Noréus, E. Widenkvist, R. I. Smith, G. Svensson, K. Edström, S. T. Norberg, S. G. Eriksson, and S. Hull, "New in-situ neutron diffraction cell for electrode materials," *Journal of Power Sources*, vol. 248, pp. 900–904, 2014. https://doi.org/10.1016/j.jpowsour.2013.09.141.

[179] H. Cavaye, "Neutron spectroscopy: An under-utilised tool for organic electronics research?," *Angewandte Chemie International Edition*, vol. 58, no. 28, pp. 9338–9346, 2019. https://doi.org/10.1002/anie.201812950.

[180] Z. L. Wang, Y. Liu, and Z. Zhang, eds., *X-ray and Neutron Scattering*, pp. 344–371. Boston, MA: Springer US, 2002. https://doi.org/10.1007/0-387-23814-X_12.

[181] B. Salieri, D. A. Turner, B. Nowack, and R. Hischier, "Life cycle assessment of manufactured nanomaterials: Where are we?," *NanoImpact*, vol. 10, pp. 108–120. https://doi.org/10.1016/j.impact.2017.12.003.

[182] N. Melzack, R. G. A. Wills, and A. J. Cruden, "Data in support of the publication 'an environmental perspective on developing dual energy storage for electric vehicles - a case study exploring al-ion vs. supercapacitors alongside li-ion'," 2022. https://doi.org/10.5258/SOTON/D2145 [Dataset].

[183] N. Vukajlović, D. Milićević, B. Dumnić, and B. Popadić, "Comparative analysis of the supercapacitor influence on lithium battery cycle life in electric vehicle energy storage," *Journal of Energy Storage*, vol. 31, p. 101603, 2020. https://doi.org/10.1016/j.est.2020.101603.

[184] H. Bi, H. Zhu, L. Zu, S. He, Y. Gao, and J. Peng, "Combined mechanical process recycling technology for recovering copper and aluminium components of spent lithium-iron phosphate batteries," *Waste Management Research*, vol. 37, no. 8, pp. 767–780, 2019. https://doi.org/10.1177/0734242X19855432.

[185] L. A.-W. Ellingsen, G. Majeau-Bettez, B. Singh, A. K. Srivastava, L. O. Valøen, and A. H. Strømman, "Life cycle assessment of a lithium-ion battery vehicle pack," *Journal of Industrial Ecology*, vol. 18, no. 1, pp. 113–124, 2014. https://doi.org/10.1111/jiec.12072.

[186] M. Shahjalal, P. K. Roy, T. Shams, A. Fly, J. I. Chowdhury, M. R. Ahmed, and K. Liu, "A review on second-life of li-ion batteries: prospects, challenges, and issues," *Energy*, vol. 241, p. 122881, 2022. https://doi.org/10.1016/j.energy.2021.122881.

[187] "Datasheet rs pro cb series epoxy-coated solid electrolytic tantalum capacitor," data sheet, RS PRO. Available online https://docs.rs-online.com/b810/0900766b816c110d.pdf.

[188] "Chip monolithic ceramic capacitor meet aec-q200 for infotainment grt188r61c105ke13 (0603, x5r, 1uf, dc16v)," data sheet, muRata, 2015. Available onlinehttps://www.mouser.co.uk/datasheet/2/281/1/GRT188R61C105KE13_01-1989539.pdf.

[189] C. Minke, U. Kunz, and T. Turek, "Carbon felt and carbon fiber - a techno-economic assessment of felt electrodes for redox flow battery applications," *Journal of Power Sources*, vol. 342, pp. 116–124, 2017. https://doi.org/10.1016/j.jpowsour.2016.12.039.

[190] K. S. Karunadasa and C. Manoratne, "Microstructural view of anatase to rutile phase transformation examined by in-situ high-temperature x-ray powder diffraction," *Journal of Solid State Chemistry*, vol. 314, p. 123377, 2022. https://doi.org/10.1016/j.jssc.2022.123377.

[191] M. Bauccio, "Asm engineered materials reference book, 2nd ed.," 1994.

[192] S. A. E. L. M. A. M. B. P. M. Lam E, Alizadeh-Meghrazi M, "Exploring textile-based electrode materials for electromyography smart garments," *J Rehabil Assist Technol Eng*, 2022. http://dx.doi.org/10.1177/20556683211061995.

[193] A. de Morais, F. L. Pissetti, A. M. S. Lucho, and Y. Gushikem, "Influence of copper hexacyanoferrate film thickness on the electrochemical properties of self-assembled 3-mercaptopropyl gold electrode and application as a hydrazine sensor," *Journal of Solid State Electrochemistry*, vol. 14, pp. 1383–1390, 2010. https://doi.org/10.1007/s10008-009-0965-4.

[194] C. Xu, K. Märker, J. Lee, A. Mahadevegowda, P. J. Reeves, S. J. Day, M. F. Groh, S. P. Emge, C. Ducati, B. Layla Mehdi, C. C. Tang, and C. P. Grey, "Bulk fatigue induced by surface reconstruction in layered ni-rich cathodes for li-ion batteries," *Nature Materials*, vol. 20, no. 1, pp. 84–92, 2021. https://doi.org/10.1038/s41563-020-0767-8.

[195] H. Lahan and S. K. Das, "An approach to improve the al3+ ion intercalation in anatase tio2 nanoparticle for aqueous aluminum-ion battery," *Ionics*, vol. 24, no. 6, pp. 1855–1860, 2018. https://doi.org/10.1007/s11581-018-2530-6.

[196] D. Ma, L. Lai, C. Ponce de Leon, D. Yuan, and P. J. H., "Microwave-assisted self-template synthesis of mesoporous anatase tio2 spheres for non-aqueous al-ion batteries: Textural property optimization and enhanced reversible al3+ storag," *Sustainable Materials and Technologies*, vol. 32, p. e00419. https://doi.org/10.1016/j.susmat.2022.e00419.

[197] J. Joseph, A. P. O'Mullane, and K. Ostrikov, "Hexagonal molybdenum trioxide (h-moo3) as an electrode material for rechargeable aqueous aluminum-ion

batteries," *ChemElectroChem*, vol. 6, no. 24, pp. 6002–6008, 2019. https://doi.org/10.1002/celc.201901890.

[198] P. Parvizi and M. Kazazi, "Binder-free copper hexacyanoferrate electrode prepared by pulse galvanostatic electrochemical deposition for aqueous-based al-ion batteries," *Advanced Ceramics Progress*, vol. 4, no. 2, pp. 27–31, 2018. https://doi.org/10.30501/acp.2018.91122.

[199] F. Nacimiento, M. Cabello, R. Alcántara, P. Lavela, and J. L. Tirado, "Nasicon-type na3v2(po4)3 as a new positive electrode material for rechargeable aluminium battery," *Electrochimica Acta*, vol. 260, pp. 798–804, 2018. https://doi.org/10.1016/j.electacta.2017.12.040.

[200] N. Melzack, *Overwork is not evidence of passion*. Routledge, 2024.

[201] H. Collins, *Passion*. UK: Harper Collins, 2023.

[202] L. E. Houseworth, "The radical history of self-care," *Teen Vougue*, 2021. Available online https://www.teenvogue.com/story/the-radical-history-of-self-care.

[203] H. Nicholls, S. Nicholls, M. andTekin, D. Lamb, and J. Billings, "The impact of working in academia on researchers' mental health and well-being: A systematic review and qualitative meta-synthesis," *PLoS One*, vol. 17, p. e03268890, 2022. https://doi.org/10.1371/journal.pone.0268890.

[204] L. H. Danielle, C. John, C. Philip, G. Nicholas, and G. B. Adrian, "The impact of funding deadlines on personal workloads, stress and family relationships: a qualitative study of australian researchers," *BMJ Open*, vol. 4, p. e004462, 2014. https://doi.org/10.1136/bmjopen-2013-004462.

[205] H. E. S. Agency, "Demographic statistics," 2022. Available online www.hesa.ac.uk.

[206] S. Barkhuizen, N.and Rothmann and F. J. R. Van de Vijver, "Burnout and work engagement of academics in higher education institutions: Effects of dispositional optimism," *Stress and Health*, vol. 30, pp. 322–332, 2014. https://doi.org/10.1002/smi.2520.

[207] N. Maxwell, L. Connolly, and C. Ní Laoire, "Informality, emotion and gendered career paths: The hidden toll of maternity leave on female academics and researchers," *Gender, Work Organization*, vol. 26, pp. 140–157, 2019. https://doi.org/10.1111/gwao.12306.

[208] N. Megoran and O. Mason, "Second class academic citizens: The dehumanising effects of casualisation in higher education," *Union of Colleges and Universities*,

2020. Available online https://www.ucu.org.uk/media/10681/second_class_academic_citizens/pdf/secondclassacademiccitizens.

[209] A. Chitty, F. Callard, and L. Rocha, "University management tactics on strike and asos pay deductions – and ways to push back," *USSbriefs*, 2019. Available online https://medium.com/ussbriefs/university-management-tactics-on-strike-and-asos-pay-deductions-and-ways-to-push-

[210] K. Trigwell and H. Dunbar-Goddet, "The research experience of postgraduate research students at the university of oxford," *Institute for the Advancement of University Learning, University of Oxford*, pp. 1–16, 2005.

[211] C. M. Hazell, J. E. Niven, L. Chapman, S. Roberts, P. E. andCartwright-Hatton, S. Valeix, and C. Berry, "Nationwide assessment of the mental health of uk doctoral researchers," *Humanities and Social Sciences Communications*, vol. 8, p. 305, 2021. https://doi.org/10.1057/s41599-021-00983-8.

[212] J. E. Berry, C.and Niven and C. M. Hazell, "Personal, social and relational predictors of uk postgraduate researcher mental health problems," *BJPsych Open*, vol. 7, p. e205, 2021. https://doi.org/10.1192/bjo.2021.1041.

[213] M. Price, "Time harms: Disabled faculty navigating the accomodations loop," *South Atlantic Quarterly*, vol. 120, pp. 257–277, 2021. https://doi.org/10.1215/00382876-8915966.

[214] R. Hall and K. Bowles, "Re-engineering higher education: The subsumption of academic labour and the exploitation of anxiety," *Workplace*, pp. 30–47, 2016. https://doi.org/10.14288/workplace.v0i28.18621.